

Benchmark Analyses of Sodium Natural Convection in the Upper Plenum of the Monju Reactor Vessel

*Final Report of a Coordinated
Research Project 2008–2012*



IAEA

International Atomic Energy Agency

BENCHMARK ANALYSES OF
SODIUM NATURAL CONVECTION
IN THE UPPER PLENUM OF THE
MONJU REACTOR VESSEL

The following States are Members of the International Atomic Energy Agency:

AFGHANISTAN	GHANA	OMAN
ALBANIA	GREECE	PAKISTAN
ALGERIA	GUATEMALA	PALAU
ANGOLA	HAITI	PANAMA
ARGENTINA	HOLY SEE	PAPUA NEW GUINEA
ARMENIA	HONDURAS	PARAGUAY
AUSTRALIA	HUNGARY	PERU
AUSTRIA	ICELAND	PHILIPPINES
AZERBAIJAN	INDIA	POLAND
BAHAMAS	INDONESIA	PORTUGAL
BAHRAIN	IRAN, ISLAMIC REPUBLIC OF	QATAR
BANGLADESH	IRAQ	REPUBLIC OF MOLDOVA
BELARUS	IRELAND	ROMANIA
BELGIUM	ISRAEL	RUSSIAN FEDERATION
BELIZE	ITALY	RWANDA
BENIN	JAMAICA	SAN MARINO
BOLIVIA	JAPAN	SAUDI ARABIA
BOSNIA AND HERZEGOVINA	JORDAN	SENEGAL
BOTSWANA	KAZAKHSTAN	SERBIA
BRAZIL	KENYA	SEYCHELLES
BRUNEI DARUSSALAM	KOREA, REPUBLIC OF	SIERRA LEONE
BULGARIA	KUWAIT	SINGAPORE
BURKINA FASO	KYRGYZSTAN	SLOVAKIA
BURUNDI	LAO PEOPLE'S DEMOCRATIC	SLOVENIA
CAMBODIA	REPUBLIC	SOUTH AFRICA
CAMEROON	LATVIA	SPAIN
CANADA	LEBANON	SRI LANKA
CENTRAL AFRICAN	LESOTHO	SUDAN
REPUBLIC	LIBERIA	SWAZILAND
CHAD	LIBYA	SWEDEN
CHILE	LIECHTENSTEIN	SWITZERLAND
CHINA	LITHUANIA	SYRIAN ARAB REPUBLIC
COLOMBIA	LUXEMBOURG	TAJIKISTAN
CONGO	MADAGASCAR	THAILAND
COSTA RICA	MALAWI	THE FORMER YUGOSLAV
CÔTE D'IVOIRE	MALAYSIA	REPUBLIC OF MACEDONIA
CROATIA	MALI	TOGO
CUBA	MALTA	TRINIDAD AND TOBAGO
CYPRUS	MARSHALL ISLANDS	TUNISIA
CZECH REPUBLIC	MAURITANIA, ISLAMIC	TURKEY
DEMOCRATIC REPUBLIC	REPUBLIC OF	UGANDA
OF THE CONGO	MAURITIUS	UKRAINE
DENMARK	MEXICO	UNITED ARAB EMIRATES
DOMINICA	MONACO	UNITED KINGDOM OF
DOMINICAN REPUBLIC	MONGOLIA	GREAT BRITAIN AND
ECUADOR	MONTENEGRO	NORTHERN IRELAND
EGYPT	MOROCCO	UNITED REPUBLIC
EL SALVADOR	MOZAMBIQUE	OF TANZANIA
ERITREA	MYANMAR	UNITED STATES OF AMERICA
ESTONIA	NAMIBIA	URUGUAY
ETHIOPIA	NEPAL	UZBEKISTAN
FIJI	NETHERLANDS	VENEZUELA, BOLIVARIAN
FINLAND	NEW ZEALAND	REPUBLIC OF
FRANCE	NICARAGUA	VIET NAM
GABON	NIGER	YEMEN
GEORGIA	NIGERIA	ZAMBIA
GERMANY	NORWAY	ZIMBABWE

The Agency's Statute was approved on 23 October 1956 by the Conference on the Statute of the IAEA held at United Nations Headquarters, New York; it entered into force on 29 July 1957. The Headquarters of the Agency are situated in Vienna. Its principal objective is "to accelerate and enlarge the contribution of atomic energy to peace, health and prosperity throughout the world".

IAEA-TECDOC-1754

**BENCHMARK ANALYSES OF
SODIUM NATURAL CONVECTION
IN THE UPPER PLENUM OF THE
MONJU REACTOR VESSEL**

**FINAL REPORT OF A COORDINATED RESEARCH
PROJECT 2008–2012**

**INTERNATIONAL ATOMIC ENERGY AGENCY
VIENNA, 2014**

COPYRIGHT NOTICE

All IAEA scientific and technical publications are protected by the terms of the Universal Copyright Convention as adopted in 1952 (Berne) and as revised in 1972 (Paris). The copyright has since been extended by the World Intellectual Property Organization (Geneva) to include electronic and virtual intellectual property. Permission to use whole or parts of texts contained in IAEA publications in printed or electronic form must be obtained and is usually subject to royalty agreements. Proposals for non-commercial reproductions and translations are welcomed and considered on a case-by-case basis. Enquiries should be addressed to the IAEA Publishing Section at:

Marketing and Sales Unit, Publishing Section
International Atomic Energy Agency
Vienna International Centre
PO Box 100
1400 Vienna, Austria
fax: +43 1 2600 29302
tel.: +43 1 2600 22417
email: sales.publications@iaea.org
<http://www.iaea.org/books>

For further information on this publication, please contact:

Nuclear Power Technology Development Section
International Atomic Energy Agency
Vienna International Centre
PO Box 100
1400 Vienna, Austria
Email: Official.Mail@iaea.org

© IAEA, 2014
Printed by the IAEA in Austria
November 2014

IAEA Library Cataloguing in Publication Data

Benchmark analyses of sodium natural convection in the upper plenum of the Monju reactor vessel : final report of a coordinated research project 2008–2012. — Vienna : International Atomic Energy Agency, 2014.
p. ; 30 cm. — (IAEA-TECDOC series, ISSN 1011-4289 ; no. 1754)
ISBN 978-92-0-109614-2
Includes bibliographical references.

1. Fast reactors — Testing. 2. Fast reactors — Cooling.
3. Sodium cooled reactors. I. International Atomic Energy Agency. II. Series.

FOREWORD

The IAEA supports Member States in the area of advanced fast reactor technology development by providing a major fulcrum for information exchange and collaborative research programmes. The IAEA's activities in this field are mainly carried out within the framework of the Technical Working Group on Fast Reactors (TWG-FR), which assists in the implementation of corresponding IAEA support, and ensures that all technical activities are in line with expressed needs of Member States. Among this broad range, the IAEA proposes and establishes coordinated research projects (CRPs), aimed at improving Member State capability in fast reactor design and analysis.

An important opportunity to perform collaborative research activities was provided by the system startup tests carried out by the Japan Atomic Energy Agency (JAEA) in the prototype loop type sodium cooled fast reactor Monju, in particular a turbine trip test performed in December 1995. As the JAEA opened the experimental dataset to international collaboration in 2008, the IAEA launched the CRP on Benchmark Analyses of Sodium Natural Convection in the Upper Plenum of the Monju Reactor Vessel.

The CRP, together with eight institutes from seven States, has contributed to improving capabilities in sodium cooled fast reactors simulation through code verification and validation, with particular emphasis on thermal stratification and natural circulation phenomena.

The objective of this publication is to document the results and main achievements of the CRP. The IAEA expresses its appreciation to all participants in the CRP for their dedicated efforts leading to this publication. The IAEA officer responsible for this publication was S. Monti of the Division of Nuclear Power.

EDITORIAL NOTE

This publication has been prepared from the original material as submitted by the contributors and has not been edited by the editorial staff of the IAEA. The views expressed remain the responsibility of the contributors and do not necessarily represent the views of the IAEA or its Member States.

Neither the IAEA nor its Member States assume any responsibility for consequences which may arise from the use of this publication. This publication does not address questions of responsibility, legal or otherwise, for acts or omissions on the part of any person.

The use of particular designations of countries or territories does not imply any judgement by the publisher, the IAEA, as to the legal status of such countries or territories, of their authorities and institutions or of the delimitation of their boundaries.

The mention of names of specific companies or products (whether or not indicated as registered) does not imply any intention to infringe proprietary rights, nor should it be construed as an endorsement or recommendation on the part of the IAEA.

The IAEA has no responsibility for the persistence or accuracy of URLs for external or third party Internet web sites referred to in this publication and does not guarantee that any content on such web sites is, or will remain, accurate or appropriate.

CONTENTS

1. INTRODUCTION	1
1.1. Objectives of the coordinated research project.....	1
1.2. Importance of thermal stratification in the upper plenum of sodium cooled fast reactors	1
1.3. Procedure for CRP implementation.....	2
2. DESCRIPTION OF MONJU	2
2.1. Reactor	3
2.2. Heat transport system.....	4
2.2.1. Primary heat transport system	4
2.2.2. Secondary heat transport system.....	4
2.2.3. Water/steam system and turbines	4
2.3. Generator and substation.....	4
2.4. Basic specifications of the plant	5
3. TURBINE TRIP TEST FROM 40% ELECTRIC OUTPUT CONDITION CONDUCTED IN DECEMBER 1995	7
4. TIME CHANGE OF TEMPERATURES ON THE VERTICAL TC PLUG	8
5. BENCHMARK SPECIFICATIONS	18
5.1. Geometry description of the Monju reactor vessel upper plenum.....	18
5.1.1. Coordinate system applied to the descriptions	19
5.1.2. Reactor vessel wall and the three outlet nozzles	21
5.1.3. Inner barrel	23
5.1.4. Upper support plate, core barrel, in-vessel racks and in-vessel transfer machine lower guide	23
5.1.5. Upper core structure.....	25
5.1.6. Fuel handling machine (hold down arm)	32
5.1.7. Dip plate	32
5.1.8. Thermocouple plug	33
5.2. Flow inlet boundary conditions	34
6. DESCRIPTION OF MODELS	41
6.1. Description of simplified geometry	41
6.1.1. Overview	42
6.1.2. Inlet boundary regions.....	43
6.1.3. Upper core structures	45
6.2. Description of porous body model for the upper core structure.....	47
6.3. Methods, codes and models.....	49
6.3.1. 1/6 sector model.....	49
6.3.2. Full sector model	59

6.4. Thermo-physical properties.....	65
6.4.1. Provided equations.....	65
6.4.2. Other equations.....	65
7. PRELIMINARY RESULTS BASED ON BENCHMARK SPECIFICATION.....	67
7.1. Steady and transient simulations.....	67
7.1.1. CIAE.....	67
7.1.2. CEA.....	71
7.1.3. IGCAR.....	77
7.1.4. JAEA.....	81
7.1.5. University of Fukui.....	84
7.1.6. KAERI.....	86
7.1.7. IPPE.....	89
7.2. Sensitivity analysis to investigate the discrepancies with experimental data.....	97
7.2.1. CIAE.....	97
7.2.2. CEA.....	99
7.2.3. IGCAR.....	107
7.2.4. JAEA.....	113
7.2.5. University of Fukui.....	118
7.2.6. KAERI.....	121
7.2.7. IPPE.....	123
7.2.8. ANL.....	129
7.3. Outcome of sensitivity analysis and recommendations for further simulations.....	133
7.3.1. CIAE.....	133
7.3.2. CEA.....	134
7.3.3. IGCAR.....	134
7.3.4. JAEA.....	135
7.3.5. University of Fukui.....	135
7.3.6. KAERI.....	135
7.3.7. IPPE.....	135
7.3.8. ANL.....	136
8. FINAL CRP RESULTS.....	136
8.1. Steady state and transient results.....	136
8.1.1. CIAE.....	136
8.1.2. CEA.....	139
8.1.3. IGCAR.....	139
8.1.4. JAEA.....	142
8.1.5. University of Fukui.....	142
8.1.6. KAERI.....	143
8.1.7. IPPE.....	146
8.1.8. ANL.....	149
8.2. Comparison of results.....	151
9. CONCLUSIONS.....	155

REFERENCES.....	159
LIST OF ABBREVIATIONS.....	163
CONTRIBUTORS TO DRAFTING AND REVIEW.....	165

1. INTRODUCTION

1.1. OBJECTIVES OF THE COORDINATED RESEARCH PROJECT

The JAEA performed a turbine trip transient test from 40% rated electrical power in December 1995, as a system startup test (SST) of the Japanese prototype fast breeder reactor Monju, and obtained detailed experimental data in the upper plenum of the reactor vessel (RV). These measurements captured the thermal stratification phenomena. The data, considered to be useful for the validation of thermal-hydraulic codes for sodium cooled fast reactors (SFR), were offered to the IAEA which decided to launch a coordinated research project (CRP) titled ‘Benchmark analyses of sodium natural convection in the upper plenum of Monju reactor vessel’.

The overall objective of the CRP was to improve Member States’ analytical capabilities in the field of fast reactor in-vessel sodium thermal-hydraulics. A necessary condition towards achieving this objective is a wide international validation effort of the data and codes currently employed for the simulation of the various physical effects involved in this field. The CRP contributed towards achieving this objective with the help of benchmark exercises focusing, in this first stage, on the numerical simulation of thermal stratification of sodium observed in the Monju reactor vessel at a turbine trip test conducted in December 1995 during the original startup experiments, and with the help of a thorough assessment of the calculation versus measured data comparisons.

The CRP’s specific research objectives were:

- Review of the detailed description of the boundary conditions of the above mentioned test, as well as of all the experimental data obtained and specification of the benchmark models;
- Validation of various multi-dimensional fluid dynamics codes in use in Member States through simulation of sodium cooled fast reactor upper plenum temperature distributions and comparison with measured data;
- Identification of weaknesses in current methodologies and of the R&D needs to resolve the identified open issues.

1.2. IMPORTANCE OF THERMAL STRATIFICATION IN THE UPPER PLENUM OF SODIUM COOLED FAST REACTORS

Thermal-hydraulic phenomena in the RV upper plenum of SFRs such as thermal stratification in the post-scrum transients may cause severe thermal stress problems. The thermal stratification occurs in low flow rate conditions such as plant shutdown under pony motor operation, with buoyancy force largely affecting both flow and temperature fields. Mock-up tests using water and sodium as working fluids have been conducting in many organizations in order to evaluate these phenomena and validate numerical simulation codes. However, in the past detailed calculations were not feasible and/or satisfactory because of the limited computational power and lack of suitable numerical algorithms. Recently, numerical analysis codes with highly advanced algorithms have been developed and the computational performances have been also improved remarkably [1]. As a consequence, thermal-hydraulic analyses of large and complex regions have turned out to be practicable with reasonable computational costs, making the utilization of high performance thermal-hydraulic codes become common practice for the design and the safety analysis of SFRs. However, due to the limited availability of experimental data coming from the few SFRs in operation, these codes have not been extensively validated so far. The data measured during the original startup tests

of the Monju reactor represent, therefore, a unique occasion to validate thermal-hydraulics codes for natural circulation in complex geometry.

1.3. PROCEDURE FOR CRP IMPLEMENTATION

The CRP was carried out between 2008 and 2012, with the aim to improve the participants' analytical capabilities in the field of fast reactor in-vessel sodium thermal-hydraulics. Eight research organizations from seven countries with an active programme on SFRs – namely China, France, India, Japan, Republic of Korea, Russian Federation and the USA – contributed to this CRP. The experimental data for the benchmark analysis were provided by the JAEA [2] and concerned the measurements of thermal stratification of sodium observed at the turbine trip test during the original SST. In particular, the CRP participants were provided with the vertical temperature distribution and outlet temperatures of fuel subassemblies measured during the test. The thermal-hydraulic simulations performed in view of the subsequent comparison with the experimental data were rather challenging due to the complex geometry of the upper plenum of the Monju RV which, in particular, includes an inner barrel with many flow holes, as well as an upper core structure (UCS) composed of fingers, control rod guide tubes (CRGTs), and flow guide tubes (FGTs). The approaches for the development of the models and simulation of various parameters of the participating organizations were discussed in the four research coordination meetings (RCMs) held in 2008 at the IAEA headquarters, in 2009 at the Commissariat à l'énergie atomique et aux énergies alternatives (CEA), France, in 2010 at the Argonne National Laboratory (ANL), USA, and in 2012 at the JAEA, Japan. Preliminary results were also presented at various international conferences by the various organizations participating in the CRP [3–10].

This report describes the main results of the simulations and the comparison with the experimental data. These comparisons substantiate the claim that the CRP was successful since (i) it contributed towards validating different thermal-hydraulic codes used by the participants in this efforts, and (ii) it identified the key parameters that affect the thermal stratification phenomena in the upper plenum of advanced SFRs.

2. DESCRIPTION OF MONJU

Monju is a nuclear power plant which breeds fuels by fast neutrons and is cooled by sodium. It is a power generating prototype reactor and has been developed to confirm its function as a power generating plant and the technical feasibility of power increasing capability. Thus, the data obtained while generating power will be utilized for the development of a future fast breeder reactor. The main cooling system of the reactor consists of three loops. The thermal output is 714 MW, and the electric output is 280 MW, due to the high thermal efficiency. The schematic of the reactor is shown in Fig. 1. The heat transport system including the generator and substation are shown in Fig. 2.

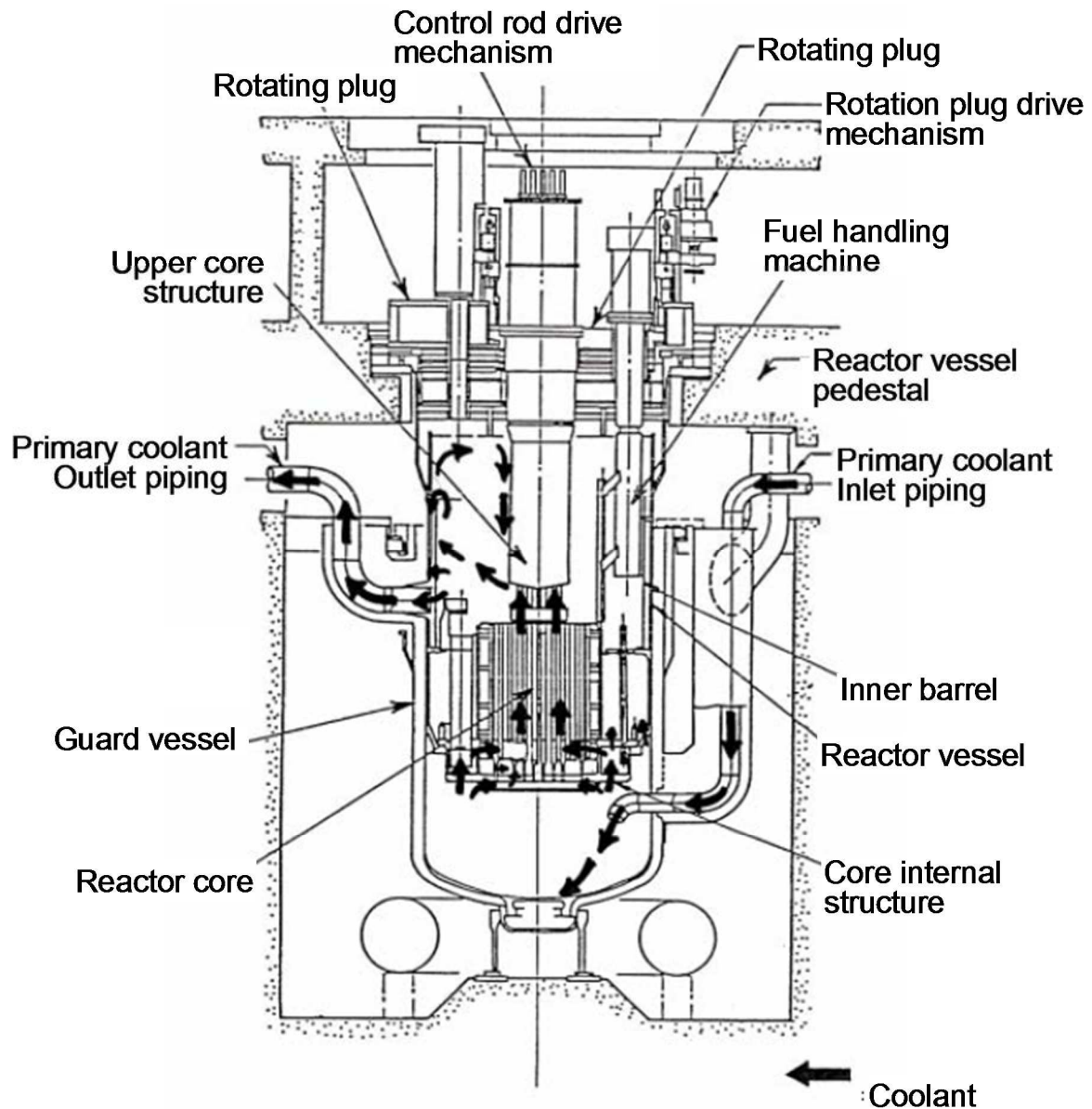


FIG. 1. The schematic of MONJU reactor.

2.1. REACTOR

The reactor of the Monju plant consists of core fuel assemblies, blanket fuel assemblies, control rods, core internals structure, upper core structure, shield plug, reactor vessel, guard vessel, etc. The cylindrical reactor vessel is a vertical type, made of stainless steel and installed in a guard vessel. The reactor vessel is fabricated adopting peripheral welding structure of twelve forged rings, aiming at the improvement of reliability and the simplification of the in-service inspection (ISI) system.

The nuclear heat generated in the core is cooled by the sodium which flows into the reactor vessel through three inlet nozzles located at the lower part of the vessel and flows out through three outlet nozzles. The top of the reactor vessel is covered by a shield plug to shield the heat and radiation from the core, which consists of a fixed plug and an off-centered rotating plug. A fuel handling machine can be mounted on the upper side of the rotating plug, and the upper core structure is suspended on the downside of it. Nineteen control rods are driven by

the control rod drive mechanisms mounted on the rotating plug. The control rods are designed to free fall into the core in case of emergency, by cutting current supply to the electromagnets connecting the rod top to the rod drivers.

Horizontal displacement of the reactor guard vessel is restricted by a lower support structure equipped on the floor. The lower support structure has a highly accurate inlay structure, aiming at absorption the thermal expansion effect and maintaining the installation accuracy.

2.2. HEAT TRANSPORT SYSTEM

2.2.1. Primary heat transport system

Each loop of the primary heat transport system (PHTS) consists of an intermediate heat exchanger (IHX), a pump, a reactor vessel (RV) and pipes connecting these components. The heated sodium in the core is transported from the RV to the IHX where heat is transferred from primary to secondary sodium and the cooled sodium is circulated back to a RV by pump. The sodium entered the RV from its lower part is heated in the core while flowing upward.

2.2.2. Secondary heat transport system

Each loop of the secondary heat transport system (SHTS) consists of a steam generator (SG), a pump and pipes connecting the two and the IHX. The secondary sodium heated in the IHX is transported to the SG where steam is produced. One SG consists of an evaporator (EV) which produces steam from water and a super heater (SH) which produces superheated steam. The sodium out of the SG is circulated back to the IHX by the pump.

2.2.3. Water/steam system and turbines

The superheated steam from the three SHs goes to a turbine through main steam stop valves, and generates electricity by driving the turbine and a generator connected to it. The turbine consists of one high-pressure and two low-pressure turbines, all in series. The steam from the turbine goes to a condenser where it is condensed by seawater and sent to a feed water line by pumps. The feed water is heated while going through low-pressure heaters, a deaerator and high-pressure heaters and finally sent to three EVs.

2.3. GENERATOR AND SUBSTATION

Electricity is generated by the turbine-driven generator. A single generator produces 280 MW(e) and its speed is 3600 rpm. The generated electricity, after its voltage being increased from 15 kV to 275 kV, is sent to a switch yard through underground cables and connected to power lines.

Plant Specifications

Thermal output : 714 MW / Electrical output : 280 MWe
 Fuel : MOX
 PHTS Hot/Cold-leg temp. : 529/397 °C
 Coolant: Sodium (3 Loop-Type)

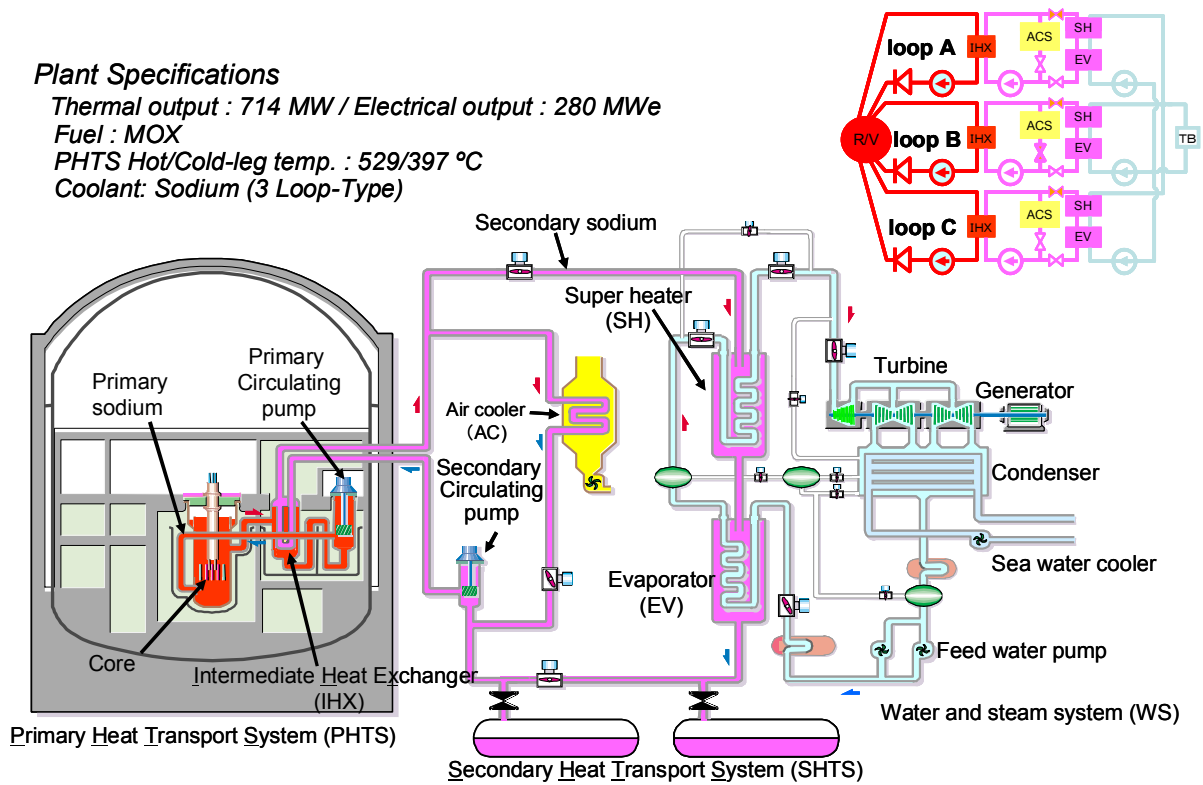


FIG. 2. Schematic of heat transport system, generator and substation of Monju.

2.4. BASIC SPECIFICATIONS OF THE PLANT

Reactor type	Sodium-cooled FBR
Purpose	Development of FBR and power generation
Thermal output	714 MW
Electric output	280 MW

Fuel

Composition	Pu-U mixed oxide
Pu enrichment (%Pu fiss.)	16/21 (inner/outer)
Fiss. Pu mass	1 t*
Breeding ratio	1.2*
Average burn-up	80,000 MWd/t*

Core fuel subassemblies (S/A)

No. of fuel subassemblies	198
No. of fuel pins per S/A	169
Length of fuel pin	2.8 m*
Length of S/A	4.2 m*
Material of fuel pin	SS 316 equivalent
Max. temp. of fuel pin	675 °C*

Radial breeder blanket subassemblies

No. of blanket subassemblies	172
No. of fuel pins per S/A	61
Length of fuel pin	2.8 m*

Length of S/A	4.2 m*
Fuel pin material	SS 316 equivalent

Control rods

No. of control rods	3/10/6 (fine control/coarse control/backup shutdown)
No. of elements per rod	19
Effective height of absorber	0.93 m*
Material of control element	Boron Carbide (B ₄ C)

Reactor vessel

Form	Cylindrical vessel with end-plate at the bottom
Inner diameter	7.1 m*
Height	17.8 m*
Material	SS 304

Primary heat transport system (PHTS)

Coolant	Sodium
Sodium Quantity	760 t*
Flow rate/loop	5,100,000 Kg/h* (/loop)
RV inlet/outlet sodium temp.	397/529 °C*

Secondary heat transport system (SHTS)

Coolant	Sodium
Sodium Quantity	760 t*
Flow rate/loop	3,700,000 Kg/h* (/loop)
IHX secondary inlet/outlet temp.	325/505 °C*

Water-steam system

Feed water temperature	241 °C*
Turbine inlet steam temp.	483 °C*
Max. EV inlet feed water pressure	1.62×10 ⁷ Pa (absolute value)
Turbine inlet steam pressure	1.26×10 ⁷ Pa (absolute value)
Feed water flow rate	379,000 Kg/h* (/loop)

Note: * indicates approximate figures.

3. TURBINE TRIP TEST FROM 40% ELECTRIC OUTPUT CONDITION CONDUCTED IN DECEMBER 1995

The purpose of this test was to confirm the safety feature of Monju plant against turbine failure, by generating a simulated 'condenser vacuum low' signal to confirm that the plant is safely shutdown as designed.

The major plant responses following the simulated anomaly signal are shown in Fig. 3.

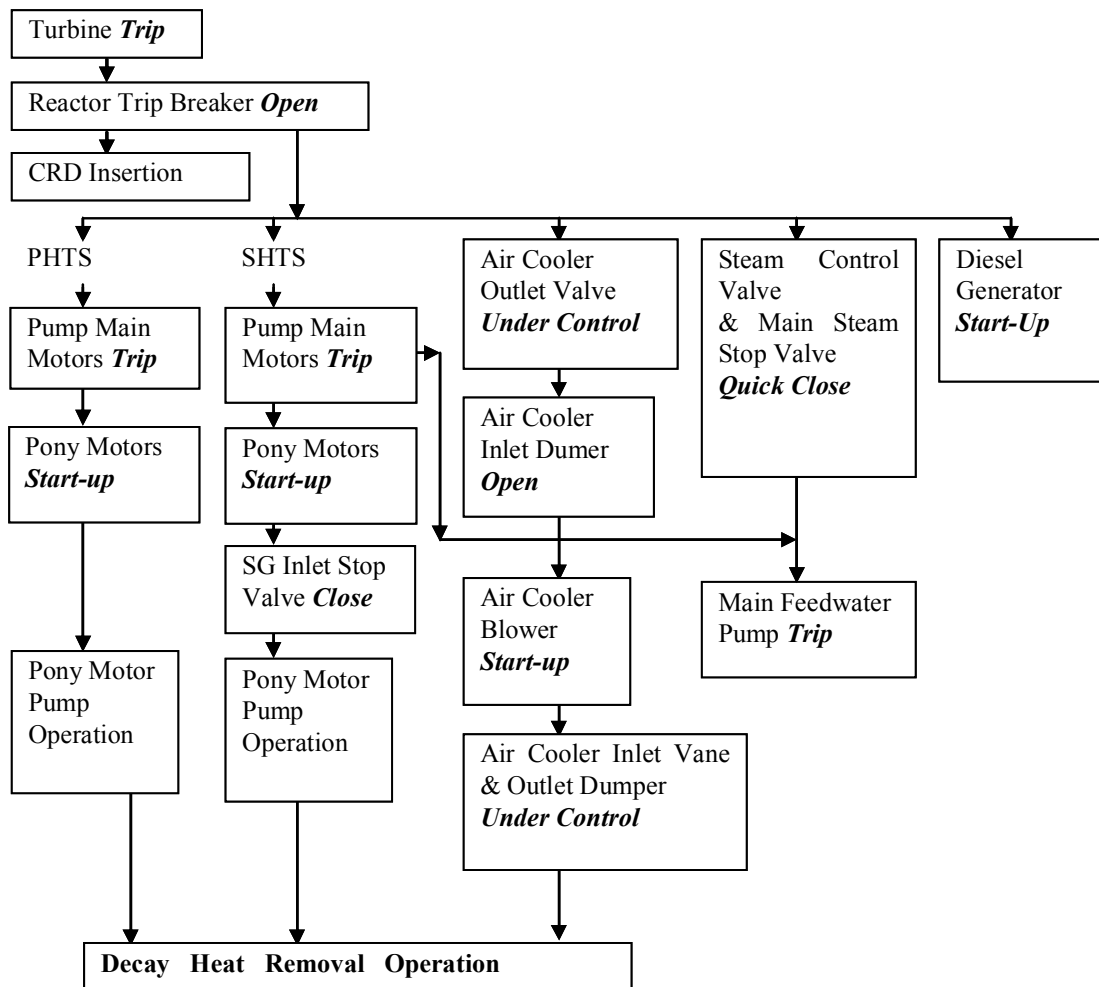


FIG. 3. The turbine trip test sequence of 40% rated power operation.

After these actions, the residual heat was released to the atmosphere by means of sodium-air heat exchangers installed in parallel with the SGs, via sodium circulation in PHTS and in SHTS, maintaining by pony motor operations approximately 10% and 8% of the nominal flow rates, respectively. The decay heat removal capability in case of turbine failures has been confirmed, though the PHTS sodium flow rate was so small that sodium temperature stratification took place in the reactor vessel upper plenum.

4. TIME CHANGE OF TEMPERATURES ON THE VERTICAL TC PLUG

Temperatures measured by the vertical array of thermocouples in the reactor upper plenum during the turbine trip test in December 1995 are provided basically on the same time points as the flow inlet boundary data submitted at the kick-off meeting of the CRP, with some additional time points in steep temporal gradients. Each temperature value is the average within the 1 second time window, in order to cancel oscillations of temperatures measured at intervals of 0.1 second.

The vertical positions of the TCs inserted in the RV upper plenum are shown in Fig. 4, and the temperature changes measured by the TCs are given in Figs. 5–14. Time constant (amount of time required for a thermocouple to indicated 63.2% of step change in temperature of a surrounding media) of these TCs is measured to be 57 ± 9 ms in a separate test.

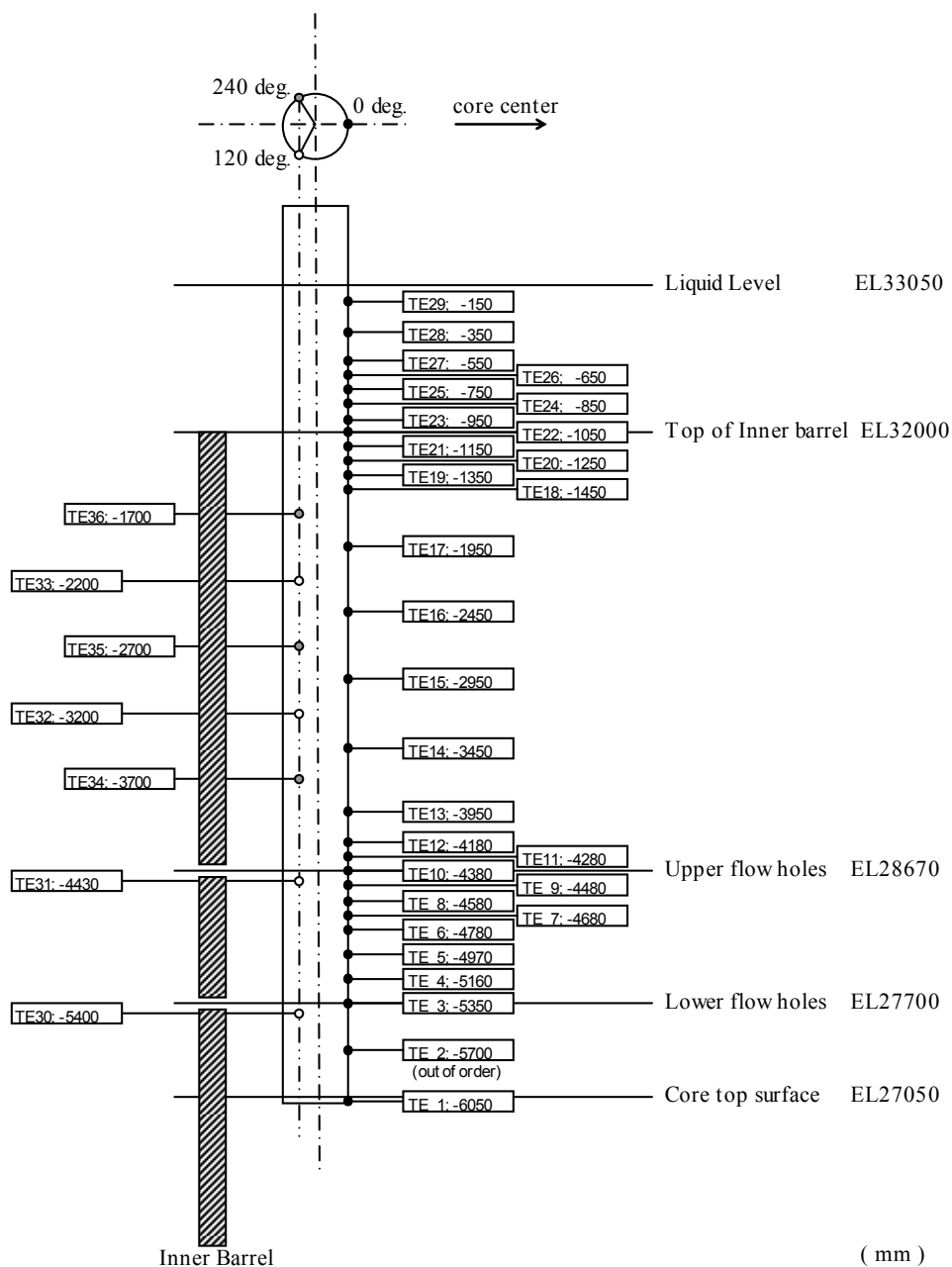


FIG. 4. Vertical positions of TCs inserted in the RV upper plenum.

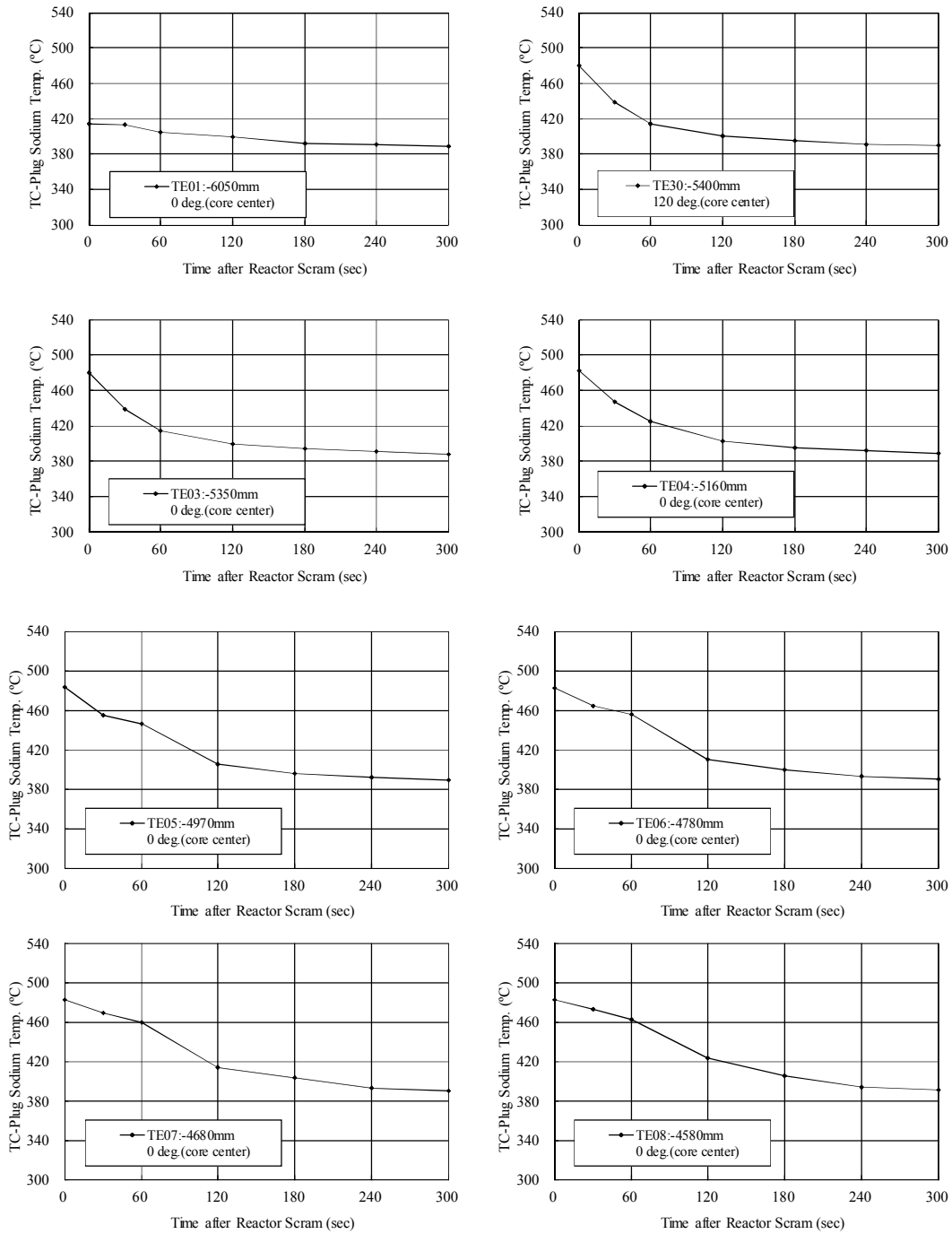


FIG. 5. TC-Plug sodium temperature 0-300 s (1/5).

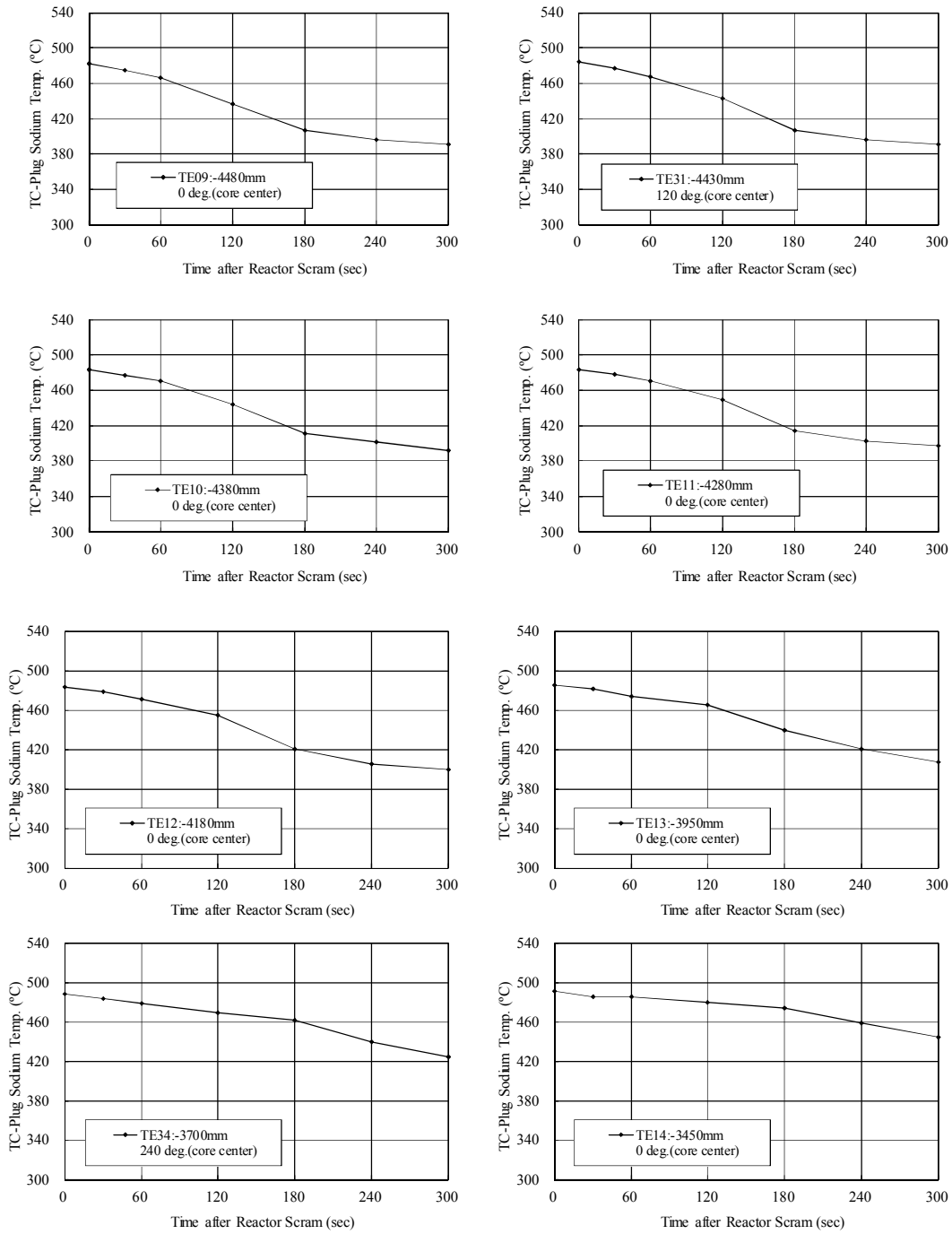


FIG. 6. TC-Plug sodium temperature 0-300 s (2/5).

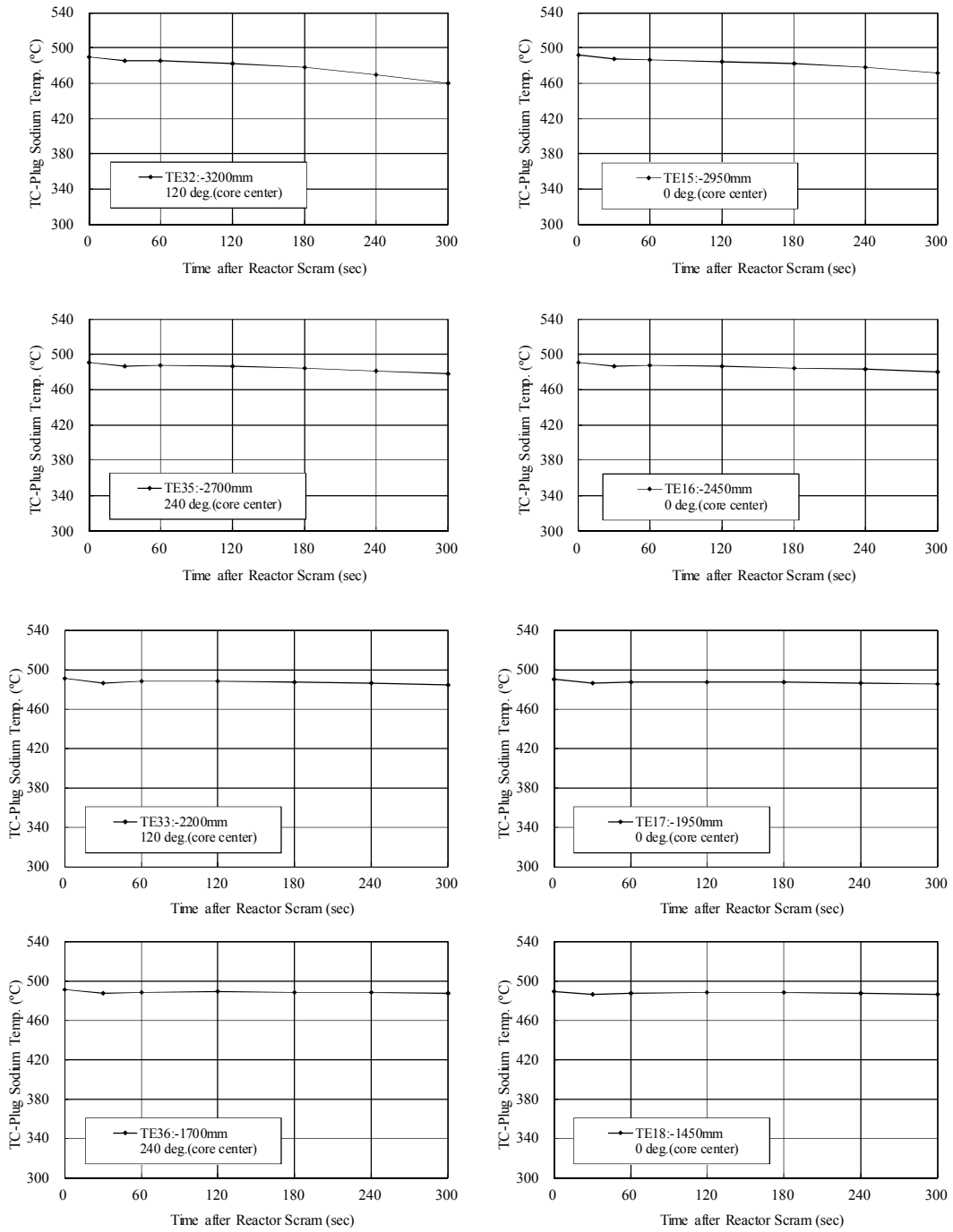


FIG. 7. TC-Plug sodium temperature 0-300 s (3/5).

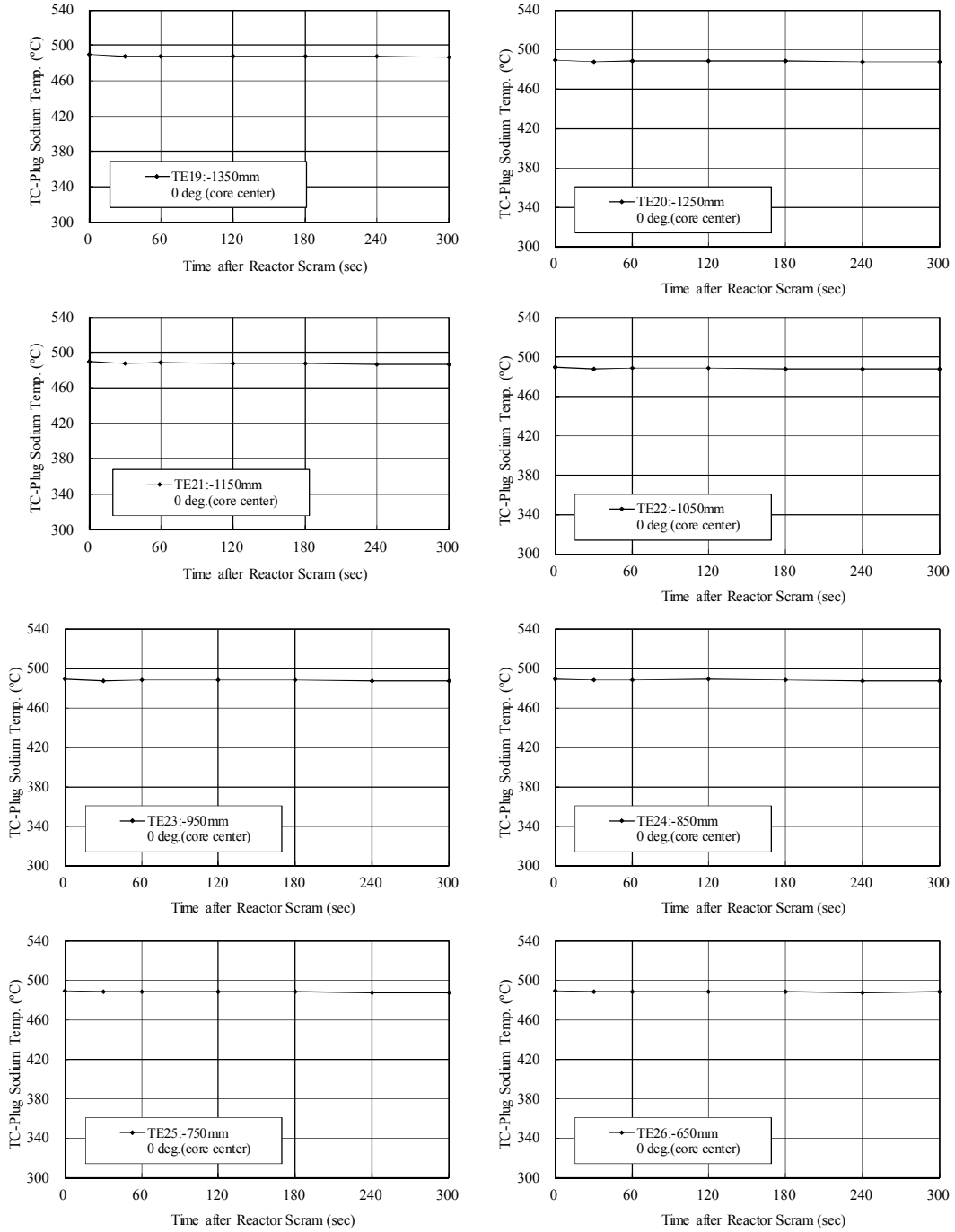


FIG. 8. TC-Plug sodium temperature 0-300 s (4/5).

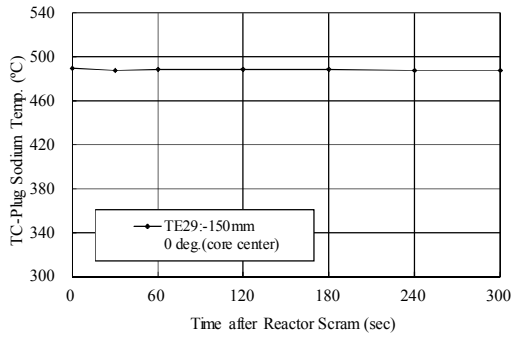
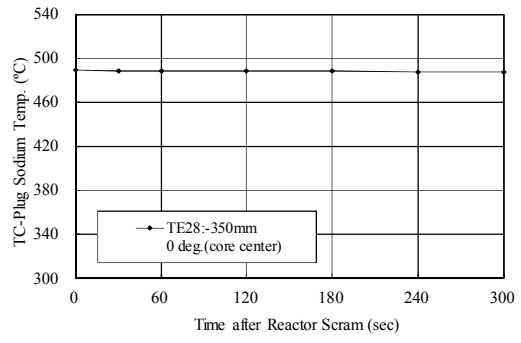
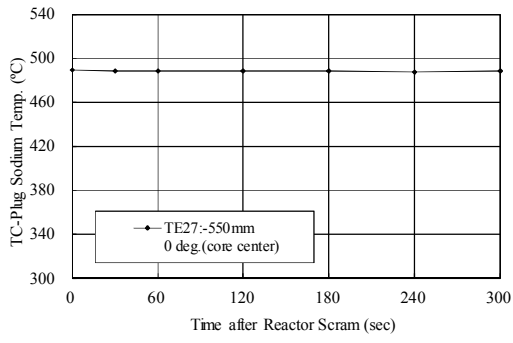


FIG. 9. TC-Plug sodium temperature 0-300 s (5/5).

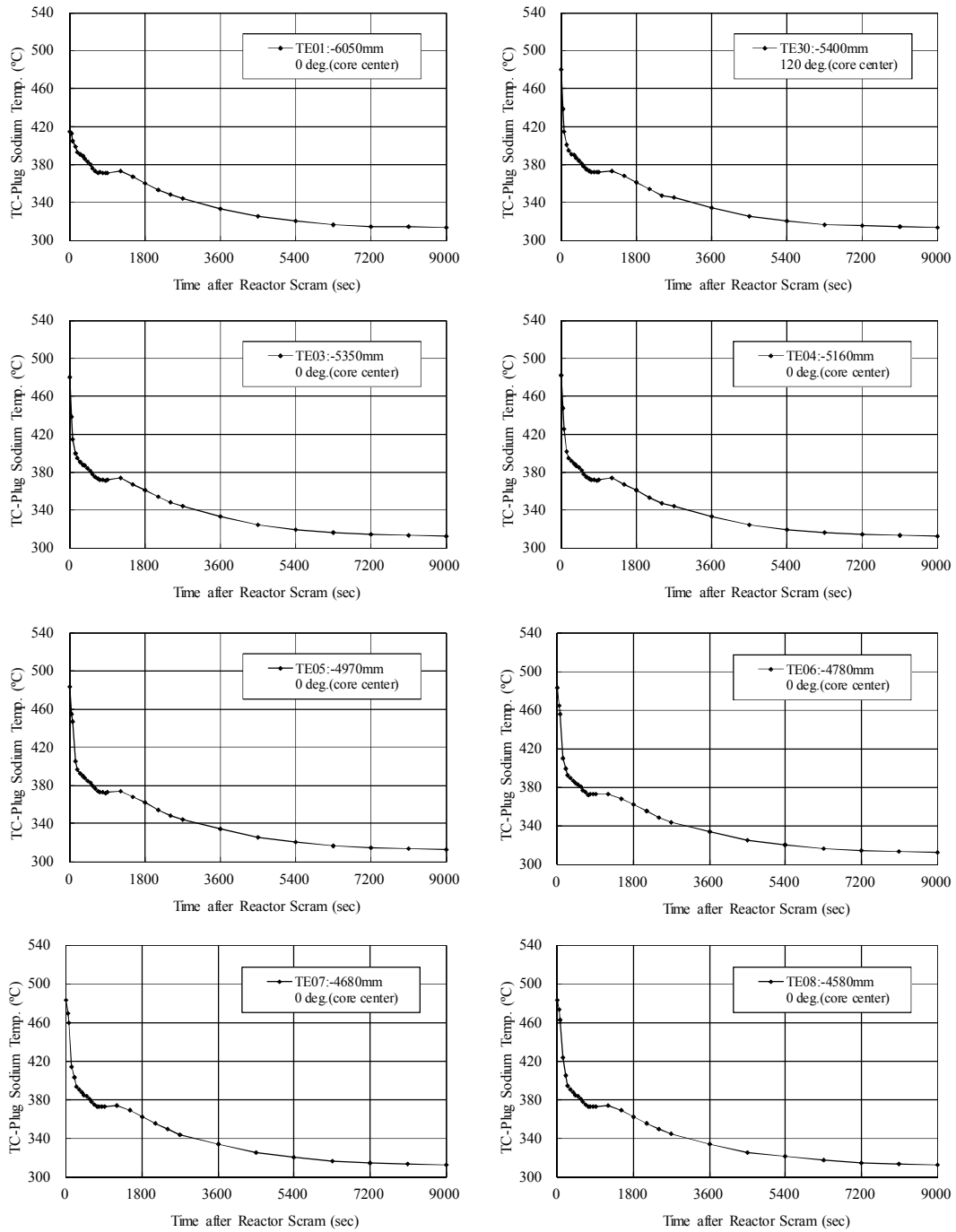


FIG. 10. TC-Plug sodium temperature 0-9000 s (1/5).

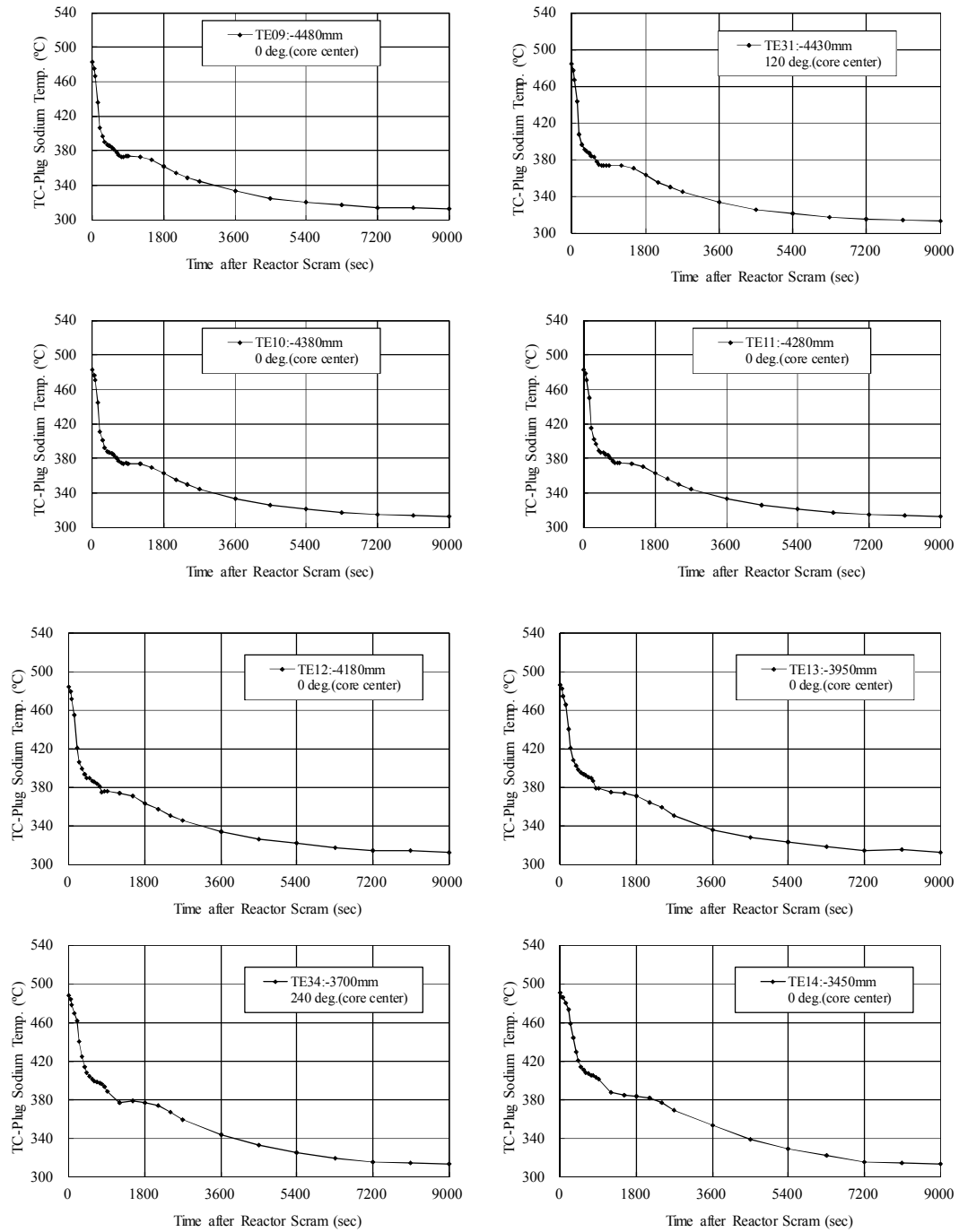


FIG. 11. TC-Plug sodium temperature 0-9000 s (2/5).

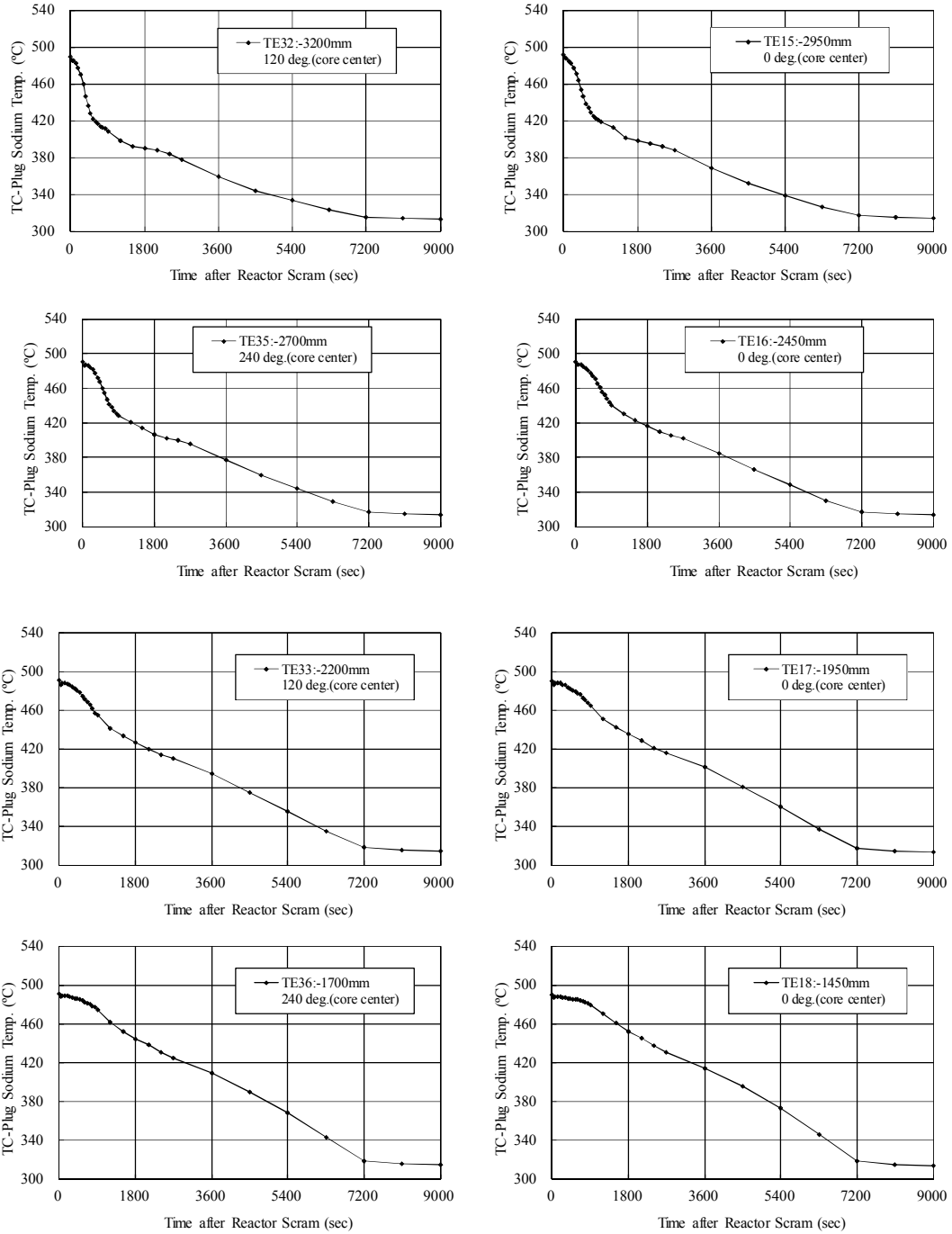


FIG. 12. TC-Plug sodium temperature 0-9000 s (3/5).

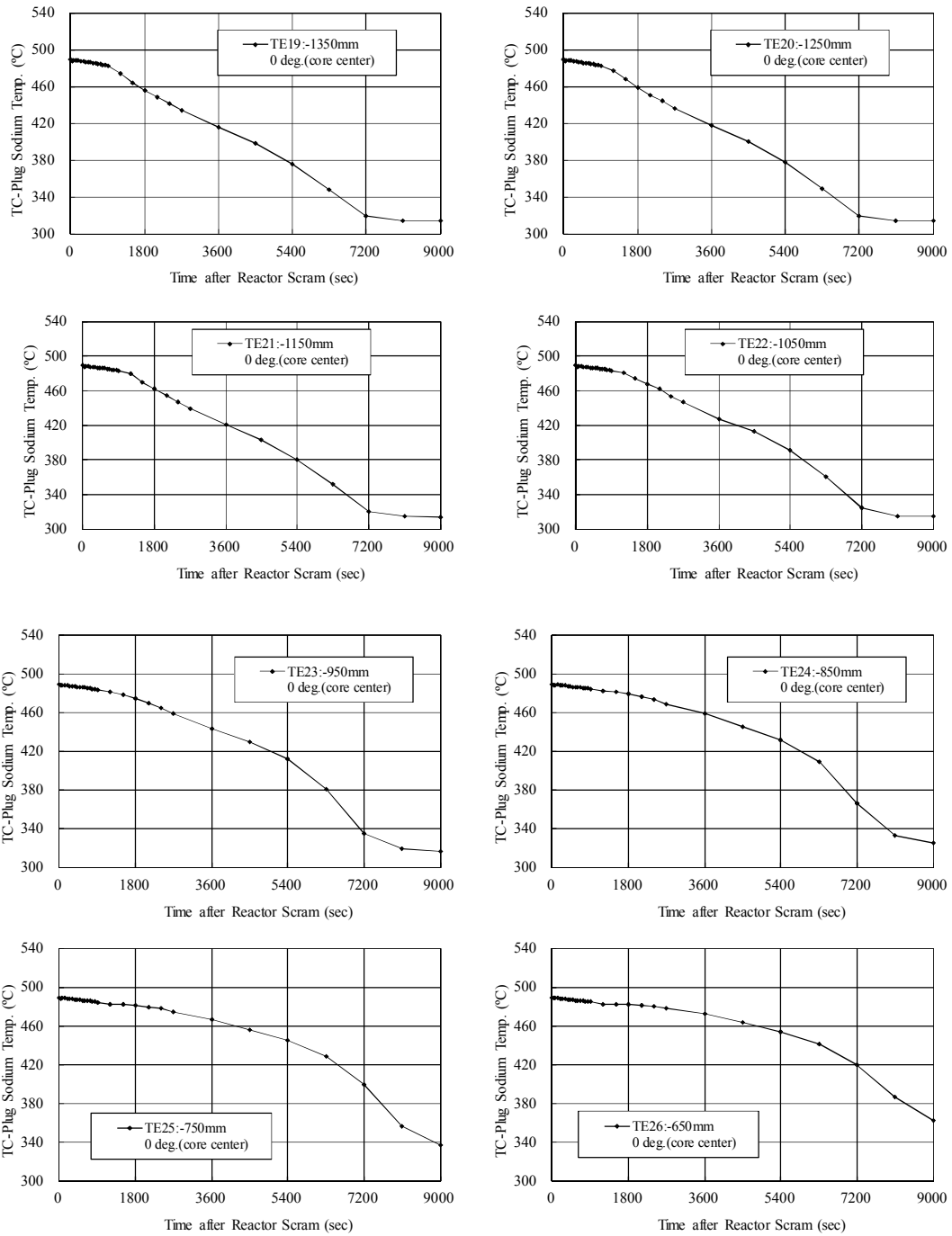


FIG. 13. TC-Plug sodium temperature 0-9000 s (4/5).

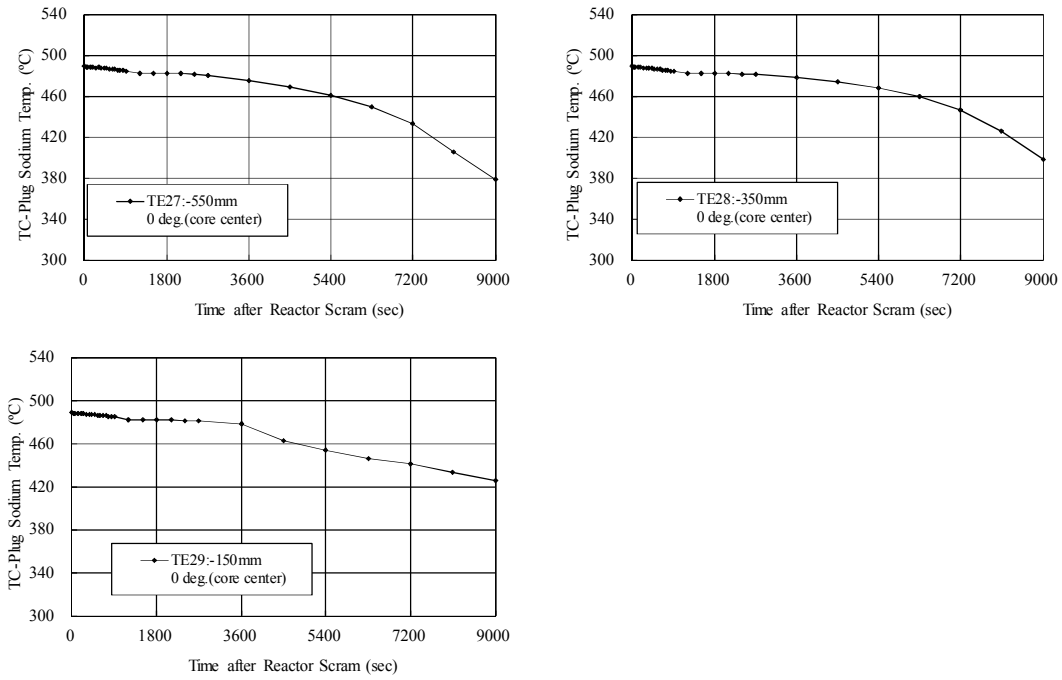


FIG. 14. TC-Plug sodium temperature 0-9000 s (5/5).

5. BENCHMARK SPECIFICATIONS

5.1. GEOMETRY DESCRIPTION OF THE MONJU REACTOR VESSEL UPPER PLENUM

The following descriptions are limited to those components and structures that form the boundary conditions for the thermal-hydraulic analysis of liquid sodium in the upper plenum of Monju reactor, as shown in Fig. 15. The inlet and outlet boundaries are given at the reactor core top surface and thermocouple positions in the reactor outlet nozzles, respectively.

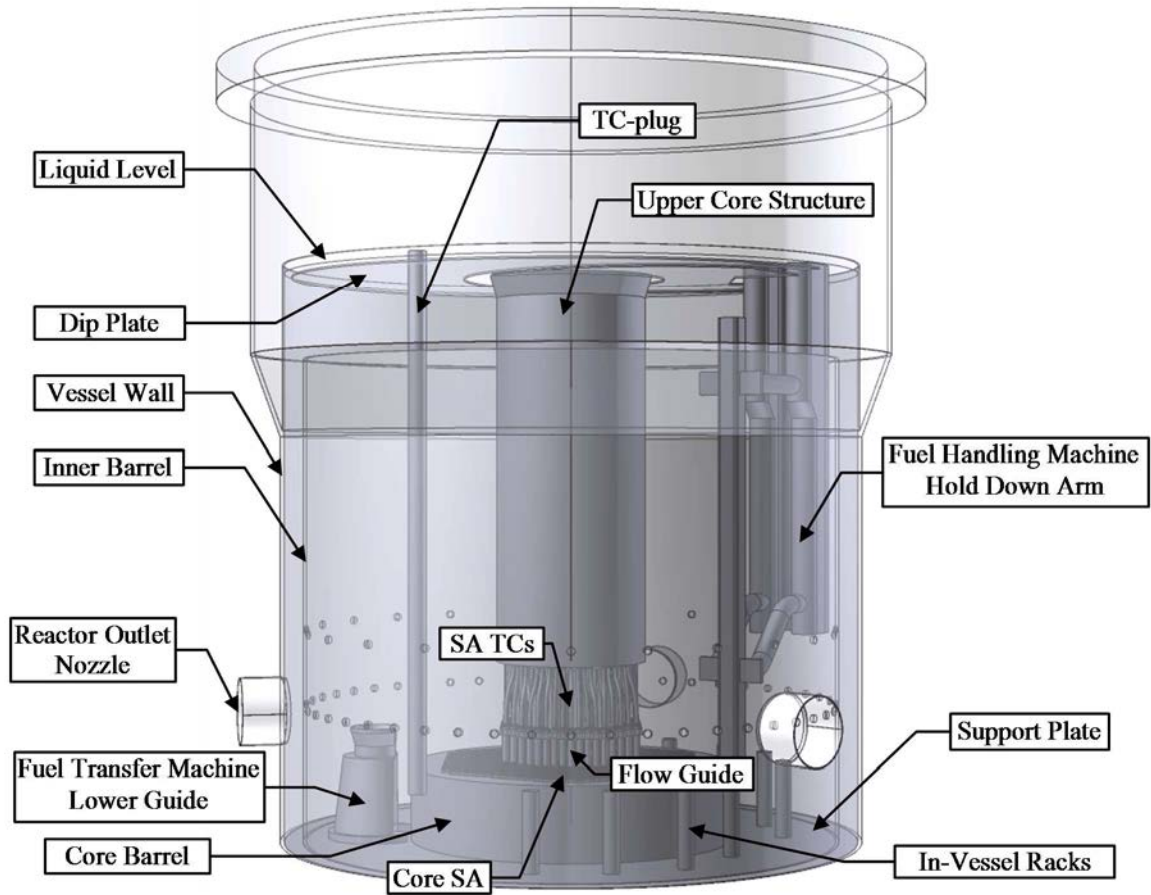


FIG. 15. Components and structures forming the boundary conditions for the thermal-hydraulic analysis of the CRP.

5.1.1. Coordinate system applied to the descriptions

Positions of the components and structures are specified in R- θ -Z or X-Y-Z coordinates. The θ coordinate is defined as shown in Fig. 16, around the symmetric axis of the vessel wall.

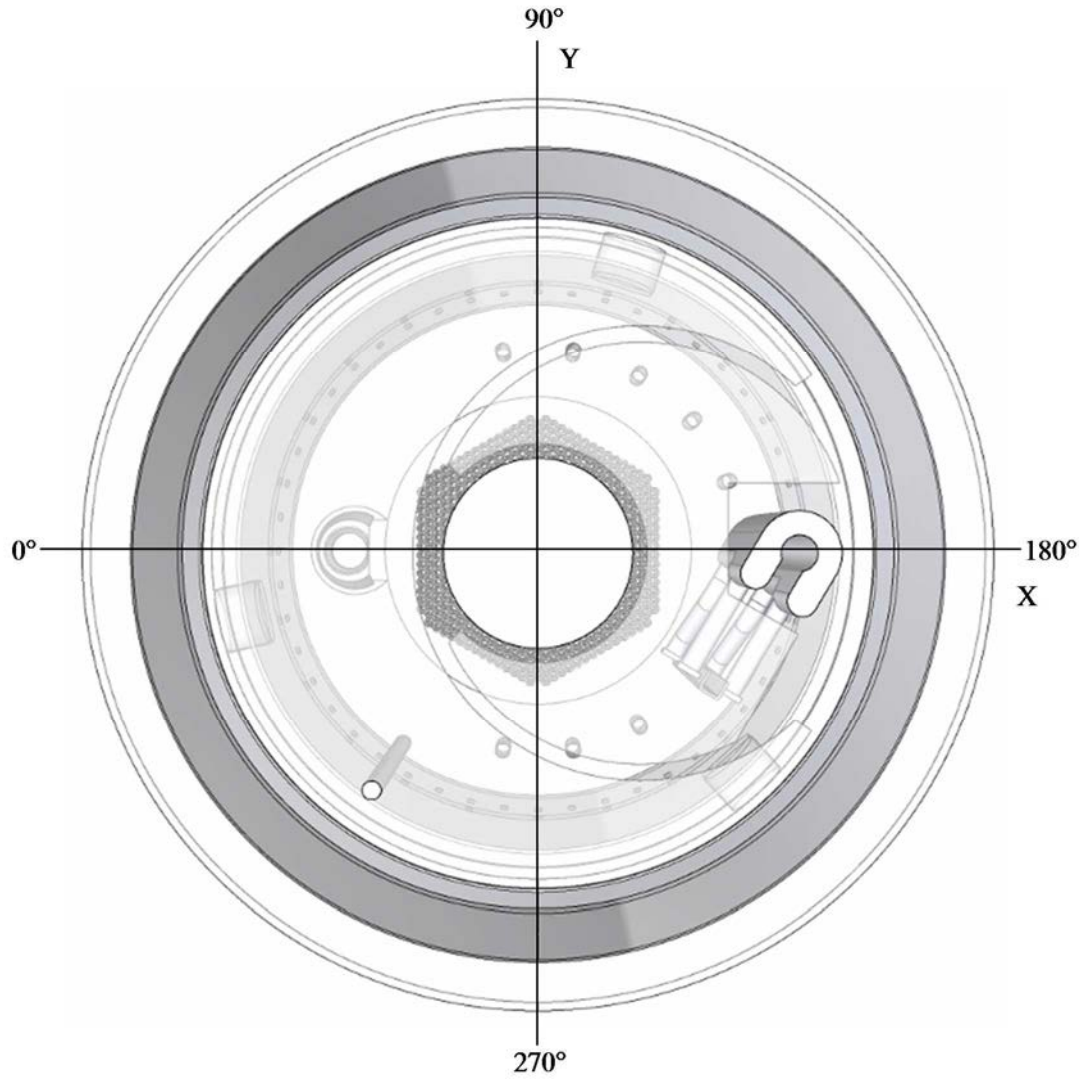


FIG. 16. Definition of the θ coordinate and X-Y coordinates (displayed on the top view with perspective effect).

The vertical coordinate is defined as the same as elevation level (EL). The elevation levels of important positions of components inside the reactor upper plenum are shown in Fig. 17.

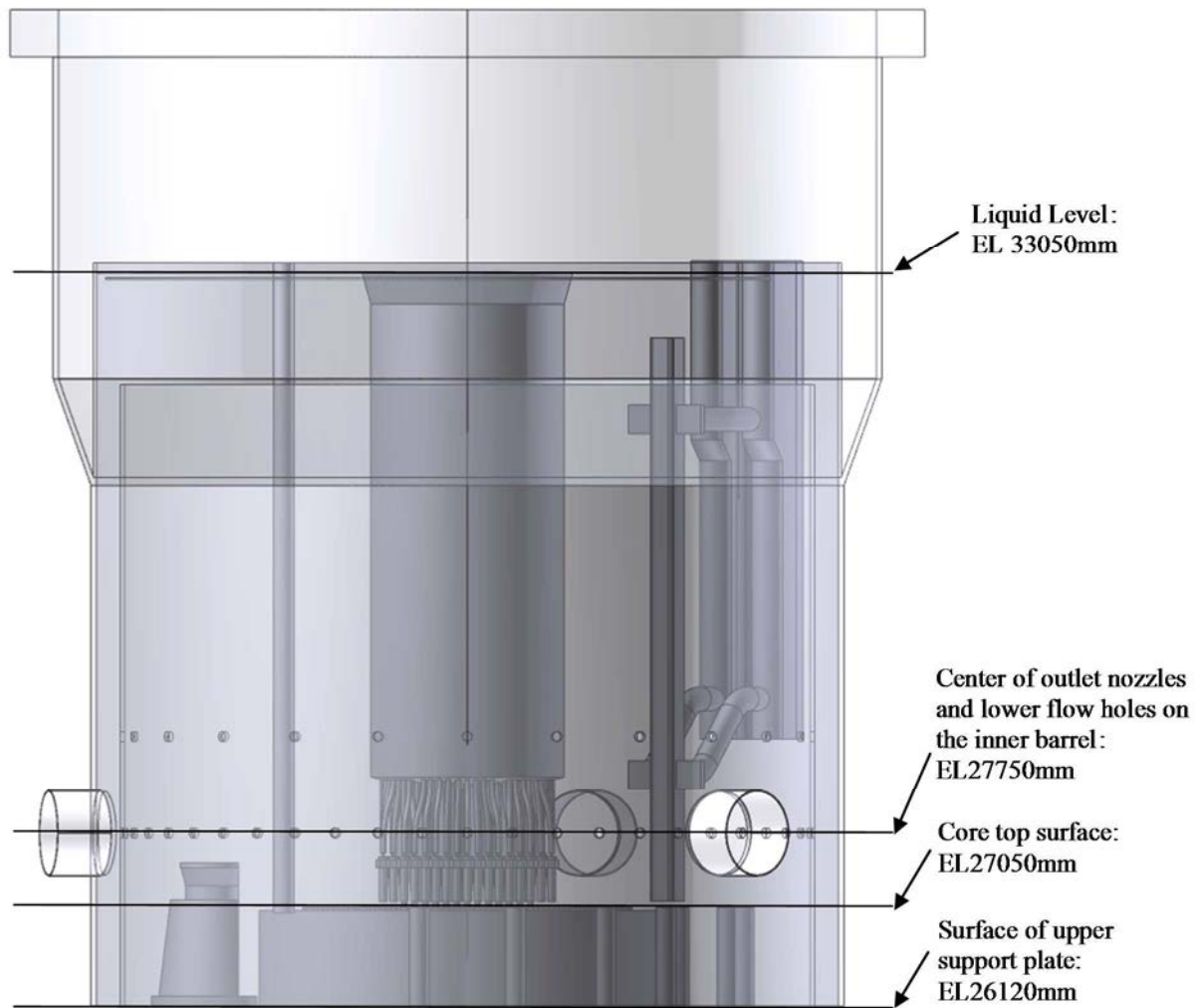


FIG. 17. Elevation levels of important positions inside the reactor upper plenum.

5.1.2. Reactor vessel wall and the three outlet nozzles

The reactor vessel wall and the outlet nozzles are shown in Fig. 18.



FIG. 18. Vessel wall above the core support plate and three outlet nozzles.

Note that the upper skirt structure is also shown for understanding of the entire shape of the reactor vessel, but this structure doesn't form the boundary conditions.

Reactor vessel wall

- Shape: vertical circular cylinder;
- Inner diameter: 7060 mm, wall thickness: 50 mm;
- Vertical positions (of sodium-filled region): top - EL33050 mm (liquid level),
bottom - EL26120 mm;
- Hollows: 3 holes connected to the outlet nozzles (inner diameter: 790.6 mm);
- Material: Type 304 stainless steel;
- Contacts with coolant on the inner surface;

Three outlet nozzles

- Shape: horizontal hollow circular cylinder;
- Directions: 107.5, 227.5 and 347.5 degrees;
- Vertical positions of the cylinder axis: EL27750 mm;
- Inner diameter: 790.6 mm;
- Material: Type 304 stainless steel (forged);
- Contact with coolant at inner surface;

5.1.3. Inner barrel

The inner barrel with flow holes is shown in Fig. 19.

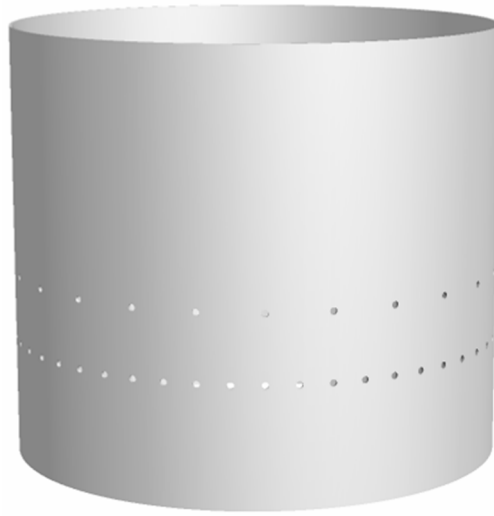


FIG. 19. Inner barrel with flow holes.

- Shape: vertical circular cylinder with upper and lower lines of flow holes;
- Vertical positions: top: EL 32000 mm, bottom: EL 126120 mm;
- Inner diameter: 6520 mm, outer diameter: 6600 mm;
- Flow holes:
 - Shape: circular hole on the cylinder wall;
 - Upper flow holes: equally spaced 24 holes;
 - Vertical center position of upper holes: EL28670 mm;
 - Diameter: 92 mm;
 - Lower flow holes: equally spaced 48 holes;
 - Vertical center position of upper holes: EL27750 mm;
 - Diameter: 92 mm;
- Material Type: 304 stainless steel;
- Contact with coolant at the inner and outer surface and inner surface of flow holes.

5.1.4. Upper support plate, core barrel, in-vessel racks and in-vessel transfer machine lower guide

The upper support plate, core barrel, in-vessel racks and in-vessel transfer machine lower guide are shown in Fig. 20.

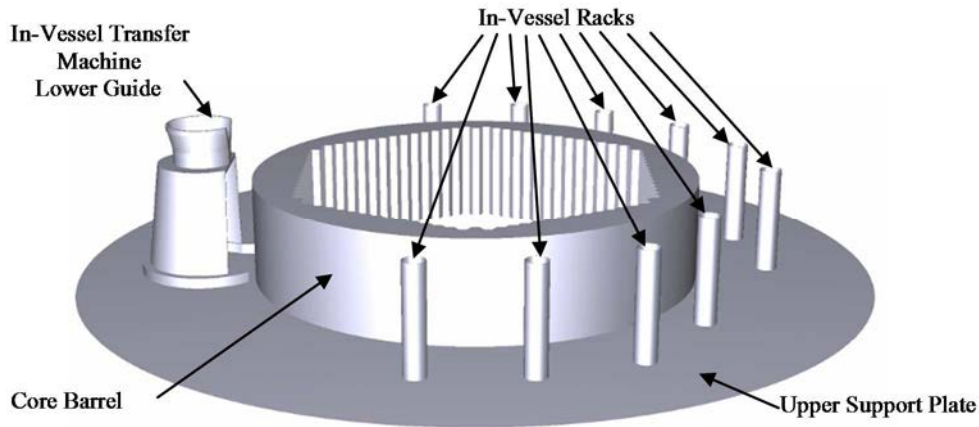


FIG. 20. Upper support plate, core barrel, in-vessel racks and in-vessel transfer machine lower guide.

Upper support plate

- Shape: horizontal circle plate with a concentric hollow for the core barrel;
- Vertical position: EL 26120 mm;
- Outer diameter: 7060 mm, hollow diameter: 3955 mm;
- Contact with coolant at the top surface.

Core barrel

- Top surface:
 - Shape: horizontal circle with a concentric hexagonal hollow for subassemblies;
 - Vertical position: EL 27020 mm (30 mm below the core top);
 - Outer diameter: 3955 mm.
- Side surface:
 - Shape: circular cylinder;
 - Top: EL 27020 mm, bottom: EL 26120 mm, outer diameter: 3955 mm.

In-vessel racks

- Shape: vertical circular hollow cylinder;
- Outer diameter: 190, wall thickness: 2.5 mm;
- Vertical position: located on the upper support plate(EL26120 mm),top: EL27050 mm;
- Horizontal positions:
 - 1) distance from the vessel center: 2630 mm;
directions: 80, 100, 120, 140, 160, 180, 240, 260 and 280 degrees;
 - 2) distance from the vessel center: 2370 mm;
direction: 217.14 degrees;
- Contact with coolant at inner, top and outer surfaces;
- Material type: 304 stainless steel.

In-vessel transfer machine lower guide

In-vessel transfer machine lower guide is shown in Fig. 21.

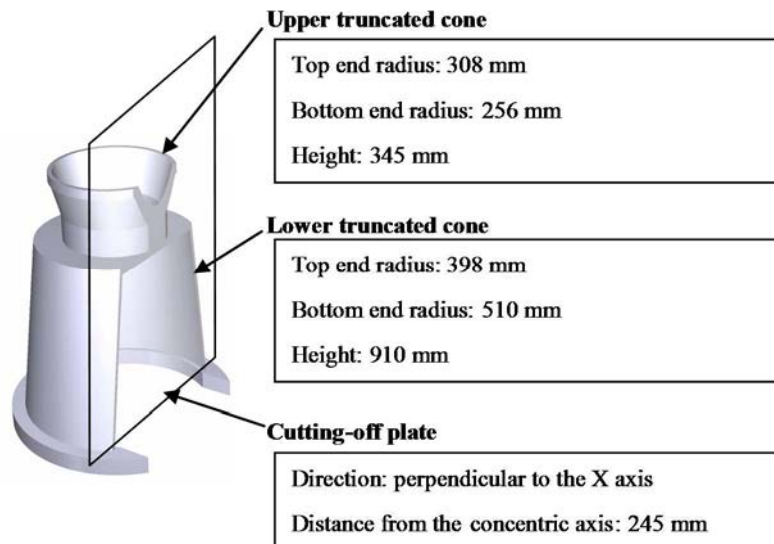


FIG. 21. In-vessel transfer machine lower guide.

- Shape: concentrically connected two vertical circular truncated cones, eccentricly cut-off by a plumb-bob vertical plane;
- Horizontal position: direction: 0 degree, distance from the vessel center: 2423.5 mm;
- Thickness varies depending on the positions but can be averaged to about 20 mm;
- Material type: 304 stainless steel.

5.1.5. Upper core structure

The upper core structure (UCS) is a stainless steel-made structure suspended from the rotating plug to hold and guide the control rod drive mechanism and the containment of thermocouples for monitoring the sodium temperature at the outlet of fuel assemblies. This structure consists of a main body, control rod guide tubes, flow guide tubes and fingers, flow guide tubes and a honeycomb structure (HS).

A scheme of the UCS is reported in Fig. 22.



FIG. 22. UCS overall view.

The space between the reactor core top surface and the bottom surface of the UCS main body has very complicated geometry, because hundreds of guide tubes are penetrating the main body and the honeycomb structure suspended above the reactor core top surface.

The guide tubes are divided into two categories:

- 1) Control rod (CRD) guide tubes: 19 vertical straight cylinders to secure CRD insertion/withdrawal actions;
- 2) Fingers and flow guide tubes for sodium temperature and velocity measurement at SA outlets.

Each bottom end of the flow guide tubes is positioned concentrically 50 mm above the corresponding subassembly to guide the sodium to a penetration in the honeycomb structure, where a thermo/flow meter is installed at the bottom end of the finger suspended from the UCS main body. On the other hand, cross section of the CRD guide tubes is larger than that of subassembly, to push aside the surrounding penetrations of the honeycomb structure for instrumentation cables. Furthermore, horizontal positions of the outermost S/As with the

instrumentations are outside of the projected cross section of the UCS main body. Therefore, some of the fingers and flow guide tubes are crooked due to the horizontal deviations among vertical portions. X and Y coordinates of center positions of the fingers and guide tubes at the core top, the honeycomb structure and at the connection to the UCS main body are shown in Figs. 25–27.

Curves of the fingers and flow guide tubes between horizontally deviated positions are given in Fig. 23.

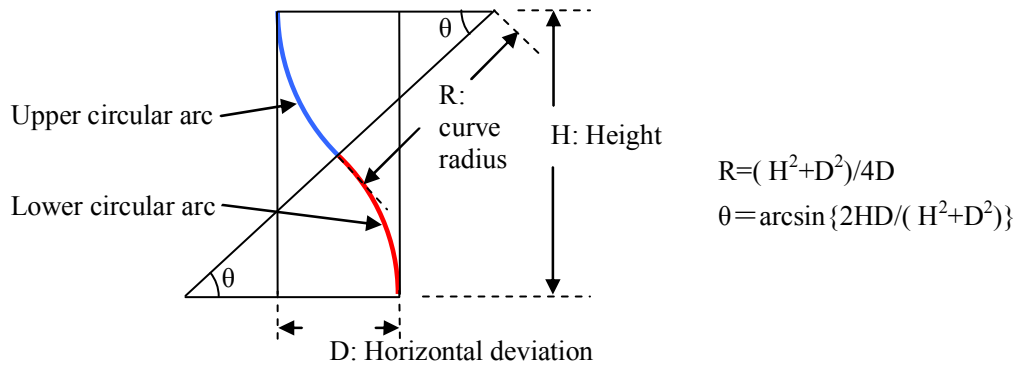
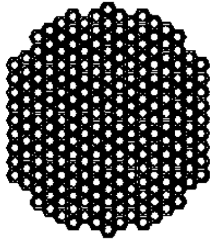


FIG. 23. Curve geometry of fingers and guide.

Note that the fingers and flow guide tubes are drawn as Bezier curves due to the software handling restrictions. Also, the positions and sizes of many holes in the honeycomb structure other than penetrations for flow guide or CRD guides are not available. The corresponding geometry data are built to visually match the drawings. The participants were guided to appropriately interpret the data into each analytical input data.

Sub-assembly address

The addresses of CRDs and subassemblies equipped with thermo/flow meters are shown in Fig. 24. The coordinates of the center positions of subassemblies, of penetration centers in the honeycomb structure and of the guide tube centers at the connection to the UCS main body are shown in Figs. 25–27.



Top of SAs
EL 27050mm



X and Y coordinates (mm)

same color : symmetric with respect to the origin

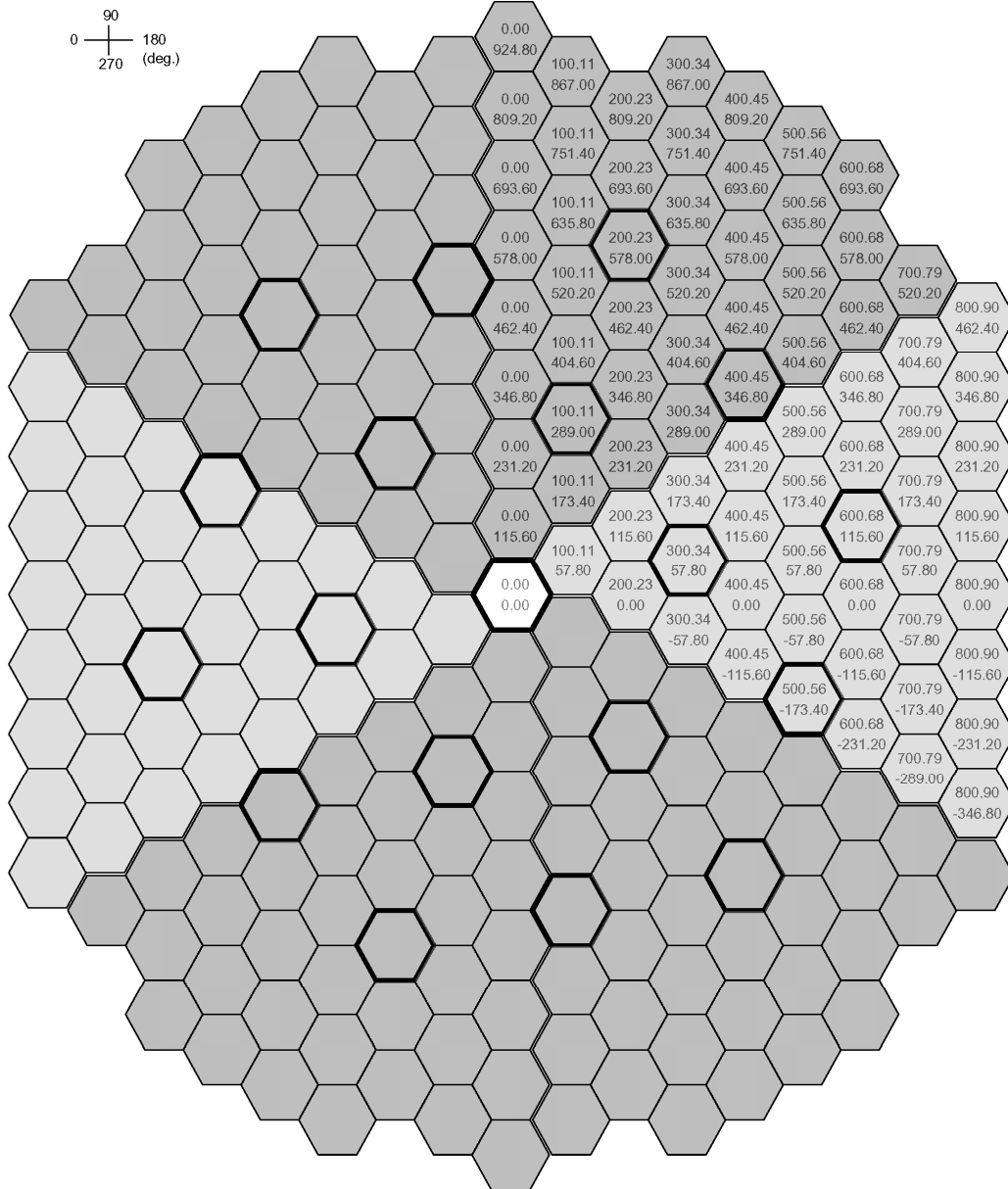


FIG. 25. X and Y coordinates of center positions of subassemblies.

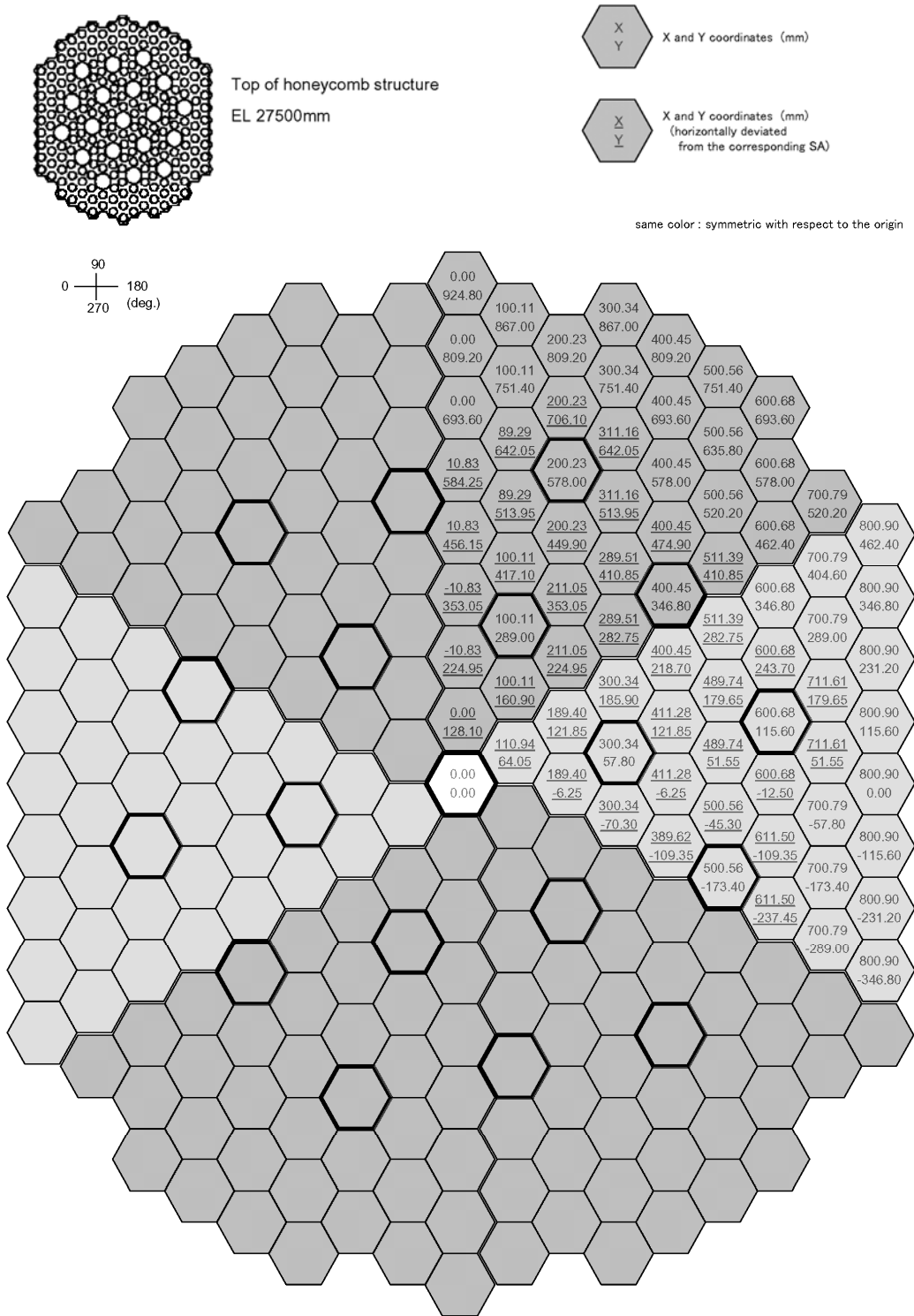


FIG. 26. X and Y coordinates of penetration centers in the honeycomb structure.

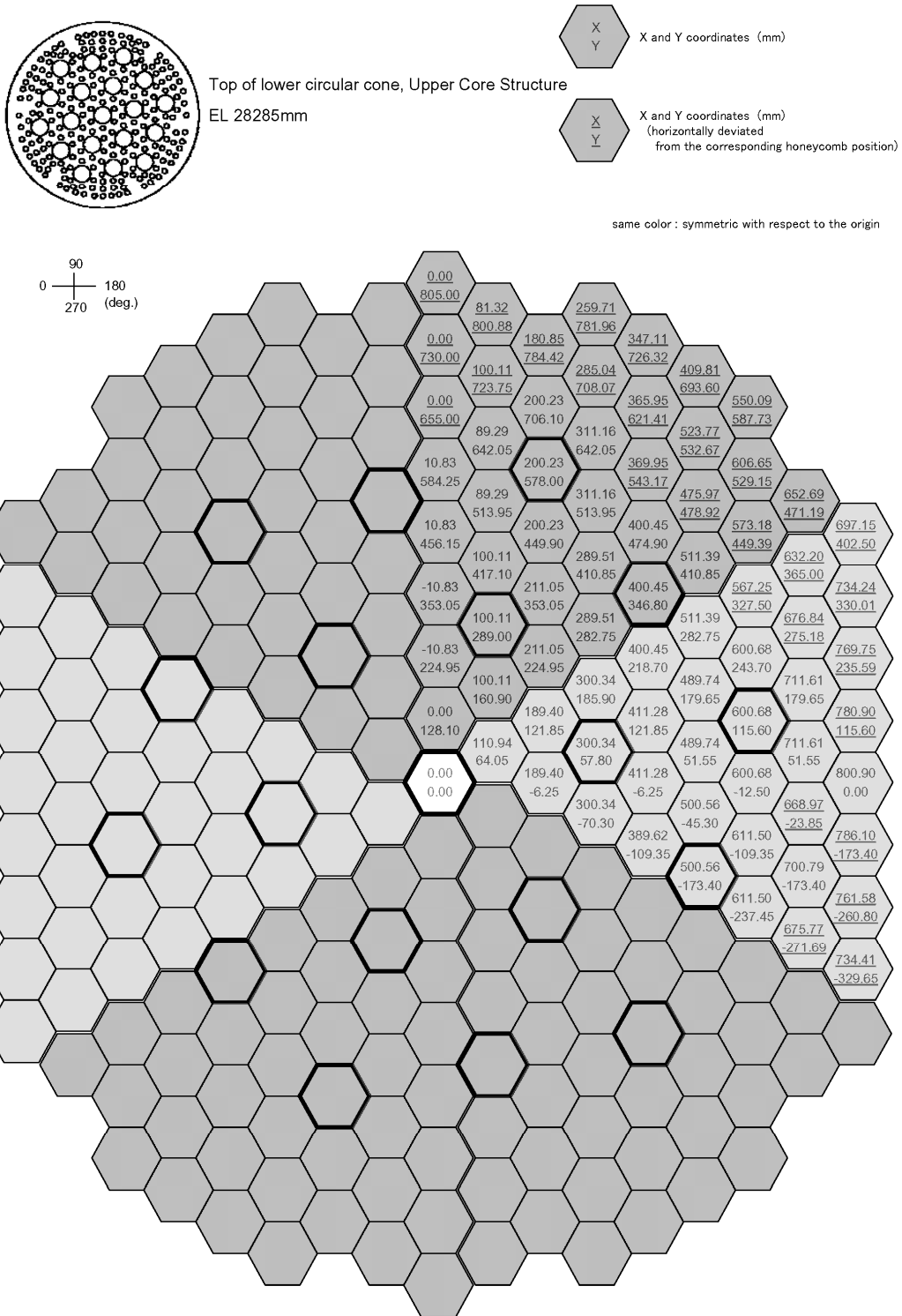


FIG. 27. X and Y coordinates of the guide tube centers at the connection to the UCS main body.

5.1.6. Fuel handling machine (hold down arm)

A scheme of the fuel handling machine is reported in Fig. 28.

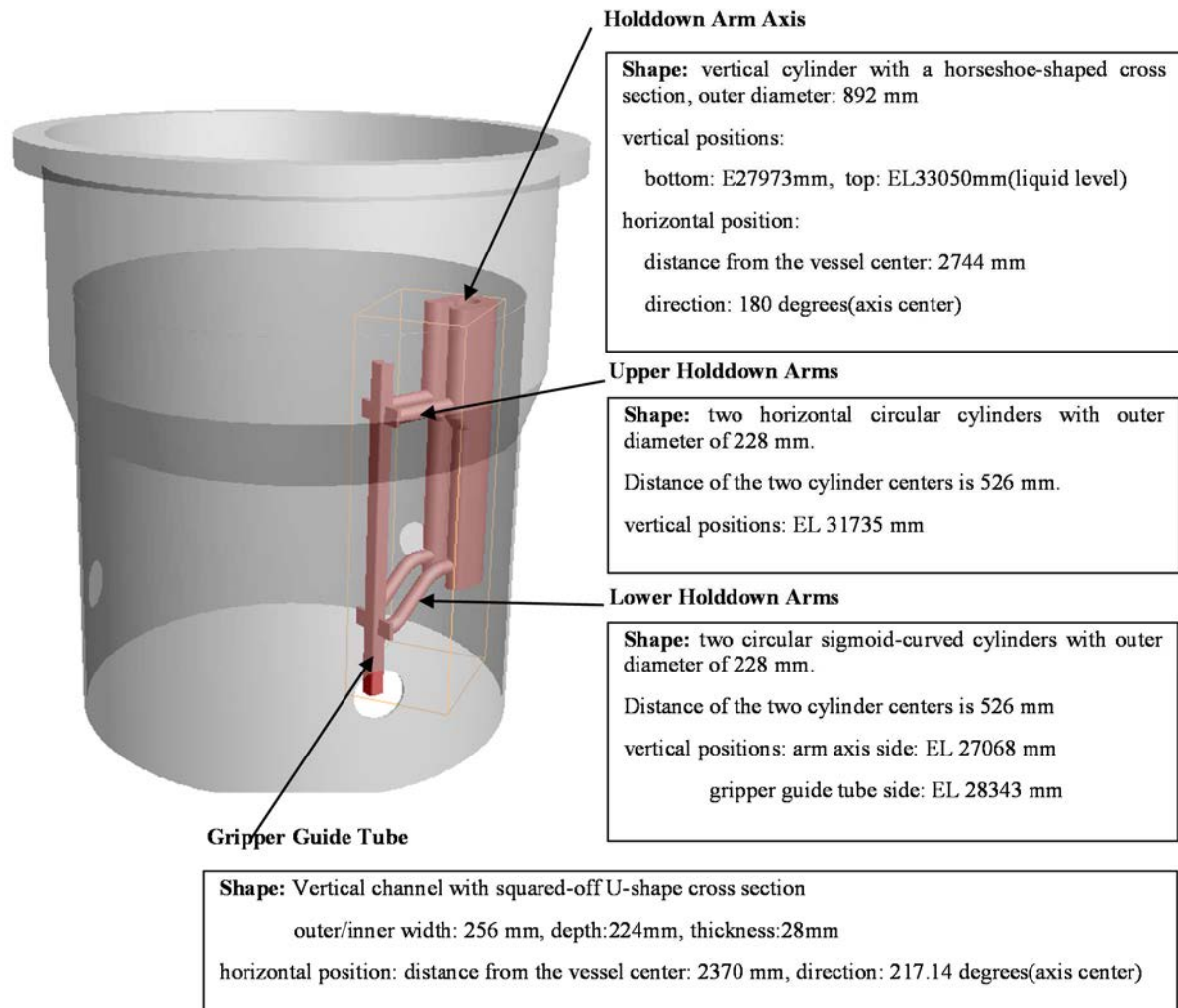


FIG. 28. Fuel handling machine hold down arm.

The fuel handling machine itself is removed from the upper plenum under plant operation conditions;

- Contact with coolant at outer surface;
- Thermal capacity: stagnant inner sodium + cylinder tube (Type 304 stainless steel).

5.1.7. Dip plate

A dip plate is prepared to prevent sloshing of the sodium surface in the reactor vessel during the operation, consisting of stator and rotor, installed under the plugging structure of the reactor vessel. The 'rotor' can be rotated for fulfilling fuel handling functions, but the both two parts were fixed during the target test as shown in Fig. 29.

The top surface is 'dipped' inside the liquid sodium at EL 33015 mm (35 mm below the liquid level) with the thickness of 20 mm.

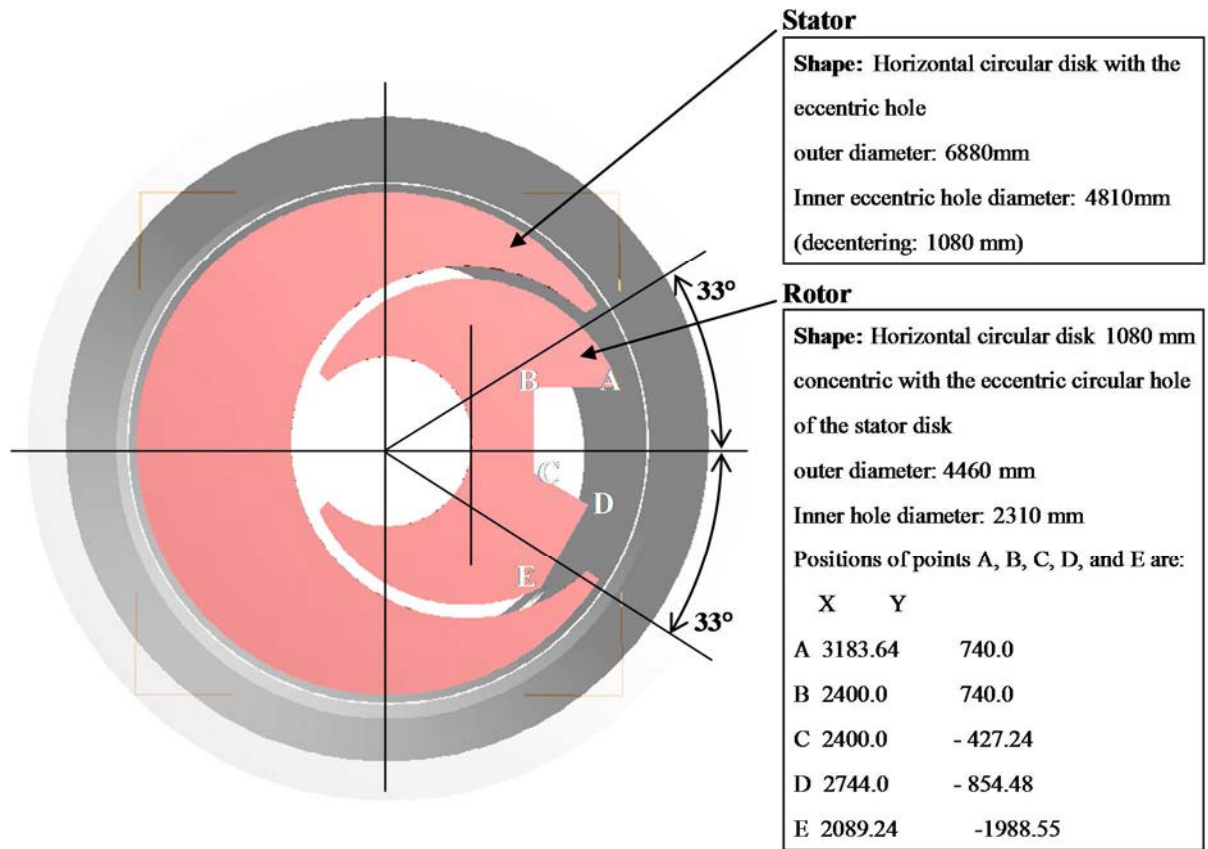


FIG. 29. Dip plate (top view).

- Material: Type 304 stainless steel;
- Contact with coolant at the upper and bottom surfaces.

5.1.8. Thermocouple plug

Location of the thermocouple plug (TP) is shown in Fig. 30.

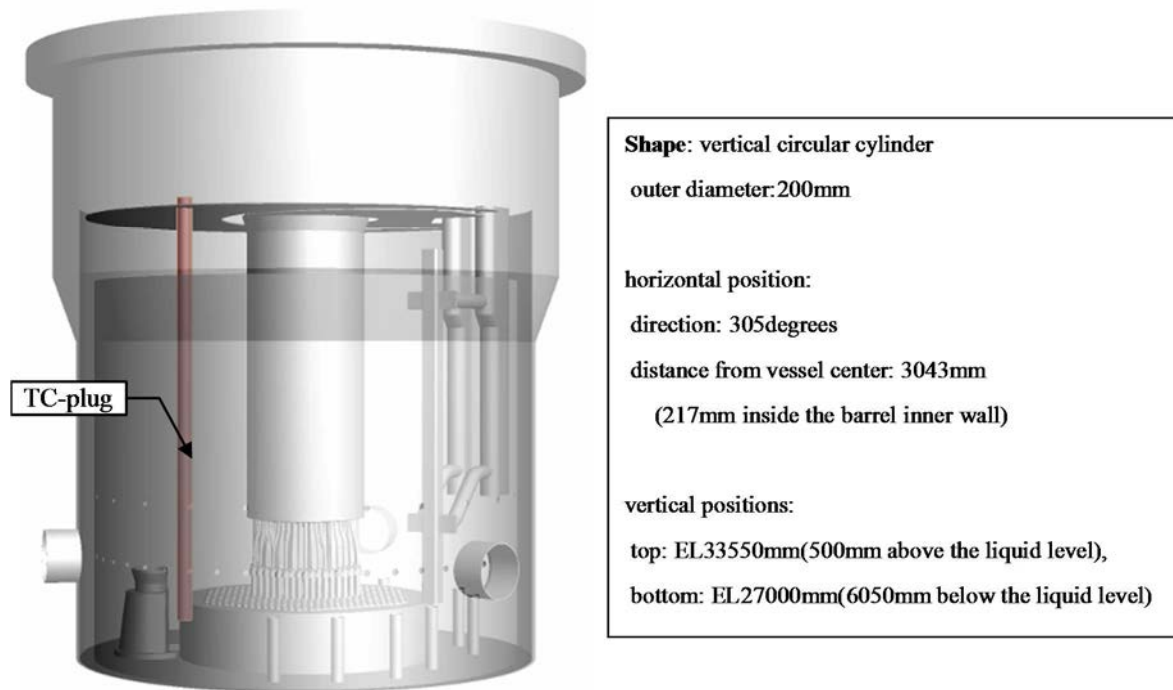


FIG. 30. Location of thermocouple plug.

Vertical positions of thermocouples relative to the liquid level are reported below:

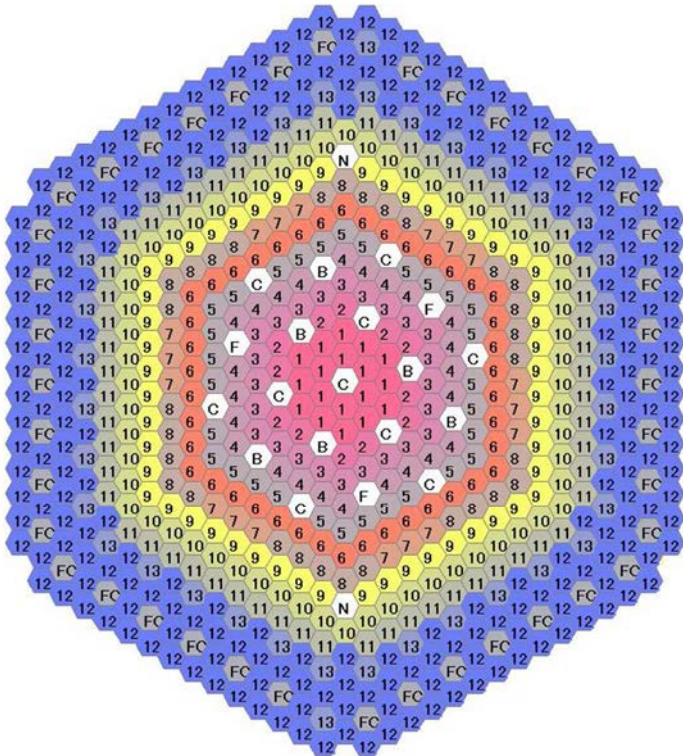
TE1:-6050mm, TE2:-5700mm, TE30:-5400mm, TE3:-5350mm, TE4:-5160mm,
 TE5:-4970mm, TE6:-4780mm, TE7:-4680mm, TE8:-4580mm, TE9:-4480mm,
 TE31:-4430mm, TE10:-4380mm, TE11:-4430mm, TE12:-4180mm, TE13:-3950mm,
 TE34:-3700mm, TE14:-3450mm, TE32:-3200mm, TE15:-2950mm, TE35:-2700mm,
 TE16:-2450mm, TE33:-2200mm, TE17:-1950mm, TE36:-1700mm, TE18:-1450mm,
 TE19:-1350mm, TE20:-1250mm, TE21:-1150mm, TE22:-1050mm, TE23:-950mm,
 TE24:-850mm, TE25:-750mm, TE26:-650mm, TE27:-550mm, TE28:-350mm,
 TE29:-150mm.

These positions are substantial when temperature measurement data are provided.

5.2. FLOW INLET BOUNDARY CONDITIONS

The flow inlet boundary conditions of the Monju reactor vessel upper plenum are given only at the reactor core top surface. Sodium in the upper plenum flows out into hot-leg piping only through the three outlet nozzles.

Based on designed flow distribution among the core fuel subassemblies, the entire core channels are divided into in-total eighteen regions shown in Fig. 31.



Core Region	Flow Channel ID
Inner Driver Core	1
	2
	3
	4
	5
Outer Driver Core	6
	7
	8
Neutron Source	N
Blanket	9
	10
	11
Neutron Shielding	12
	13
	FC
Coarse Control Rods	C
Fine Control Rods	F
Backup Control Rods	B

FIG. 31. Region division scheme of the flow channels of Monju reactor core.

Temporal changes of outlet sodium temperature measured at the core top thermometers are given in Table 1. Similarly, temporal changes of sodium flow rate per single assembly of the flow channels are given in Table 2. These temporal changes of temperatures and flow rates are plotted in Figs. 32–35.

TABLE 1. S/A OUTLET SODIUM TEMPERATURE (°C)

time(sec)	CORE1						CORE2		
	Channel-1 (1st array)	Channel-1 (2nd array)	Channel-2 (3rd array)	Channel-3 (4th array)	Channel-4 (5th array)	Channel-5 (6th array)	Channel-6 (7th array)	Channel-7 (8th array)	Channel-8 (8th array)
0	513.0	510.6	509.5	500.4	499.1	482.2	492.4	497.2	469.9
2	513.0	510.5	509.5	500.3	499.1	482.2	492.4	498.1	469.9
4	512.9	510.4	509.4	500.3	498.9	482.1	492.3	497.9	469.9
6	509.4	506.7	506.5	499.1	498.2	479.4	491.8	497.2	468.9
8	501.3	498.2	498.4	495.0	495.0	472.1	489.3	494.1	464.9
10	490.9	487.8	488.1	489.0	489.9	463.0	485.1	489.5	458.5
12	480.1	476.9	477.2	481.9	484.0	454.1	479.6	483.6	451.4
14	469.5	466.3	466.7	474.5	477.7	445.6	473.5	476.9	444.3
16	459.5	456.4	457.0	467.3	471.0	438.0	467.2	470.8	437.5
18	450.5	447.7	448.1	460.3	464.6	431.1	460.7	464.4	431.3
20	443.4	440.9	441.3	454.3	458.6	425.8	454.7	458.7	426.1
30	416.4	415.2	415.5	428.8	433.2	405.0	428.8	433.8	406.2
40	404.5	404.2	404.6	414.1	417.3	395.4	412.3	418.4	396.1
50	400.0	399.5	400.5	406.3	408.1	391.4	403.2	409.5	391.4
60	398.2	397.8	398.7	402.1	402.9	389.8	398.3	404.6	389.4
120	390.3	390.0	390.5	390.4	390.0	383.8	387.6	392.0	383.2
300	383.1	383.2	382.9	381.8	380.9	378.5	380.2	382.2	377.5
600	369.0	368.2	367.7	366.4	365.6	363.6	364.7	366.5	364.7
900	371.2	371.9	371.4	370.1	369.4	368.4	369.1	370.4	366.7
1200	371.8	372.0	371.5	370.5	369.7	368.5	369.5	370.3	367.4
1500	365.3	364.9	364.3	363.4	362.8	361.1	362.3	363.2	361.2
1800	356.1	355.8	355.2	354.4	353.6	352.0	353.0	354.1	352.9
3600	329.7	329.6	329.2	328.5	327.9	326.8	327.5	328.6	327.0
5400	318.5	318.6	318.3	317.6	317.0	316.1	316.7	317.5	315.9
7200	313.0	313.4	312.9	312.3	311.7	311.1	311.5	312.6	310.7
9000	312.4	312.8	312.4	311.8	311.2	310.6	311.0	312.0	310.2

time(sec)	BLANKET			N-SHIELDING			N-SOURCE	CR		
	Channel-9 (9th array)	Channel-10 (10th array)	Channel-11 (11th array)	Channel-12	Channel-13	Channel-FC	Channel-N	Channel-C	Channel-F	Channel-B
0	427.4	410.0	415.0	422.6	458.7	405.0	382.0	389.0	385.0	421.0
2	427.3	409.9	414.9	422.5	458.6	404.9	381.9	388.9	384.9	420.9
4	427.3	409.9	414.9	422.5	458.5	404.9	381.9	388.9	384.9	420.9
6	427.1	409.8	414.8	422.3	458.3	404.8	381.8	388.8	384.8	420.8
8	427.1	409.8	414.7	422.3	458.3	404.8	381.8	388.8	384.8	420.7
10	427.0	409.7	414.6	422.2	458.2	404.7	381.7	388.7	384.7	420.6
12	426.8	409.5	414.4	422.0	457.9	404.5	381.6	388.6	384.6	420.4
14	426.4	409.2	414.1	421.7	457.5	404.2	381.4	388.3	384.4	420.1
16	426.0	408.8	413.7	421.2	456.9	403.8	381.1	388.0	384.0	419.6
18	425.6	408.4	413.4	420.8	456.4	403.5	380.8	387.7	383.8	419.3
20	424.9	407.9	412.8	420.3	455.7	403.0	380.4	387.3	383.4	418.7
30	421.0	404.5	409.3	416.5	450.8	399.8	377.9	384.6	380.8	415.0
40	415.3	399.6	404.1	411.0	443.6	395.1	374.2	380.6	376.9	409.5
50	409.4	394.4	398.7	405.2	436.2	390.1	370.4	376.4	372.9	403.8
60	405.1	390.7	394.9	401.1	430.9	386.6	367.6	373.4	370.1	399.8
120	392.3	379.6	383.2	388.7	414.8	376.0	359.3	364.4	361.5	387.6
300	382.1	370.9	374.1	379.0	402.3	367.7	352.9	357.4	354.8	378.0
600	371.4	361.7	364.5	368.7	388.9	358.9	346.0	349.9	347.6	367.8
900	368.7	359.3	362.0	366.1	385.6	356.6	344.2	348.0	345.8	365.2
1200	369.2	359.8	362.6	366.7	386.3	357.1	344.6	348.4	346.2	365.8
1500	365.2	356.4	359.0	362.8	381.3	353.8	342.0	345.6	343.6	362.0
1800	358.0	350.0	352.3	355.7	372.2	347.8	337.3	340.5	338.7	355.0
3600	330.5	326.3	327.5	329.3	338.0	325.1	319.6	321.3	320.3	329.0
5400	318.5	315.9	316.6	317.7	322.9	315.2	311.9	312.9	312.3	317.5
7200	312.3	310.6	311.1	311.8	315.3	310.1	307.9	308.6	308.2	311.7
9000	311.5	309.8	310.2	310.9	314.1	309.3	307.3	307.9	307.6	310.8

TABLE 2. S/A SODIUM FLOW RATE (KG/SEC)

time(sec)	CORE1						CORE2			
	Channel-1 (1st array)	Channel-1 (2nd array)	Channel-2 (3rd array)	Channel-3 (4th array)	Channel-4 (5th array)	Channel-5 (6th array)	Channel-6 (7th array)	Channel-7 (8th array)	Channel-8 (8th array)	
0	10.24	10.24	9.69	9.25	8.63	8.07	9.32	7.95	7.24	
2	10.41	10.27	9.89	9.55	8.55	8.15	9.46	8.01	7.17	
4	9.47	9.33	9.07	8.59	7.88	7.59	8.64	7.76	6.64	
6	8.45	7.98	7.54	7.37	6.88	6.59	7.72	6.49	5.89	
8	7.58	6.68	6.84	6.45	6.00	5.82	6.58	5.65	4.99	
10	6.65	6.10	6.00	5.58	5.13	5.13	5.90	4.78	4.33	
12	6.12	5.37	5.23	4.82	4.48	4.50	5.45	4.18	3.63	
14	5.45	4.54	4.47	4.26	3.79	4.18	4.96	3.49	2.87	
16	5.09	3.65	3.90	3.80	3.34	3.55	4.68	3.16	2.46	
18	4.61	3.30	3.34	3.47	2.80	3.15	4.33	2.79	1.96	
20	4.38	2.92	2.90	3.19	2.39	2.68	4.01	2.53	1.65	
30	3.22	1.42	1.80	2.06	1.30	1.54	3.15	1.51	0.66	
40	2.87	1.05	1.51	1.74	1.08	1.23	2.85	1.34	0.55	
50	2.98	1.24	1.69	1.82	1.22	1.22	2.84	1.47	0.61	
60	3.06	1.41	1.80	1.95	1.36	1.31	2.85	1.55	0.84	
120	2.98	1.98	2.30	2.15	1.79	1.79	2.73	1.85	1.34	
300	2.83	2.25	2.56	2.25	2.06	2.20	2.52	1.99	1.56	
600	2.72	2.13	2.37	2.11	1.92	2.12	2.35	1.86	1.50	
900	2.67	2.23	2.56	2.25	2.09	2.20	2.48	1.98	1.65	
1200	2.71	2.27	2.51	2.31	2.07	2.24	2.49	2.00	1.63	
1500	2.69	2.22	2.47	2.22	1.95	2.16	2.51	1.91	1.60	
1800	2.60	2.19	2.43	2.23	1.96	2.18	2.46	1.88	1.58	
3600	2.53	2.15	2.28	2.04	1.85	2.08	2.34	1.87	1.58	
5400	2.42	2.11	2.18	2.08	1.82	2.07	2.28	1.88	1.67	
7200	2.48	2.17	2.17	2.08	1.80	2.13	2.40	1.86	1.65	
9000	2.51	2.14	2.28	2.12	1.85	2.11	2.38	1.85	1.71	

time(sec)	BLANKET			N-SHIELDING			N-SOURCE	CR		
	Channel-9 (9th array)	Channel-10 (10th array)	Channel-11 (11th array)	Channel-12	Channel-13	Channel-FC	Channel-N	Channel-C	Channel-F	Channel-B
0	2.270	1.090	0.502	0.0710	0.0920	0.0770	1.860	4.150	4.150	1.490
2	2.337	1.122	0.517	0.0731	0.0947	0.0793	1.915	4.272	4.272	1.534
4	2.131	1.023	0.471	0.0666	0.0863	0.0723	1.746	3.895	3.895	1.398
6	1.785	0.857	0.395	0.0558	0.0723	0.0605	1.462	3.263	3.263	1.171
8	1.542	0.740	0.341	0.0482	0.0625	0.0523	1.263	2.819	2.819	1.012
10	1.364	0.655	0.302	0.0427	0.0553	0.0463	1.118	2.494	2.494	0.896
12	1.101	0.528	0.243	0.0344	0.0446	0.0373	0.902	2.012	2.012	0.722
14	0.866	0.416	0.191	0.0271	0.0351	0.0294	0.709	1.582	1.582	0.568
16	0.726	0.349	0.161	0.0227	0.0294	0.0246	0.595	1.327	1.327	0.477
18	0.545	0.261	0.120	0.0170	0.0221	0.0185	0.446	0.996	0.996	0.357
20	0.508	0.244	0.112	0.0159	0.0206	0.0172	0.416	0.929	0.929	0.334
30	0.333	0.160	0.074	0.0104	0.0135	0.0113	0.273	0.609	0.609	0.219
40	0.293	0.141	0.065	0.0092	0.0119	0.0099	0.240	0.535	0.535	0.192
50	0.203	0.097	0.045	0.0063	0.0082	0.0069	0.166	0.370	0.370	0.133
60	0.188	0.090	0.041	0.0059	0.0076	0.0064	0.154	0.343	0.343	0.123
120	0.133	0.064	0.029	0.0042	0.0054	0.0045	0.109	0.244	0.244	0.088
300	0.235	0.113	0.052	0.0074	0.0095	0.0080	0.193	0.430	0.430	0.155
600	0.135	0.065	0.030	0.0042	0.0055	0.0046	0.111	0.247	0.247	0.089
900	0.242	0.116	0.054	0.0076	0.0098	0.0082	0.199	0.443	0.443	0.159
1200	0.191	0.092	0.042	0.0060	0.0078	0.0065	0.157	0.350	0.350	0.126
1500	0.224	0.108	0.050	0.0070	0.0091	0.0076	0.184	0.410	0.410	0.147
1800	0.162	0.078	0.036	0.0051	0.0066	0.0055	0.133	0.296	0.296	0.106
3600	0.071	0.034	0.016	0.0022	0.0029	0.0024	0.058	0.129	0.129	0.046
5400	0.148	0.071	0.033	0.0046	0.0060	0.0050	0.121	0.271	0.271	0.097
7200	0.190	0.091	0.042	0.0060	0.0077	0.0065	0.156	0.348	0.348	0.125
9000	0.172	0.082	0.038	0.0054	0.0070	0.0058	0.141	0.314	0.314	0.113

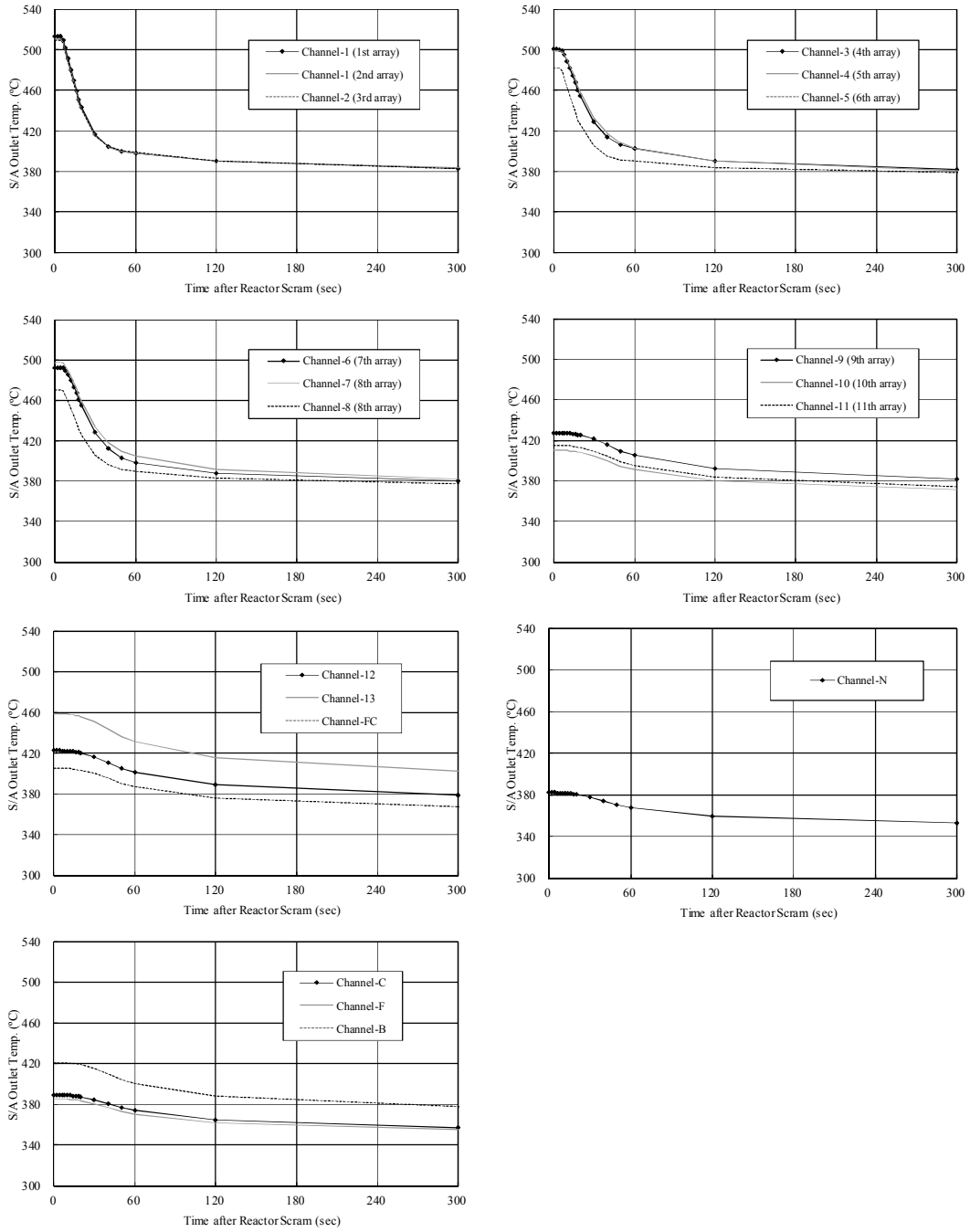


FIG. 32. S/A outlet sodium temperature (1/2).

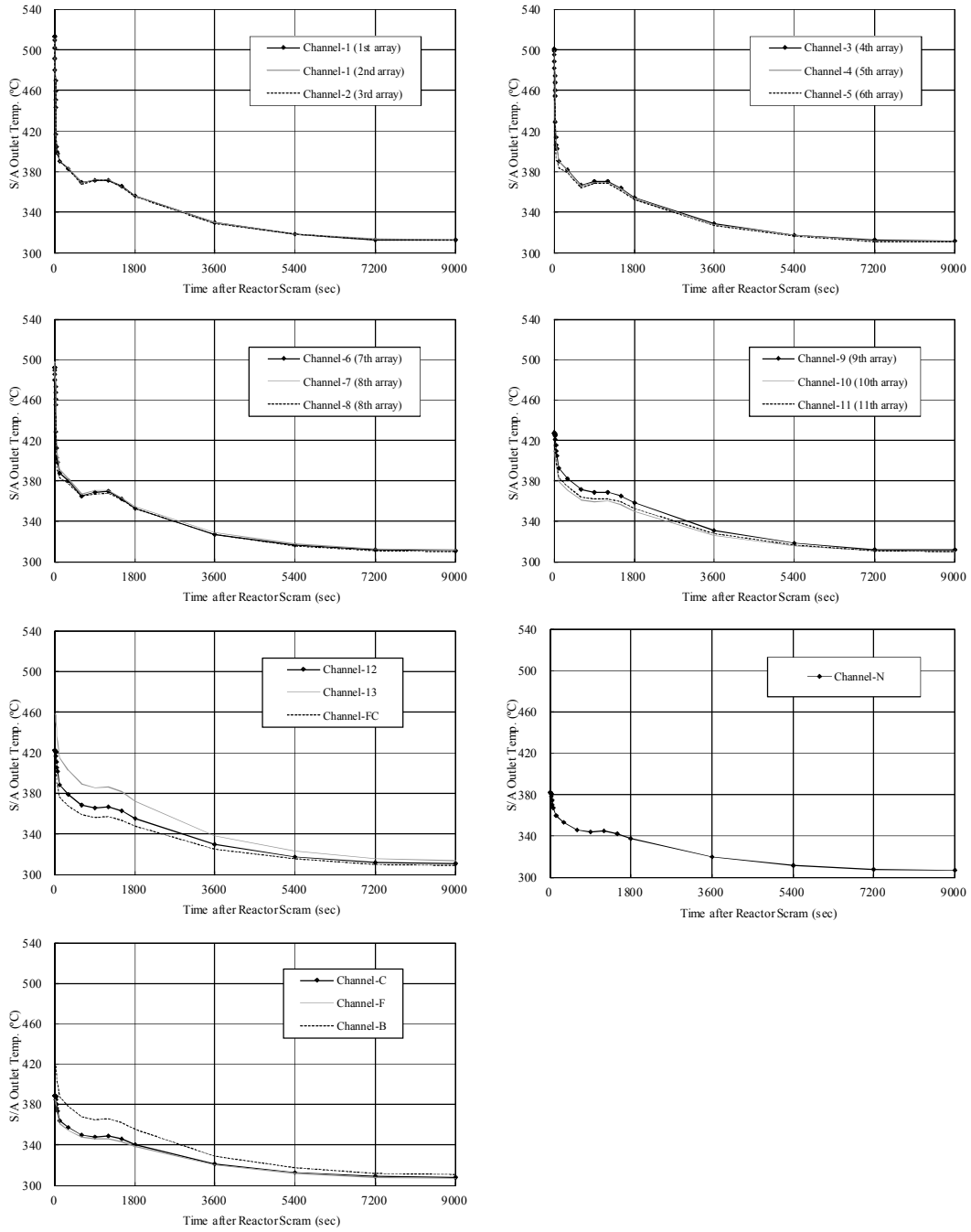


FIG. 33. S/A outlet sodium temperature (2/2).

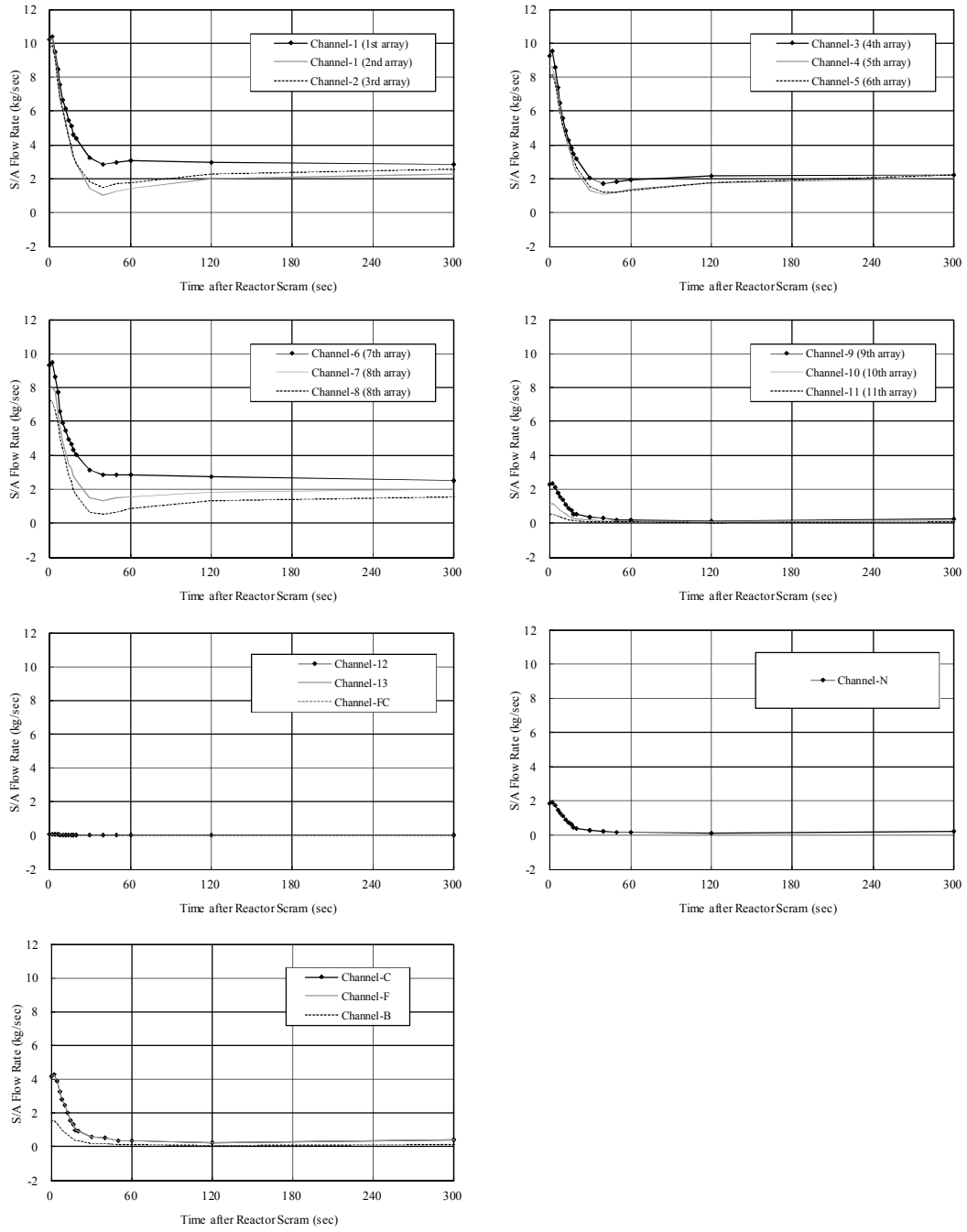


FIG. 34. S/A sodium flow rate (1/2).

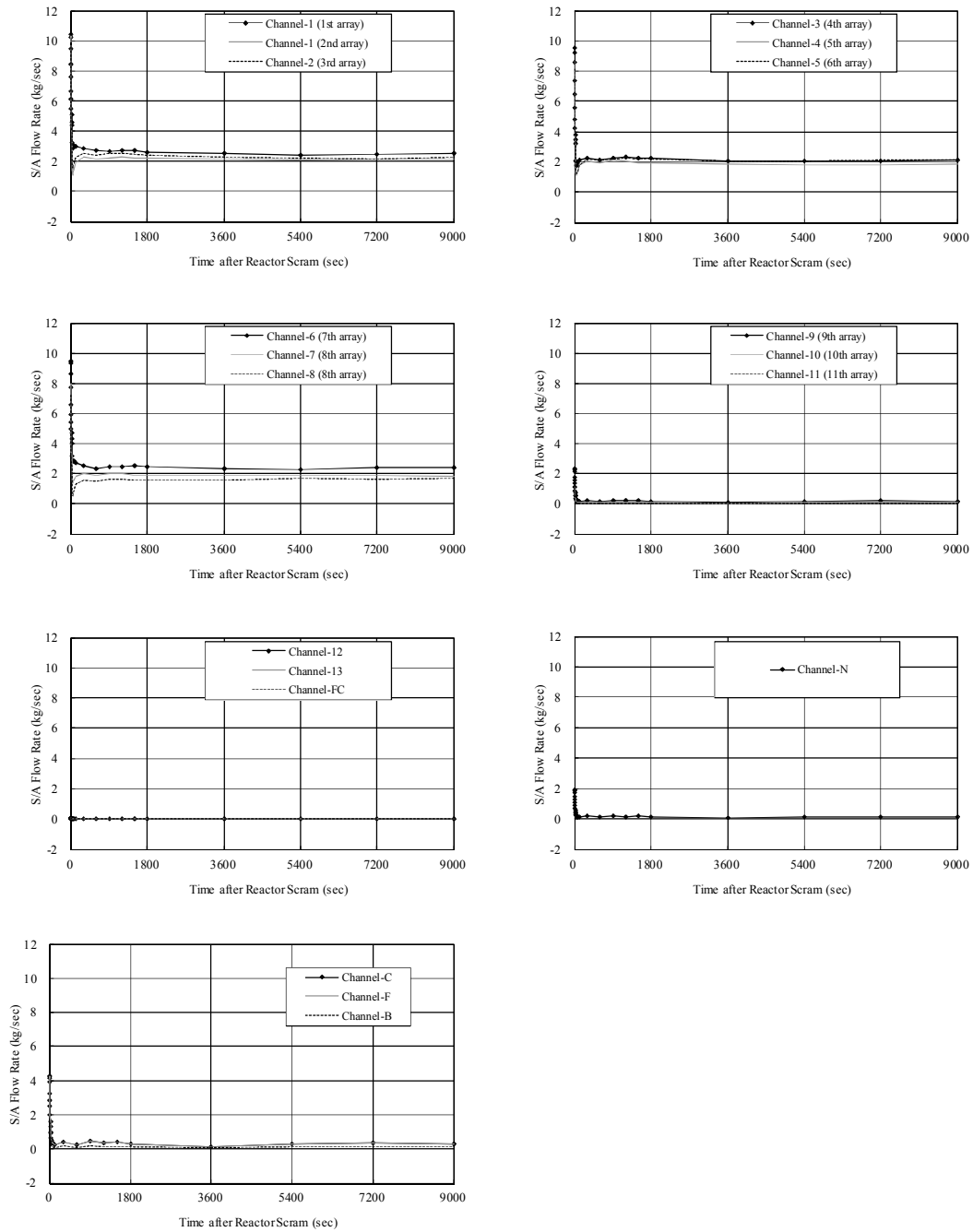


FIG. 35. S/A sodium flow rate (2/2).

6. DESCRIPTION OF MODELS

6.1. DESCRIPTION OF SIMPLIFIED GEOMETRY

In order to simplify the process of model development as well as the comparison of predictions from code to code, a geometric representation of the Monju upper plenum was developed and shared with all participants via a neutral CAD file. Several simplifications were made to the actual Monju plenum geometry, in order to create a 60° (or 1/6) segment. Because some participants may disagree with particular simplifications, utilization of the

simplified geometry was not required for the benchmark exercise. The simplified geometry is described in further detail in the following sections.

6.1.1. Overview

The simplified geometry consists of a 60° ‘symmetric’ segment of Monju upper plenum developed on the basis of the geometric information given in Section 5. The simplified model was developed using a commercially available Gambit geometric modeling and mesh generation software (distributed by ANSYS/FLUENT). The simplified model includes only the region between the support plate at the bottom, and the dip plate on top. The dip-plate is modeled as a solid wall. In the geometric representations, the elevations are adjusted with respect to the support plate (assuming the support plate is at elevation 0 mm). The thickness of the reactor vessel is ignored and the inner barrel is modeled as an adiabatic gap in the flow domain (i.e. the conductive heat transfer through the thickness of the inner barrel is neglected). The front, side, top, and isometric views of the simplified model geometry are shown in Fig. 36.

To achieve symmetry, the fuel handling machine hold-down arm and lower guide, fuel transfer machine lower guide, in-vessel spent fuel storage racks, and the thermocouple plug are excluded. Also, the reactor outlet nozzle is rotated 12.5 degrees clockwise to align it symmetrically with respect to the hexagonal core configuration. One of the symmetry planes cuts the outlet nozzle in half. Although the outlet nozzle in the CAD model is considerably longer than what is indicated in the JAEA benchmark specifications, based on earlier experiences, extending the outlet end of pipes/nozzles away from the computational domain is deemed to be important to avoid the undue influence of the outlet boundary conditions on the upstream results.

Other than the larger control rod guide tubes, the complex geometric structures above the core (flow guide tubes, honeycomb structure, thermocouples and flow meters, and fingers) are excluded in the simplified model and this region is modeled using the porous media approach.

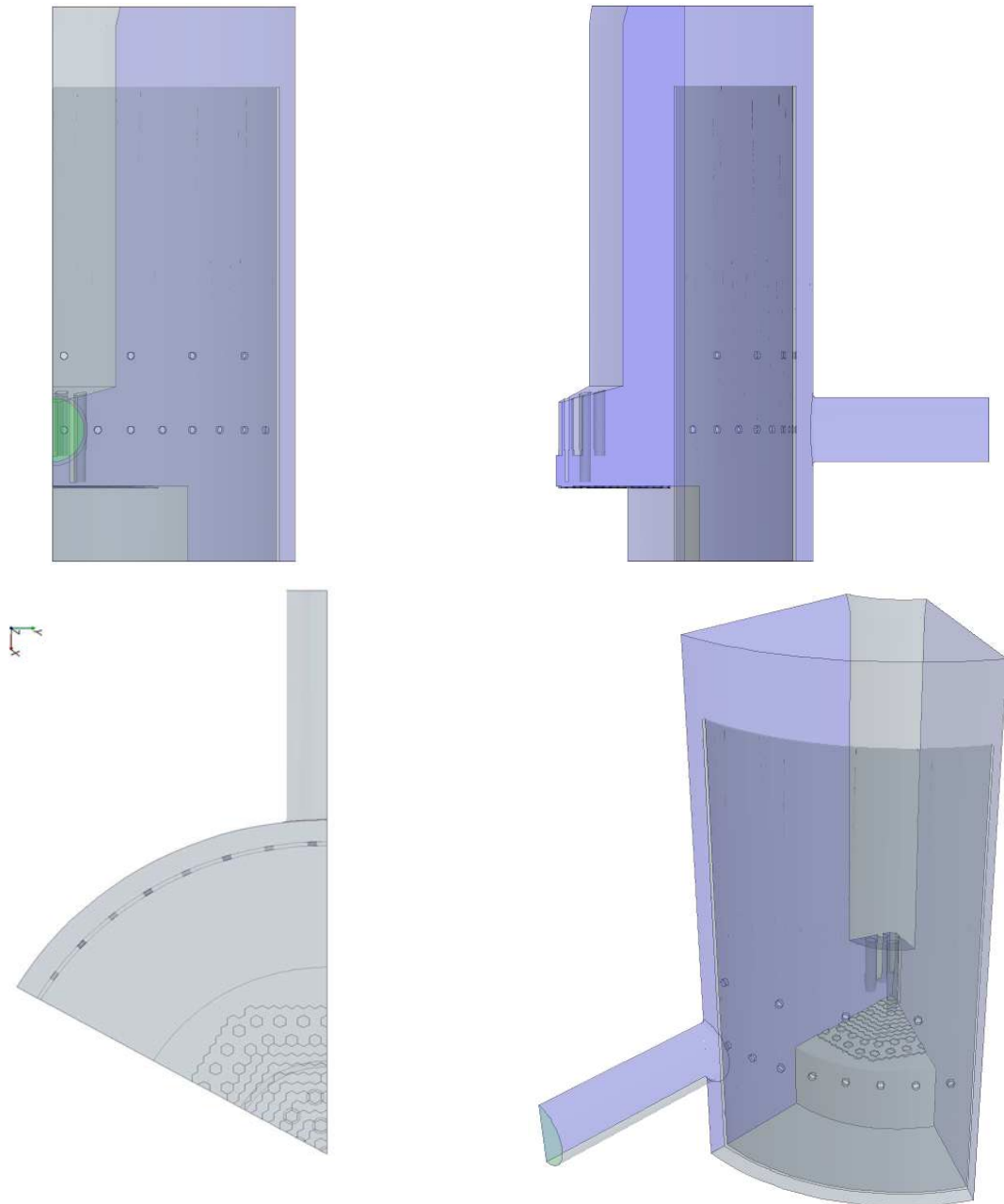


FIG. 36. Front (top left), side (top right), top (bottom left), and isometric (bottom right) transparent views of the Monju simplified upper plenum model.

6.1.2. Inlet boundary regions

The 1/6 symmetric segment (60° section) corresponds to the W-SW portion of the core as shown in Fig. 37. All of the subassembly outlets (inlets of the upper plenum model) are taken as hexagonal with uniform velocity profiles. In order to distinctly identify different inlet zones at the inner core, outer core, radial blanket subassemblies, neutron shielding zone, and control assembly outlets, the subassembly outlets are placed at slightly different elevations to match the configuration shown in Fig. 37. That is, the top ends of the subassemblies in the same zone are slightly offset (by 10 mm) for easy identification of nineteen different inlet boundaries, each with a distinct flow rate and core outlet temperature as described in Section 5.2. Having each inlet zone modelled with a geometrically distinguishable ‘face’ makes the boundary condition implementation much easier with most CFD software.

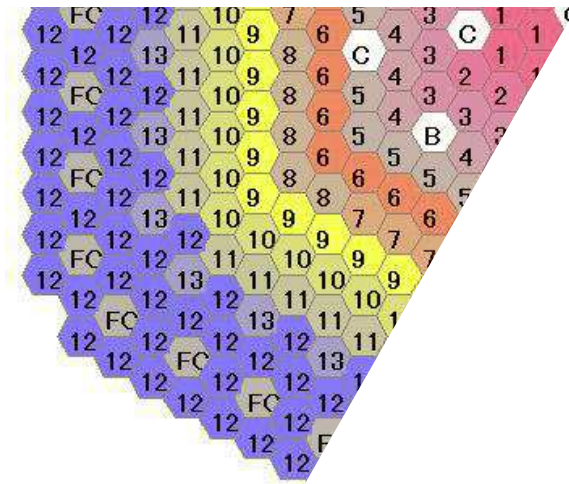


FIG. 37. W-SW portion of the Monju reactor core included in the 1/6 symmetric upper plenum model.

The core region of the simplified model has some differences with the real geometry. The simplified model core outlet zone definitions are summarized in Table 3. In brief, the influence of the blanket subassemblies, neutron shielding, and control rods, and neutron source channels are either under- or over-estimated since the actual core configuration does not comply with a 1/6 symmetry. Since the influence of the inner and outer driver core subassemblies are captured in exact proportions to the actual core configuration, however, the differences are not considered to be significant.

TABLE 3. MONJU SIMPLIFIED MODEL CORE OUTLET ZONE DEFINITIONS.

Core region	Flow channel ID	Number of assemblies in 1/6 symmetric simplified model
Inner driver core	1-inner row	1
	1-outer row	$1+2(\frac{1}{2})$
	2	2
	3	$3+2(\frac{1}{2})$
	4	4
Outer driver core	5	$4+2(\frac{1}{2})$
	6	7
	7	$2+2(\frac{1}{2})$
Blanket assemblies	8	5
	9	9
	10	$9+2(\frac{1}{2})$
Neutron shielding	11	10
	12	41
	13	6
Control rods	FC	$6+2(\frac{1}{2})$
	C-coarse control rods	$2+(\frac{1}{6})$
	F-fine control rods	0
Neutron source	B-backup control rods	1
	N	0

The CAD model files for the common simplified upper plenum model were provided in various formats including IGES, ACIS, Parasolid, Step, and Catia V4.

6.1.3. Upper core structures

In addition to the large cylindrical main body, the Monju UCS includes flow guide tubes that channel a portion of the hot sodium above the core outlets into the region where the thermocouples and flow meters are located, a thin honeycomb grid that holds the flow guide tubes in place, the large diameter control rod guide tubes, and the fingers that extend from the bottom end of UCS main body down to just above the honeycomb grid to support the thermocouples and flow meters above the flow guide tube exits. The main body and control rod guide tubes are modeled explicitly in the simplified geometry. However, the dimensions of the flow guide tubes, honeycomb structure and fingers are much smaller, and so their influence on the flow field is accounted for through a multi-region direction-dependent porous media representation described in Section 6.2.

A combined view of the control rod and flow guide tubes as well as honeycomb structure is shown in Fig. 38. Since the control rod guide tubes are much larger in diameter with respect to the other components of the upper core structure, they are included in the symmetric model explicitly. The influence of other components is captured via porous media formulation.

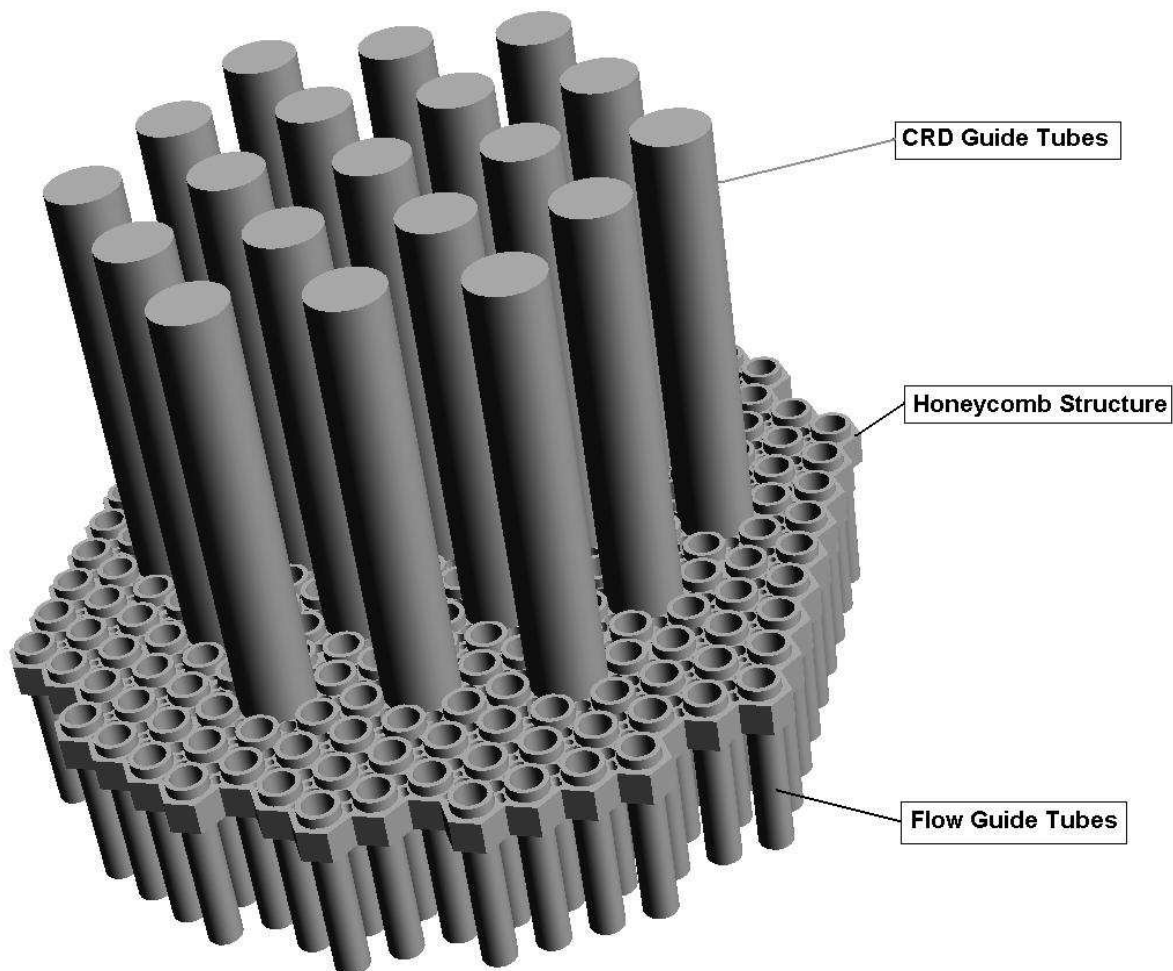


FIG. 38. Combined view of the control rod and flow guide tubes held together by the honeycomb grid in Monju upper core structures (the fingers are excluded from the view).

There are three complete and one 1/6 (at the center of the core) control rod assemblies in the simplified model. Since the circular control rod guide tube cross section area is greater than the hexagonal subassembly cross section area, the 1/6 symmetric simplified model cuts through a small portion of the coarse control rod C in channel 2. Also, although the backup control rod in channel 2 is not part of the simplified model, one of the symmetry planes cuts through a small portion of the control rod guide tube belonging to it and, therefore, it is included in the simplified model. In a way, the small portion of the backup control rod guide tube included in the simplified model completes the cut off coarse control rod guide tube in the second channel.

The guide tubes for backup control rods (marked as B in Fig. 37) are taller than the guide tubes for coarse control rods (marked as C in Fig. 37). The guide tubes for coarse control rods extend just below the honeycomb grid while the bottom end of the guide tubes for backup control rods align with the bottom end of the flow guide tubes (50 mm above the subassembly outlets). The outer diameter for both types of control rod guide tubes above the honeycomb grid is 167 mm. The outer diameter of the backup control rod guide tubes below the honeycomb grid is 156 mm. Both types of control rod guide tubes are included in the simplified model as solid objects with adiabatic boundaries.

The bottom inlet of the flow guide tubes are placed 50 mm above the core outlets. There is a flow guide tube for each of the 198 core subassembly outlets (33 in the simplified model) of the channels 1-8, and 16 guide tubes (3 in the simplified model) for some of the subassemblies belonging to the channel 9. The fingers with thermocouples and flow meters extend into the top outlet end of the flow guide tubes just above the honeycomb structure. The honeycomb grid itself is a 75 mm thick perforated plate with holes of different diameters to support the flow and control rod guide tubes.

In order to support the development of the porous media model (see Section 6.2), calculations were performed to determine the flow allocation through various pathways in the UCS. Details of the flow splits are provided in Table 4. From this table, the flow rate through the honeycomb region at the is approximately 60% of the total flow at the initial condition, and 67% at the flow rates reached 1 hour into the test. Thus, the difference in flow splits between the initial (nominal) and final (under the influence of natural convection) conditions is not significant. However, the flow resistance of the honeycomb grid is important for the flow distribution inside the flow guide tube region. Therefore, the porous media representation of the upper core structures must take the influence of honeycomb grid into account as a distinct component.

TABLE 4. CALCULATED FLOW SPLITS IN UPPER CORE STRUCTURE

Flow Path	Relative Flow $t=0$	Relative Flow $t=1$ hour
Bypassing upper core structure	15%	3%
Through flow guide tubes	47%	52%
Vertical flow between flow guide tubes, through honeycomb structure	13%	15%
Lateral flow between flow guide tubes, bypassing honeycomb structure	25%	30%

From Table 4, approximately half of the core subassembly flow is channelled through the flow guide tubes. The porous medium that represents the flow guide tubes occupies the region vertically between 27,100 mm and 27,525 mm as marked by the lower and upper end of the actual flow guide tubes. It is 425 mm high and starts 50 mm above the core subassembly outlets. The lateral extent of this porous region reaches to the boundary between the channels 8 and 9 and, in the simplified model, it is approximated as a cylindrical zone with a diameter of 2,200 mm. The influence of the honeycomb grid is simplified via representation of this component as a zero thickness porous baffle at vertical elevation of 27,425 mm (375 mm above the core subassembly outlets).

The fingers are located vertically between the porous region representing the flow guide tubes and the solid bottom wall of the upper core structure main body. In the complete Monju model, there are 214 fingers (36 in the simplified 1/6 symmetric model), each equipped with a thermocouple at its end. Some of the flow guide tubes are bent outward, such that the horizontal positions of the outermost instrumented subassemblies are outside the projected cross section of the UCS main body. Therefore, the lateral extent of the porous medium representing the fingers has the distinct shape shown in Fig. 39. There is a 39 mm gap between the porous media representing the fingers and the flow guide tubes. The thermocouples and flow meters located in this gap have a small diameter (19 mm) compared to the diameter of the fingers (47.7 mm). Therefore, their influence is neglected in the simplified model and no pressure loss correlations are specified for this gap.

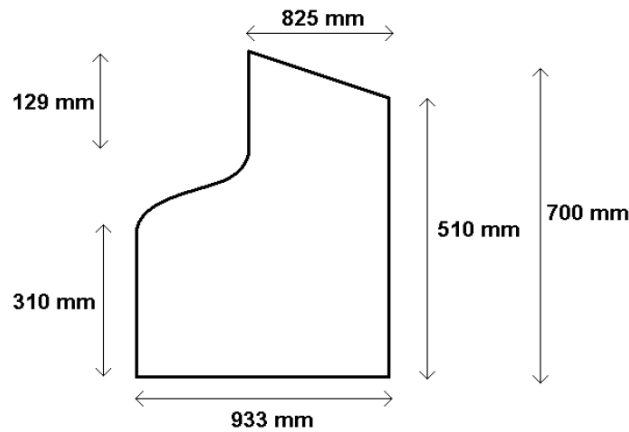


FIG. 39. The geometric dimensions of the area occupied by fingers in the Monju upper core structures and modeled as porous medium.

6.2. DESCRIPTION OF POROUS BODY MODEL FOR THE UPPER CORE STRUCTURE

The UCS is modeled by a porous media with directional pressure losses [11]. The two regions (FGT and fingers) are filled with tube bundles. The correlation defining the friction coefficient C_f , which is used to predict the pressure loss within these regions, is valid for flow inside and outside of tube bundles with a circular pitch [11]:

$$C_f = a Re^{-b} \quad \text{with} \quad Re = \frac{UD}{\nu} \quad (1)$$

Here, Re is the Reynolds number, U the local velocity, D a characteristic diameter and ν the kinematic viscosity. The correlation distinguishes the axial and the transverse direction of the flow. The different parameters of the correlation are given in the Table 5.

TABLE 5. PARAMETERS FOR THE PRESSURE LOSS CORRELATION

	a	b	U	Characteristic diameter D
Axial direction	0.316	0.25	Axial velocity \vec{U}_a	Hydraulic diameter D_h
Transverse direction	4.03	0.27	Transverse velocity \vec{U}_t	External diameter of tubes D_e

A volumetric porosity of 0.83 is defined for the fingers region to simulate the acceleration of the flow outside of the tubes due to mass conservation considerations. The hydraulic diameter D_h is defined by:

$$D_h = \frac{4 S}{P} \quad (2)$$

S is the fluid cross-section and P the wetted perimeter of the tubes. The axial velocity \vec{U}_a and transversal velocity \vec{U}_t are then calculated as a function of tube direction vector \vec{d}_a :

$$\vec{U}_a = (\vec{U} \cdot \vec{d}_a) \vec{d}_a \quad \text{and} \quad \vec{U}_t = \vec{U} - \vec{U}_a \quad (3)$$

The tube direction vector \vec{d}_a defines the main tube alignment and is simplified as the global vertical direction $(0,0,1)^T$. In CFD codes, the directional pressure loss \vec{P}_L is treated usually as a source term in the Navier-Stokes equation. The parameters of the correlation for both regions are gathered in Table 6.

TABLE 6. PRESSURE LOSS PARAMETERS

	Type	Pressure loss correlation	Parameters
FGT area	Circular pitch bundle	$\vec{P}_L = \frac{d\vec{U}}{dt} = -\rho C f_a \frac{ \vec{U}_a }{2 \cdot D_h} \vec{U}_a - \rho C f_t \frac{ \vec{U}_t }{2 \cdot D_e} \vec{U}_t$	$D_h=72$ mm $D_e=76$ mm
FGR area		$C f_a = 0.316 \text{ Re}^{-0.25}$ with $\text{Re} = \frac{ \vec{U}_a D_h}{\nu}$ $C f_t = 4.03 \text{ Re}^{-0.27}$ with $\text{Re} = \frac{ \vec{U}_t D_e}{\nu}$	$D_h=47.7$ mm $D_e = \begin{cases} 0.24 \text{ m} & \text{for } EL \leq 27874 \\ 0.17 \text{ m} & \text{for } EL \geq 28135 \\ \text{linear between the two } EL \end{cases}$

It is important to verify that the implementation of the transversal pressure loss leads to angle independent results for flow source in the centre of a symmetric rod bundle. The plate of the honeycomb structure is modelled like a plate without any thickness. The singular pressure loss which is applied on the plate is a grid pressure loss correlation [11]. The directional pressure loss $\Delta \vec{P}$ applied on the HS plate is defined as:

$$\Delta \vec{P} = \frac{1}{2} \rho K |\vec{U}| (\vec{U} \cdot \vec{n}) \quad (4)$$

Here, ρ is the fluid density, K the pressure loss coefficient of the HS and \vec{n} the normal vector of the surface of the HS plate. According to Ref. [12], the value of the pressure loss coefficient K is constant during the trip test and is equal to 60.

6.3. METHODS, CODES AND MODELS

6.3.1. 1/6 sector model

6.3.1.1. CEA

The CFD reference code of the CEA is called Trio_U [13]. Trio_U is a CFD code for strongly unsteady low Mach number, turbulent flows. The code is especially designed for industrial LES calculations on structured and non-structured grids of hundreds of millions of nodes. Trio_U is based on an object oriented, intrinsically parallel approach and is coded in C++. The parallelism is implemented by the overlapping domain decomposition method where the data exchange is assured when necessary by means of MPI libraries. The flexible code structure allows the user to choose a suitable discretization method and to combine various appropriate physical models, including different treatments of turbulence. Several convection and time marching schemes as well as a wide range of boundary conditions are available. This flexibility is implemented for massively parallel computing without a significant reduction of the overall performance of the code.

For unstructured grids, the hybrid Finite Volume based Finite Element method is applied. This method consists in determining for a continuous problem a discrete solution in the space of the finite element by maintaining the balance notation of finite volumes. The space discretization is performed on triangles (2D cases) and on tetrahedral cells (3D cases). In Trio_U, the main unknown velocity and temperature is located in the centre of the faces of an element what results in a P1 non-conforming discretisation element. The pressure is discretized in the centre (P0) and in the vertices (P1) of the element. This localization of unknowns is known as staggered mesh which avoids the presence of spurious pressure modes, improves the velocity/pressure coupling and extends the divergence free basis. The standard numerical scheme used for RANS calculation is presented in Table 7; more details on the actually used numerical scheme are given in the following chapters of this report. More information on the code and the discretization can be found in Refs. [13–14].

TABLE 7. STANDARD NUMERICAL SCHEME FOR RANS CALCULATIONS

Meshing	Tetrahedrons	At least 9 calculation point between Walls
Discretization	Finite Volume Elements	P0/P1 for the Pressure P1 non-conform for Velocity
Time scheme		1 st order Euler implicit scheme
Momentum transport	Convection	1 st order upwind
	Diffusion	2 nd order centred
	Wall treatment	Wall law « Reichardt » with $y^+ > 30$
	Turbulence:	k-ε model with standard coefficients
Solution procedure	Transient calculation	Implicit fractional step method
Thermal effects	Boussinesq hypothesis	$\Delta\rho/\rho < 0.1$ Pr = 0.0039 at 700°C turbulence model (k-ε) includes thermal stratification effects

6.3.1.2. IGCAR

(1) 3-D model

For 3-D simplified benchmark model, a segment of the Monju upper plenum excluding fuel handling and transfer system is considered. A 60° sector of the hot pool is taken for this study (Fig. 40). To maintain symmetry with respect to hexagonal core, outlet nozzle is rotated 12.5° . Upper core structure and control rod guide tube are represented explicitly in this model. Flow guide tubes, honeycomb grid, and fingers are accounted by appropriate porous media models. Nozzle is extended and thus outflow boundary condition is applied. The flow holes in the inner barrel are also modeled explicitly. Inner barrel is accounted by an adiabatic gap. Zone based staggering is applied to S/A outlets to identify inlet zones.

The free surface of sodium is assumed as a wall with zero shear. All external walls are adiabatic. Boussinesq approximation is employed to account for the buoyancy effect in the vertical momentum equation. High Reynolds number standard k- ϵ model [15] is enabled for simulating turbulence. Computations have been carried out using the commercial CFD code STAR-CD [16]. About 0.28 million hexahedral mesh have been employed for the simulation.

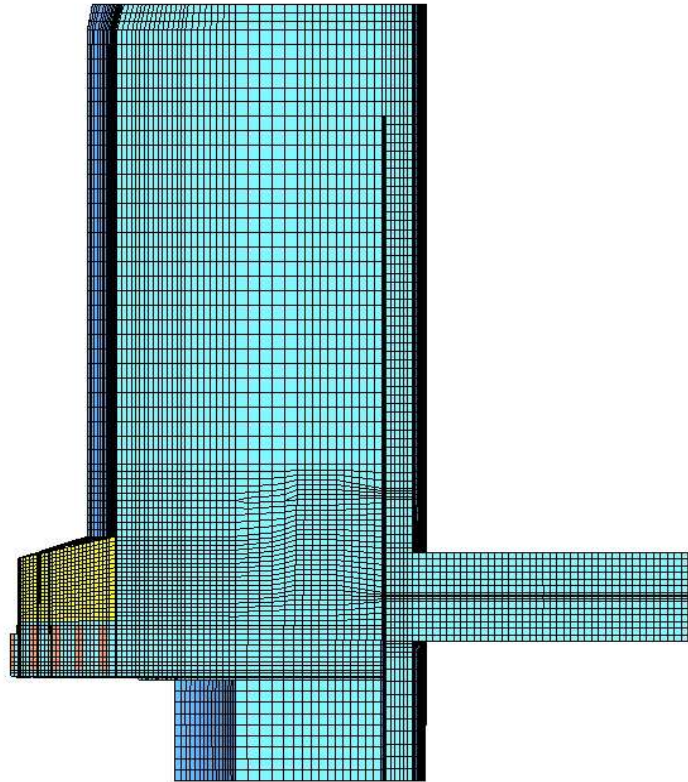


FIG. 40. Computational domain of benchmark model.

(2) Algorithm

Details of solver and algorithms are given in Table 8:

TABLE 8. DETAILS OF SOLVER AND ALGORITHMS

	Steady / transient	
	steady	transient
Pressure velocity coupling algorithm	SIMPLE	PISO
Convergence Accelerator	Conjugate Gradient method	Conjugate Gradient method

(3) Schemes for combining convection and diffusion fluxes

Details of schemes are given in Table 9.

TABLE 9. DETAILS OF SCHEMES FOR COMBINING CONVECTION AND DIFFUSION FLUXES

Schemes	Steady / transient	
	steady	transient
Momentum equation	MARS scheme	MARS scheme
Energy equation	1 st order Upwind	1 st order Upwind
Turbulence equations	MARS scheme	MARS scheme

(4) Turbulence parameters

Turbulence parameters are given in Table 10.

TABLE 10. TURBULENCE PARAMETERS

	Steady / transient	
	steady	transient
Intensity, %	5.0	5.0
Mixing Length, m	0.00005	0.00005

(5) Porous body formulation

The flow through the main body and control rod guide tubes of the UCS are assumed as zero. Other components, viz., flow guide tubes, honeycomb grid and fingers are modeled as porous sub-region as recommended by CEA [17]. Direction dependant pressure loss coefficients are used to account for the resistance offered by fine-scale structures of UCS. The pressure loss coefficient, for flow guide tubes and fingers are calculated from friction factor correlations for pin bundle configurations [17].

6.3.1.3. KAERI

(1) Methods and code

Computations are carried out using the commercial code CFX-13 and the details of the numerical method are summarized in Table 11.

TABLE 11. SUMMARY OF NUMERICAL SCHEME

Dimension	3D calculation
Physical properties	Sodium at 400 °C
Mesh	1.3 million tetrahedral elements
Unsteady term (all)	2 nd -order backward difference scheme
Convection term (all)	Higher-order (more than 2 nd -order) scheme
Diffusion term (all)	Central difference scheme
Buoyancy term	Boussinesq assumption
Turbulence model	k- ω shear stress transport (SST) model

(2) Numerical grids

Using the CAD model of the simplified 60° geometry, the numerical grids are generated with the ICEM CFD software. A total of 1.3 million tetrahedral elements are generated in the whole computational domain. Fig. 41 shows the numerical grids employed in the present study for a simulation of the whole solution domain.

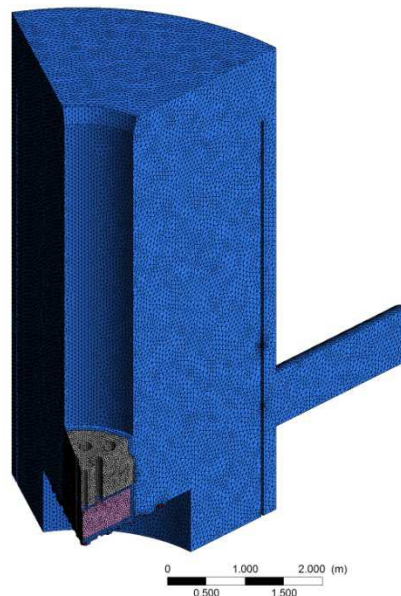


FIG. 41. Numerical grids.

(3) Turbulence model

The turbulence model employed in the present simulation is the shear stress transport (SST) model. In this model, the transport equations for the turbulence kinetic energy (k) and its frequency (ω) are solved. The governing equations for k and ω are as follows;

$$\frac{D}{Dt}(\rho k) = \frac{\partial}{\partial x_j} \left[(\mu + \sigma_{k3} \mu_t) \frac{\partial k}{\partial x_j} \right] + \rho(P_k + G_k) - \rho \beta^* \omega k \quad (5)$$

$$\frac{D}{Dt}(\rho \omega) = \frac{\partial}{\partial x_j} \left[(\mu + \sigma_{\omega3} \mu_t) \frac{\partial \omega}{\partial x_j} \right] + \rho \frac{\gamma_3}{\mu_t} (P_k + G_k) - \rho \beta_3 \omega^2 + 2\rho(1 - F_1) \frac{\sigma_{\omega2}}{\omega} \frac{\partial k}{\partial x_j} \frac{\partial \omega}{\partial x_j} \quad (6)$$

In this model the Reynolds stresses and turbulent heat fluxes are expressed as follows:

$$\overline{u_i u_j} = -\nu_t \left(\frac{\partial U_j}{\partial x_i} + \frac{\partial U_i}{\partial x_j} \right) + \frac{2}{3} k \delta_{ij} \quad (7)$$

$$\overline{\theta u_j} = -\frac{\nu_t}{Pr_t} \left(\frac{\partial T}{\partial x_j} \right) \quad (8)$$

where the turbulent eddy viscosity is given as follows:

$$\mu_t = -\frac{\rho a_1 k}{\max(a_1 \omega, SF_2)}, \quad \nu_t = \frac{\mu_t}{\rho} \quad (9)$$

$$F_1 = -\tanh((arg1)^4), \quad F_2 = \tanh((arg2)^2) \quad (10)$$

$$arg1 = \min \left(\max \left(\frac{\sqrt{k}}{\beta^* \omega y}, \frac{500\nu}{y^2 \omega} \right), \frac{4\rho k \sigma_{\omega2}}{CD_{k\omega} y^2} \right), \quad arg2 = \max \left(\frac{2\sqrt{k}}{\beta^* \omega y}, \frac{500\nu}{y^2 \omega} \right) \quad (11)$$

$$CD_{k\omega} = \max \left(\frac{2\rho \sigma_{\omega2}}{\omega} \frac{\partial k}{\partial x_j} \frac{\partial \omega}{\partial x_j}, 10^{-10} \right) \quad (12)$$

The coefficients of the SST model are a linear combination of the corresponding coefficients such that

$$\phi_3 = F_1 \phi_1 + (1 - F_1) \phi_2 \quad (13)$$

Where F_1 is a blending function defined by Eq. (10), and the σ_{k3} , $\sigma_{\omega3}$, β_3 , and γ_3 are calculated by Eq. (13) using the following values of constants;

$$\sigma_{k1} = 0.85, \quad \sigma_{\omega1} = 0.500, \quad \beta_1 = 0.0750, \quad \gamma_1 = \beta_1 / \beta^* - \sigma_{\omega1} \kappa^2 / \sqrt{\beta^*} \quad (14)$$

$$\sigma_{k2} = 1.00, \quad \sigma_{\omega2} = 0.856, \quad \beta_2 = 0.0828, \quad \gamma_2 = \beta_2 / \beta^* - \sigma_{\omega2} \kappa^2 / \sqrt{\beta^*} \quad (15)$$

and

$$\beta^* = 0.09, \quad a_1 = 0.31, \quad \kappa = 0.4187, \quad Pr_t = 0.9, \quad \nu = \mu / \rho \quad (16)$$

$$S_{ij} = \frac{1}{2} \left(\frac{\partial U_i}{\partial x_j} + \frac{\partial U_j}{\partial x_i} \right), \quad S = \sqrt{2S_{ij}S_{ij}} \quad (17)$$

$$P_k = -u_i u_j \frac{\partial U_j}{\partial x_i}, \quad G_k = \beta g_i \frac{v_t}{Pr_t} \frac{\partial T}{\partial x_i} \quad (18)$$

(4) Boundary conditions

The time-dependent mass flow rate and temperature are prescribed at the each subassembly outlet using the experimental data provided by JAEA. The mass flow rate and temperature at each subassembly are assumed to be spatially uniform. The turbulent kinetic energy and its frequency are specified using the turbulence intensity (5%) and the geometric data of each subassembly outlet. All the walls are treated as adiabatic, and no slip boundary condition is specified at the wall since the calculation is carried out all the way to the wall without using the wall functions. The symmetry condition is specified at the two lateral surfaces of the 60° geometry. The pressure boundary condition is specified at the outlet nozzle.

6.3.1.4. IPPE

(1) GRIF code structure

GRIF is the Russian computational tool for 1-phase thermal-hydraulics analysis of the transients in the reactor as a whole and in its parts.

The code should be classified as ‘system’ code and it contains of the following modules:

- 3D thermal-hydraulic model for calculation of sodium velocity, pressure and temperature in the primary circuit;
- 3D model for simulation of inter-wrapper sodium thermal-hydraulics.

The code also includes the following modules:

- Primary pump model (analytical correlation);
- Module «Wrapper» for calculation of temperature distributions in the Sa wrappers;
- Module «IHX» for simulation of flow and temperature in the IHXs;
- Module «DHX» for simulation of flow and temperature in the DHXs;
- Module «PIN» option of 1D-3D models for fuel pins, absorber pins and shielding elements simulation;
- Module «REACTIVITY», analytical correlations with recalculated reactivity coefficients;
- Module «KINETICS» ‘Point’ kinetics with 6 groups of delayed neutrons.

Only one but important module of the GRIF code (3D thermal hydraulic model) is used as a tool for the analysis of Monju NC tests.

(2) GRIF code approach

For the simulation of heat and mass transfer in the reactor the set of 3D and mass momentum and heat transfer equations are solved in the GRIF code, taking into account the following:

- Porous body formulation is used for the simulation of flow and heat exchange in the regions with complex internal structure;

- The coolant is assumed as incompressible;
- The Bousinesq approach is used for the simulation of NC phenomena;
- Cartesian or cylindrical coordinates with non-uniform meshing could be chosen for modelling;
- Only algebraical model could be used for simulation of turbulence phenomena.

(3) Nodalization scheme

The simplified Monju upper plenum model includes a 60° symmetric segment of the Monju upper plenum (in the azimuthal direction) and the region between the bottom support plate and the top dip plate (in the axial direction). A schematic view of Monju upper plenum is shown in Fig. 42. The large cylindrical main body of the upper core structure is represented explicitly in the numerical model but the heat exchange between sodium and the main body is not taken into account. The other upper core structure components (flow guide tubes, honeycomb grid, and fingers) are left out from the porous media models. The holes on the inner vessel barrel are represented explicitly but by using one mesh cell for each hole.

The 1/6 part of Monju upper plenum is covered with the following non-uniform (R*Z*Fi)-mesh: (33*43*24). Mesh indexes are accordingly (i, k, j).

Vertical cross-sections of the model are presented in Fig. 43, horizontal cross-sections in Fig. 44.

Table 12 gives the distribution of subassemblies among the rings of core model.

TABLE 12. DISTRIBUTION OF SUBASSEMBLIES AMONG THE RINGS OF CORE MODEL

SA types	Ring number 'I'	Number of SAs
Fuel Inner SA+1 Control rods	2	19
Fuel Inner Sa+Control rods	3	18
Fuel Inner SA	4	24
Fuel Inner SA+6 Control rods	5	24
Fuel Inner SA+6 Control rods	6	36
Fuel Outer SA	7	42
Fuel Outer SA	8	18
Fuel Outer SA	9	30
Fuel Outer SA+2 NS	10	54
Blanket	11	60
Blanket	12	60
Neutron shielding	13-15	240
Neutron shielding	16	36
Neutron shielding	17	42

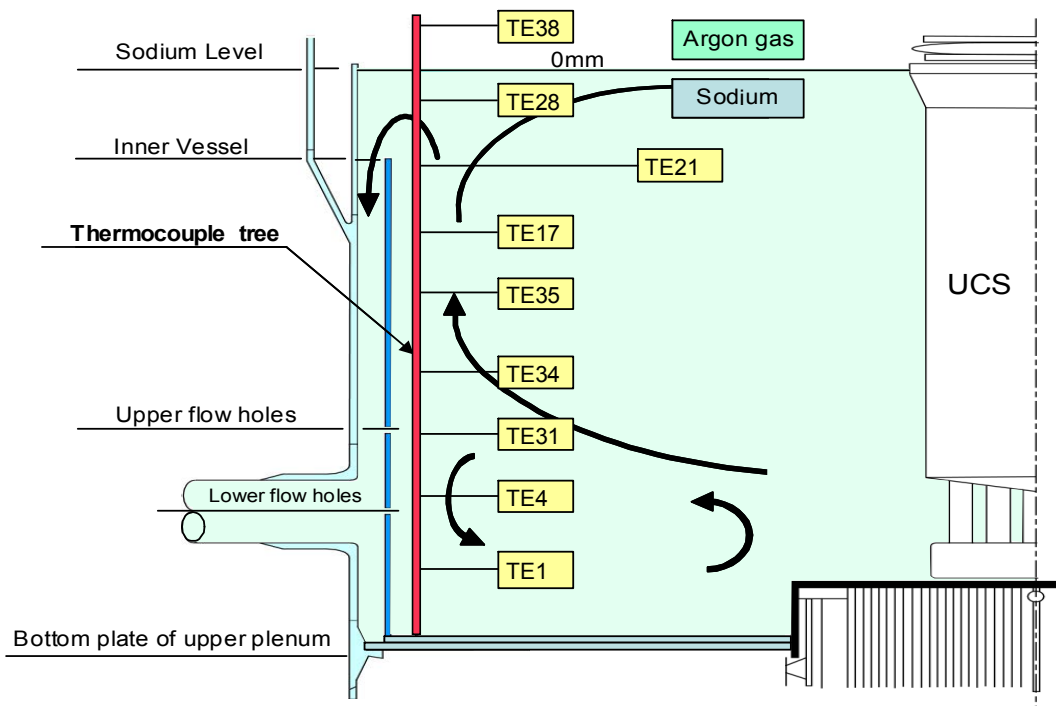


FIG. 42. Schematic view of Monju upper plenum.

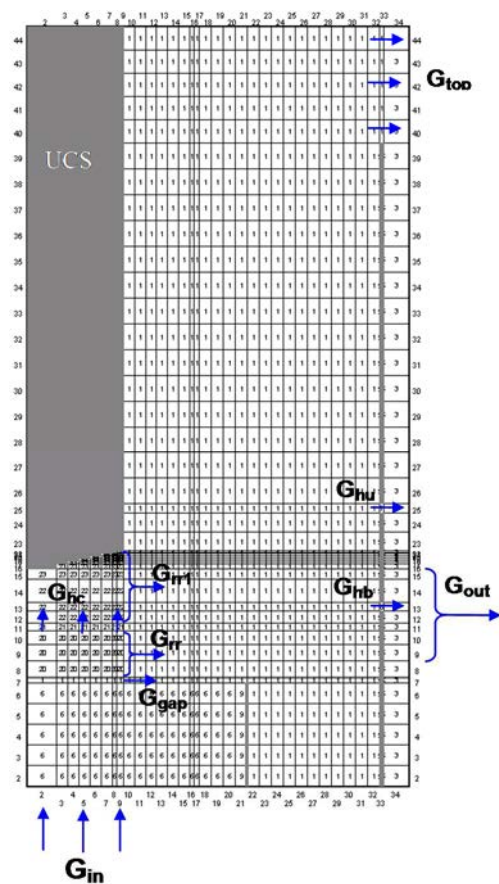


FIG. 43. Vertical cross-sections of calculative domain.

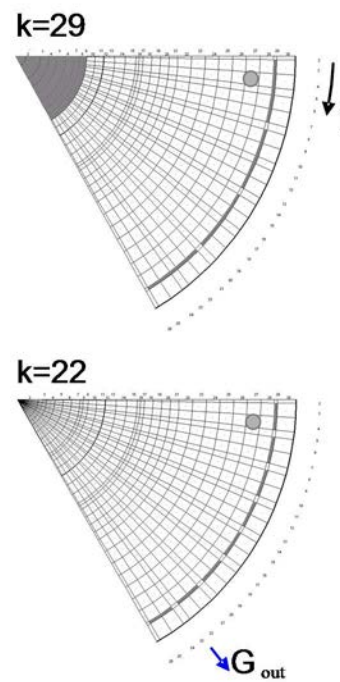


FIG. 44. Horizontal cross-sections of calculative domain.

(4) Other code performance parameters

Mesh size and time step size combination:

Radial: range 0.04–0.23, most typical 0.11;

Axial: range 0.08–0.023, most typical 0.2;

Azimuthal: range 0.014–0.051(rad), most typical 0.05.

The time step size range is 0.01 s at the beginning of transient and 0.5 s after 1000 seconds from the beginning of the transient.

The calculations were performed on the ‘hp workstation xw6200’.

Calculation of one transient of 9000 seconds takes 15 ours of computer time.

6.3.1.5. ANL

(1) CFD mesh and model

The volume mesh for the simplified model is built using various options at ANL. Starting with the CAD model of the simplified model, a finely triangulated surface mesh enclosing the volume occupied by the liquid sodium is prepared with commercial STAR-CD CFD software [18] as the first step. This common surface mesh established the basis to generate volume meshes using both trimmed hexahedral and polyhedral cells, each with a coarse and a refined grid with total computational cell count ranging from 0.4 to 3.5 million. All volume meshes included local refinements around the upper core structure, in the outlet nozzle, and around the flow holes on the inner barrel. The steady-state calculations (to simulate the conditions before the test is initiated as well as one hour after the transient) are performed to assess sensitivity of the calculated results to the mesh structure.

Although the grid independent solutions are obtained with both types of meshes at steady-state, the transient calculations are pursued with an optimal CFD grid using polyhedral mesh with 100 mm base (reference) cell size. Near the surfaces of various upper plenum components, additional constraints are specified to enforce local cell refinements. These constraints include minimum 36 points to represent the curvature of a circle and several volumetric controls to enforce reduced base cell size. Specifically, the base cell size is limited to 25 mm in the region just above the subassembly outlets and inside the outlet nozzle, 50 mm in the porous region representing the upper core structures, 12.5 mm in the transition region between the reactor vessel and outlet nozzle, and 6.25 mm around each flow hole to assure accurate representation of the pressure drop for bypass flow through them. ‘Medium’ growth rate is specified to assure gradual transition between the bulk volume mesh and the regions with local refinements.

The polyhedral mesh has four layers of prismatic cells near the wall boundaries with 25 mm total thickness and 1.3 as the ratio of the thickness of consecutive layers (about 4 mm for the thickness of near-wall boundary layer). Around the holes through the inner barrel, 8 prismatic cell layers with a total thickness of 20 mm is enforced using 1.25 as the ratio of the thickness of consecutive layers. Inside the outlet nozzle, 8 prismatic cell layers with a total thickness of 25 mm is enforced using 1.2 as the ratio of the thickness of consecutive layer. With these parameters, the final mesh has about 840,000 CFD cells as a reasonably refined near-optimal mesh suitable for simulations of hours long transient. An isometric view of the final CFD mesh as well as cross section cuts through the holes, outlet nozzle, and core subassembly outlets are shown in Fig. 44.

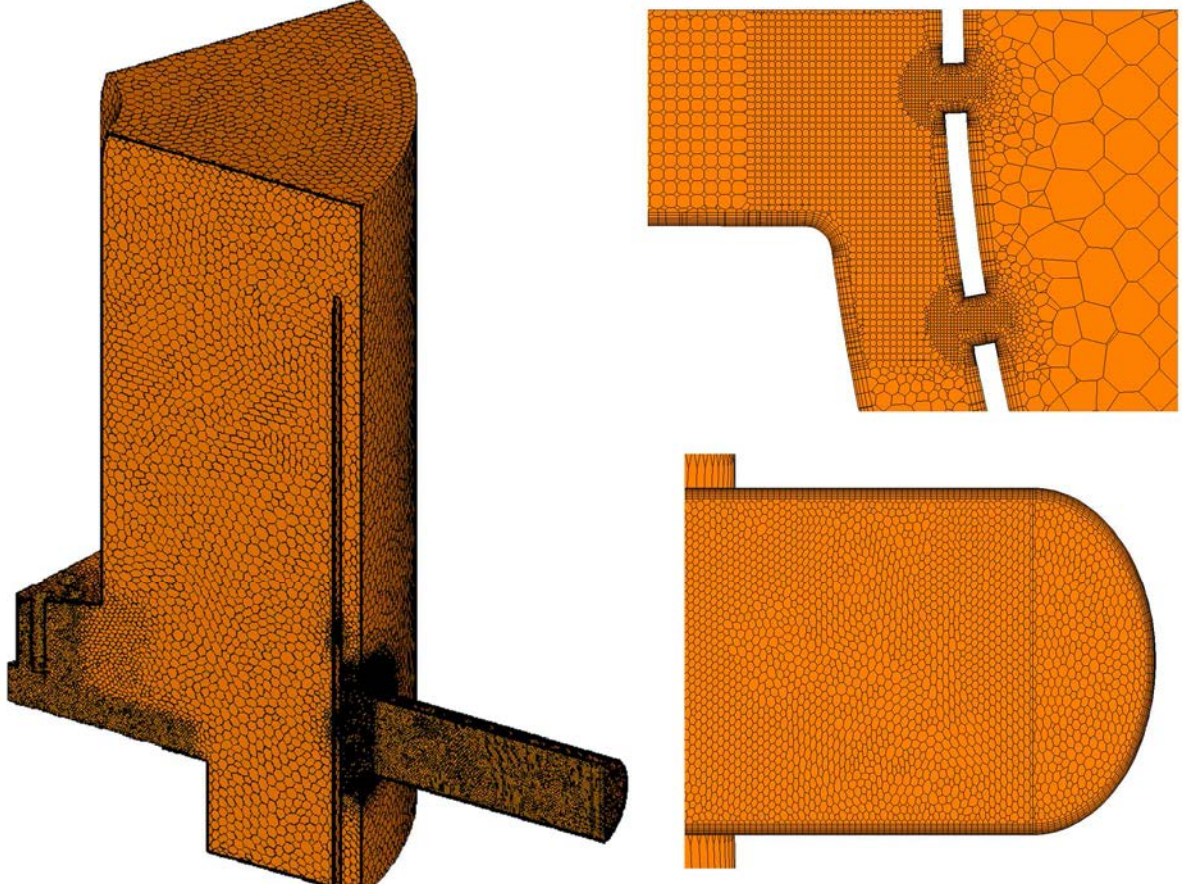


FIG. 45. Complete and enlarged cross section views of the CFD mesh for the simplified Monju model.

Other than the larger control rod guide tubes, the complex geometric structures above the core (flow guide tubes, honeycomb structure, thermocouples and flow meters, and fingers) are excluded in the simplified model. Instead, this crowded region is modelled using the porous media approach. In STAR-CD, the pressure drop for flow through a porous medium is formulated as an additional force per unit volume in the momentum conservation equation:

$$F_p = -K \cdot v \quad (19)$$

where K is the porous resistance tensor and $v = \dot{m}/(\rho A_{total})$ is the superficial velocity. The porous resistance tensor has the following form:

$$K_i = \alpha_i |v| + \beta_i \quad (20)$$

where α_i and β_i are directionally dependent user supplied coefficients. The values for these coefficients are specified based on characterization of distributed resistance of various components as determined by CEA [19]. The porous-baffle effect of the honeycomb grid which poses some resistance to axial flow is neglected.

The inlet boundary conditions at the core subassembly outlets are specified in user subroutines as the time dependent values for the sodium flow rates and subassembly outlet temperatures and linearly interpolated between the tabulated values. The subassembly mass flow rates (in kg/s) are converted to velocities (in m/s) by taking into account the proper density of the liquid sodium at the specified outlet temperature of the corresponding subassembly. These ‘superficial’ velocities are then specified to apply uniformly at the

subassembly outlet neglecting the effect of the reduced cross section flow area due to potential blockage of structures or fuel pins. This approximation is expected to underestimate the pressure drop near the subassembly outlets; however, it is consistent with the porous media representation of the upper core structures. Other than the two symmetry planes and the end of the outlet nozzle, all other boundaries in the simplified model are treated as adiabatic walls. The end of the outlet nozzle is modelled as flow-split outlet boundary to avoid any inflow due to temporal pressure fluctuations.

The calculations are performed using the realizable $k-\epsilon$ turbulence model with standard wall functions. The prismatic cell layers are used to provide appropriate wall boundary thicknesses suitable with the Reynolds-Averaged Navier-Stokes (RANS) turbulence models intended to be used in simulations. Also, the sharp edge between the outlet nozzle and reactor vessel is rounded to avoid large pressure fluctuations and recirculation around that edge. The second-order proprietary MARS scheme is evaluated for both the initial steady-state and transient reference case calculations. The algebraic set of finite volume equations resulting from discretization of conservation and turbulence transport equations are solved using the well-established Semi-Implicit Method for Pressure Linked Equations (SIMPLE) in conjunction with a first-order, fully-implicit Euler scheme. The SIMPLE method usually provides accurate results for lower computational cost, but a separate calculation using the more conventional PISO transient solver scheme that involves predictor-corrector stages for each time step is also performed for comparisons. The algebraic multi-grid (AMG) solver is used to accelerate the convergence.

6.3.2. Full sector model

6.3.2.1. CIAE

A 360° full sector model, as showed in Fig. 46, has been used for considering the non-symmetry layout of the nozzle outflow and the inlet flow per S/A from the reactor core of Monju in CIAE. Most of the structures in the reactor block are simulated in detail without any approximation. For example, the bottom parts of the UCS, including the fingers, honeycomb structure and flow guide tubes which have effects on the flow direction in the normal conditions and shutdown condition of the reactor are modelled by fine mesh. It should be pointed out that these trimmed grids for modelling complicated structure of the bottom parts of UCS only show the shape of the solid parts, not the entity. So the thermal capacity of the structures is not considered in the simulation as well as the heat transfer and thermal conductivity of the inner barrel.

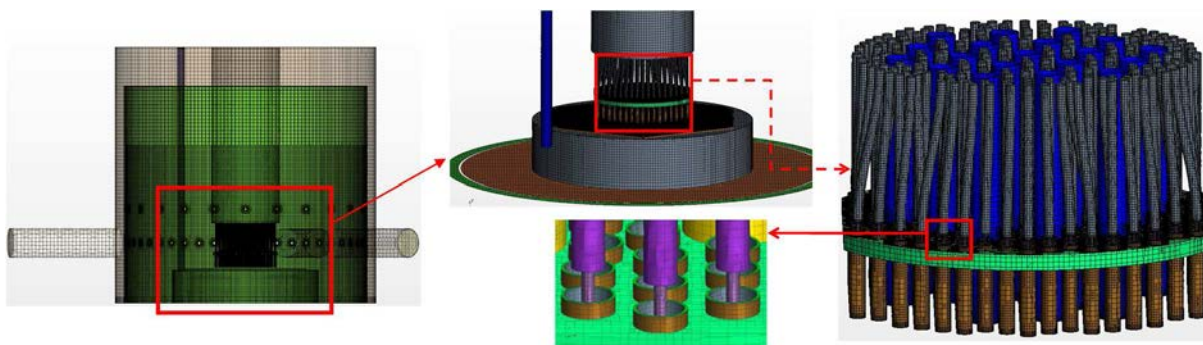


FIG. 46. 360° model for the reactor block with the detailed part.

6.3.2.2. JAEA

(1) Governing equations

In this study, multi-dimensional thermal-hydraulic analysis code FrontFlow/Red [20], which was developed by University of Tokyo under the project of Revolutionary Simulation Software, was applied to the present calculations. The governing equations applied in this code were mass, momentum and energy conservation equations for incompressible fluid, which were discretized by FVM. The standard k- ϵ model with the re-normalization group theory (RNG k- ϵ model) was also applied as the turbulence model.

Buoyancy force was considered as the third terms in the Eq. (21). Flow holes on the HS are too small compared to the plenum size to be modelled even by the present detailed grids. Hence, the HS was assumed as a porous medium; only these holes were modelled by porous media approaches with pressure loss correlations, which were also added in the fourth terms of the Eq. (21):

$$\frac{\partial(\rho u_i)}{\partial t} + \frac{\partial(\rho u_i u_j)}{\partial x_j} = -\frac{\partial p}{\partial x_i} + \frac{\partial}{\partial x_j} \left[(\mu + \mu_t) \left(\frac{\partial u_i}{\partial x_j} + \frac{\partial u_j}{\partial x_i} \right) \right] + (\rho - \rho_0) g_i - \delta(z - z_0) K \frac{1}{2} \rho |u_i| |u_i| \quad (21)$$

where z_0 is the location of the bottom of the HS. ρ , μ and p are the density, viscosity and pressure of liquid sodium, respectively. ρ_0 is the density at a reference temperature in the upper plenum. μ_t is the turbulent viscosity ($\mu_t = C_\mu k^2 / \epsilon$) and K is the pressure loss coefficient which was evaluated and proposed as $K = 25$ [21]. $\delta(z)$ is the Dirac delta function.

(2) Discretization of governing equations

FrontFlow/Red employs implicit methods to solve the algebraic finite volume equations for hexahedron, tetrahedron, triangular prism and square pyramid meshes using the general curvilinear coordinate system with the collocated grid arrangement of the variables, in which the velocity components and the pressure are defined at the cell center and the fluxes are defined on the cell-bounding surfaces. Rhie-Chow correction [6–12] is also used to remove oscillations in the pressure solutions. The fully-implicit scheme of SIMPLE method was applied to all equations in the present steady state calculations. The first order upwind and the second order central difference scheme were respectively applied to the advection and diffusion terms. ICCG for the pressure Poisson equation and BiCGSTAB for the other equations were also applied to the matrix solvers. In order to avoid converging to inadequate solutions and to accelerate convergence of the iterative process, a pseudo time-marching approach was applied in the present calculations: The discretized transient equations were solved by using under-relaxation factors.

(3) Calculation models

The region from the support plate to the dip plate except for the upper skirt structure was basically modelled in detail without any approximation, although only honeycomb structure (HS) was modelled with porous media approaches: The shapes of the outlets of core subassembly, FHM, TC-plug, in-vessel racks and IVTM lower guide were modelled in detail by using hexahedron, tetrahedron, triangular prism and square pyramid meshes. These models and the close-up views of the FHs are shown in Fig. 47.

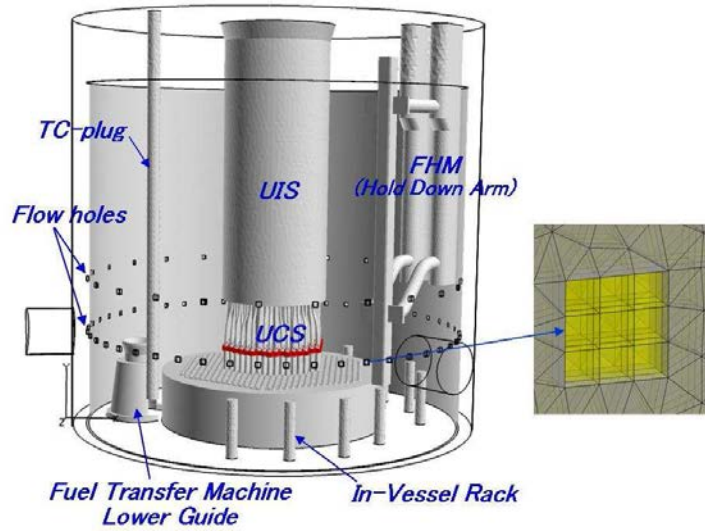


FIG. 47. Analytical model of Monju RV upper plenum.

The close-up views in the UCS region and around HS are also shown in Fig. 48. The red painted region is the HS and flow holes opened between the FGTs and CRGTs were modelled by the porous media approaches. The total number of the mesh increased to approximately 18 millions of which the maximum and minimum sizes were 50.0 mm near the sodium surface and 3.0 mm in the UCS region, respectively.

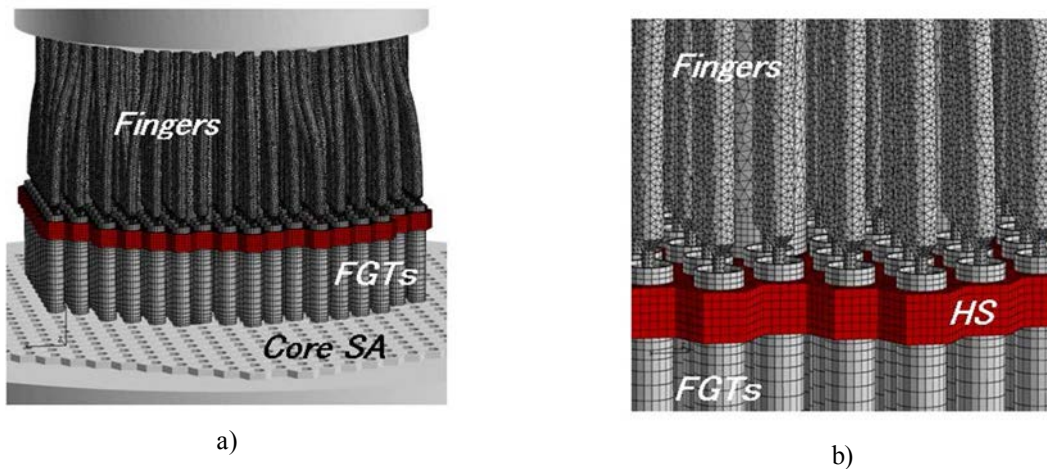


FIG. 48. (a) Close-up view of UCS region (b) Close-up view around HS

(4) Boundary and initial conditions

We applied the detail mesh around the flow holes in the present study. The velocity condition on the structure surfaces was given as logarithmic law (log-law) conditions in all the cases. The thermal conduction calculation with heat transfer correlations was performed for the inner barrel. In the previous calculations, every flow hole on the inner barrel was composed of 27 hexahedron meshes, however, it had approximately 2300 tetrahedrons in the present calculations. The flow rates of the outlets of core subassembly were also given as the 40% rated operational conditions, while those of the RV outlet nozzles were free outlet conditions.

The temperature conditions on the structure surfaces except for the inner barrel and the upper support plate were assumed as adiabatic conditions. The inner barrel surfaces were assumed

as a heat transfer conditions. The heat transfer correlations of Eq. (22) were given on the surfaces of the inner barrel for the thermal conduction calculations in all the cases.

$$Nu = \begin{cases} 3.64 & (Pe < 47.5) \\ 5.0 + 0.038 \cdot Pe^{0.68} & (Pe \geq 47.5) \end{cases} \quad (22)$$

where Nu and Pe are Nusselt and Peclet number whose characteristic lengths were given as the distance between the neighbouring cell center and the surface of the inner barrel which was measured in the previous SSTs.

6.3.2.3. University of Fukui

The whole upper plenum with the internals was modeled using CAD software named ‘Design Modeler’ by ANSYS Inc. (2009), and a calculation model with approximately 25 million tetrahedral meshes was created using meshing software ‘Meshing’ by ANSYS Inc. (2009). Figs. 49–50 show the overall mesh configuration of the upper plenum, i.e., a top view and a view in a cross section plane going through the center of the core and the center of the TC-plug. The honey comb structures for flow guides, the inner barrel, the fuel handling machine, and other internals are modeled using tetrahedral meshes. Hexahedral meshes are used for the layers of the outer shroud. The upper instrumentation structure (UIS) located in the center of the upper plenum is treated as a solid body with a heat capacity corresponding to steel and sodium. In the heat transfer calculation, no sodium flow is assumed inside the UIS, and heat is transferred by conduction from the center to the surface; and then transferred to the sodium of the upper plenum by convection. The fuel handling machine which is not illustrated in the figure is treated as a body without heat capacity. The column illustrated at the center of Fig. 49 represents a control rod guide tube. Since the flow guide tubes above the core seem to be important to rectify the flow, their configurations are considered explicitly in the present analysis. However, the mesh for the flow guide tubes is not illustrated in Fig. 50. The TC-plug is situated on the left hand side of the figure. Since three temperatures were measured at one axial elevation, the locations of the thermocouples are modeled exactly in order to accurately calculate the temperature response of each thermocouple. The inner barrel is modeled taking into account the heat transfer between the sodium inside of the inner barrel and sodium outside the inner barrel.

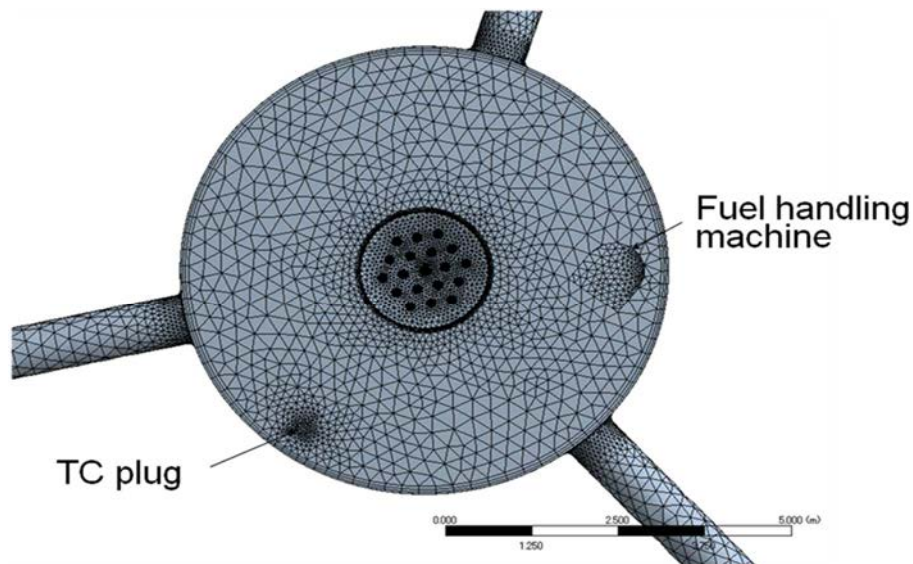


FIG. 49. Top view of the upper plenum meshing.

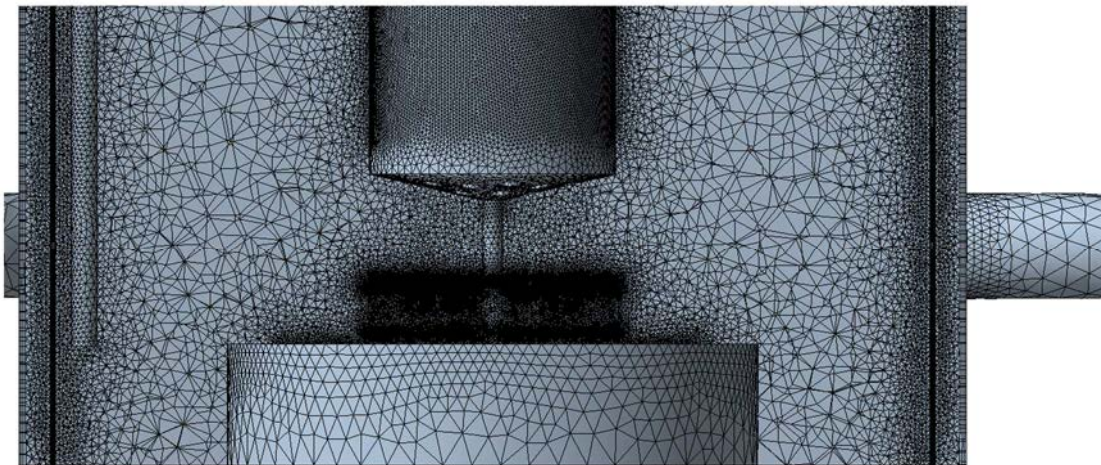


FIG. 50. Tetrahedral mesh configuration in the plenum (25 million).

Figure 51 shows the assumed configuration of a flow-hole with chamfer. The original model is illustrated on the left hand side. Although there is no information on the configuration, 5 mm chamfer is assumed on both sides of the flow-hole in the present analysis according to the engineer's intuition. Even if this configuration does not fully represent the actual configuration of the flow-holes, the effects of the chamfer on the moving velocity with which the thermal stratification interface rises can be investigated with the present model. The assumed rounded edge configuration is also discussed in the present study.

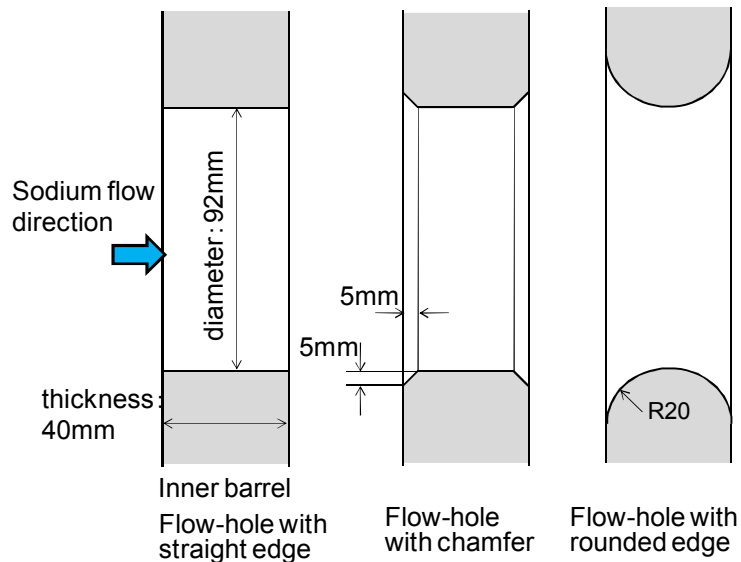


FIG. 51. The configuration of the flow-holes. Left: straight edge as used in earlier analysis, center: chamfered edge, right: rounded edge on the both flow-hole edges

Fig. 52 illustrates the meshes around the flow-holes for both cases. The inner barrel is illustrated at the center of the figure, and the reactor vessel is situated on the right hand side. Since there are many flow-holes to be analyzed in our model, the relatively large mesh sizes have been chosen to make the calculation system, so the shape of the mesh is somewhat rough. However, the difference of the meshes between the two cases can be seen from the figures. The overall complexity of the mesh is more or less the same between the two calculation cases.

The FLUENT12.1 code was used to compute the thermal hydraulics in the upper plenum.

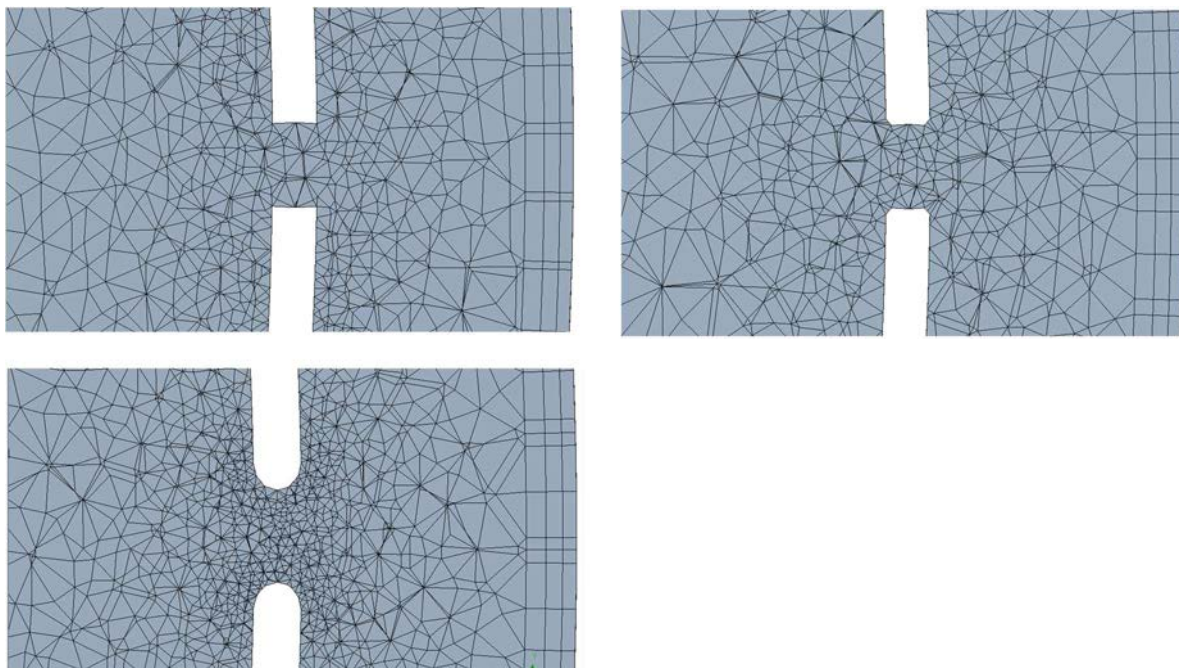


FIG. 52. Meshes around the flow-hole. Left above: straight edge, Right above: chamfered edge, Left below: rounded edge.

Notice that between these three models, the complexity of the overall mesh is more or less the same.

6.4. THERMO-PHYSICAL PROPERTIES

6.4.1. Provided equations

The following thermo-physical properties of liquid sodium and stainless steel were provided by JAEA in the 2nd RCM.

1) Liquid sodium

— Thermal conductivity; λ [W/(m·K)]

$$\lambda = 124.67 - 0.11381 \cdot T + 5.5226 \times 10^{-5} \cdot T^2 - 1.1842 \times 10^{-8} \cdot T^3, \quad T; [\text{K}] \quad (23)$$

— Specific heat; c_p [kJ/(kg·K)]

$$c_p = 1.6582 - 8.4790 \times 10^{-4} \cdot T + 4.4541 \times 10^{-7} \cdot T^2 - 2992.6 \cdot T^{-2}, \quad T; [\text{K}] \quad (24)$$

— Density; ρ [kg/m³]

$$\rho = \rho_c + f \left(1 - \frac{T}{T_c} \right) + g \left(1 - \frac{T}{T_c} \right)^h, \quad T; [\text{K}] \quad (25)$$

Where $\rho_c = 219.0$, $f = 275.32$, $g = 511.58$, $h = 0.5$ and $T_c = 2503.7$.

— Viscosity; μ [Pa·s]

$$\ln(\mu) = -6.4406 - 0.3958 \cdot \ln(T) + \frac{556.835}{T}, \quad T; [\text{K}] \quad (26)$$

2) Stainless steel

— Thermal conductivity; λ [W/(m·K)]

$$\lambda = 12.66 - 0.01924 \cdot T - 5.882 \times 10^{-6} \cdot T^2; \quad T; [^\circ\text{C}] \quad (27)$$

— Specific heat; c_p [kJ/(kg·K)]

$$c_p = 490.5 + 8.834 \times 10^{-2} \cdot T + 1.666 \times 10^{-4} \cdot T^2, \quad T; [^\circ\text{C}] \quad (28)$$

— Density; ρ [kg/m³]

$$\rho = 8035.5 - 0.4049 \cdot T - 5.02 \times 10^{-5} \cdot T^2, \quad T; [^\circ\text{C}] \quad (29)$$

6.4.2. Other equations

CEA

Liquid sodium is used as coolant in the reactor. The fluid is treated as incompressible and all physical properties are temperature independent. At the reference temperature 400°C, the physical properties of sodium are:

Density: $858 \text{ kg}\cdot\text{m}^{-3}$

Dynamic viscosity: $2.81 \cdot 10^{-4} \text{ kg}\cdot\text{m}^{-1}\cdot\text{s}^{-1}$

Thermal conductivity: $69.7 \text{ W}\cdot\text{m}^{-1}\cdot\text{K}^{-1}$
Heat capacity: $1284 \text{ J}\cdot\text{kg}^{-1}\cdot\text{K}^{-1}$
Volumetric thermal-expansion coefficient: $2.68\cdot 10^{-4} \text{ K}^{-1}$.

University of Fukui

The following thermo-physical properties for liquid sodium and stainless steel are used in the computation. The original data is taken from the handbook published by IAEA, i.e., Thermo-physical Properties of Material For Nuclear Engineering: A Tutorial and Collection of Data (2008). The unit of the temperature is Kelvin.

1) Liquid sodium: $400 \text{ K} < T < 1100 \text{ K}$

— Thermal conductivity (W/m/K):

$$k = 99.492 - 0.039094T \quad (30)$$

— Specific heat (J/kg/K):

$$C_p = 1575.2 - 0.57747T + 9.4364 \times 10^{-5}T^2 + 2.0502 \times 10^{-7}T^3 - 4.4644 \times 10^{-11}T^4 \quad (31)$$

— Density (kg/m^3):

$$\rho = 1021.9 - 0.26198T + 3.083 \times 10^{-5}T^2 - 1.2419 \times 10^{-8}T^3 \quad (32)$$

— Dynamic viscosity (Pa·s):

$$\mu = 2.301 \times 10^{-3} - 7.2866 \times 10^{-6}T + 9.6134 \times 10^{-9}T^2 - 5.7003 \times 10^{-12}T^3 + 1.2569 \times 10^{-15}T^4 \quad (33)$$

2) Stainless steel (S.S. 304)

— Thermal conductivity (W/m/K):

$$k = 14.5 + 2.77556 \times 10^{-16}T + 1.25 \times 10^{-5}T^2 \quad (34)$$

— Specific heat (J/kg/K):

$$C_p = 480 - 0.0125T + 2.375 \times 10^{-4}T^2 \quad (35)$$

— Density (kg/m^3):

$$\rho = 8160.9 - 0.45T \quad (36)$$

KAERI

Liquid sodium is used as a coolant in the Monju reactor. The physical properties are assumed to be constant for the whole computational domain, which means that the physical properties do not vary with temperature. The reference temperature is 400°C , and the physical properties of sodium at this reference temperature are given in Table 13.

TABLE 13. PHYSICAL PROPERTIES OF SODIUM AT 400°C

Quantity	Value	Dimension
Density	858	kg/m^3
Dynamic viscosity	2.81×10^{-4}	$\text{kg}/(\text{m}\cdot\text{sec})$
Thermal conductivity	69.7	$\text{W}/(\text{m}\cdot\text{K})$

Heat capacity	1284	J/(kg-K)
Volumetric thermal-expansion coefficient	2.68×10^{-4}	1/K

IPPE

The following thermo-physical properties for liquid sodium and stainless steel are used in the computation. The unit of the temperature is Kelvin.

1) Liquid sodium:

— Thermal conductivity:

$$\lambda = 90.604 - 0.048523 \cdot (T - 273), \text{ W/m/K} \quad (37)$$

— Specific heat:

$$C_p = 1436.74 - 0.58049 \cdot (T - 273) + 4.6229 \cdot 10^{-4} \cdot (T - 273)^2, \text{ J/kg/K} \quad (38)$$

— Density:

$$\rho = 949.0 - 0.223 \cdot (T - 273) - 1.75 \cdot 10^{-5} \cdot (T - 273)^2, \text{ kg/m}^3 \quad (39)$$

— Kinematic viscosity:

$$\nu = 1.2162 \cdot 10^{-5} \cdot \rho^{1/3} \cdot e^{0.6976 \cdot \rho / T}, \text{ m}^2/\text{s} \quad (40)$$

2) Stainless steel:

— Thermal conductivity:

$$\lambda = 25 \text{ W/m/K} \quad (41)$$

— Specific heat:

$$C_p = 599 \text{ J/kg/K} \quad (42)$$

— Density:

$$\rho = 7900 \text{ kg/m}^3 \quad (43)$$

7. PRELIMINARY RESULTS BASED ON BENCHMARK SPECIFICATION

7.1. STEADY AND TRANSIENT SIMULATIONS

7.1.1. CIAE

In the primary calculation, the sharp edge of the flow holes is used, just as shown in Fig. 53.

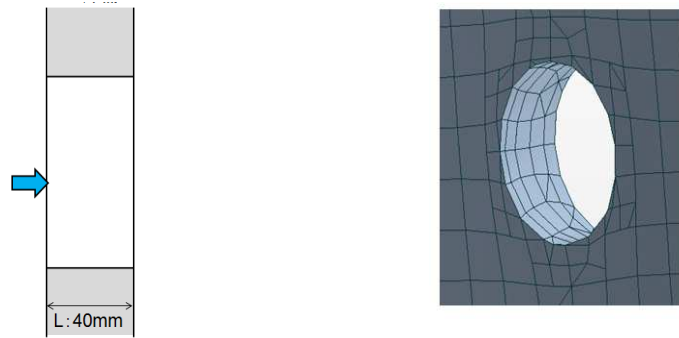


FIG. 53. Configuration of the flow holes and the mesh description.

Figs. 54–55 show the velocity and temperature distribution in the cross section. It can be seen that the sodium mixing in the upper plenum is very strong and two clear eddies are formed in the upper part and bottom part (cavity) due to the forced flow. Sodium from the outlet of the reactor core flow obliquely upward to the upper region of the reactor vessel in a direction of 45° with the horizontal. When it reaches to the top of the vessel and changes the flow direction then goes into the annulus region between the inner barrel and the reactor vessel wall and finally to the reactor outlet nozzle. This flow is the main flow path and the flow rate is about 85% of the total flow. Meanwhile, there is a small fraction of the sodium flows through the two rows of holes in the inner barrel finally to the outlet of the vessel under the normal condition of 40% power. This kind of flow is weak and some part under the core barrel may be the flow stagnant area which induces the uniform temperature.

It is clear in Fig. 54 that it can be divided two parts: high temperature part and lower temperature one according to the temperature distribution of the sodium temperature in the reactor vessel. The high temperature part is above the core barrel which has the approximate well-proportioned temperature 490°C except that of the core part outlet region. This part is greatly affected by the boundary conditions. The lower temperature part is the area which is below the lower flow holes in the inner barrel, where the sodium temp is greatly affected by the structures around the core.

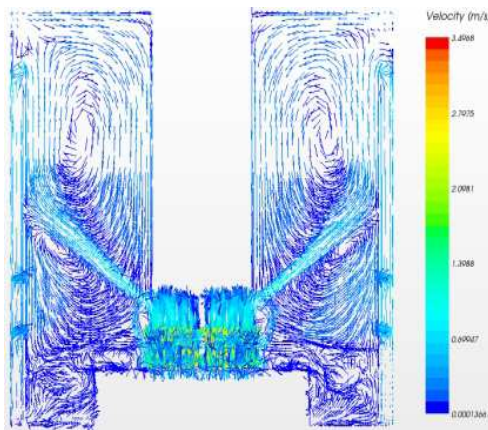


FIG. 54. Velocity distribution under the steady condition.

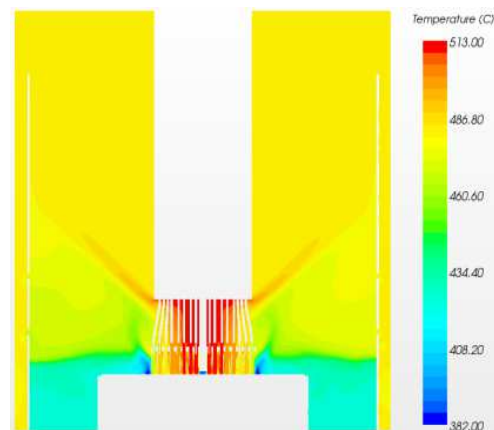


FIG. 55. Temperature distribution under the steady condition.

Transient simulation of the thermal stratification in the upper plenum of Monju is a long and slow-motion process which is carried out only for a duration of 190 minutes in CIAE. The

standard k-epsilon model for the turbulence analysis is used at the beginning of the numerical simulation of this transient process.

Fig. 56 shows the velocity distribution of vertical section at 30s, the mixing intensity of the hot sodium in the upper plenum is still strong, and the flow rate from the core outlet remains at a relative lower level, and at the same time the mass flow rate through the holes in the inner barrel increases and the flow through the annulus between inner barrel and reactor vessel wall decreases. Fig. 57 shows that the temperature in the annulus mass flow is still high due to the high flow rate in this area. At this time, the flow pattern in the upper plenum changes quickly and strongly for reduction of the mass flow rate from the reactor core. With the gradual weaken of kinetic energy of the sodium out of the core, the mixing intensity of the hot sodium in the upper plenum is gradually reduced, and the horizontal kinetic energy of the coolant is disappeared after 60 seconds. So after 60 seconds, in the Fig. 58 and Fig. 59, it can be seen that the flow rate from the core outlet remains at a relative lower level, the thermal stratification can be formed in the area above the upper flow holes. Then in the following time, for example 120s, 240s and 600s, the interface of stratification goes upwards slowly and the flow pattern of sodium keeps almost the same, no obvious change takes place. This can be shown in the velocity and temperature distribution in Figs. 60–65. In order to compare to the test data, we choose these key time point to show the development of the thermal stratification in the upper plenum of Monju Reactor.

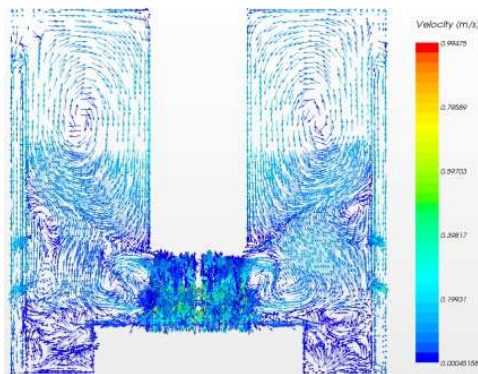


FIG. 56. Velocity distribution of the vertical section at 30s.

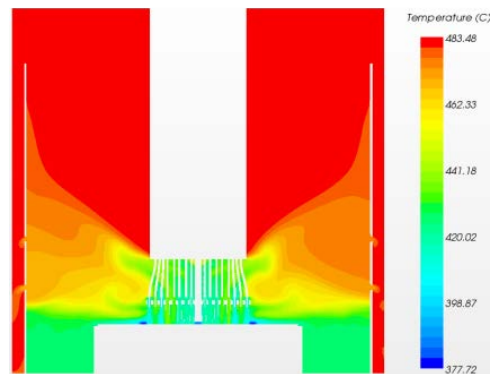


FIG. 57. Temperature distribution of the vertical section at 30s.

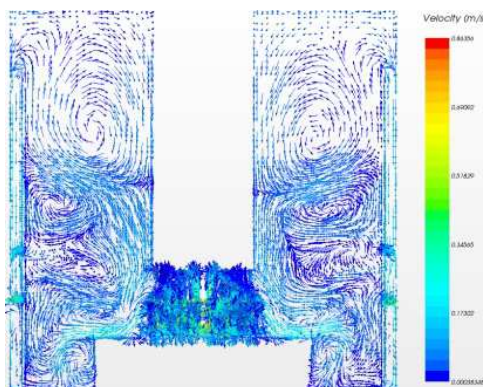


FIG. 58. Velocity distribution of the vertical section at 60s.

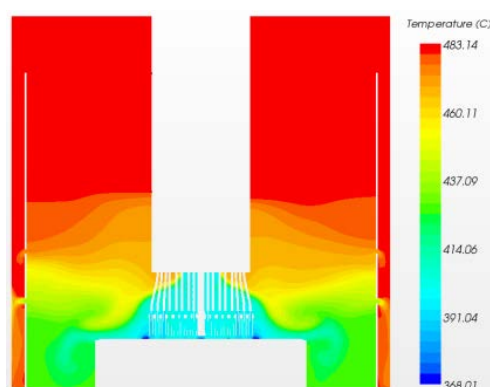


FIG. 59. Temperature distribution of the vertical section at 60s.

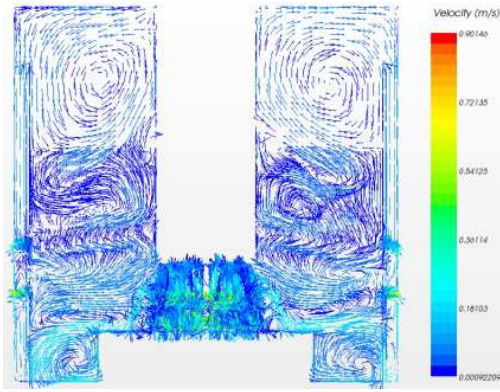


FIG. 60. Velocity distribution of the vertical section at 120s.

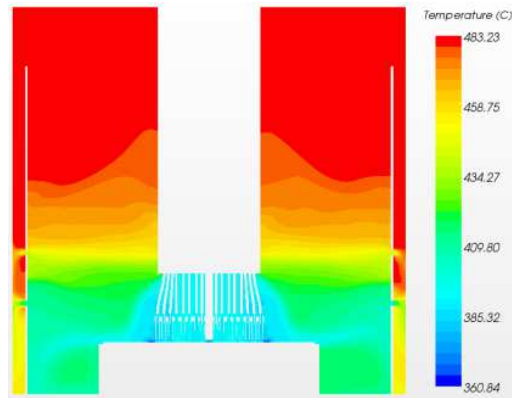


FIG. 61. Temperature distribution of the vertical section at 120s.

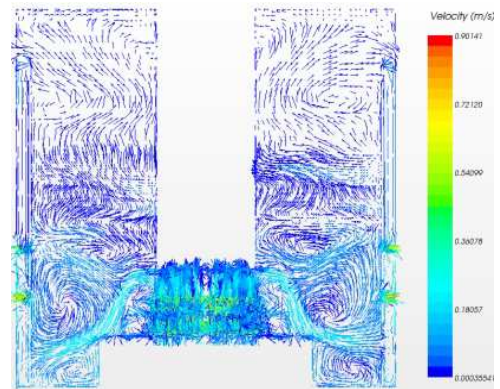


FIG. 62. Velocity distribution of the vertical section at 240s.

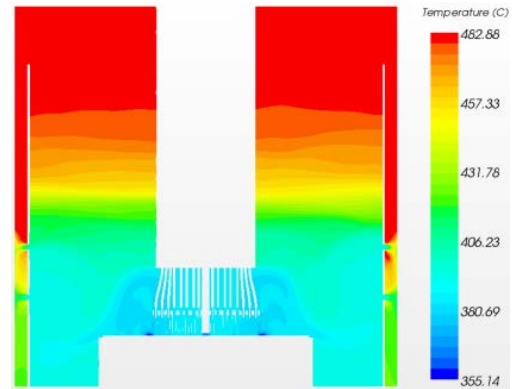


FIG. 63. Temperature distribution of the vertical section at 240s.

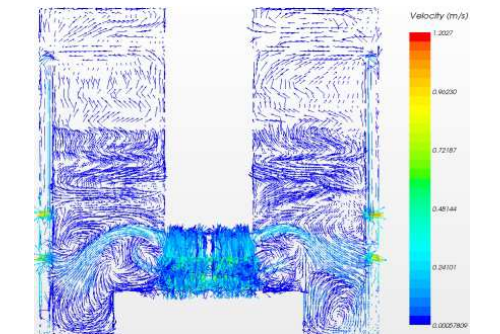


FIG. 64. Velocity distribution of the vertical section at 600s.

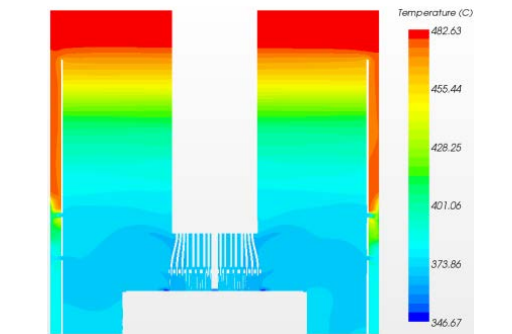


FIG. 65. Temperature distribution of the vertical section at 600s.

In the later time of the transient process, we focus on two time points, 1200 s and 2800 s, just as shown in Figs. 66–69. From these figures, it can be seen that the interface of the stratification has been moved to the top of the upper plenum, above the surface of the inner barrel, remains almost the same height level. It also can be seen that with the time goes on, the average temperature in the upper plenum gets down and colder sodium with lower velocity from the core outlet will fill the bottom part of the upper plenum first then the pushes the higher sodium up gradually.

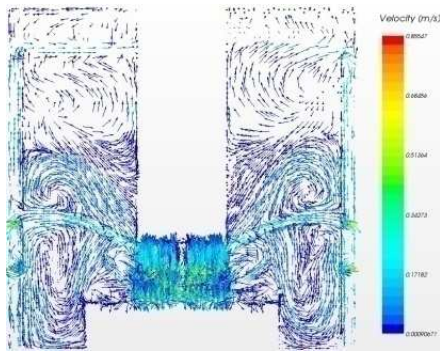


FIG. 66. Velocity distribution of the vertical section at 1200s.

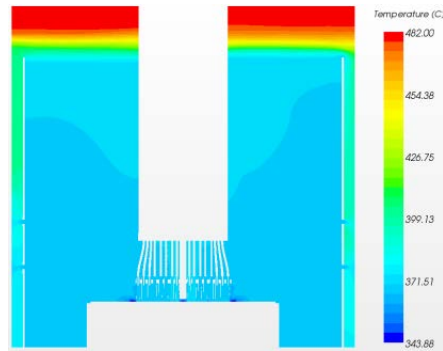


FIG. 67. Temperature distribution of the vertical section at 1200s.

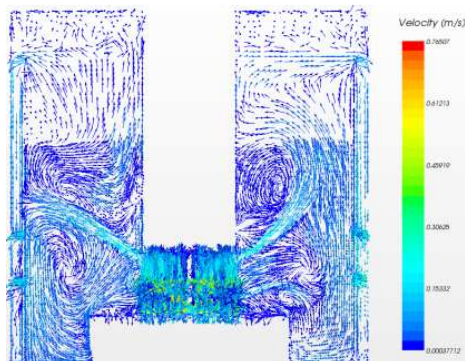


FIG. 68. Velocity distribution of the vertical section at 4800s.

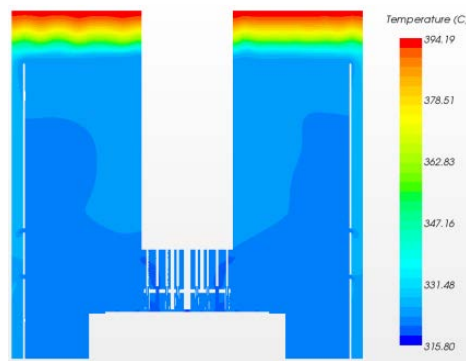


FIG. 69. Temperature distribution of the vertical section at 4800s.

7.1.2. CEA

(1) CAD model and meshing

ANL has provided the CAD model of the simplified 60° geometry in IGES format (see Section 6.1). This model has been imported into the commercial mesh generator ICEMCFD. The upper core structure regions ‘flow guide tubes’ and ‘fingers’ are defined as internal sub-domains and the honeycomb structure is implemented as an internal, permeable wall. A pure tetrahedral mesh of 335000 elements has been created by using the Delaunay method. This coarse mesh is shown on Fig. 70 on the examples of a horizontal cut plane through the lower line of the inner barrel flow holes and of a view of the symmetry plane going through the outlet pipe.

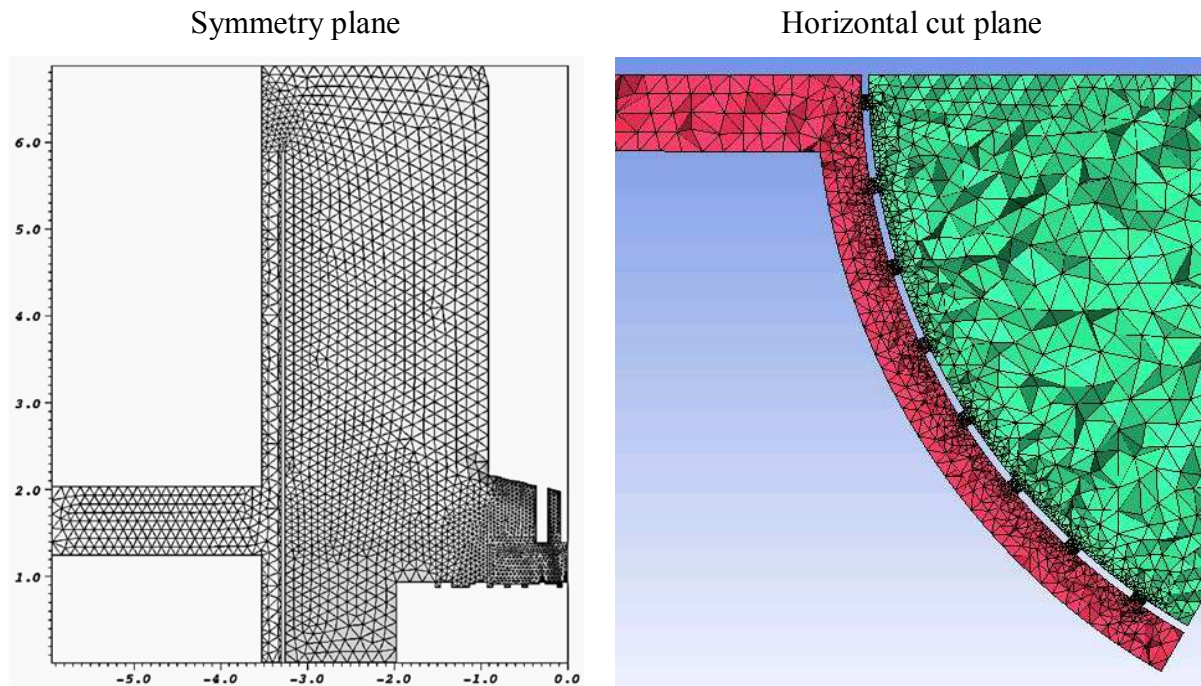


FIG. 70. Visualisation of the coarse mesh.

(2) Thermal-hydraulic conditions of the calculations

The thermal hydraulic conditions of the reference calculation are given in this section. The conditions of the sensitivity studies which differ from these conditions are summarised later in Section 7.2.

(3) Boundary conditions

The upper plenum inlet conditions at the sub assembly (S/A) outlets are given in the data description report [2]. The time-dependant courses are linearly interpolated between given values.

For each S/A an outflow sodium velocity is calculated from the given S/A sodium flow rates. The surface of an S/A outlet is 11573 mm^2 and the sodium density at 400°C is used. A uniform spatial distribution of the temperature and of the velocity is assumed for each S/A outlet. The turbulent kinetic energy k and its dissipation rate ϵ are predicted from the assembly diameter and a fluctuation velocity which is assumed to be 10% of the mean S/A outflow velocity.

All walls of the upper plenum are treated as adiabatic. The two lateral surfaces of the 60° geometry are modelled with the symmetry hypothesis. A pressure outlet condition is used for the outlet nozzle boundary, associated with free out-stream conditions for the velocity and the temperature.

(4) Initial conditions for the pump trip

At the beginning of the pump trip transient, well established temperature and the velocity fields are assumed in the upper plenum. Thus, a first steady state calculation is performed in order to obtain these fields. The upper plenum inlet conditions at the S/A outlets are those of the beginning of the test ($t=0\text{s}$). Starting from a reposing ($\vec{u}=0$) and isothermal situation ($T=400^\circ\text{C}$), the steady state flow field in the upper plenum is considered as established when all 120 temperature samples placed along the thermocouple plug are temporally stabilized; this is especially important for those located near the bottom of the upper plenum.

(5) The numerical scheme

The numerical scheme used ion Trio_U is summarised in Table 14.

TABLE 14. NUMERICAL SCHEME USED IN THE TRIO_U CALCULATIONS

General	Physical properties	Sodium at 400°C Gravity: $g_z = -9.81 \text{ m}^2 \cdot \text{s}^{-1}$
	Mesh	Tetrahedral
	Discretization	P0/P1 for: pressure P1NC for: U, T, k and ε
Time scheme		1 st order Euler implicit
Navier-Stokes equation	Convection	1 st order upwind
	Diffusion	Centered
	Pressure solver	Cholesky
	Thermal effects	Boussinesq hypothesis
	Wall law	Logarithmic wall law
	Turbulence	RANS: Boussinesq approximation with turbulent viscosity μ_t
Turbulence	Turbulence model	High Reynolds k – ε model
	k – ε convection	1 st order upwind
	k – ε diffusion	Centered
Thermal equation	Temperature convection	1 st order upwind
	Temperature diffusion	Centered
	Wall law	Logarithmic wall law
	Turbulence	Turbulent Prandtl number Pr
Mass conservation	Incompressible fluid $\text{div}(\mathbf{u})=0$	Pressure solver (projection method)

Turbulent mixing is treated with the high Reynolds form of the k- ε model. The model allows to some extent the presence of buoyancy effects [22]. In the Boussinesq hypothesis framework, the turbulent viscosity is linked to the turbulent kinetic energy k and the dissipation rate of the turbulent kinetic energy ε via:

$$\nu_t = C_\mu \frac{k^2}{\varepsilon}. \quad (44)$$

Conservation equations are written for both the turbulent kinetic energy k and the turbulent dissipation rate ε .

$$\frac{\partial k}{\partial t} + \bar{u} \nabla k = \nabla \cdot \left(\frac{\nu_t}{\sigma_k} \nabla k \right) - \varepsilon + P + G. \quad (45)$$

$$\frac{\partial \varepsilon}{\partial t} + \bar{u} \nabla \varepsilon = \nabla \cdot \left(\frac{\nu_t}{\sigma_\varepsilon} \nabla \varepsilon \right) - C_{\varepsilon 2} \frac{\varepsilon^2}{k} + C_{\varepsilon 1} P \frac{\varepsilon}{k} + C_{\varepsilon 1} C_{\varepsilon 3} G \frac{\varepsilon}{k} \quad (46)$$

The production of turbulence kinetic energy is calculated by

$$P = -\overline{u_i u_j} \frac{\partial \bar{u}_i}{\partial x_j} \quad \text{with} \quad -\overline{u_i u_j} = \nu_t \left(\frac{\partial \bar{u}_i}{\partial x_j} + \frac{\partial \bar{u}_j}{\partial x_i} \right) - \frac{2}{3} k \delta_{ij} \quad (47)$$

Buoyancy effects for incompressible flows are treated by:

$$G = \frac{V_t}{Pr_t} \beta_T g \nabla \bar{T} . \quad (48)$$

The following empirical coefficients (Table 51) are used.

TABLE 15. COEFFICIENTS OF THE STANDARD HIGH REYNOLDS NUMBER k-ε MODEL

C_μ	σ_k	σ_ϵ	$C_{\epsilon 1}$	$C_{\epsilon 2}$	$C_{\epsilon 3}$	Pr_t	Sc_t
0.09	1.0	1.3	1.44	1.92	1.0	0.9	0.9

To take into account the effect of thermal stratification, the following assumption is made [22]:

$$C_{\epsilon 3} = 0 \quad \text{if} \quad G < 0 \quad (\text{stable stratification with reduced buoyancy effects})$$

$$C_{\epsilon 3} = 1 \quad \text{if} \quad G > 0 \quad (\text{unstable stratification with full buoyancy effects})$$

This extension of the standard k-ε model has been tested for Sodium flow by analysing various natural and mixed convection experiments [23].

(6) Reference calculation

The temperature profile inside the Plenum is measured with the thermocouple plug. The vertical positions of the temperature probes are relative to the liquid level and are given by the Measured Level (ML). The top of the Inner Barrel is thus situated at ML -1000 and the two lines of flow holes are located between ML -4000 and ML -6000. The plug is situated at 3043 mm from the vessel centre and at a direction of 305°, what gives a direction of 55° for the 60° model [24].

(7) Steady state flow before the pump trip

Fig. 71 shows on the left hand side the temperature - and velocity distribution in the symmetry plane of the upper plenum at the beginning of the test. The main part of the sodium leaving the S/A outlets is hotter than the sodium in the upper plenum. It is transported in form of a free jet into the upper region of the upper plenum and passes above the inner barrel to the outlet pipe. The comparison between the calculated and measured temperature profiles is given on the right hand side of Fig. 71. The measured values given by Yamaguchi in Ref. [25] have been digitalized and smoothed out.

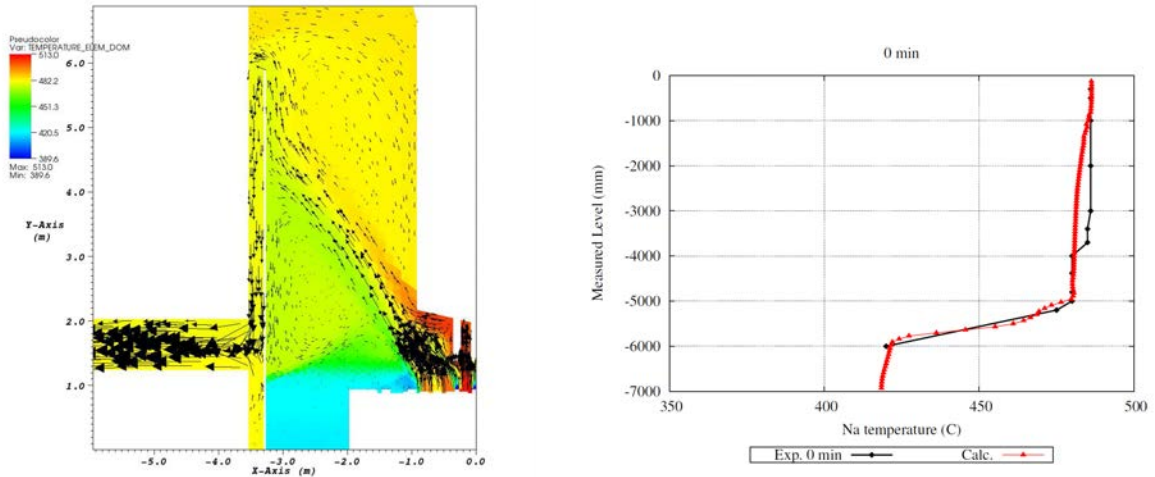


FIG. 71. Temperature distribution and temperature profiles before the pump trip.

For the beginning of the pump trip test the calculated temperature profile is in accordance to the measured profile. Hence, the steady state model seems to be able to determine correctly the forced convection flow at the beginning of the trip test [24].

(8) The transient of the pump trip

Two minutes after the beginning of the pump trip test, the first experimental temperature profile is compared to the calculated one in Fig. 72 (left hand side). The temperature profiles show that the thermal stratification becomes visible approximately between the top of inner vessel (ML=-2000mm) and the upper flow holes (ML=-4400). For $ML < -5000$, the calculation slightly overestimates the temperature of the experiment.

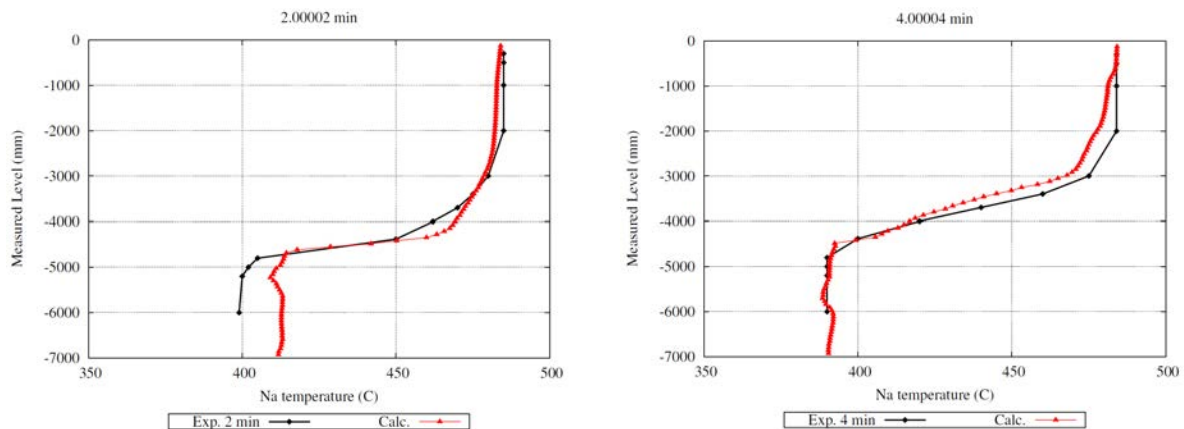


FIG. 72. Temperature profiles 2 and 4 minutes after the beginning of the pump trip.

Four minutes after the beginning of the pump trip, in the lower part of the Plenum, the calculated profile becomes consistent with the experimental profile (right hand side of Fig. 72). In the upper part of the Plenum ($ML > -3000$), the calculated temperature is slightly underestimates the measured temperature. This is an indicator that the cooling of the upper part of the Plenum is overestimated in the calculation.

The temperature distribution is shown in Fig. 73 for the instant ten minutes after the beginning of the pump trip. On the left hand side, the temperature - and velocity distribution in the symmetry plane of the Upper Plenum is shown. The sodium leaving the S/A outlets is colder than the Sodium in the Upper Plenum. Due to buoyancy effects, the colder Sodium is now distributed in the lower part of the Upper Plenum, mainly in form of large eddies. The Sodium is predominantly transported through the holes of the Inner Barrel to the outlet pipe. On the right hand side of this figure, calculated and measured profiles are compared. In the lower part of the Plenum up to the upper flow holes at ML=-4400, the calculated profiles are close to the experimental ones. Above the upper flow holes, the calculated thermal stratification rises faster upward than the experimentally determined stratification. It seems that the mass flow rate going through the flow holes is underestimated and the mass flow rate going above the Inner Barrel is overestimated [24].

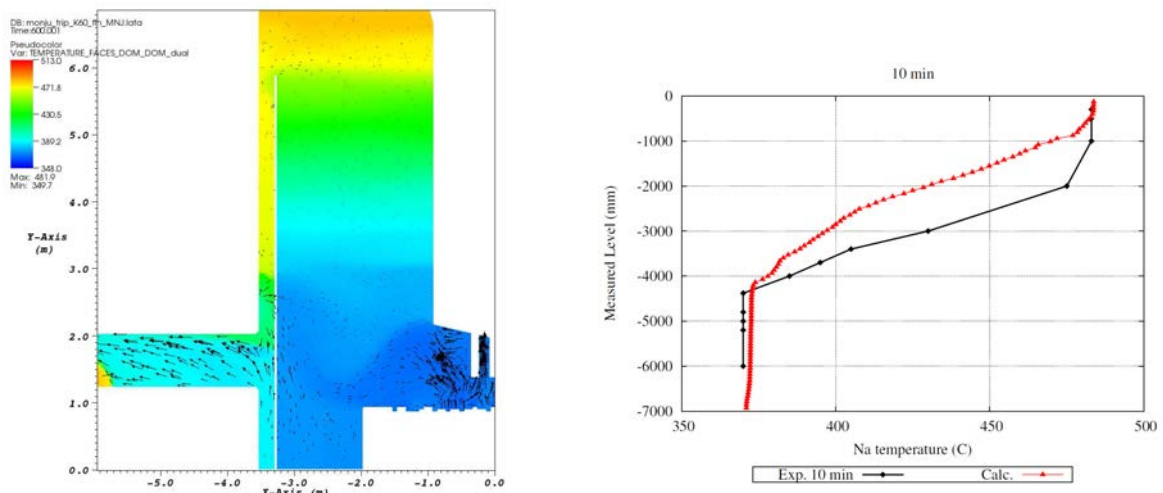


FIG. 73. Temperature distribution and temperature profiles 10 minutes after the beginning of the pump trip.

At a later time than about 15 minutes after the beginning of the pump trip, the calculation shows a completely mixed Upper Plenum and a uniform axial temperature distribution. In the experiment however such a temperature distribution has been reached more than one hour after the beginning of the pump trip [24].

(9) Flow repartition

Fig. 74 shows for the calculation the repartition the flow rate between the flow going above the Inner Barrel and going through the flow holes. At the beginning of the pump trip, at $t=0s$, 92% of the flow passes above the Inner Barrel and only 8% of the flow is going through the flow holes.

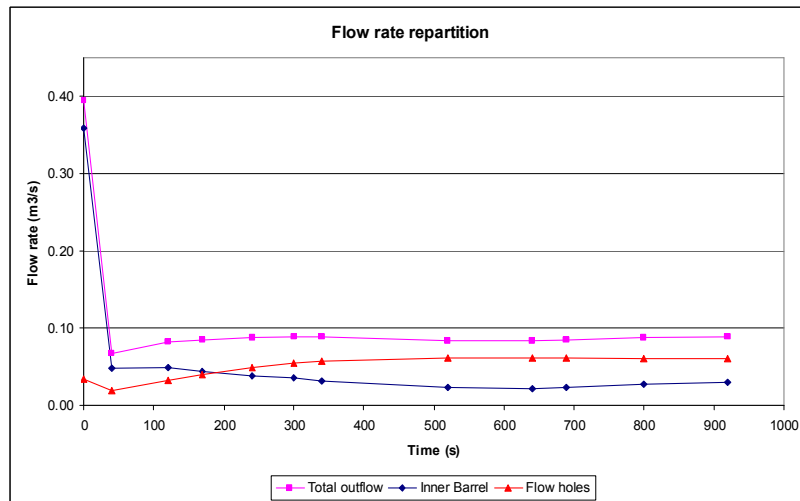


FIG. 74. Repartition of the flow path between flow holes and above the inner barrel.

Later, at a time above 600 seconds, the main part of the flow passes through the flow holes (70%) and only 30% passes above the Inner Barrel. The flow rate which passes through the flow holes can be further divided in two flow rates which are approximately constant during the trip test:

- The lower line flow represents 70% of the holes flow rate (8 holes).
- The upper line flow rate represents 30% of the holes flow rate (4 holes).

7.1.3. IGCAR

(1) Benchmark model steady state

The simplified benchmark model proposed by ANL is used for the preliminary study. The predicted velocity and temperature distributions in the hot pool at a vertical section through outlet nozzle are depicted in Fig. 75 and Fig. 76 respectively. Sodium from core outlet enters the pool at ~ 30 deg inclination to the horizontal. On meeting the inner barrel, it turns upwards towards free surface. But the flow does not travel up to free surface. It turns out radially at the top of the inner barrel and then passes downwards through the annulus between inner barrel and the reactor vessel, before leaving through the outlet nozzle. There is an anti-clockwise recirculation region near the main body of UCS. The sodium between the core barrel and the inner barrel is nearly stagnant, leading to stratification.

The cavity between core barrel and the inner barrel is isothermal at ~ 710 K. There is large temperature variation in the axial distance between core top and main body of UCS. Above this, again the pool is isothermal at ~ 755 K.

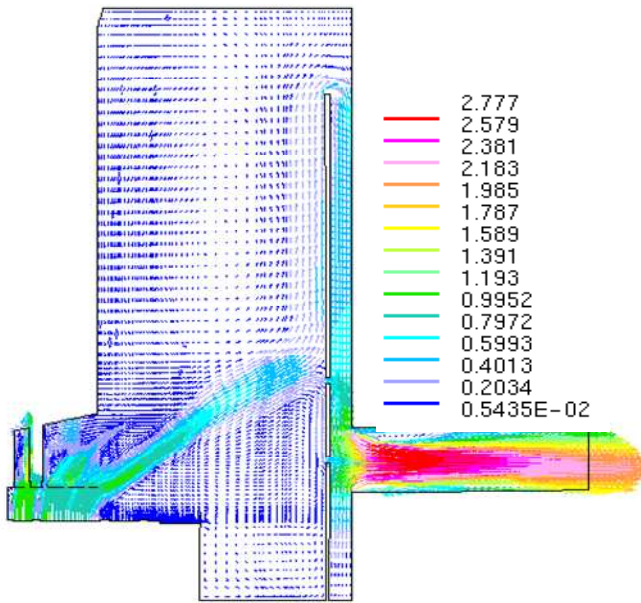


FIG. 75. Steady state velocity field (m/s) in benchmark model.

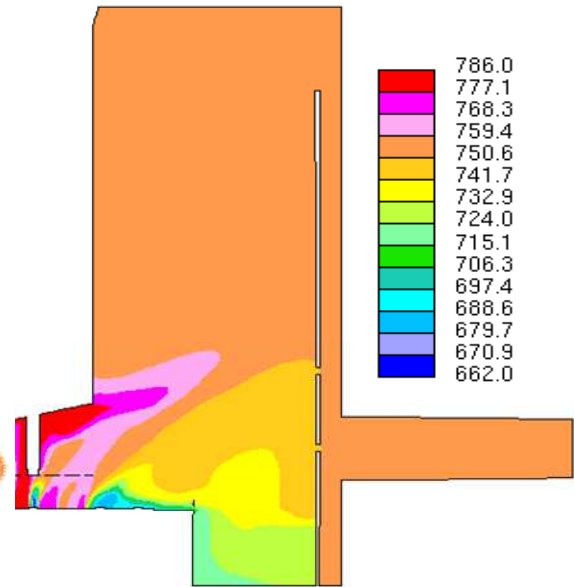


FIG. 76. Steady state temperature field (K) in benchmark model.

(2) Benchmark model transient

The predicted evolutions of velocity and temperature fields in a vertical plane through outlet nozzle are depicted in Fig. 77 and Fig. 78 respectively. Calculations have been carried out for a duration of 3600 s. It is evident that the communication from hot pool to outlet nozzle is primarily through the holes in the inner barrel. But, there is still significant flow from hot pool to outlet nozzle via. The annulus between inner barrel and reactor vessel, as evident from the temperature contours. The thermal stratification interface moves upwards gradually.

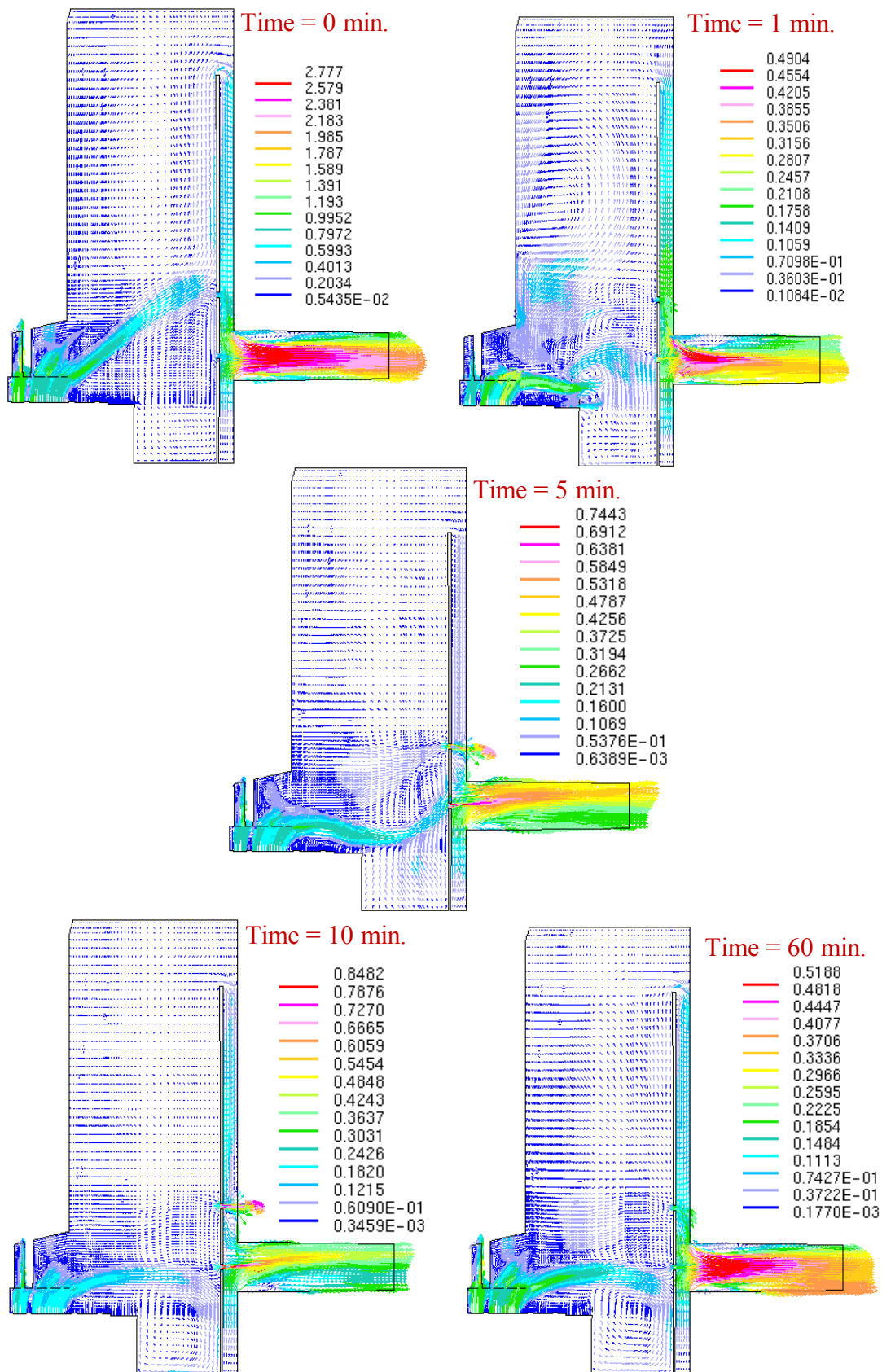


FIG. 77. Velocity vectors (m/s) at different instants.

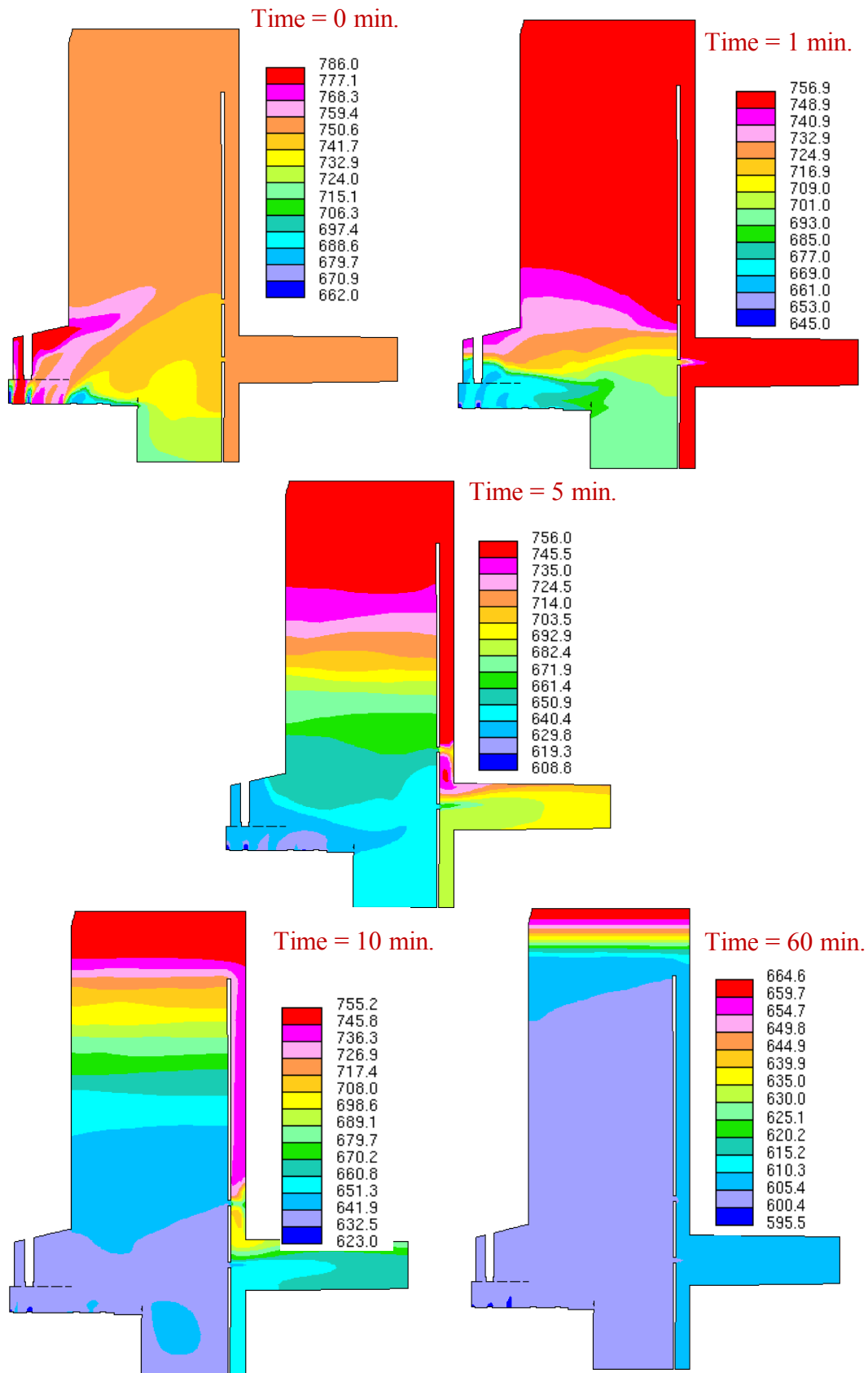


FIG. 78. Temperature contours (K) at different instants.

(3) Comparison of predicted results with plant data

The predicted temperature distribution along the height of the hot pool at three different instants is depicted in Fig. 79 along with the plant measurements. It is clear that the CFD simulation over-predicts the upward movement of stratification interface. Further, the temperature gradient at the interface is sharper in numerical simulations than in the measurements.

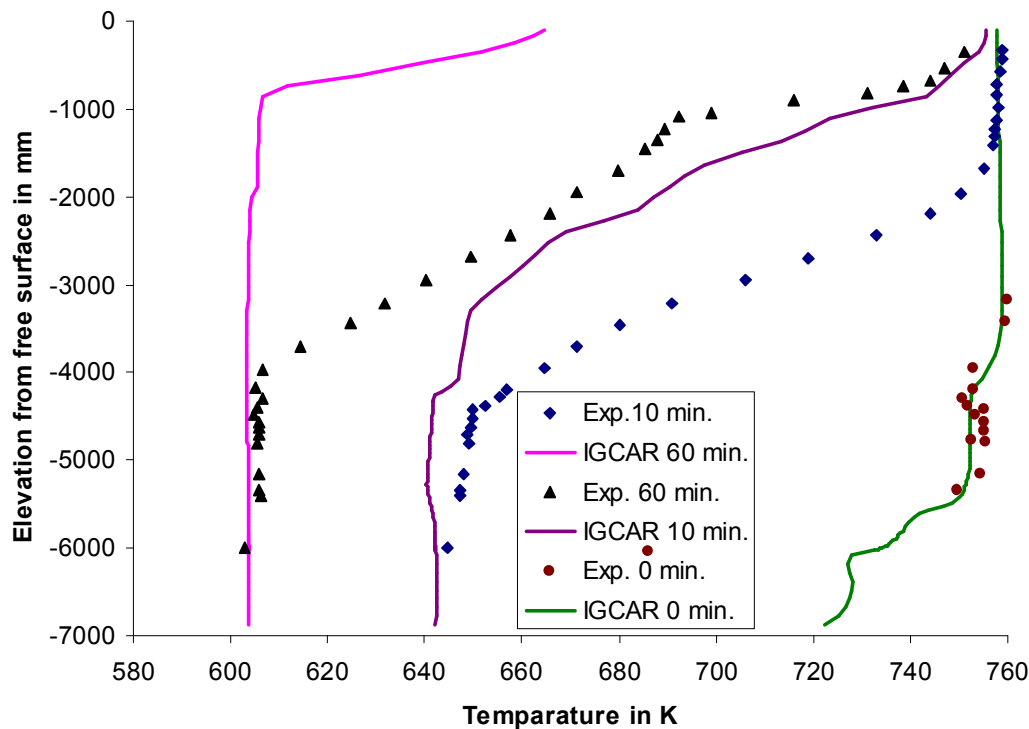


FIG. 79. Comparison of predicted data with plant measurements.

7.1.4. JAEA

(1) Boundary and initial conditions for steady state calculations

We calculated three cases, which had different boundary conditions and buoyancy forces: The velocity condition on the structure surfaces was given as logarithmic law (log-law) conditions in all the cases. The flow rates of the outlets of core subassembly were also given as the 40% rated operational conditions, while those of the RV outlet nozzles were free outlet conditions.

The temperature conditions on the structure surfaces except for the inner barrel were assumed as adiabatic in Cases 1 and 2. On the other hand, the inner barrel surfaces were assumed as adiabatic and the temperature on support plate was assumed 375°C in Case 3 which was measured in the previous SSTs. The initial temperatures were 477°C and initial velocities were zeros in the upper plenum.

Buoyancy force affects to the thermal stratification in the upper plenum in case of scram transients. However, there is a possibility that the effect could be negligible in the steady state conditions with larger flow rates and higher temperatures. Hence, we calculated Case 2 without buoyancy and Cases 1 and 3 with buoyancy in order to evaluate the effect of

buoyancy. In the present calculations, the pseudo time step and Courant number were 0.1 and approximately 120, respectively.

(2) Heat and mass balance in upper plenum

The difference between total inflow enthalpy from the core subassembly outlets and total outflow enthalpy from the outlet nozzles was less than 0.1% in Cases 1 and 2 and the difference in Case 3 was approximately 0.3%. Temperatures on the TC-plug did not change more than 0.3°C even in thousands of additional calculations except in the region formed temperature stratification and the region around a jet flow. Amplitude of temperature changes on the TC-plug around the jet flow were approximately 1°C and that in the region formed temperature stratification were approximately 10°C. Compared to the SST results, the average temperature of the outlet nozzles was approximately 2°C lower and the total mass outflow from the outlet nozzles was approximately 1.6% smaller. Considering sodium leak flow from the intermediate plenum through the support plate which has been evaluated as 1.4% of the total flow rate in the SSTs, the error of the flow rate is small enough to be tolerable.

(3) Velocity and temperature distribution in upper plenum

Fig. 80 shows the velocity and temperature distribution in Case 1 calculation on the vertical cross section, of which location in the circumferential direction is illustrated in the upper part of this figure. Sodium from the top of the UCS region flow obliquely upward direction to the upper region of the upper flow holes on the inner barrel. From this region, the flow is divided to the upward and downward direction along the inner barrel. The upward flow mainly overflows into the annular region between the RV wall and the inner barrel, while the downward flow, which partially flows out from the two levels of the flow holes, mainly recirculates to the core top region through the upper part of the support plate. Concerning the temperature distribution around the jet flow, the difference appeared between the upper and lower regions of the jet flow.

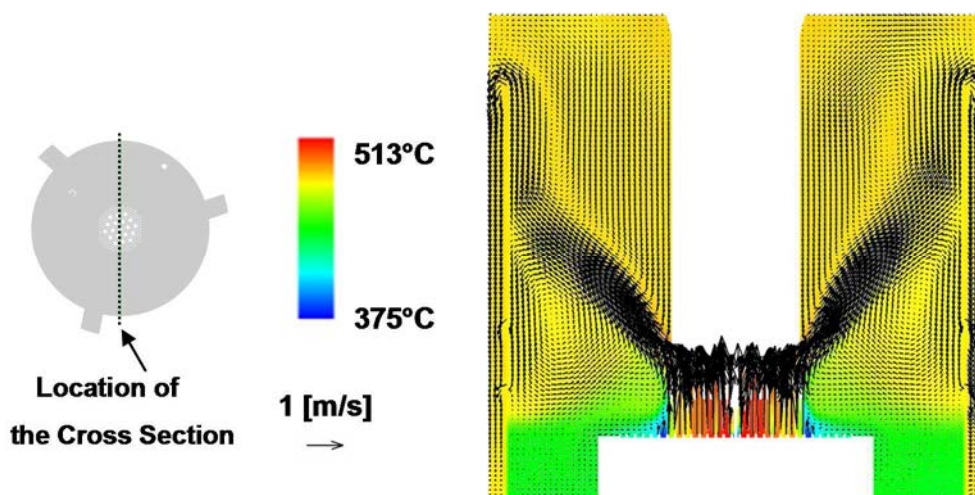


FIG. 80. Velocity and temperature distribution in case 1 calculation.

The velocity and temperature distribution on the same location in Case 2 results are shown in Fig. 81. While the velocity is distributed similar characteristics, the temperature in Case 2 shows different distribution from that in Case 1, i.e. the temperature from the sodium surface to the support plate is only approximately 2°C difference in Case 2, while that is

approximately 40°C difference in Case 1. The gravity forces were added in the momentum equation in Case 1, while they were neglected in Case 2, i.e. the difference between the two was only with and without buoyancy forces. In case with the buoyancy forces, the colder sodium from the outlets of the blanket and reflector subassembly mainly flows down and accumulates in the outer region of the core barrel. In case without buoyancy forces, however, the colder sodium does not flow down but it is well mixed with the hotter sodium in all regions.

The results of Case 3 are shown in Fig. 82. In this calculation, the boundary temperature on the support plate is different from Cases 1 and 2. While the velocity distribution has similar characteristics to Cases 1 and 2 in the core top region, the temperature distribution is apparently different in the lower region. The temperature distribution in Case 3 has steeper gradient than that in Cases 1 and 2. This difference is caused obviously by the boundary condition of the support plate.

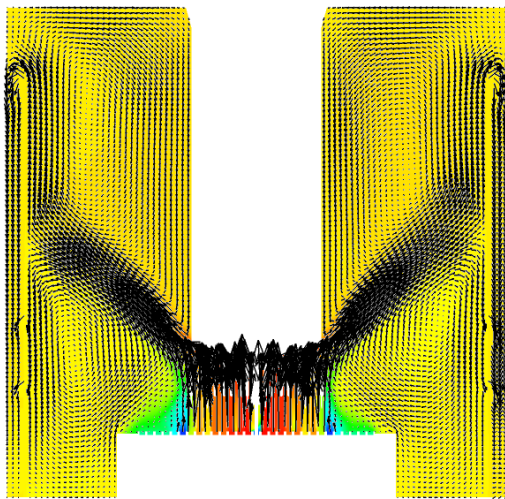


FIG. 81. Velocity and temperature distribution in case 2 calculation.

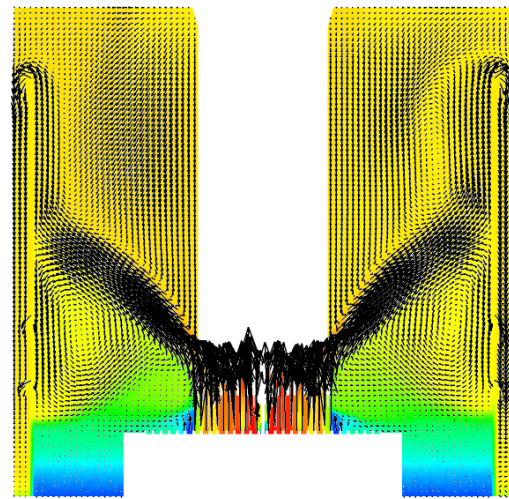


FIG. 82. Velocity and temperature distribution in case 3 calculation.

(4) Vertical temperature distribution on TC-plug

Temperature distributions of all the cases in the vertical direction on the TC-plug are shown in Fig. 83. The measured temperatures on the TC-plug are also plotted in this figure. Temperatures on the TC-plug agreed at the height from -5000 to 0 mm in all cases and their differences from measured ones were 5 to 10°C. These tendencies were similar on the opposite side. On the other hand, the calculated temperatures at the lowest level of the TC-plug were respectively around 30°C, 65°C and 18°C higher in Cases 1, 2 and 3 than the measured temperature of approximately 415°C: The calculated temperatures in Case 1 dropped down largely from -5700 mm to -6000 mm, while those in Case 2 were almost constant from the top to the bottom. In Case 3, the calculated temperatures in the region under -5700 mm also dropped down and became lower than those in Case 1, but they were still around 15°C higher than the measured one.

We applied RNG $k-\varepsilon$ model in these calculations, which calculated larger eddy viscosity. Hence, it is estimated this turbulent model calculated the flatter temperature distributions in

the upper region and also calculated the higher temperatures in the lower region. The calculation models applied in [26–27] were different from our model: A porous media approach was applied in the UCS region and the fine mesh partitioning was also applied around the flow holes of the inner barrel in these references. As reported in [27], our coarse mesh partitioning of a flow hole might overestimate the pressure drop and eventually might affect the temperature profile. However, our temperature distributions along the TC-plug and jet profile from the upper part of the UCS region to the inner barrel agreed well with our results reported in [27]. These results indicate that the porous media approach was reasonable and that the flow rate through the flow holes did not affect the thermal-hydraulics of the upper plenum in the present steady state condition.

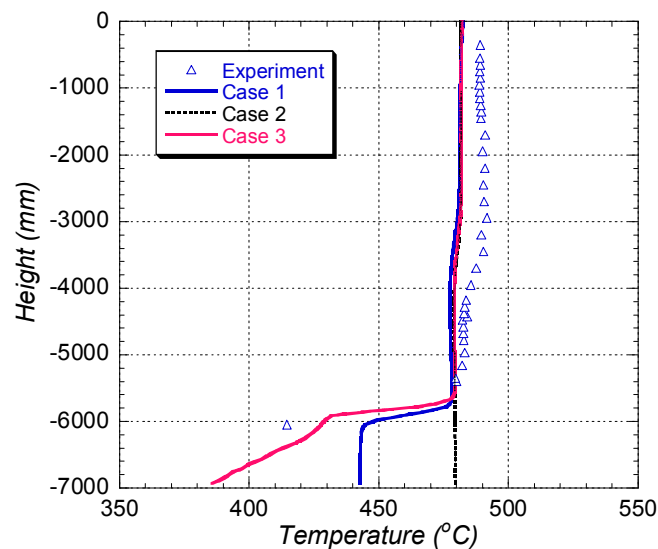


FIG. 83. Temperature distribution on TC-plug.

7.1.5. University of Fukui

(1) Steady-state and transient simulations

After the initial steady state calculation, the transient calculation is conducted using the FLUENT code based on the boundary conditions provided by IAEA. Fig. 84 shows the comparison between the calculation and measured results indicated as ‘Test’. As one can understand from this figure, temperature near the sodium surface at time zero is under predicted by 8°C. The temperature distribution due to the thermal stratification interface is higher than that of measurement. These are two major problems of the benchmark calculation. Therefore, different flow-hole configuration is tried whether the calculation using the CFD code to predict better result in terms of thermal stratification interface.

It is clear that there are two problems in our computed result. One is under prediction of the temperature near the liquid sodium surface. The other one is over prediction of the thermal stratification surface. The first problem will be solved when the boundary conditions of the benchmark is re-evaluated.

Fig. 85 illustrates contour maps of velocity and temperature distribution inside the upper plenum at 0 second and 10 minutes. The flow from the reactor is bended at the bottom of the UIS under the steady state condition. However, the flow from the reactor goes towards the flow-hole direction and the temperature distribution is stratified when the flow rate is decreased. These contour maps suggest that the height of the thermal stratification interface is greatly affected by the discharge flow rate from the flow-hole.

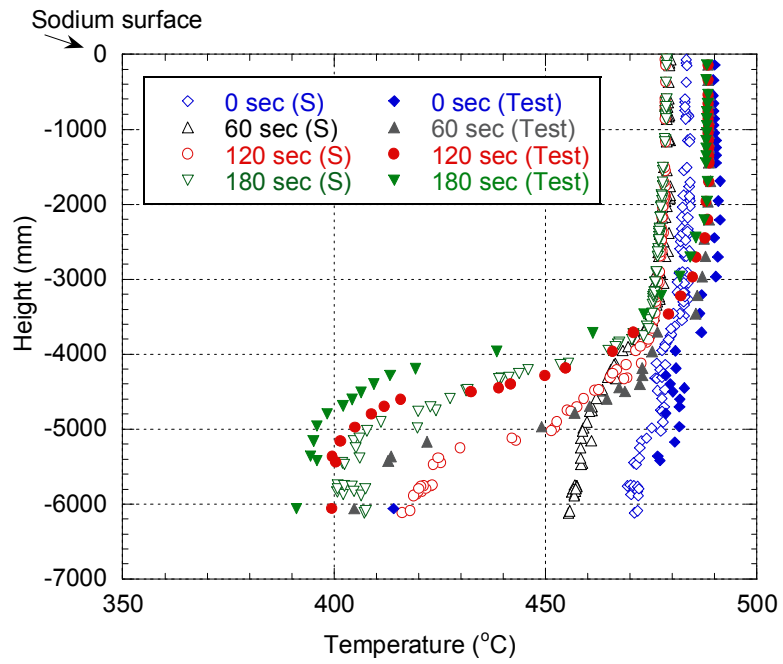
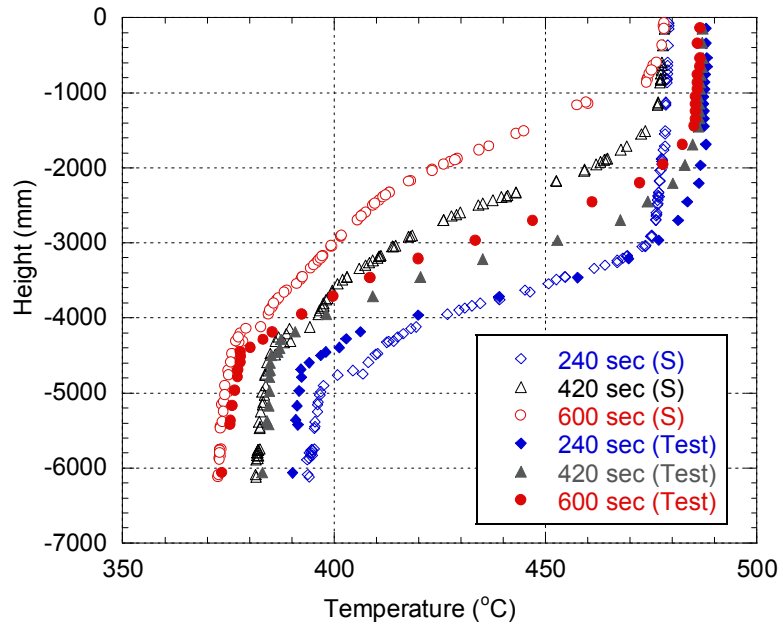


FIG. 84. Comparison of calculation and measured results ('Test').

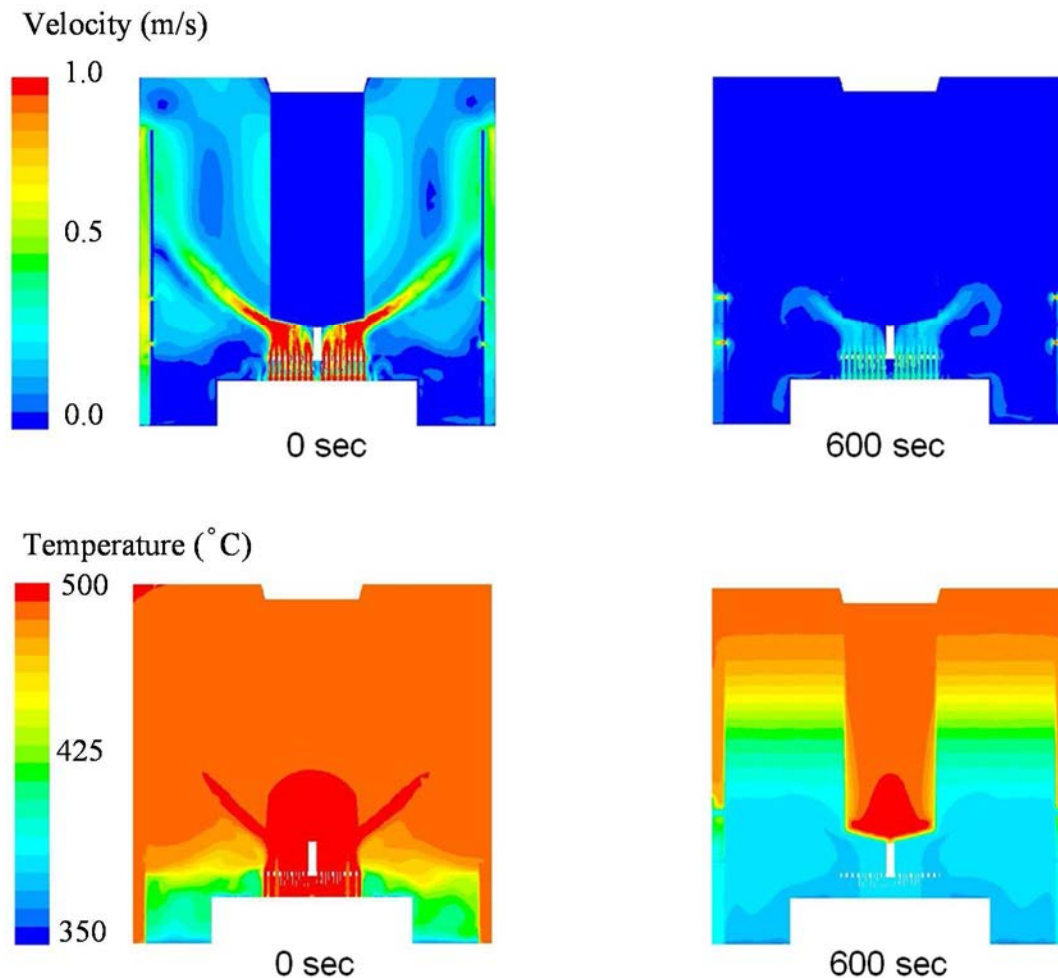


FIG. 85. Velocity and temperature contour maps at 0 sec and 10 min.

7.1.6. KAERI

(1) Steady-state solution

A steady-state computation is performed to provide the initial condition for a transient simulation. The time marching strategy with a time step size of 0.01 seconds provides a complete convergence after 70,000 time marching. This buoyancy dominated solution was obtained when the initial guess was imposed with zero velocity and a constant temperature and pressure. Fig. 86 shows the steady-state velocity magnitude and temperature contour plots on the symmetry plane through the outlet. This buoyancy dominated solution shows that the hot sodium moves upward along the outer wall of the UCS main body by a strong buoyancy force and passes the upper symmetry plane, and then flows downward to the annular region between the inner barrel and reactor vessel and flows out of the reactor at the outlet. For both solutions, the flow field is almost stagnant with significantly colder sodium below the core outlet level. It is noted that the sodium in most of the upper plenum and outlet region is rather well mixed and the temperature of the sodium is nearly uniform except for a certain region. Small flow holes in the inner barrel do not play a significant role in mixing the fluid on the opposing sides of the inner barrel for steady-state conditions (in a normal operation). Small flow holes on the inner barrel do not play a significant role in mixing the fluid on the opposing sides of the inner barrel for the steady-state conditions.

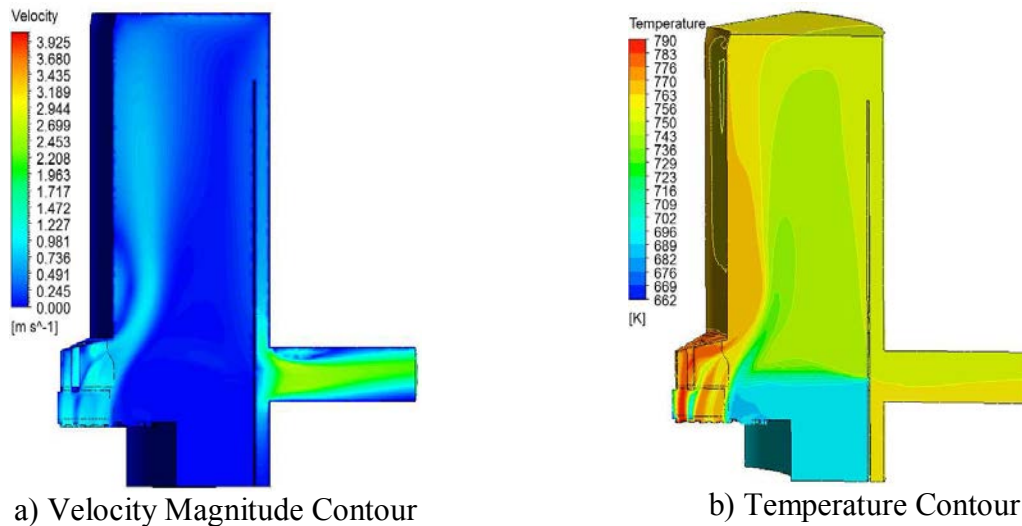


FIG. 86. Steady-state velocity magnitude and temperature contours.

Fig. 87 shows the predicted vertical temperature distribution along the thermocouple tree together with the experimental data. The predicted temperature distribution agrees fairly well with the experimental data, especially when the complex structures of the core upper plenum and the assumptions introduced for the 1/6 simplified model are considered. It was noted that the temperature varies rapidly at a height of $y=1.4$ m, and does not vary significantly above this height. The temperature at the upper region is under-predicted.

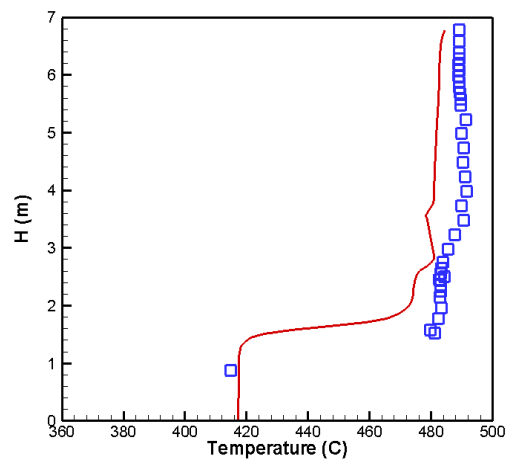


FIG. 87. Vertical temperature profile along the thermocouple tree.

(2) Transient solution

Fig. 88 shows the transient evolution of the temperature field at the upper plenum of the Monju reactor. When the transient starts and the core outlet temperature gradually drops owing to a reactor shutdown, the cooler sodium stays near the bottom of the vessel and the hotter primary sodium at the higher elevation in the upper plenum stays largely stagnant. As the transient continues, the cold sodium in the lower portion of the plenum moves upward and a thermal stratification begins to form. A rather stable thermal stratification is established at 5 minutes for both solutions. It is noted that the two solutions behave very similarly after 2 minutes, although they behave very differently before 1 minute. A slow movement of cold

sodium is observed between 3 and 5 minutes. The rapid coastdown of the mass flow rate after a pump trip is finished at about 5 minutes, and the mass flow rate from the core becomes nearly constant after 5 minutes. Thus, the type of flow until 5 minutes is a mixed convection and the natural convection begins after 5 minutes. At 10 minutes, the thermal stratification interface moves upward rather quickly even though the flow is a natural convection. At 15 minutes, the thermal stratification interface reaches the top of the inner barrel and the temperature field in most of the upper plenum is mixed and homogenized. This shows that a relatively strong thermal mixing has occurred in a large portion of the upper plenum. Thus, the computed temperature field contradicts the real physics of the fluid flow and heat transfer in this region. A stable thermal stratification should form and persist after 3 minutes. The origin of this discrepancy is due to the turbulence model employed in the present calculation.

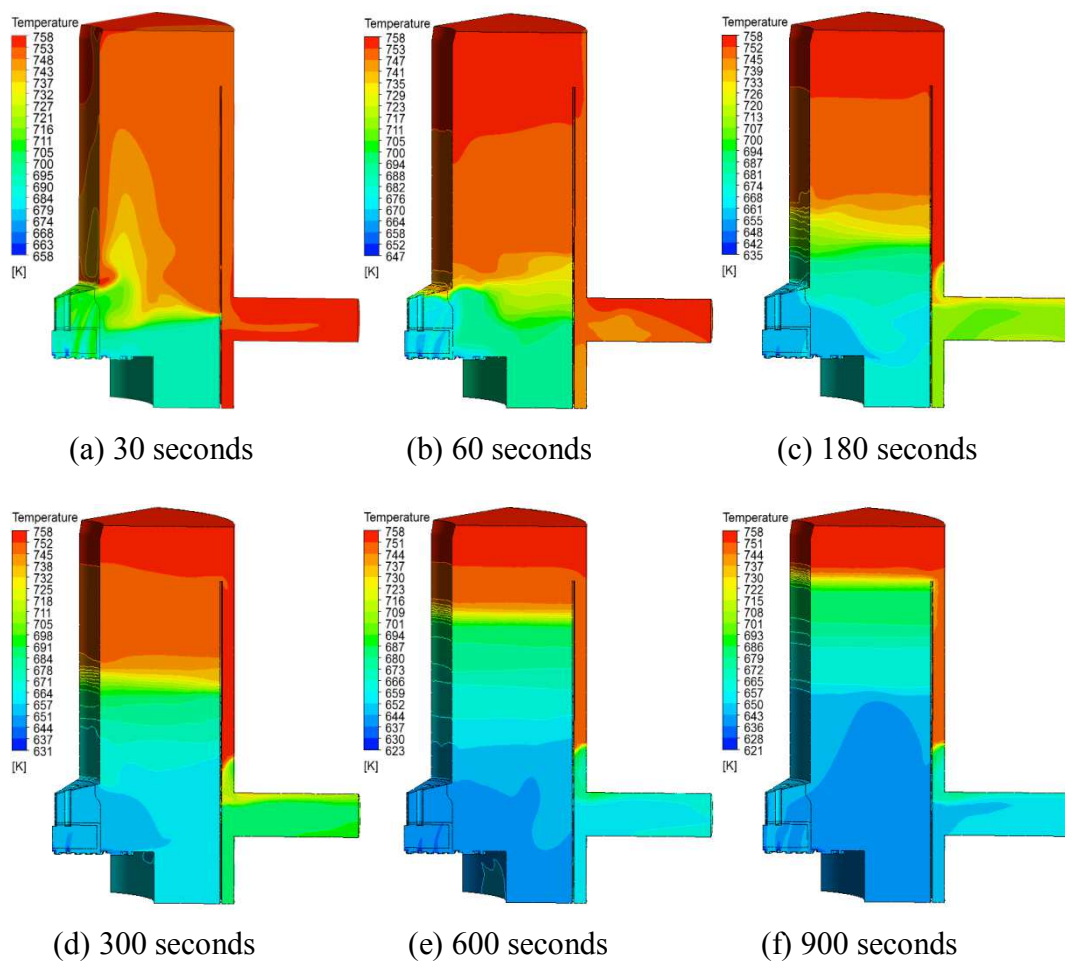


FIG. 88. Evolution of temperature contour during the transient calculations.

Fig. 89 shows the predicted transient temperature profiles along the thermocouple tree together with the experimental data. It is observed that the predicted temperature profiles agree very well the experimental data until 300 seconds. However, the predicted results deviate greatly from the experimental data at 600 and 900 seconds. The temperature at the upper region is under-predicted.

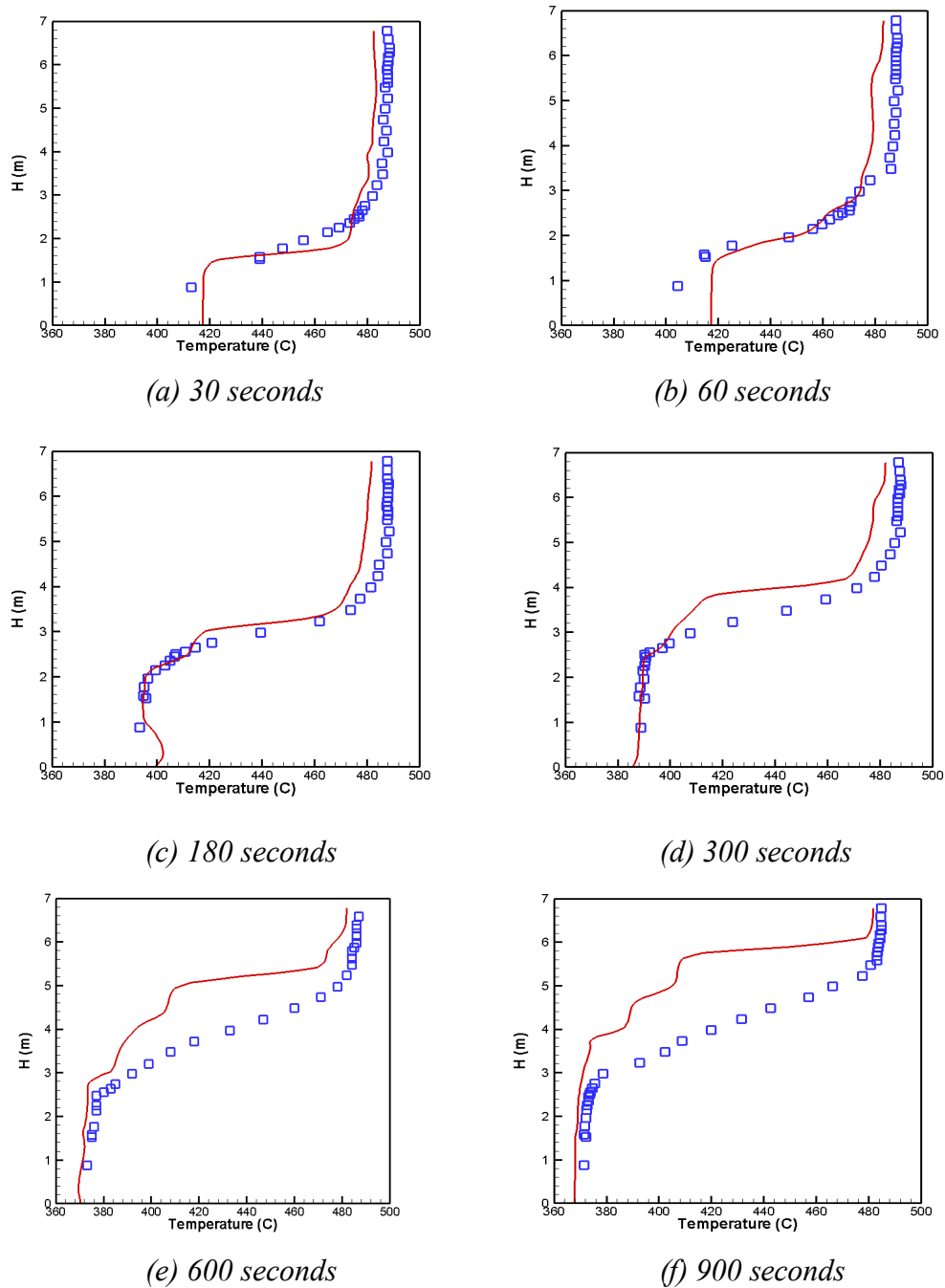


FIG. 89. Temperature profiles along the thermocouple tree during the transient calculations.

7.1.7. IPPE

(1) Steady state results

Results of GRIF calculations for steady state were compared with results calculated by Kamide and H. Ohshima. From the comparison of flow and temperature distributions that are presented on Fig. 90 one can conclude that calculated flow patterns are rather different. GRIF predicts the ‘ascending flow mode’ when the hot sodium ejecting from UCS region into plenum goes upward washing the upper column body and as a result only one large recirculation zone forms in the plenum. Another flow pattern that can be called as ‘jet flow mode’ was predicted by calculations of H. Kamide and H. Ohshima. In that case strong jet ejecting from UCS region crosses the plenum space and divides it on two recirculation zones.

As a result, the temperature distributions for these two different flow patterns are quite different.

It is worth to mention that the results of calculations of other CRP participants (ANL, CEA, IGCAR) that were be presented on 2nd RCM also predicted the ‘jet flow mode’ for steady state. The possible reason of such difference of preliminary GRIF results will be explained in section 7.2 where the results of sensitivity study are presented.

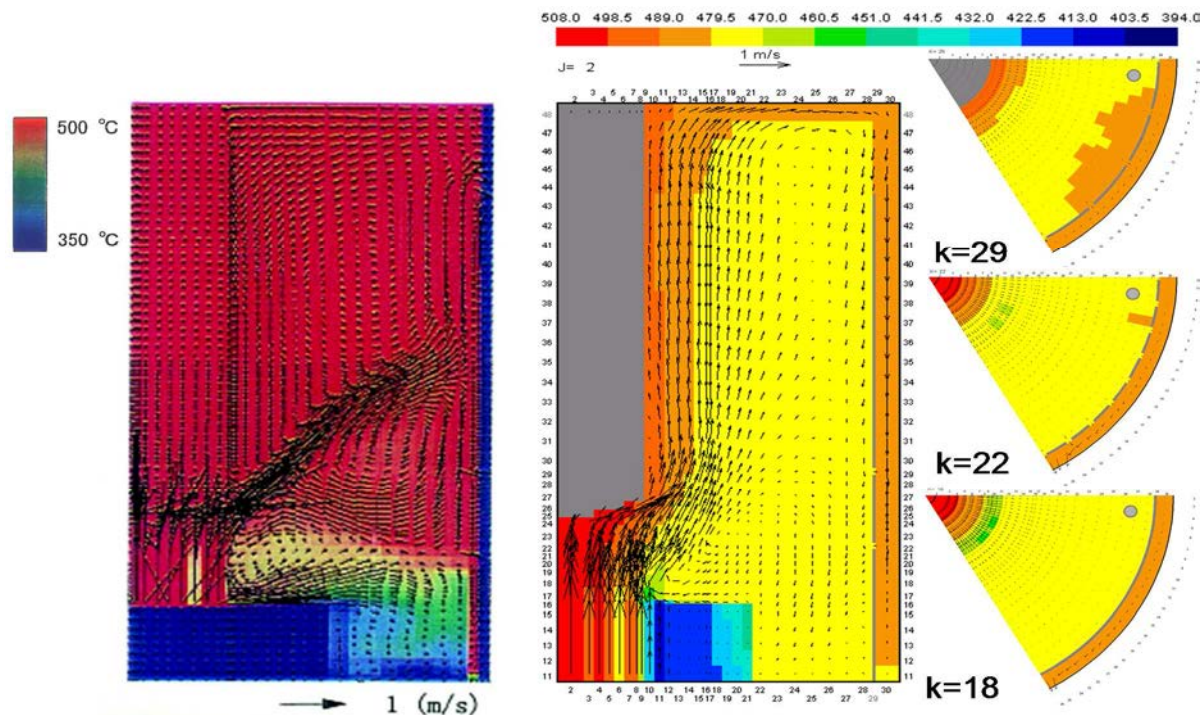


FIG. 90. Velocity and temperature distributions for initial steady state. Results of preliminary GRIF calculations and comparison with H. Kamide and H. Ohshima results.

- (a) H. Kamide and H. Ohshima results; (b) GRIF results - Vertical cross-section $j=2$;
(c) GRIF results - Horizontal cross-sections.

Data in Table 16 show that sodium flow through upper (G_{hu}) and lower (G_{hb}) rows of holes is relatively small in initial steady state conditions and main part of sodium leaves upper plenum through the gap between the top of inner barrel and dip plate.

TABLE 16. FLOWS IN INNER BARREL REGION, [KG/S]

G_{hb}	G_{hu}	G_{top}
7.0	4.0	327.

(2) Transient results

GRIF calculations shows (Fig. 91) that ‘ascending flow mode’ in upper plenum invariably keeps during initial period of transient but for later stages the stratification of the sodium in the plenum begins to influence on the flow pattern. But the comparison of measured and calculated temperature distribution along plenum height (Fig. 92) shows that GRIF code overestimates coolant mixing in the upper plenum.

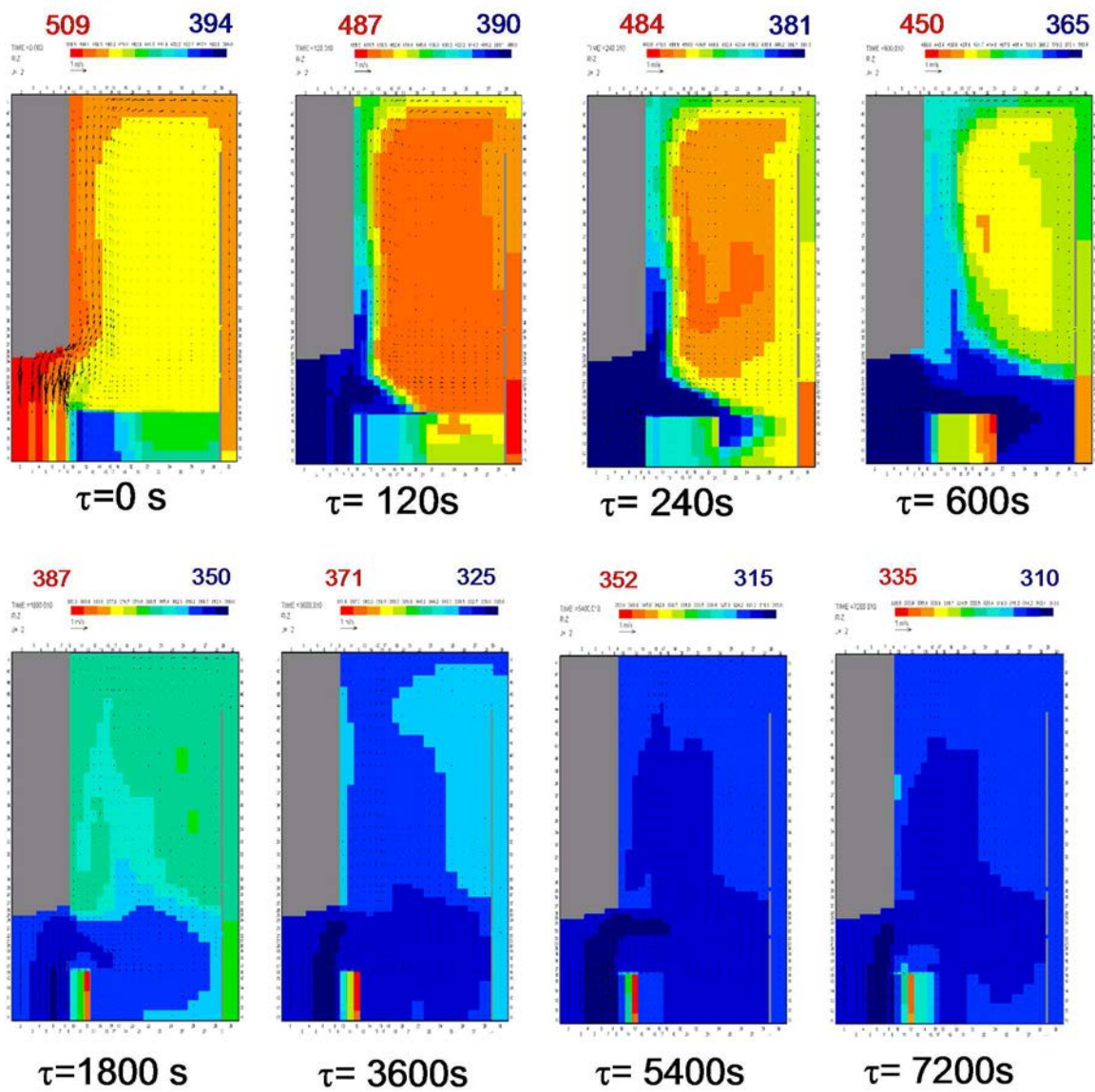


FIG. 91. Transient velocity and temperature distributions. Blind@GRIF calculations.

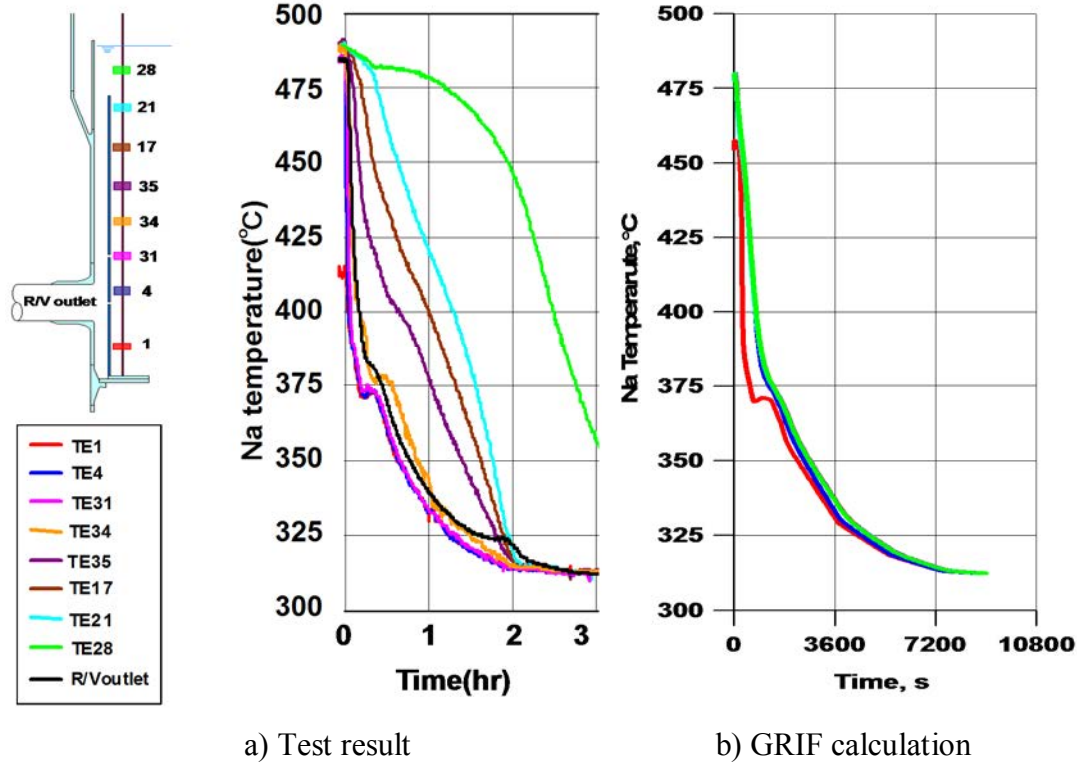


FIG. 92. Sodium Temperature variations at the position of thermocouple tree.

7.1.8 ANL

(1) Initial steady-state

The steady-state calculations are completed to obtain the initial state from which the transient calculations are assumed to start, but also to assess the suitability of the CFD mesh for the simulation of expected natural convection conditions in the Monju upper plenum during the long transient. These initial simulations exhibited some convergence difficulties with both trimmed hexahedral and polyhedral mesh structures, requiring an approach to the initial (steady-state) solution by means of time steps. In the first stage, steady-state calculations are run to force the solver to achieve a time-averaged flow field and temperature distributions with limited convergence. In the second stage, a time-dependent null transient is computed for an additional one minute of simulation time to allow the solution to settle into one of its common modes of fluctuations typically observed in mixed convection flow regimes.

The velocity magnitude contour plots on the symmetry plane through the outlet nozzle, and on the horizontal plane that cuts through the lower holes on the inner barrel and the outlet nozzle are shown in Fig. 93. The temperature contour plots on the same planes are shown in Fig. 94. The results indicate a fairly large annular recirculation zone in the upper plenum with hot plume from the core first spreading conically outward and then upward flow along the inner barrel inner surface, followed by a downdraft along the vertical surface of the upper core structure main body. The flow field between the inner barrel and reactor vessel is uniformly downward, converging toward the outlet nozzle. As expected, the small holes on the inner barrel do not play a significant role on mixing of the fluid on opposing sides of inner barrel for the initial steady-state conditions.

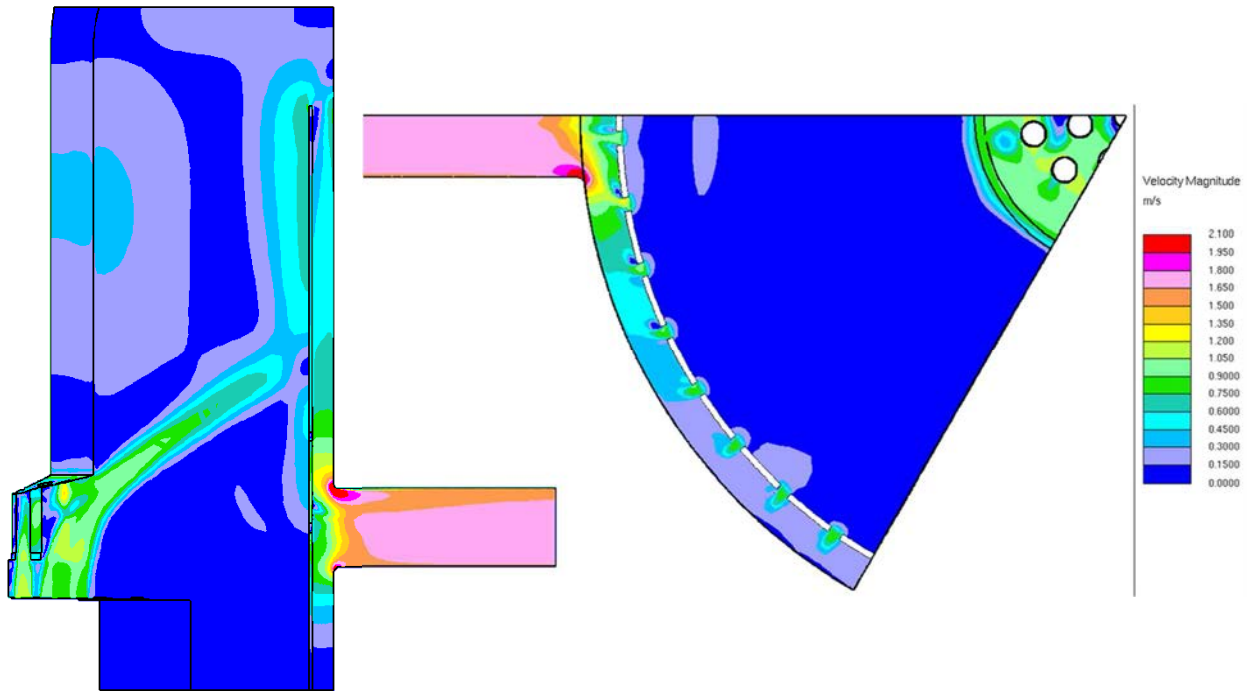


FIG. 93. Velocity magnitude plots for initial conditions on the symmetry plane through the outlet nozzle (left) and the horizontal plane that cuts through the lower holes on the inner barrel (right).

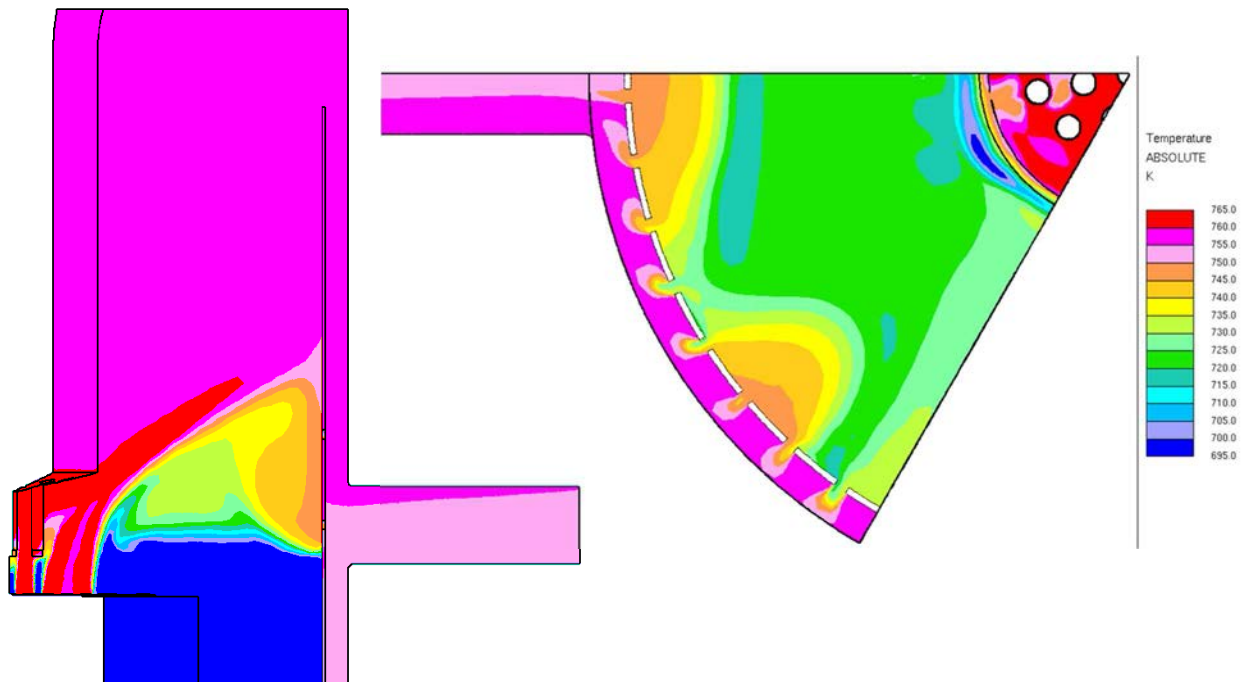


FIG. 94. Temperature contour plots for initial conditions on the symmetry plane through the outlet nozzle (left) and on the horizontal plane that cuts through the lower holes on the inner barrel (right).

The temperature contour plots in Fig. 94 indicate substantial thermal striping near the core subassembly outlets, but otherwise fairly uniform temperatures for the well-mixed flow in the bulk of the upper plenum. Although there is no major thermal stratification in the upper portion of the upper plenum initially, the results predict a significantly lower temperature for the stagnant sodium below the core barrel. The temperatures along the thermocouple tree for the initial conditions are compared with the test data in Fig. 95 for both the polyhedral and trimmed hexahedral meshes. The consistency of the results with both mesh types confirms the grid independence of the solutions.

In agreement with the test data, the steady-state calculations predict significantly cooler liquid sodium in the reactor vessel below the core outlet with the only thermocouple at that elevation measuring about 75°C lower temperature than what is calculated for upper part of the plenum. In the upper portion of the reactor vessel, the fairly uniform sodium temperature is predicted about 5°C cooler than the experimental data. Since most of sodium coolant in the upper plenum above the elevation of the holes on the inner barrel is at that temperature, this discrepancy corresponds to either an underestimation of flow through the bypass holes or about 4% uncertainty in energy balance for measured core flow or power during the initial steady-state conditions.

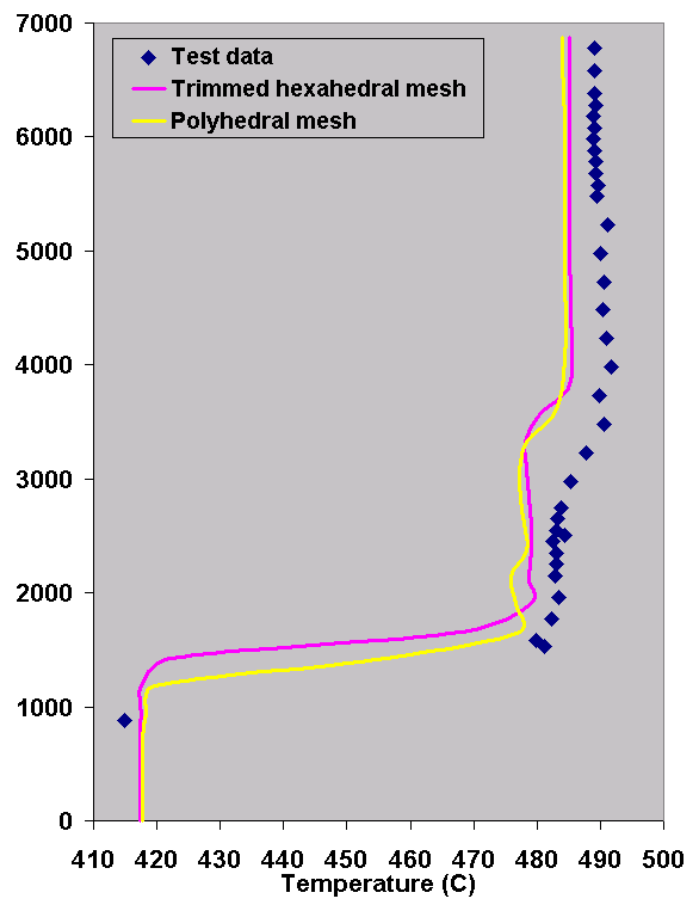


FIG. 95. Comparison of temperature distributions along the thermocouple tree.

(2) Transient analysis

The transient calculations started following a 60 seconds long null transient and completed in several stages. The critical first minute of simulations (when the flow rate nominally drops down to 1/5th of the initial, steady-state value due to primary pump trip) is completed using 5 msec time steps. Following four minutes of the tests during which the core outlet temperature

drops more than 100 K on average following the reactor shutdown and the flow rate coasts down to the natural circulation levels are simulated with 10 msec time steps. The remaining transient calculations are performed using 50 msec time steps.

The temperature contour plots on the symmetry plane through the outlet nozzle calculated with the SIMPLE transient solver option are shown in Fig. 96 during first five minutes of the transient. Despite a sudden drop in the flow rate through the core following the pump trip and subsequent flow coast-down, the temperatures in the upper plenum decrease at a much slower rate primarily due to thermal stratification. At the beginning of the transient, the bulk of the primary sodium in the upper plenum (except in lower elevations below the core outlet) is more or less at the same temperature (about 755 K). When the transient starts and core outlet temperature gradually drops due to reactor shutdown, the cooler (more dense) sodium stays near the bottom of the vessel and the hotter (and less dense) primary sodium at the higher elevations in the upper plenum stays largely stagnant. The calculations predict that the resulting thermally stratified mixing pattern prevails for only about fifteen minutes into the transient.

Normally, the thermal stratification in the upper plenum impedes the natural circulation and degrades the passive safety performance of a reactor. When the colder and denser sodium is trapped at lower elevations, the upper plenum outlet temperature (as well as in the outlet nozzle) could stay high for a long period of time. Since the natural circulation flow rate in the primary system depends heavily on the temperature differential and elevation difference between the reactor core and main heat sink (in this case, the intermediate heat exchanger), a thermally stratified upper plenum translates to lower natural circulation flow rates.

In Monju design, however, two sets of holes on the inner barrel provide alternative flow paths between the core outlet and outlet nozzle, bypassing the thermally stratified region of the upper plenum, which poses larger impedance to natural circulation flow patterns following a reactor shutdown. Because of these bypass flow paths through the holes on the inner barrel, the average temperature through the outlet nozzle (the inlet temperature into the intermediate heat exchanger) starts decreasing as early as two minutes into the transient while most of the upper plenum above the core remains hot. Once the colder sodium fills the annular gap between the reactor vessel and inner barrel below the elevation of the outlet nozzle, the average temperature in the outlet nozzle follows the average core outlet temperatures fairly closely.

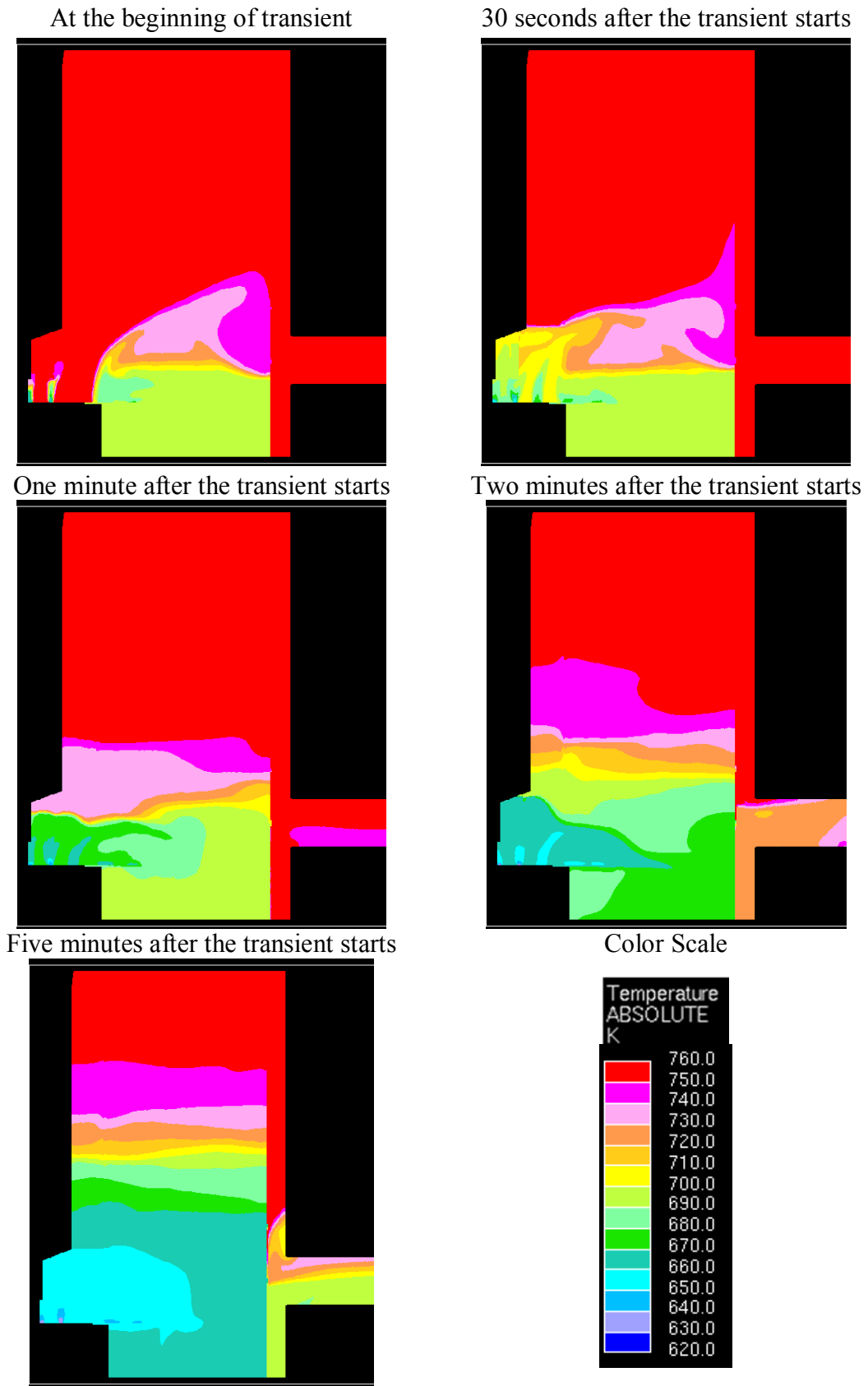


FIG. 96. The temperature contour plots on the symmetry plane through the outlet nozzle.

A comparison of the calculated transient temperatures along the thermocouple tree with the test data at various points during the test is shown in Fig. 97. Although during the initial stages of the transient (first few minutes) the calculated results are in reasonably good agreement with the test data along the entire height of the upper plenum, around the 5 minute mark the discrepancy above the elevation of the holes on the inner barrel (2,550 mm mark in Fig. 97) starts growing. Only 15 minutes into the transient, the calculations indicate fairly uniform sodium temperature almost along the entire height of the upper plenum except at elevations above the upper end of the inner barrel, whereas the test data shows still significant stratification at elevations above the holes on the inner barrel at that point. In fact, the test data indicates that the thermal stratification persists in the upper plenum for well over an hour.

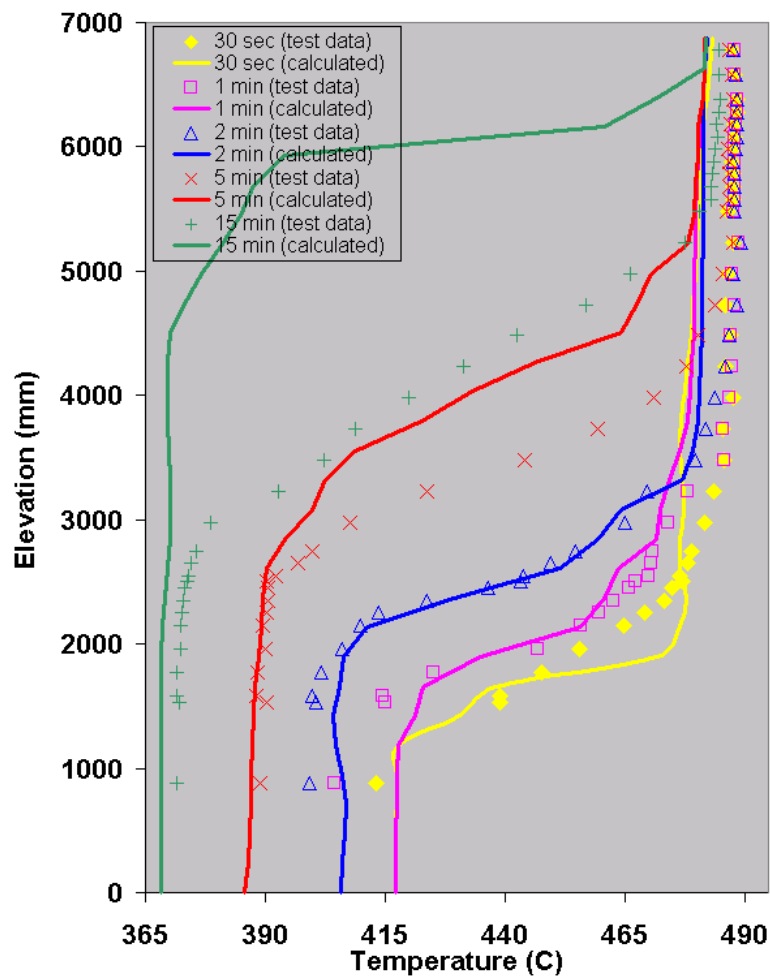


FIG. 97. Comparison of transient results with test data for various stages during the test.

7.2. SENSITIVITY ANALYSIS TO INVESTIGATE THE DISCREPANCIES WITH EXPERIMENTAL DATA

7.2.1. CIAE

Fig. 98 shows the axial temperature comparison between the analysis and the test data. The lines with the symbols show the experimental data and the smooth line is the numerical analysis data. It can be seen from this figure that at the beginning of the reactor trip, or about 600 seconds after the reactor trip condition, the calculation data agrees with the test data well. But in the following time of the process, it has a great discrepancy with that of the test above

the -4000mm height level. For example, the calculation data is lower than that of the test data at 1800 second at height level -3000mm, and it reach to the lowest point at -1000mm, which means that the formation and development of the thermal stratification in the calculation is faster than that in the test.

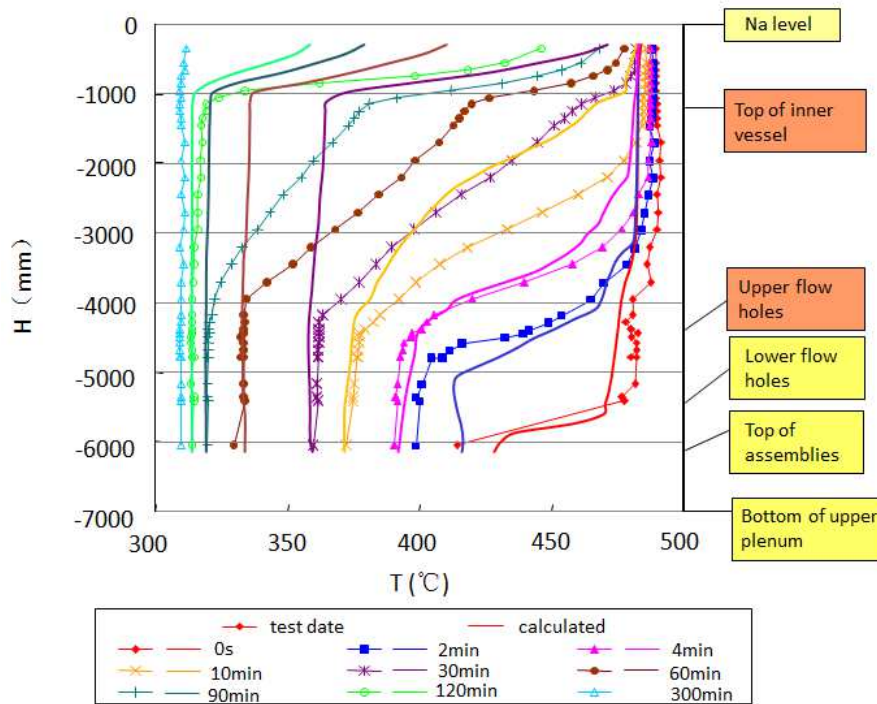


FIG. 98. The temperature comparison between the analysis and test data.

The flow rate relationship between the annulus flow and the by-pass flow through the flow-holes in the inner barrel are shown in Fig. 99. The flow rate in the annulus reaches the lowest point at about 600 second after the reactor trip. Then it increases in the following time which effect the thermal stratification process. So the flow rate distribution in the annulus and the bypass flow rate in the inner barrel is the key.

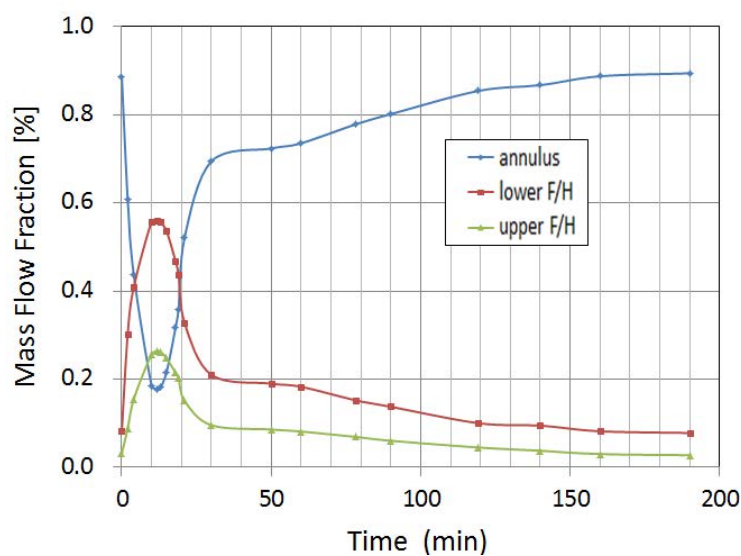


FIG. 99. The flow rate distribution in the different flow pathes (flow holes with sharp edge).

7.2.2. CEA

Compared to the coarse mesh of the reference calculation (334000 tetrahedrons, see Section 7.1.1), two refined pure tetrahedral mesh of respectively 1.2 Million tetrahedrons (fine mesh) and 3 Million tetrahedrons (finest mesh) have been created for the sensitivity calculations. The commercial mesh generator ICEMCFD has been used for this purpose by applying the Octree method. The meshing of both, the flow holes and the volume of the upper plenum has been refined for an improved treatment of the pressure loss of the flow holes and of sharp velocity and temperature gradients in the upper plenum. This revised finest mesh is shown on Fig. 100 on the examples of a horizontal cut plane through the lower line of the Inner Barrel flow holes and of a view of the symmetry plane going through the outlet pipe.

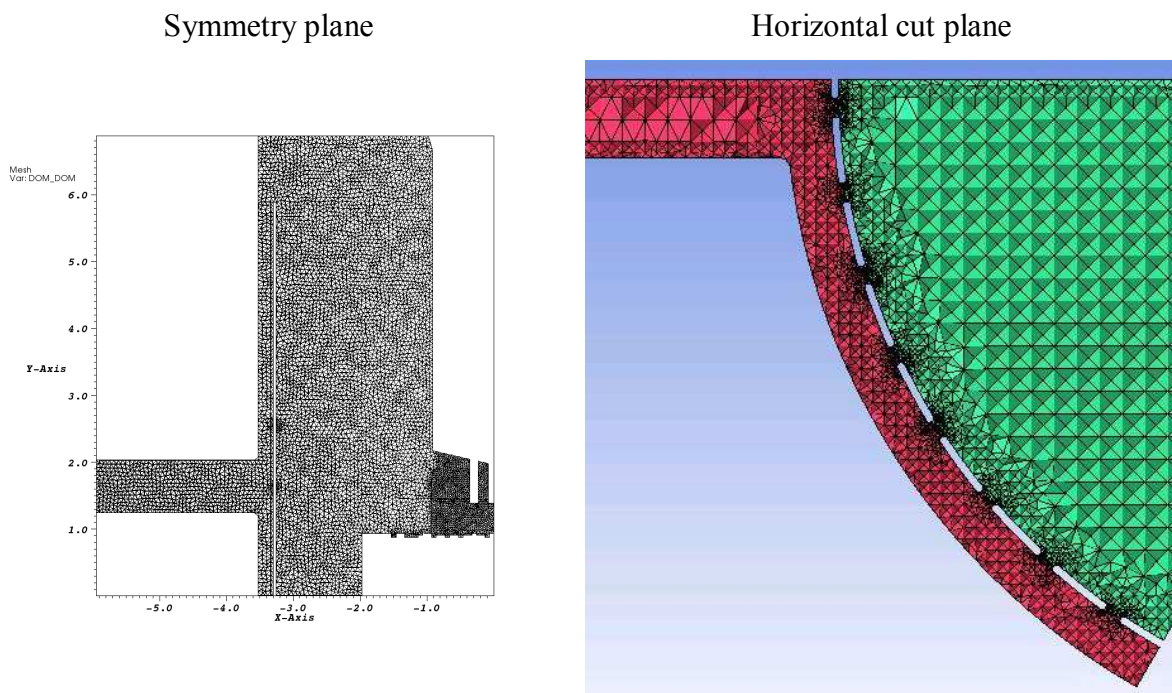


FIG. 100. Visualisation of the finest mesh.

(1) Steady state calculation

At the beginning of the trip transient, the temperature field and the velocity flow are well established in the Upper Plenum. A first calculation is performed in order to obtain this initial condition. The boundaries conditions for the calculation are the conditions at the beginning of the test. Starting from a reposing ($\vec{u}=0$), isothermal flow, the flow field is considered as established in the plenum when all 120 temperature samples placed along the thermocouple plug have reached a stabilized value. At that time, the calculated temperature profile should be close to the temperature profile measured by the thermocouple plug. Three different steady solutions have been achieved which can be distinguished regarding the driving physical process:

- A momentum dominated solution S1;
- A buoyancy dominated solution S2;
- A mixed convection dominated solution S3.

All solutions have a similar reduced Froude Number $Fr = u / \sqrt{g \cdot \Delta\rho / \rho \cdot d}$ which is in the order of 3.5 (mixed convection). The resulting three different flow patterns and temperature

fields are given in Fig. 101. A vertical cut plane in a symmetry plan is shown and the temperature profiles along the thermocouple plug are compared. From these temperature profiles it seems not possible to conclude definitively on the flow patterns which have been present during the Monju experiment. Nevertheless, extensive sensitivity studies on the meshing, on the order of the numerical scheme and on the initialisation of the calculation give some insight on the code behaviour. The effects of the sensitivity studies are summarized in Table 17.

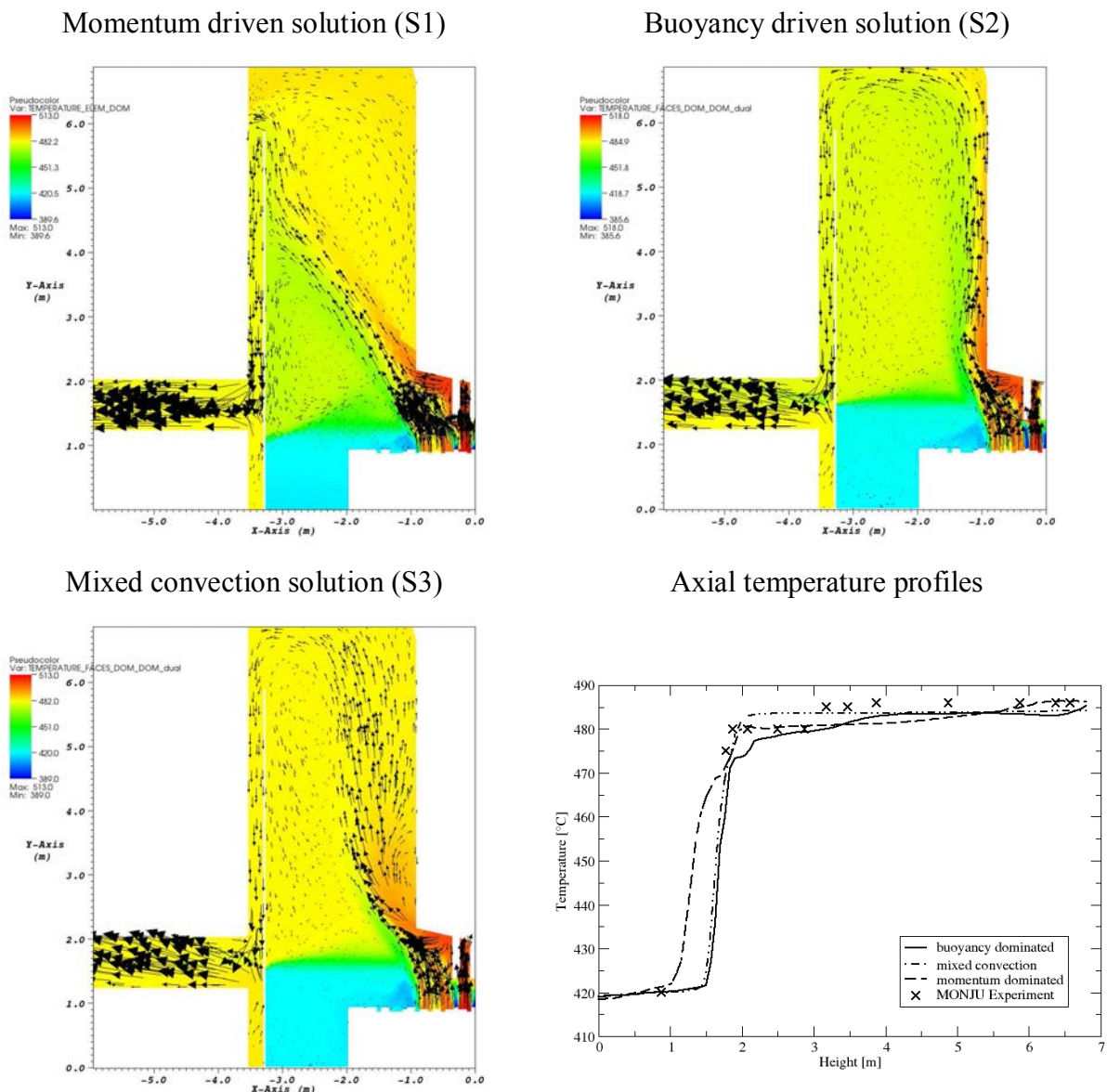


FIG. 101. Visualization of different solutions; comparison of the axial temperature profiles.

The following conclusions of the sensitivity calculations can be made:

- A bifurcation into ‘momentum’ and ‘buoyancy’ driven solutions is observed, depending on the mesh refinement and the order of the numerical scheme;
- The momentum driven solution (S1) seems to be attained for the coarse mesh and first order convection scheme (initializing with a reposing fluid);
- The buoyancy driven solution (S2) seems to be attained for the fine mesh and second order convection schemes (initializing with a reposing fluid);

- Once a stationary solution is achieved (either S1 or S2), this solution cannot be altered by changing the numerical scheme and/or the mesh refinement (stable solution);
- The modelling of the UCS has a strong influence on the flow pattern, especially on the width and angle of the jet leaving the UCS; however a real qualification of the modelling is not possible due to the lack of data.

TABLE 17. PROCEDURES TO ACHIEVE THE DIFFERENT SOLUTIONS

Initialisation at t=0s	Solution procedure	Solution
<i>Coarse mesh</i> ; Reposing flow field at T=418°C	Transient calculation to reach steady state conditions; first order convection scheme: upwind	S1
<i>Fine mesh</i> ; Reposing flow field at T=418°C	Transient calculation to reach steady state conditions; second order convection scheme: muscl	S2
<i>Fine mesh</i> ; Reposing flow field at T=513°C	Transient calculation to reach steady state conditions; first order convection scheme: upwind	S2
<i>Fine mesh</i> ; Solution S2; UCS is not modelled	Transient calculation to reach steady state conditions; second order convection scheme: muscl	S3
<i>Fine mesh</i> ; Solution S1;	Transient calculation to reach steady state conditions; convection schemes: upwind, muscl Time schemes: 1 st order explicit; 1 st order implicit	S1
<i>Coarse mesh</i> ; Solution S2;	Transient calculation to reach steady state conditions; convection schemes: upwind, muscl Time schemes: 1 st order explicit; 1 st order implicit	S2

In order to verify mesh convergence, a simulation on the finest mesh (3 Million tetrahedrons) has been achieved. Starting from a reposing flow at T=418°C and applying a second order convection scheme (muscl) the buoyancy driven solution S2 has been attained as steady state solution.

The detailed ‘history’ which had led to the flow pattern in the Monju plant before the pump trip experiment is not known by the author. Assuming the same sensitivity of the flow pattern in the Monju plant as in the sensitivity calculation, it seems hardly possible to predict clearly and without ambiguity the flow patterns at the beginning of the experiment. Nevertheless, JAEA has estimated from many scaled tests using sodium and water that the momentum driven solutions were close to the actual behaviour. According to JAEA, this assumption is supported by the measured temperature change in the middle part of the plug, 3m and 3.75m above the vessel bottom. However, the momentum driven solution S1 presented in Fig. 103 did not reproduce these temperature changes whereas the buoyancy driven solution S2 does roughly.

(2) Transient calculations

The preliminary analysis of the CEA has shown that under natural convection conditions, the stratification front has moved upwards significantly faster in the calculation than observed in the experiment (see Section 7.1.2). Concerning the modelling, several key effects might be responsible for this behavior:

- (a) Insufficiently fine meshing of the flow holes overestimates the local pressure loss of the holes;

- Significantly finer meshing of the flow holes.
- (b) Insufficiently fine meshing of the Plenum can avoid the creation of steep gradients;
 - Finer meshing of the Plenum.
- (c) Strongly dissipative convection schemes can inhibit buoyancy effects;
 - Application of less dissipative convection schemes.
- (d) Temperature dependent physical properties can modify buoyancy effects;
 - Introduction of temperature dependent physical properties.
- (e) Treatment of turbulent temperature mixing of liquid metals;
 - Adaptation of the turbulent conductivity for low Prandtl Number fluids.
- (f) Oversimplified geometry;
 - Elimination of the porosity model of the Upper Core Structure. Meshing of
 - Flow Guide Tubes,
 - Honeycomb structure,
 - Fingers.
 - Introduction of a 360° model including Upper Plenum internals,
 - Modification of the geometry of the Inner Barrel flow holes.

(3) Numerical aspects

The reference calculation has been performed with the coarse mesh and a first order upwind convective scheme. This kind of scheme introduces a strong numerical diffusion. Thus, the sensitivity calculation was made with a more accurate second order convection scheme called `ef_stab` [28], applied to the Navier-Stokes equations as well as to the transport equations of k , ϵ and the temperature [29]. Further, the meshing was refined in the Upper Plenum and especially in the flow holes (finest mesh). All other parameters of the reference calculation (see Section 7.1.2) are not modified for this first sensitivity calculation, called second calculation.

The calculated temperature profiles are compared to the experimental values of Yamaguchi [25]. Fig. 102 compares the axial temperature profiles at initial stage ($t=0\text{min}$) and for the times 2, 4 and 10 minutes after the beginning of the pump trip. Due to the high CPU cost, the transient calculation which leads to the steady state initialization of the pump trip test at $t=0\text{min}$ was stopped before the coldest temperature near the bottom of the Upper Plenum has reached the experimental level.

At the beginning of the pump trip at $t=2\text{min}$, the calculated temperature profiles near the bottom of the Upper Plenum lag behind the experimental values. The lag disappears at $t=4\text{min}$; at $t=10\text{min}$ the overestimation of the stratification formation is visible. For forced convection conditions at $t<6\text{min}$, the calculated temperature profiles are close to the profiles of the reference calculation. Under natural convection conditions at $t>6\text{min}$, a qualitative improvement of the calculated mixing behaviour is not noticed. The 2nd order upwind convection scheme of the second calculation has introduced low frequency temperature fluctuations in the Upper Plenum. This is due to the fact that the 2nd order scheme is less diffusive than the 1st order upwind convection scheme of the reference calculation. The scheme could not have been stabilized by the refined meshing.

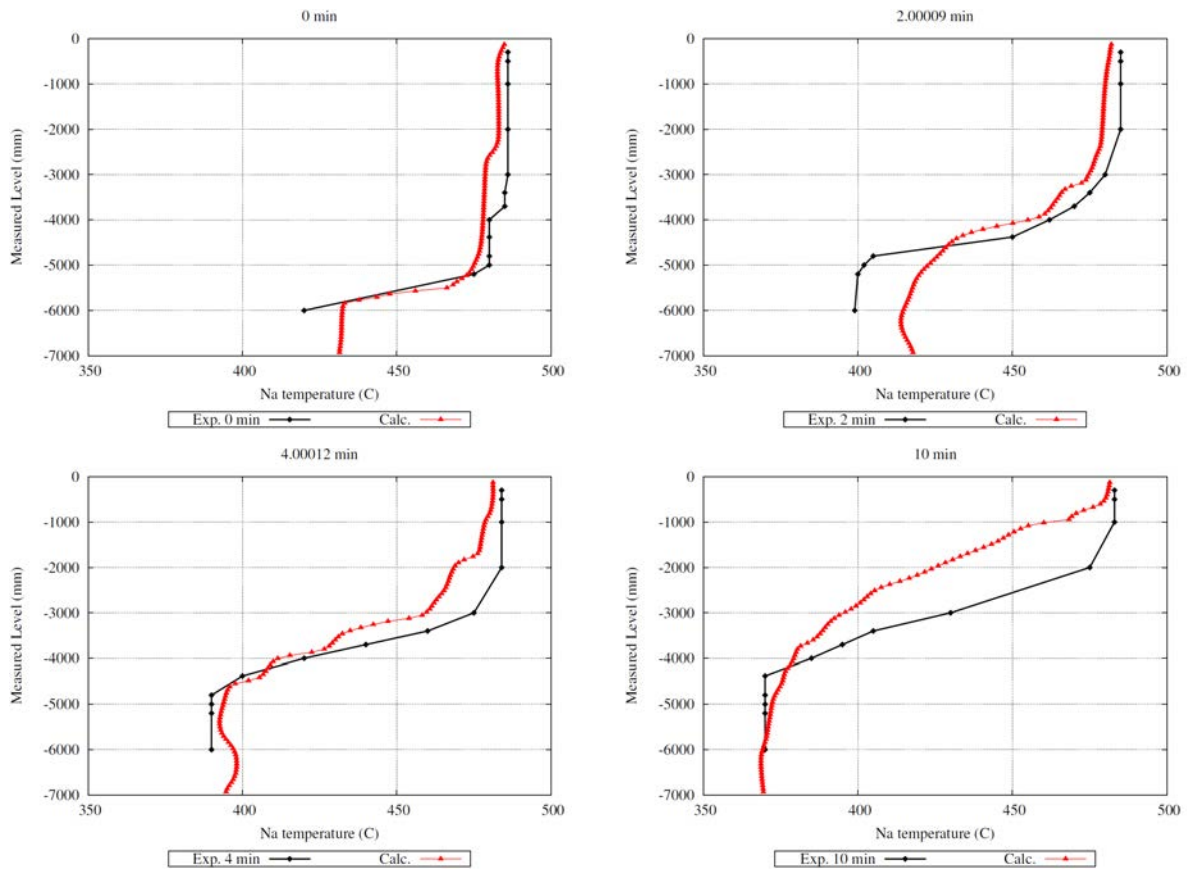


FIG. 102. Axial temperature profiles at different times.

Fig. 103 shows the repartition the flow rate between the flow going above the Inner Barrel and going through the flow holes. At the beginning of the pump trip at $t=0s$, 92% of the flow passes above the Inner Barrel and only 8% of the flow is going through the flow holes.

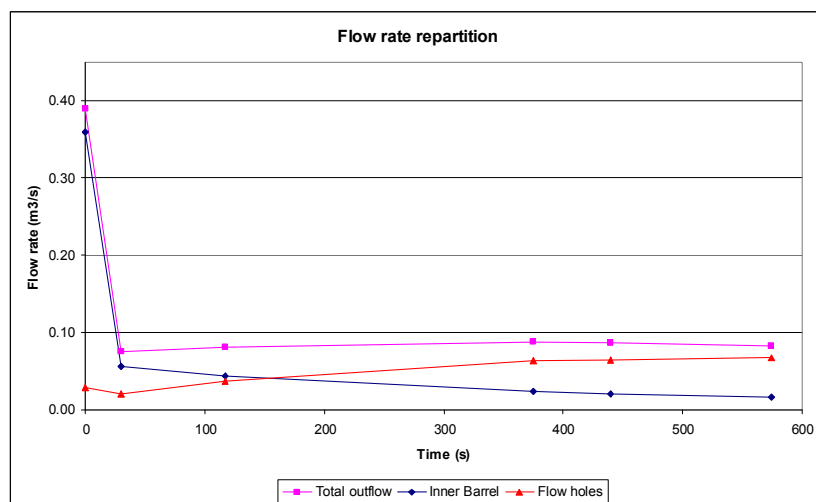


FIG. 103. Repartition of the flow path between flow holes and above the inner barrel.

Later, at times around 600 seconds, the main part of the flow passes through the flow holes (80%) and only 20% passes above the inner barrel. The flow rate which passes through the flow holes can be further divided in two flow rates which are approximately constant during the trip test:

- The lower line flow represents 70% of the holes flow rate (8 holes).
- The upper line flow rate represents 30% of the holes flow rate (4 holes).

(4) Temperature dependent physical properties

The reference calculation was performed with constant physical properties of sodium. The temperature variations inside the Plenum during the pump trip are around 150°C, what might modify the physical properties between cold and hot regions. A third calculation is performed with temperature dependant physical properties of sodium. As the fluid in Trio_U is a priori incompressible, the density, the heat capacity and the volumetric thermal expansion coefficient are taken constant. The temperature dependencies of ρ , C_p and $(\rho \cdot C_p)$ are given in Table 18.

TABLE 18. PHYSICAL PROPERTIES OF SODIUM BETWEEN 350°C AND 500°C

Quantity		ρ (kg/m ³)	C_p (kJ/kg/K)	$\rho \cdot C_p$ (kJ/m ³ /K)
Temperature	350°C	869	1.295	1125
	400°C	858	1.284	1101
	500°C	834	1.264	1054

This weak temperature dependency might not explain the enhanced cooling in the upper part of the plenum. The dependency of the dynamic viscosity and the thermal conductivity on the temperature are given in the Table 19.

TABLE 19. PHYSICAL PROPERTIES OF SODIUM BETWEEN 327°C AND 527°C

Quantity	Value			Unit
Temperature	327	427	527	°C
Dynamic viscosity	$3.21 \cdot 10^{-4}$	$2.64 \cdot 10^{-4}$	$2.27 \cdot 10^{-4}$	kg/m/s
Thermal conductivity	73.70	68.00	62.90	W/m/K

A fourth calculation has been performed in order to quantify the influence of temperature dependant dynamic viscosity and thermal conductivity on the mixing. The convection scheme used for this calculation is that of the scheme of the second calculation (2nd order upwind) and the coarse mesh of the reference calculation is used. In Fig. 104, the temperature profile of the fourth calculation is compared to the profile of the reference calculation. The instant four minutes after the beginning of the trip test is shown.

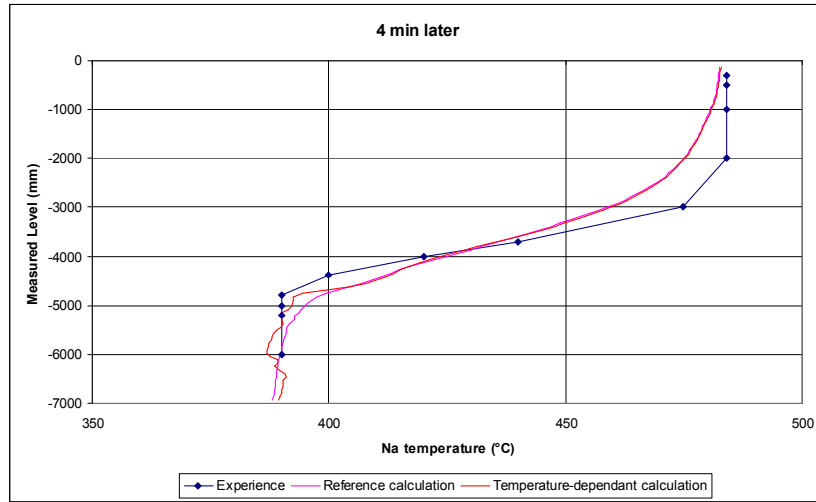


FIG. 104. Temperature profiles after 4 minutes.

(5) Further sensitivity tests

a) Treatment of turbulent temperature mixing of liquid metals

The hypothesis of the similarity of the momentum and heat transfer is justified for most fluids. The similarity is fulfilled when the Prandtl number Pr is in the order of one:

$$Pr = \nu \cdot \rho \cdot c_p / \lambda \approx 1 \quad (49)$$

The analogous hypothesis is made for the turbulent momentum and heat transfer by defining a turbulent Prandtl Number Pr_t . For liquid metals as sodium the Prandtl Number is in the order of 0.005. For fluids with such low Prandtl numbers Pr_t can be expressed by an analytical function of ν_t [30]:

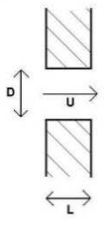
$$Pr_t = \frac{\lambda_t}{\rho \cdot c_p} = \frac{\nu_t^2}{\left(0.7 \cdot \frac{\lambda}{\rho \cdot c_p} + 0.85 \cdot \nu_t\right)} \quad (50)$$

Using this function in the reference calculation to predict the turbulent temperature transport in the upper plenum, a sensitivity calculation has been performed for the first four minutes of the pump trip. The formation of the thermal stratification did not show any modification with respect to the reference calculation.

b) Single effect study on the meshing of the Inner barrel flow holes

In order to predict the correct pressure loss of the Inner Barrel flow holes, single effect studies have been made with Trio_U. The objective was to determine for the flow holes the coarsest mesh possible which still gives in good accordance the pressure losses of single holes known from correlations. The tests are based on the pressure loss of a single, shape edged hole in a large vertical wall. The pressure loss correlation is given in Ref. [31]. The correlation as well as the associated geometry and the coefficients of the correlation are summarized in Table 20.

TABLE 20. SUMMARY OF THE PRESSURE LOSS CORRELATION OF A SINGLE SHARP HOLE IN A WALL

Correlation /d/	Geometry	Coefficients												
$\Delta P = \zeta \frac{\rho U^2}{2}$		<table border="1"> <thead> <tr> <th><i>Re</i></th> <th>ζ_0</th> <th>ε_0</th> </tr> </thead> <tbody> <tr> <td>10^4</td> <td>0.15</td> <td>2.17</td> </tr> <tr> <td>$2 \cdot 10^4$</td> <td>0.11</td> <td>2.38</td> </tr> <tr> <td>10^5</td> <td>0.04</td> <td>2.56</td> </tr> </tbody> </table>	<i>Re</i>	ζ_0	ε_0	10^4	0.15	2.17	$2 \cdot 10^4$	0.11	2.38	10^5	0.04	2.56
<i>Re</i>		ζ_0	ε_0											
10^4	0.15	2.17												
$2 \cdot 10^4$	0.11	2.38												
10^5	0.04	2.56												
$Re > 10^5: \zeta = 2.5$ $Re < 10^5: \zeta = \zeta_0 + 0.342 \varepsilon_0 \zeta'$ $\zeta' = 2.5$														

The ratio L/D is equal to 0.43 for the holes in the Inner Barrel ($D=92\text{mm}$; $L=40\text{mm}$). In the reference calculation, the flow rate inside the hole varies during the pump trip from $4 \cdot 10^{-3}$ to $4 \cdot 10^{-4} \text{ m}^3/\text{s}$ what leads to Reynolds number between $2 \cdot 10^5$ and $2 \cdot 10^4$.

Calculations with successive refinement of the meshing in the hole have shown the following accuracy of the pressure loss for 10 tetrahedral meshes per diameter, what corresponds to about 20 calculation points of the velocity for the discretisation method of Trio_U (unknowns are located on the faces of a tetrahedron):

- $Re=2 \cdot 10^5$ overestimation of the pressure loss around 20%;
- $Re=2 \cdot 10^4$ overestimation of the pressure loss around 5%.

This single effects test supports the local fine-tuning of the finest mesh within the flow holes. However, the pressure loss of the inner barrel flow holes seem to be overestimated with the coarse mesh and the fine mesh due to an insufficient fine meshing of the flow holes.

c) Rejected modifications of the geometrical modelling

In order to improve the calculated flow in the upper core structure it has been tested to replace the porosity approach of the simplified 60° model (see Section 6.2) by a complete CAD modelling strategy. It was tested to mesh the flow guide tubes, the honeycomb structure and the fingers. The resulting CAD model of the upper core structure is given in Fig. 105 for the 60° mode, where only the fingers are not shown for an improved visibility. For using this model, the limitation is not the increased total mesh number (about 15 million tetrahedrons) but the resulting time step for the transient. When respecting a mesh refinement within the flow guide tubes of about ten meshes per tube diameter, the criterion of numerical stability (Courant-Friedrichs-Lewy condition) demands time steps of about 10-5 s. It is evident that a transient of at least 600 s cannot be calculated in a reasonable time with such small time steps.

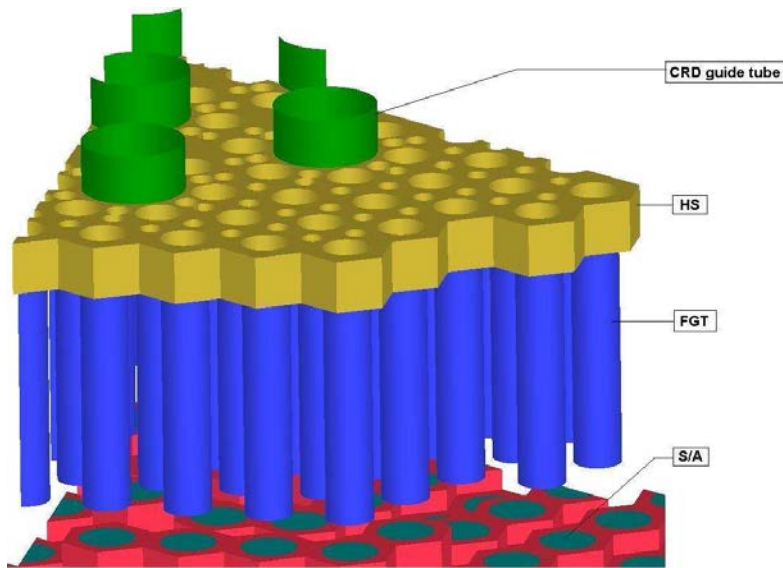


FIG. 105. Completed CAD model of the upper core structure (60° model).

7.2.3. IGCAR

(1) Thermal capacity

It may be recalled that there is significant deviation between the CFD predicted temperature distribution and the plant data, discussed in Section 7.1. Measured data indicate that stratification prevails in the hot pool for a longer duration. Also, the transient temperature gradient at the stratification interface is lower in the case of plant data. One of the possible reasons for this difference between the plant data and CFD predicted data could be the effect of thermal capacity of hot pool structures, which is not accounted in the CFD predictions reported in Section 7.1. The present section deals with an attempt to assess if the thermal capacity has any effect on the stratification characteristics. Details of the study along with input data and the thermal capacity models adopted for CFD simulations are presented in this section.

(2) Computational details

A segment of Monju upper plenum excluding fuel handling and transfer system is considered. The 60° sector of the hot pool taken for this study is depicted in Fig. 106. For studying the thermal capacity, core barrel, inner barrel, UCS, upper support plate (USP) and reactor vessel are modelled. Details of thermal capacity model are given below:

The UCS exchanges heat with sodium and it is represented by an equivalent heat capacity. The volumetric percentage of stainless steel and sodium in UCS are:

- Stagnant liquid sodium: 82.1%
- Stainless steel: 17.9%

The properties of UCS were averaged based these fractions. Sodium mass exchange between inside and outside of the UCS surface is negligible. Sodium flow from CRD assemblies into UCS through the CRD guide tubes is also negligible. The thicknesses USP, inner barrel and reactor vessel are 30 mm, 40 mm and 50 mm respectively. They are made up of SS-304 material. Heat loss through the thermal insulation of reactor vessel wall is taken to be zero.

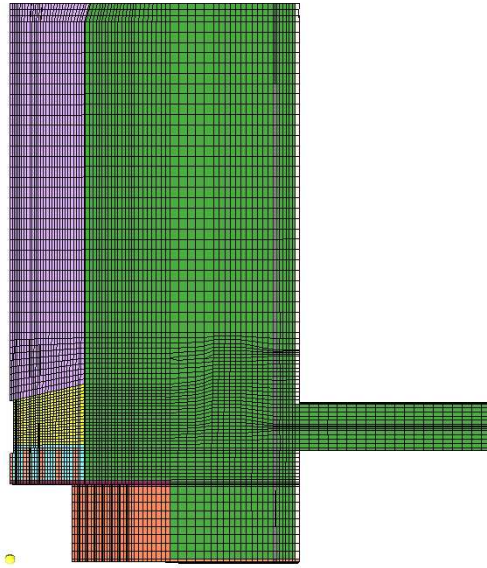


FIG. 106. Computational model accounting for the thermal capacity of hot pool structures.

(3) Steady state results

The predicted velocity and temperature distributions in hot pool at a vertical section through outlet nozzle are depicted in Fig. 106. There is an anti-clockwise recirculation region near the main body of UCS. The velocity of flow through inner barrel holes is of the order of 0.5 m/s only. The sodium between the core barrel and the inner barrel is nearly stagnant, leading to stratification. Comparing Fig. 106 with Fig. 75, it is clear that the flow pattern with thermal capacity is nearly identical to that without the capacity. That is the structural thermal capacity does not significantly affect the steady state flow field in the pool. But with thermal capacity, temperature of sodium near upper support plate is colder than that without capacity (Compare Fig. 107 and Fig. 76). This is because the peripheral sodium stream cools the core barrel.

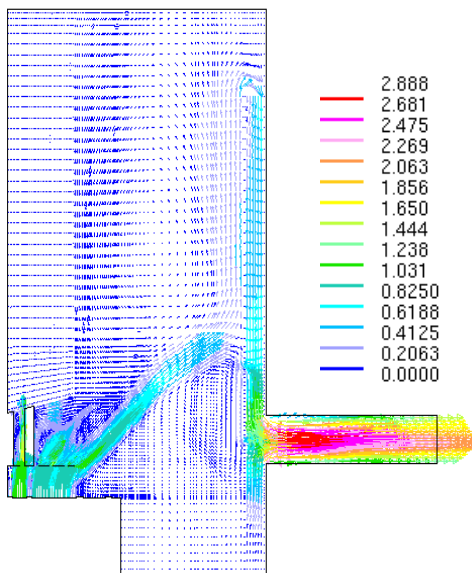


FIG. 107. Steady state velocity with thermal capacity.

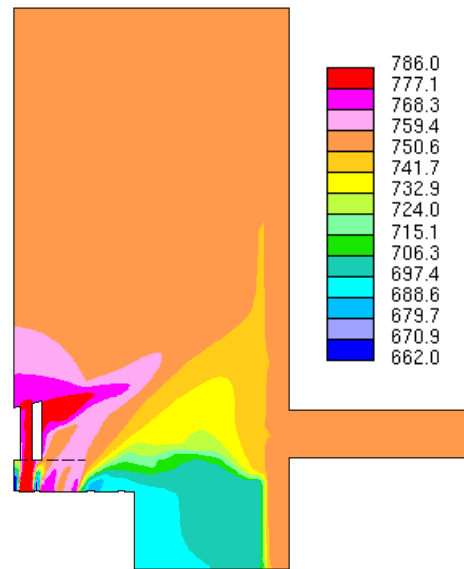


FIG. 108. Steady state temperature field with thermal capacity.

(4) Transient results

Transient calculations have been carried out for a duration of 3600 s. Predicted velocity fields in a vertical plane through outlet nozzle are depicted in Fig. 109. The corresponding temperature fields are depicted in Fig. 110. It is evident that the communication from hot pool to outlet nozzle is primarily through the holes in the inner barrel. But, there is still significant flow from hot pool to outlet nozzle via the annulus between inner barrel and reactor vessel, as evident from the temperature contours. The interface moves upwards gradually as time marches. On comparing with the corresponding results without thermal capacity effects (Fig. 77 and Fig. 78), it is clear that the thermal capacity does not significantly affect the thermal stratification characteristics.

Vertical variation of temperature along the thermocouple stack is compared in Fig. 111 and Fig. 112 for various instants. It is clear that the effect of thermal capacity on thermal stratification is only marginal.

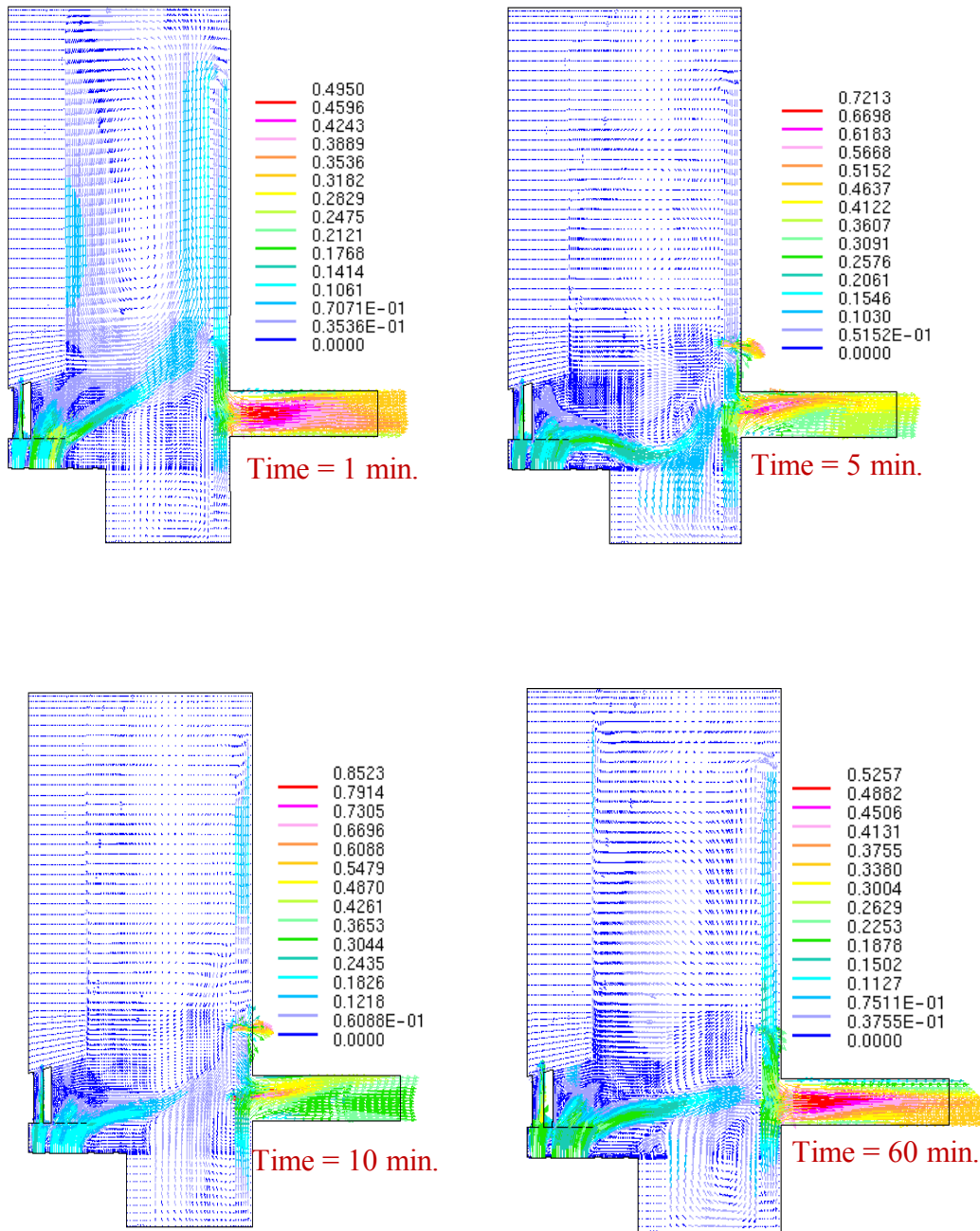


FIG. 109. Velocity vectors (m/s) at different instants with thermal capacity.

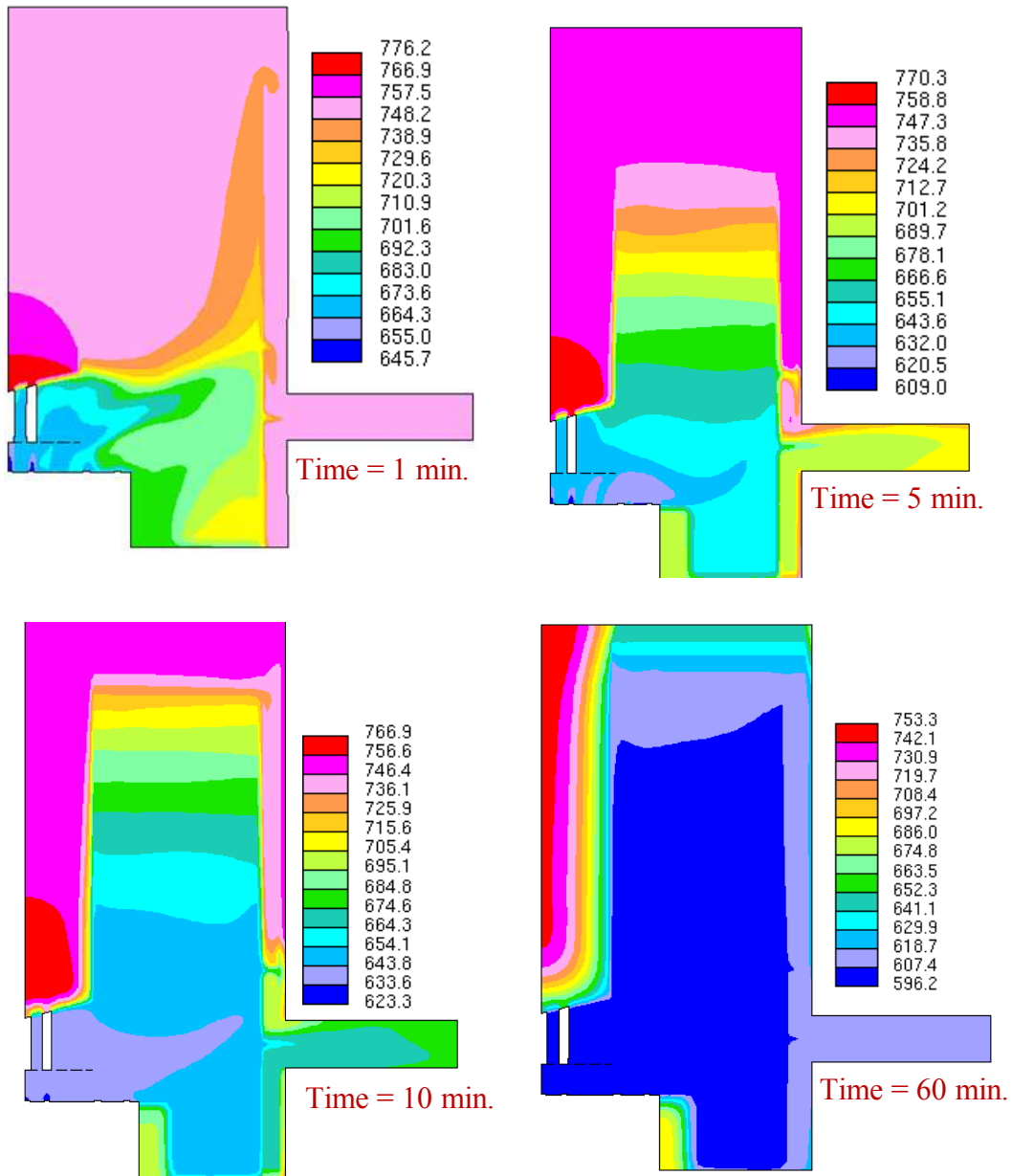


FIG. 110. Temperature contours (K) at different instants with thermal capacity effect.

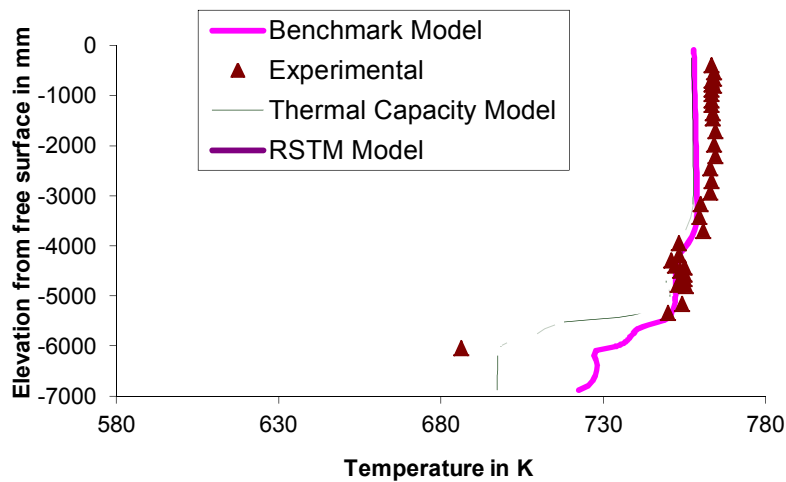


FIG. 111. Steady state thermocouple reading and CFD predicted data.

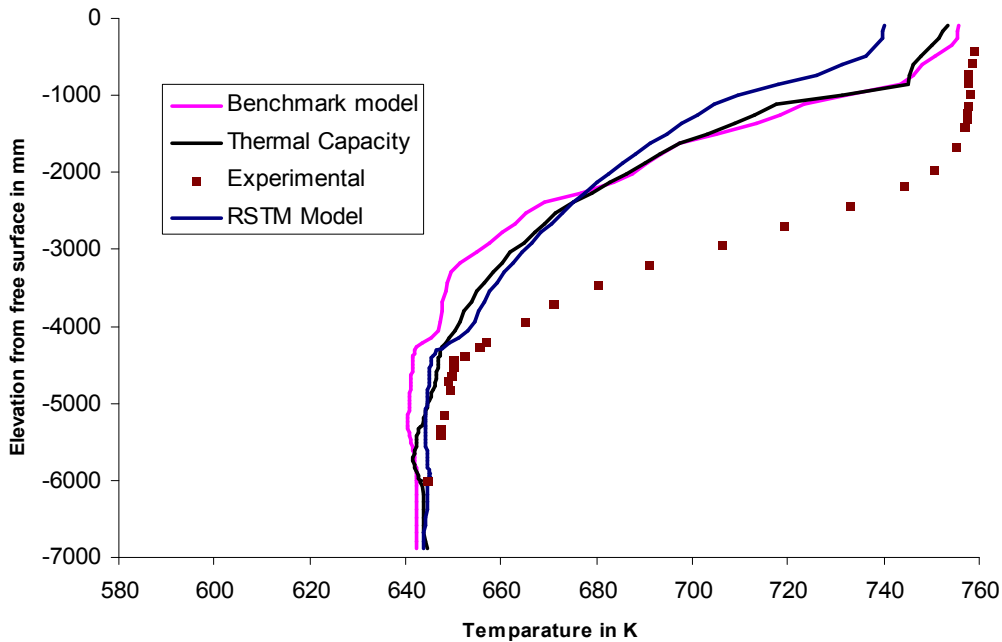


FIG. 112. Thermocouple reading and CFD predicted data at 10 minutes.

(5) Turbulence model

Turbulence model is a critical issue in CFD analysis, especially for stratified flow conditions. Most of the turbulence models have been developed mainly for forced convective flows. Identification of suitable turbulence model for buoyancy dominated flows is essential. It may be recalled that the results presented in the earlier sections are based on standard high Reynolds number $k-\epsilon$ model. In order to assess if the Reynolds Stress Model is capable of better prediction for the current situation, it has been adopted in one of the parametric studies. Other computational details are same as that of the benchmark model. The predicted thermocouple data at two instants are compared in Fig. 111 and Fig. 112 against plant data as well that predicted by the $k-\epsilon$ model. It is seen that the predictions of the Reynolds Stress Model is very similar to that of the $k-\epsilon$ model, indicating an isotropic turbulence model is adequate for the current purpose.

7.2.4. JAEA

(1) Temperature and velocity distribution in the upper plenum

A relatively high resolution mesh around the flow holes (FHs) on the inner barrel as shown in Fig. 113 was applied to case 4 in this section. The low resolution mesh used in the previous calculation (Cases 1, 2 and 3 in Section 7.1.4) is also shown in this figure in order to evaluate the FH mesh effects in steady state conditions.

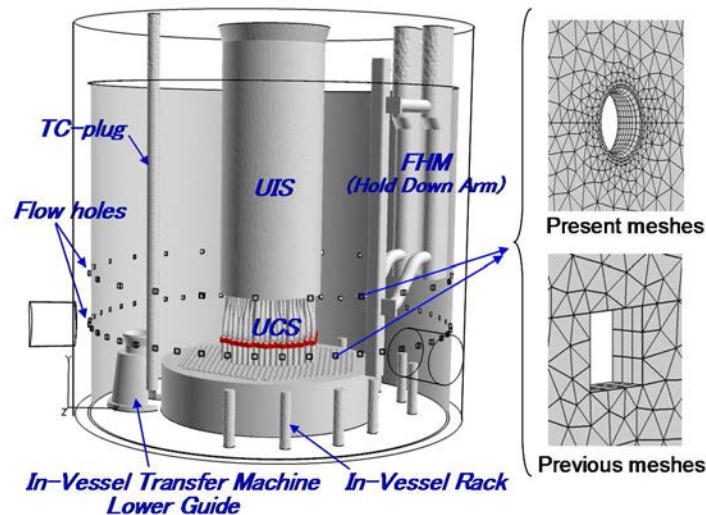


FIG. 113. Analytical model of Monju RV upper plenum.

Temperature distribution on the vertical cross section VCS-1, VCS-2 and VCS-3 are shown in Fig. 114 respectively. These temperature distributions in the upper region were similar to each other, however, those in the lower part of FHM on VCS-3 became lower than the others.

Temperature distributions on the horizontal cross section (HCS) at the different steps in the steady state are shown in Fig. 115, whose height is also shown in the upper part of Fig. 114. The velocity and temperature distributions changed in every step even after the steady state had been reached. Hence, these figures were described in every 2,000 step interval including the last calculation step, which were steps 1, 2 and 3, respectively. Temperature below the FHM became lower in every step, while that in the other region changed in the different steps. Sodium flows out obliquely upward direction to the upper area of the upper FHs of the inner barrel. From this region, the flow is divided into the upward and downward direction along the inner barrel in the region without FHM. The downward flow, which partially flows out from the two levels of the flow holes, mainly re-circulates to the core top region and mixes with colder sodium above the upper plate. In the region around FHM, however, the colder sodium cannot be mixed enough with the hotter one, since most of the jet flows in the upward direction.

The velocity distributions on VCS-2 and VCS-3 at Step 1 are shown in Figs. 116 (a) and (b), respectively. The symmetrical distributions were calculated on VCS-2 at step 1, while the slope of the jet in the left region became larger than that in the right region on VCS-3. However, the asymmetry disappeared at step 2 as shown in Fig. 116 (c). These profiles also indicate the fluctuating velocity fields in the steady state conditions

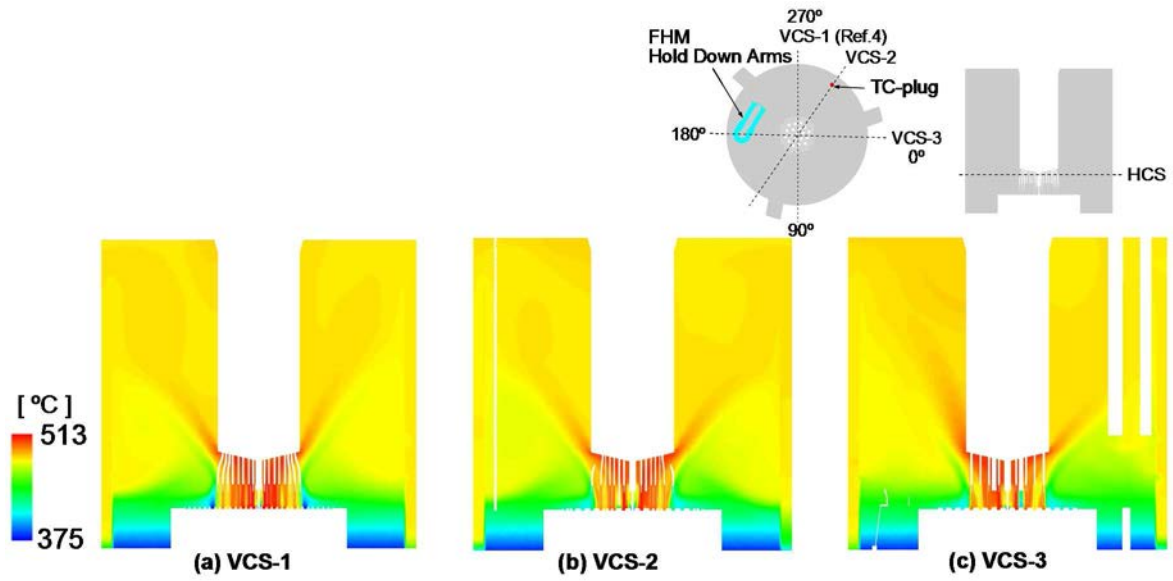


FIG. 114. Temperature distributions on VCSs.

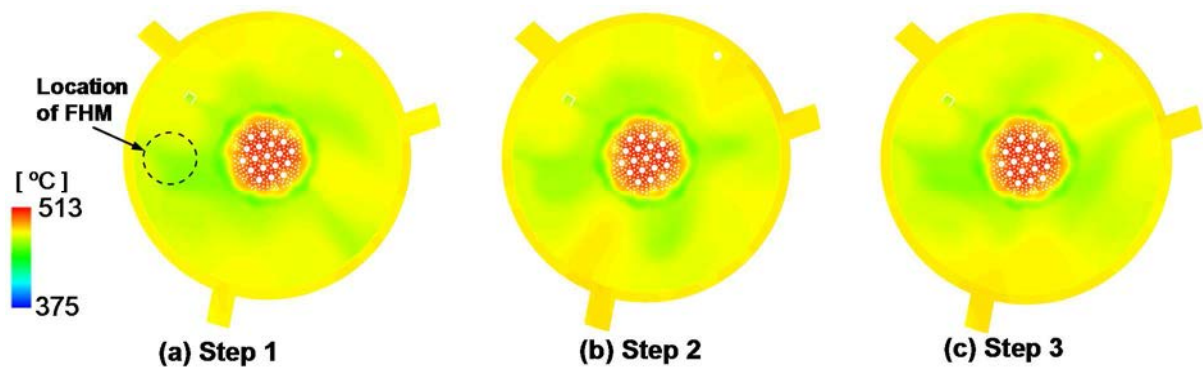


FIG. 115. Temperature distributions on HCS at different steps.

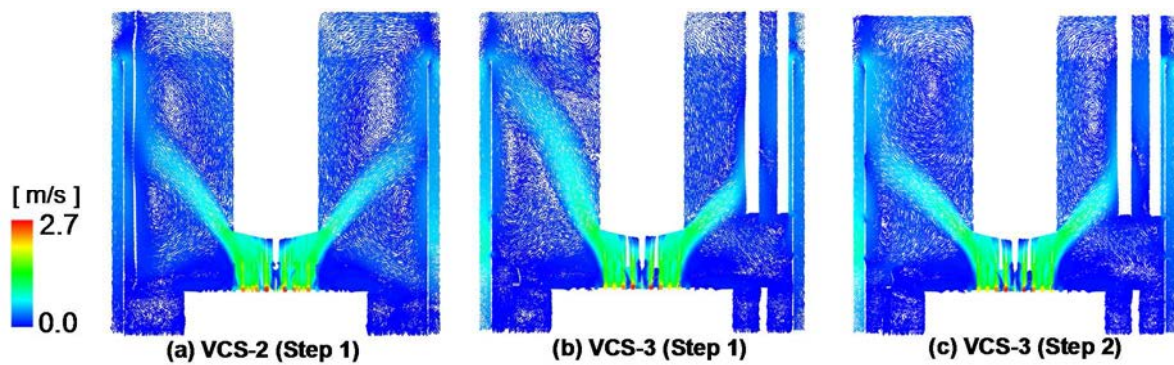


FIG. 116. Velocity distributions on VCSs at different steps.

(2) Effects of high resolution mesh around flow holes

Temperature distributions on TC-plug of these cases are shown in Fig. 117. The temperature distribution in case 4 is almost same as that in case 1; both cases have approximately 10°C

differences from the measured temperature above the UCS lower cone. The flow rates of the upper FHs were in the range from 1.2 to 2.8 kg/s in case 4, while those of the lower ones were in the range from 1.8 to 3.9 kg/s. These flow rates near RV outlet nozzles became larger than the others. It is considered that these distributions were caused by the negligible circumferential pressure drops between the inner barrel and RV wall. On the other hand, the flow rates of near-FHM flow holes became smaller than the others, since the downward flow along the inner barrel in the region near FHM became smaller than that in the other region. The flow rate in the previous calculation with rough meshes around FHs showed quite similar tendency and amounts to those in case 4, although the maximum and minimum values had some differences.

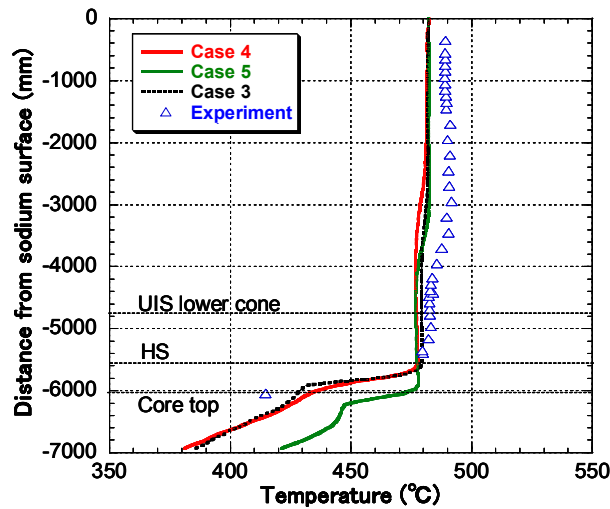


FIG. 117. Temperature on TC-plug.

The total flow rates of the upper and lower FHs in both calculations are summarized in Table 21. The percentages of the flow rates in the upper and lower FHs to the total inflow rate from the core were approximately 2.3% and 5.6%, respectively in case 4 and approximately 2.3% and 5.8%, respectively in the previous calculation. These percentages were almost equal in both results in spite of different resolution around the FHs.

TABLE 21. TOTAL FLOW RATE AND FLOW RATIO OF FHS

	Upper FHs		Lower FHs	
	Flow rate (kg/s)	Percentage (%)	Flow rate (kg/s)	Percentage (%)
Case 4	46.0	2.3	113.8	5.6
Case 3	47.3	2.3	117.2	5.8

Flow rates through all flow holes of the present full sector model and those of the 1/6 sector model by CEA [32] are plotted in Fig. 118. The 1/6 sector model was applied high resolution meshes around FHs. The results of cases 3 and 4 agreed well with those of the 1/6 sector model. In the present steady state conditions, all the percentages are so small that these differences may not largely affect to the thermal-hydraulics in the upper plenum.

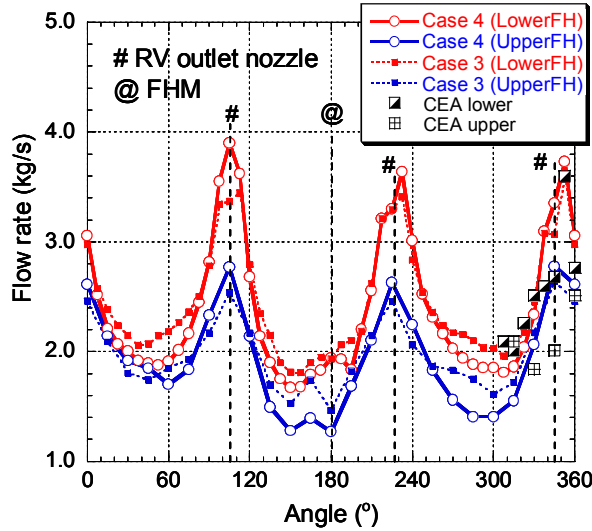


FIG. 118. Flow rate of FHs on inner barrel.

Fig. 119 shows the pressure loss coefficients calculated by Eq. (51) using above-mentioned flow rates and the pressure differences between the outside and inside of flow holes. The coefficients of the previous rough meshes are also plotted in this figure.

$$\langle \Delta P \rangle = \xi \frac{1}{2} \rho \langle u \rangle^2 \quad (51)$$

where $\langle u \rangle$ is the average velocity through a FH, $\langle \Delta P \rangle$ is the pressure difference between the inside and the outside of a flow hole with identical areas to the flow holes, and ξ is the pressure loss coefficient.

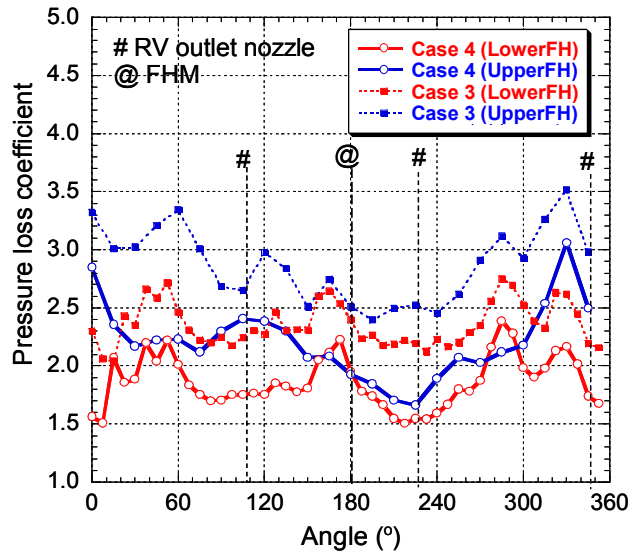


FIG. 119. Pressure loss coefficients of FHs on inner barrel.

The average coefficients of the upper flow holes and the lower ones in case 4 were approximately 2.2 and 1.9, respectively, while those in case 3 were approximately 2.9 and 2.4, respectively: The average coefficients of case 4 were approximately 30% larger than those of case 3, while flow rates of the two showed similar values. These results indicate that the coefficient becomes very sensitive because both pressure drop and velocity fluctuate at

every step in the calculations. The coefficient of 1.6 was evaluated in the mock-up tests, which was mainly for the scram transients conditions of the lower FHs.

(3) Thermal-hydraulics without flow holes on the honeycomb structure

Fig. 120 b) shows the velocity distribution of case 4 on the vertical lines described in Fig. 120 a), which shows outflow distributions in the radial direction from the UCS region. Sodium mainly flows out from the upper region of the HS, especially from the bottom of UIS: it does not flow out from the lower region. These distributions are similar to each other in the circumferential direction. In the case without flow holes on the HS (Case 5), however, the velocity in the radial direction appears below the HS and the amounts from the upper region become smaller, which are shown in Fig. 120 c). This means the transverse velocity below the HS which cannot flow into the FGTs but flow out to the upper plenum.

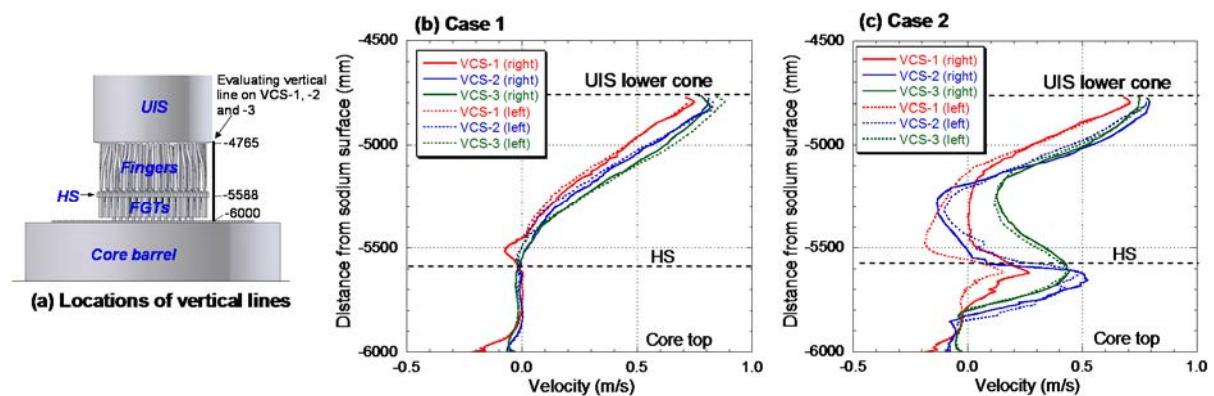


FIG. 120. Velocity distributions on vertical line along HS.

The velocity and temperature distributions on VCS-3 are shown in Fig. 121 a) and b), respectively. The slope of the jet in case 5 becomes smaller than that in case 4 and the temperature around the core barrel become higher. Colder sodium flowed out from the neutron shielding and blanket subassemblies mixed directly with hotter sodium, and flowed out from the lower region of HS. Eventually, the mixture was transported to the core side region. These temperatures on TC-plug also became higher than measured temperatures as shown in Fig. 117. From the results shown above, it becomes clear that the proper estimations of the pressure loss coefficients on the HS are also important because the coefficients affect the thermal-hydraulics in the upper plenum.

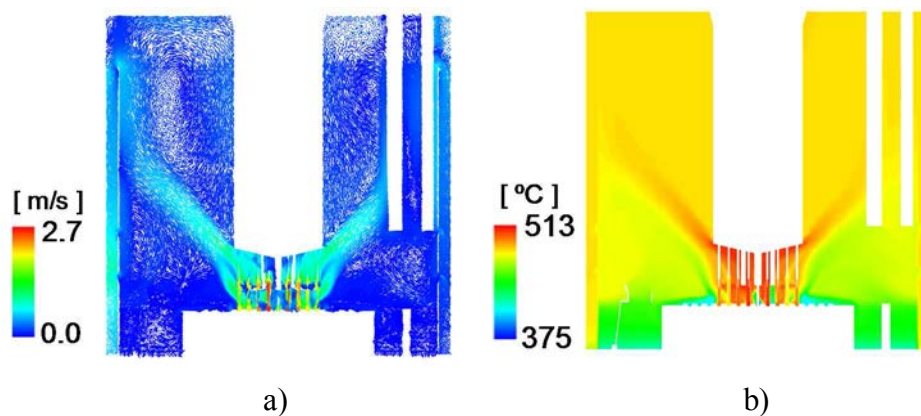


FIG. 121. Velocity and temperature distributions on VCS-3 without FHs on HS.

7.2.5. University of Fukui

(1) Problem of boundary conditions

The total flow rate from each group of subassemblies specified in the IAEA benchmark calculation is approximately 97% of the measured flow rate at the Monju plant. This discrepancy was identified when the test data by Miyakawa was investigated [33]. When we calculate the mixing temperature on the basis of boundary conditions provided by IAEA using the following equation,

$$T_m = \frac{\sum N_i w_i C p_i T_i}{\sum N_i w_i C p_i} \cong 482(^{\circ}\text{C}) \quad (52)$$

where T_m stands for mixed temperature ($^{\circ}\text{C}$), T_i for the inlet temperature ($^{\circ}\text{C}$), N_i for the number of channels, w_i for the mass flow rate (kg/s), $C p_i$ for the specific heat (J/kg/K), i for the channel group. The mixing temperature is approximately 482 $^{\circ}\text{C}$ which is lower than the measured temperature near the liquid surface.

The outlet temperatures from each subassembly groups in the IAEA benchmark are measured results except that for the shielding subassemblies. Therefore, the boundary conditions for the IAEA benchmark are somewhat hybrid (combination of calculated and measured data), and resulting in the lower simultaneous mixing temperature than measured one. The total amount of energy input into the upper plenum is underestimated if the total flow rate does not include some other flow rate.

In order to maintain consistency of the boundary conditions from the point of view of the amount of energy transferred into the upper plenum, a 1D analysis has been conducted using the NETFLOW++ code developed by Mochizuki [34]. This code has been validated using the various plant data measured at Monju. The plant calculation model using NETFLOW++ code is illustrated in Fig. 122. This model consists of the primary heat transport system (HTS), secondary HTS and water loop which includes a high-pressure turbine and high-pressure feed water heaters. The low-pressure system is assumed by the boundary conditions. The total flow rate in the table shows the targeted flow rate at 45% thermal power. Bypass flows from the high-pressure plenum and the low-pressure plenum are added and are modelled as a total flow rate in channel 11. After the steady state situation was established, the reactor trip and pump coast-down processes are calculated first, and then the forced circulation by a small capacity motor is calculated continuously. The calculated flow rates and temperatures at the outlet of the subassemblies shown in Fig. 123 are given to the CFD code as boundary conditions. The outlet temperatures from each group of subassemblies are predicted within 10 K and the flow rate in the B-loop shows good agreement with the measured data. The flow rates in the A-loop and C-loop are almost the same as that of B-loop, and these flow rates are predicted with the same accuracy. In the following analysis, the NETFLOW++ results are used as boundary conditions, replacing the boundary conditions provided in the IAEA benchmark.

(2) Effect of flow-hole configuration on temperature distribution

It was easily estimated that the configuration of the flow-hole has a considerable effect on the discharge flow rate. Therefore, the sensitivity study was conducted.

Fig. 124 shows the comparison between two calculations under the different flow-hole configurations. The height 0 stands for the liquid sodium surface. The parameter in the legend

shows time after the transient. The character ‘S’ stands for flow-hole with straight edge, and ‘C’ stands for flow-hole with chamfer. Since three calculated results at the same height where three thermocouples are installed are plotted in the same figure, the calculated results have widths. It is obvious from the comparison that the analysis with chamfer results in a lower thermal stratification interface. The interface is lowered by approximately 300 mm at 600 seconds after the start of the test. If the edge has curvature, height of the thermal stratification interface will be much lower. Therefore, much precise meshing around the flow-hole is required to trace the height of the thermal stratification if the flow-hole has the round edge.

Fig. 125 shows the comparison of calculations between the basic case and the result taking into account chamfer and heat capacity of the UIS. The character ‘C+HC’ stands for flow-hole with chamfer and heat capacity of the UIS. It is assumed that the UIS consists of steel and sodium with no flow. As shown in the figure, the interface at 600 seconds is lowered by 500 mm compared with the basic case. Therefore, the effect of the heat capacity of the UIS on the interface cannot be neglected.

(3) Preliminary result

A comparison between the test result and the simulation is illustrated in Fig. 126 when the above mentioned effects are reflected in the analysis. The calculated results trace the rising of the thermal stratification interface in general. However, the height of the thermal stratification interface is calculated lower before 240 seconds, and the thermal stratification interface is calculated higher than the test result after 420 seconds. Especially, the thermal stratification interface is higher than the experimental result by approximately 1.0 m at 600 seconds. This result prospects that the good result would be obtained if the flow-hole configuration is correctly reflected to the analysis.

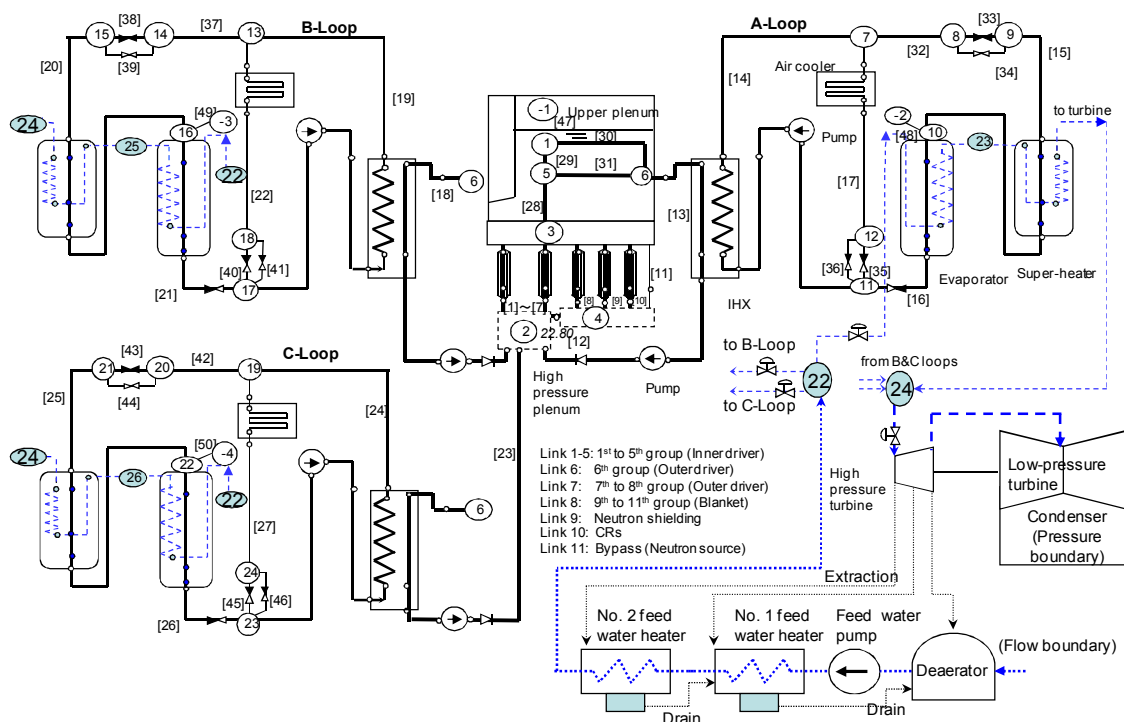


FIG. 122. Plant transient calculation model with 1D NETFLOW++ code.

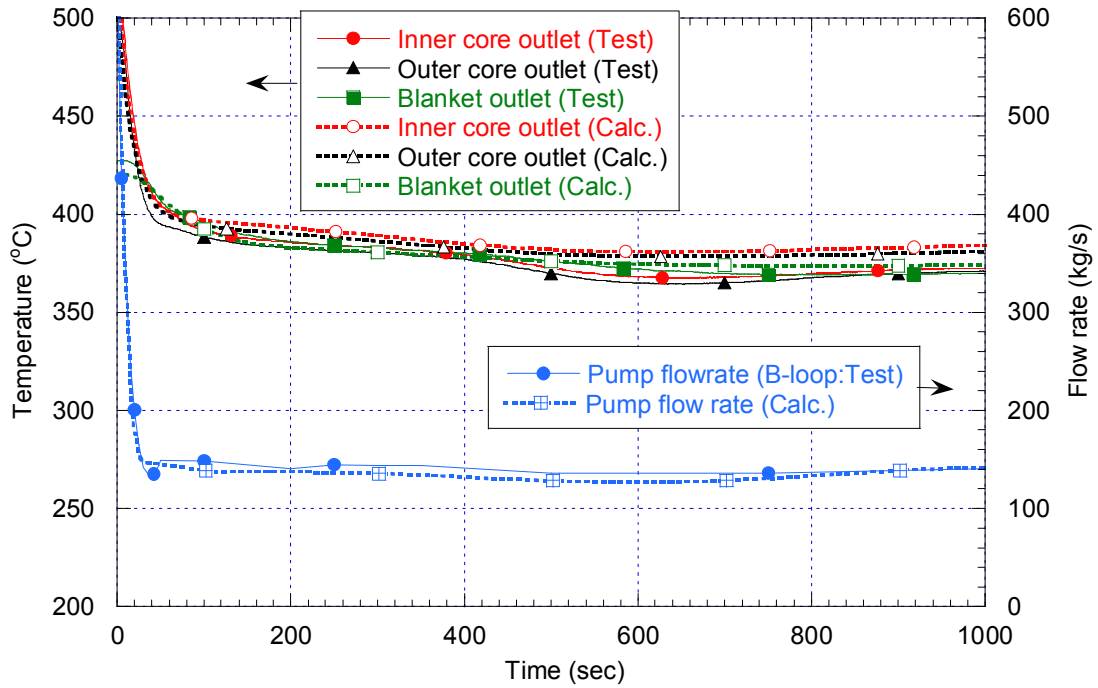


FIG. 123. Results from the NETFLOW++ analysis: outlet temperature of relevant subassemblies ('Test' and 'Calc' respectively), and the pump flow rate ('Test' and 'Calc').

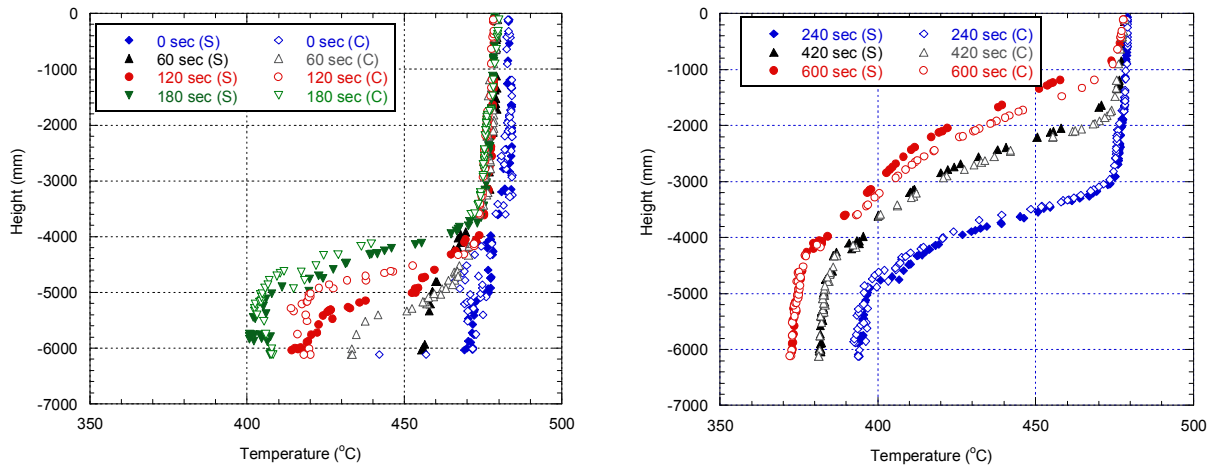


FIG. 124. Comparison between calculated results for flow-hole with straight edge (basic case) and for flow-hole with chamfer.

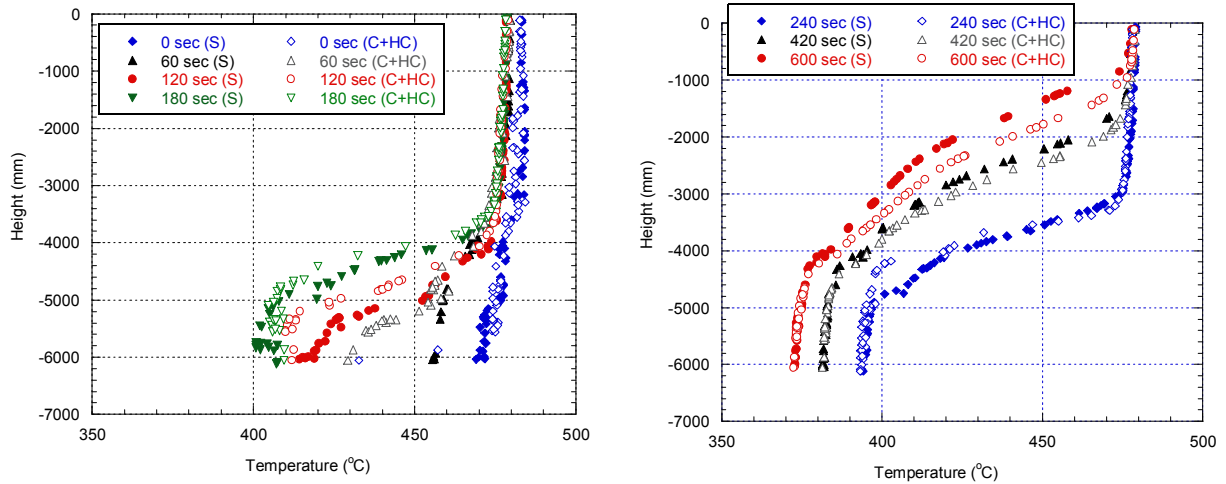


FIG. 125. Comparison between calculated results for flow-hole with straight edge and for flow-hole with chamfer.

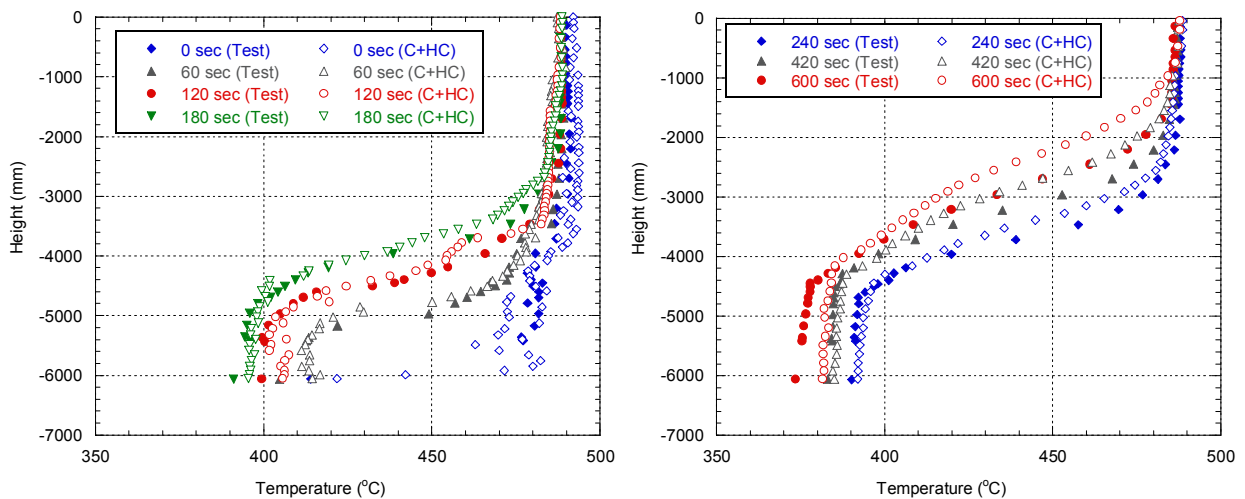


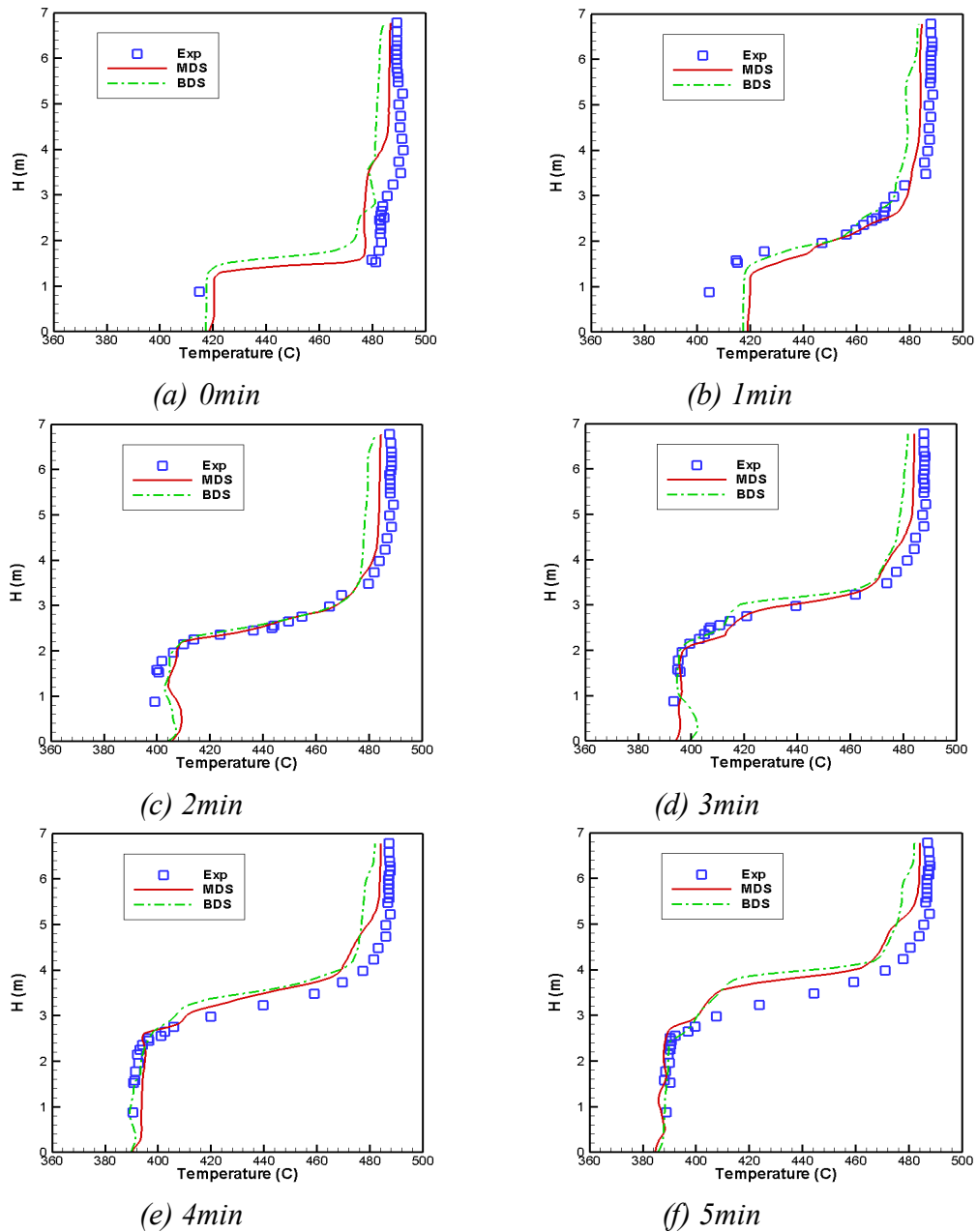
FIG. 126. Comparison between measured results and calculation taking into account the flow-hole with chamfer, heat capacity of UIS and boundary conditions at the outlet of the subassemblies.

7.2.6. KAERI

During the steady-state simulation, it was found that dual solutions exist depending on the initial guess. The buoyancy dominated solution (BDS) was obtained when the initial guess was imposed with zero velocity and a constant temperature and pressure. The momentum dominated solution (MDS) was obtained when the initial guess was imposed by a separate numerical solution, which was calculated without a buoyancy term and with a lower-order convection scheme. It is noted that Bieder et al. (2011) also found this phenomenon. They observed that the momentum dominated solution is obtained when the numerical grids is coarse and the lower-order convection scheme is used for calculation, while the buoyancy dominated solution is obtained when the numerical grids are fine and the higher-order convection scheme is used. It is not clearly understood why such dual solutions exist in the numerical solution and behave quite differently. In the common sense the inertia force will be dominant over the buoyancy force in the steady-state normal operation. The previous

experimental and numerical works also advocate that the momentum dominated solution is a correct solution.

Fig. 127 shows the predicted transient temperature profiles along the thermocouple tree together with the experimental data for both solutions. The difference between the two solutions is minimal. It is observed that the predicted temperature profiles agree very well with the experimental data until 5 minutes. However, the predicted results deviate greatly from the experimental data at 10 and 15 minutes. This is due to the use of an inadequate thermal turbulence model in the present calculation.



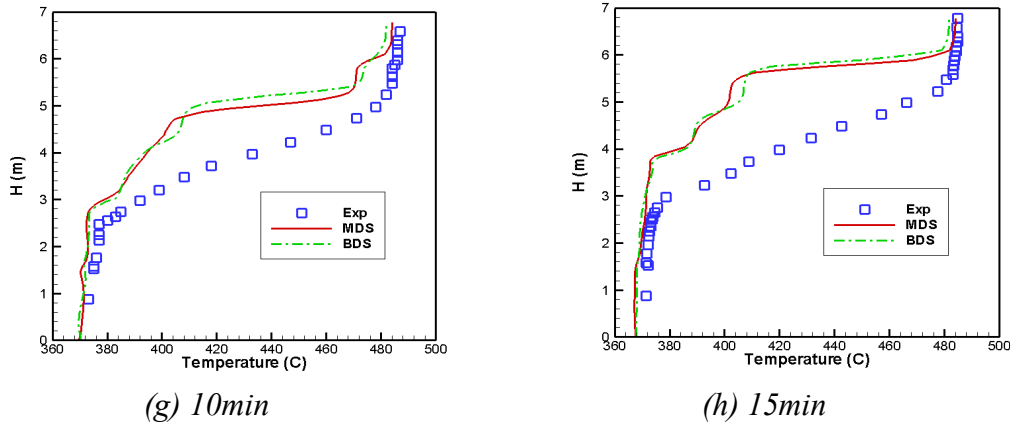


FIG. 127. Temperature profiles along the thermocouple tree during the transient calculations.

7.2.7. IPPE

(1) Parametric study of the influence of total reactor sodium flow on flow pattern in upper plenum

Parametric study was performed using 2-D R-Z computational model of upper plenum. Axial and radial finite-difference mesh were chosen the same as it was used in 3D model but the rows of holes and the outlet pipe were presented as a slots with equivalent cross-sections. The set of steady state calculations were performed (18 different cases in total). The following parameters are varied:

- Total flow through the plenum in the range $G=(0.4 - 2.0) G_0$, where G_0 is a total flow in the ‘NC-test’;
- Flow pattern taken as initial approach for the case.

The sequence of calculations of all cases is shown on Fig. 128. Calculations were started from case 1 at which the total flow was two times larger than flow in ‘NC-test’ and well pronounced ‘jet flow mode’ was calculated by code. Then the steady state flow and temperature distributions were taken as initial approach and cases from 2 to 9 were calculated with the same initial approach but decreasing from case to case the total flow. For cases from 1 to 7 ‘jet flow mode’ was invariably observed but after transition to the case 8 ($G=0.6 G_0$) flow pattern in the plenum was changed and ‘ascending flow mode’ was realized (Fig. 129 a)). Then the steady state flow and temperature distributions calculated in case 9 were taken as initial approach for next series (cases from 10 to 18) with increasing the total flow from case to case. The result of calculations, shown in Fig. 129 b) was that ‘ascending flow mode’ was observed up to the transition from case 17 ($G=1.7 G_0$) to case 18 ($G=1.8 G_0$).

The conclusion is that in the flow range $G=0.7-1.7 G_0$ the problem has two solutions and what solution of that two is realized depends on specified initial approach.

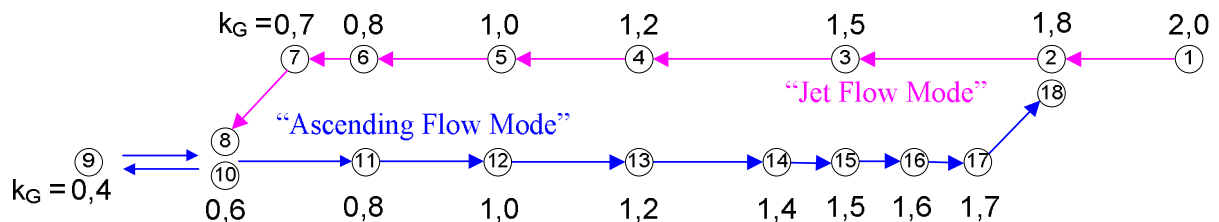
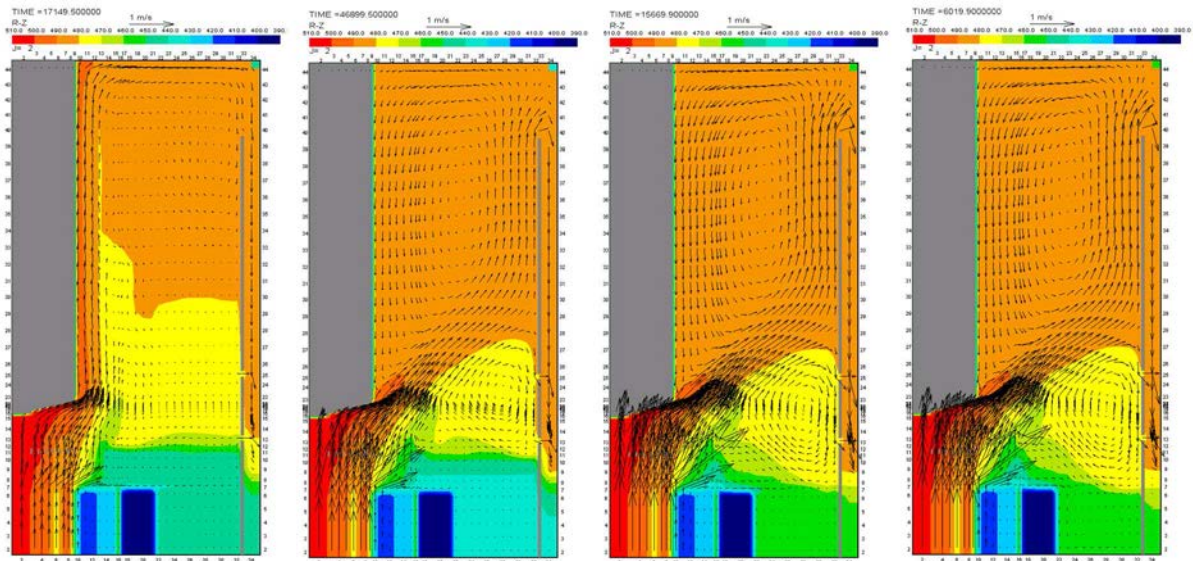


FIG. 128. Diagram that illustrates the sequence of calculations of different cases

① - Case number, ($k_G=G/G_0$)



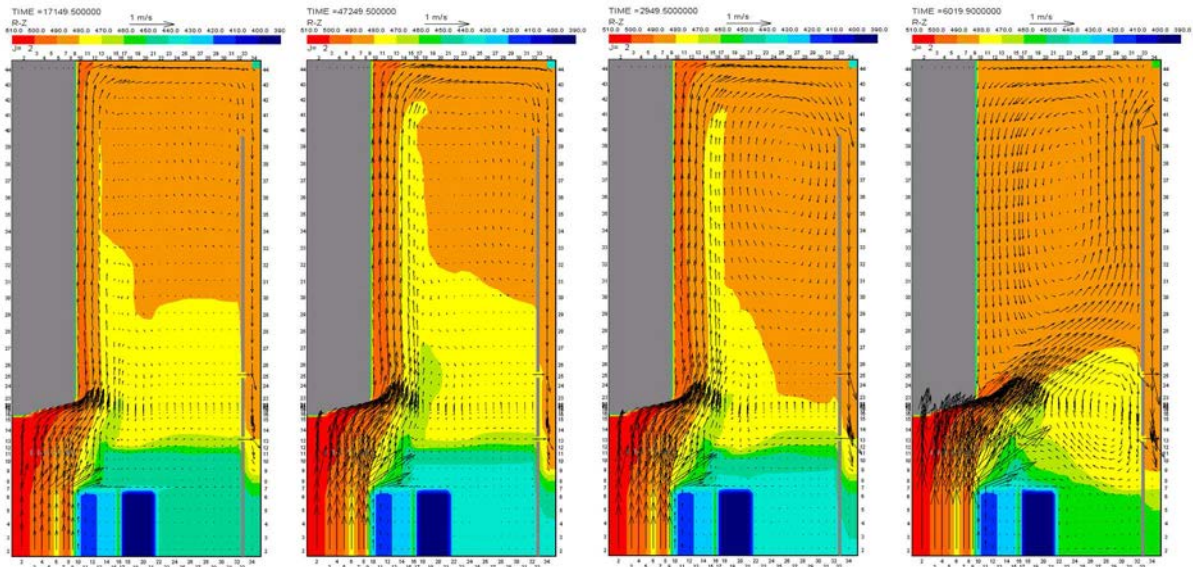
$k_G = 0,6$

$k_G = 1,0$

$k_G = 1,5$

$k_G = 1,8$

a) Initial approach: 'jet flow mode'



$k_G = 0,6$

$k_G = 1,0$

$k_G = 1,5$

$k_G = 1,8$

b) Initial approach: 'ascending flow mode'

FIG. 129. Steady state velocity and temperature distributions for cases differing by total flow ($k_G=G/G_0$).

(2) Influence of heat exchange with cold plenum (through support plate)

For analysis of the influence of heat exchange with cold plenum it was assumed that:

- The thickness of support plate is equal to 0,05m;
- Sodium temperature in the 'cold plenum' is 400°C.

Calculations of steady state temperature distributions in the Monju plenum for the parametric case for which heat losses through support plate were taken into account were performed and

the results were compared with base case. The influence of heat losses is still visible in the cavity adjoining to support plate but this effect is negligible in the upper plenum as a whole (Fig. 130).

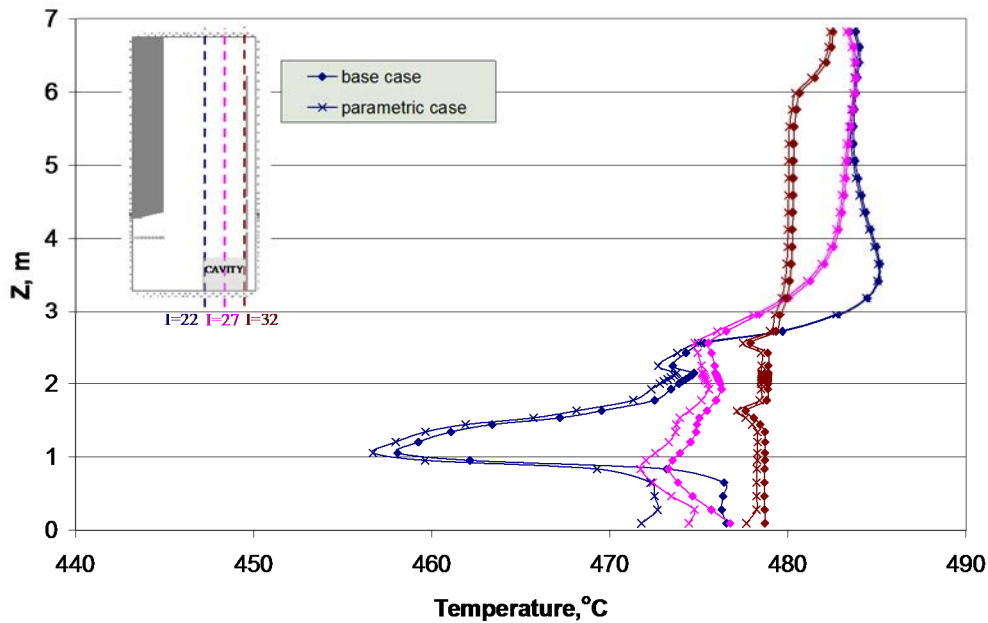
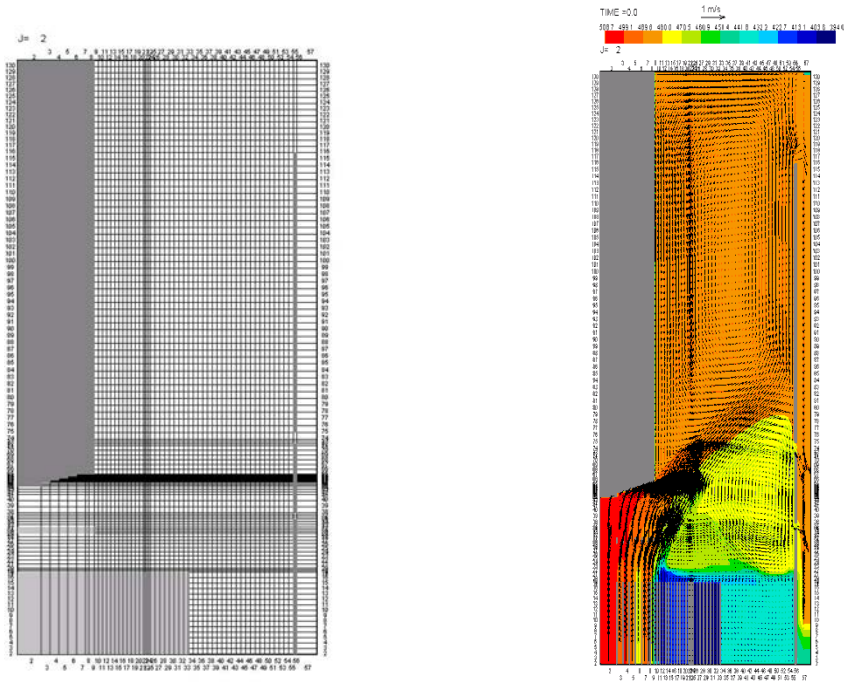


FIG. 130. Axial profiles of sodium temperature calculated with and without considering the heat losses through support plate.

(3) Effect of mesh refinement

Mesh size of space discretization could effect on accuracy of calculations of temperature profiles in the upper plenum. For analysis of that influence the calculation of steady state velocity and temperature distributions for two cases were performed:

- Case 1 – 2D - with finite-difference (R*Z) mesh - (34*44);
- Case 2 – 2D - with finite-difference (R*Z) mesh - (57*130). Calculative domain and calculated velocity and temperature fields for case 2 are shown on Fig. 131 a).



a)

b)

FIG. 131. (a) Calculative domain, (b) Velocity and temperature distributions for initial steady state, (Mesh - 57*130).

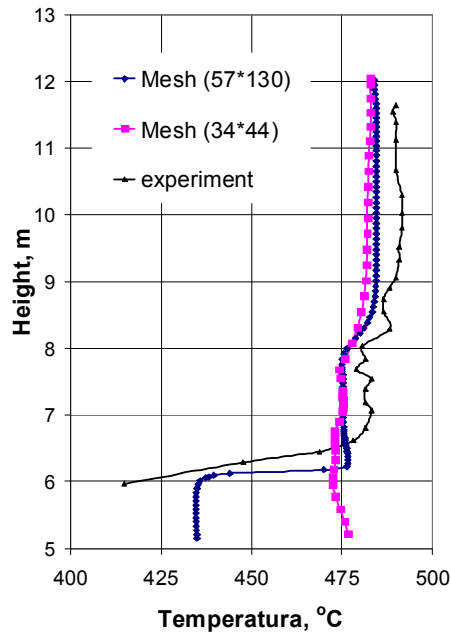


FIG. 132. Axial profiles of sodium temperature at T-pole position at initial steady state.

The comparison of calculated temperature profiles with experiment is made on Fig. 132. The conclusion is that after mesh refinement temperature in the bottom part of the plenum where the most pronounced temperature gradient is observed decreases from 476°C to 435°C and became much closer to experimental value 415 °C.

(4) Effect of thermal conduction of inner barrel

Temperature of sodium washing internal and external surfaces of inner barrel can be different especially during the transient and one can assume that heat transfer through the inner barrel due to conductivity can effect on sodium temperature distributions in its vicinity. Final analysis of this effect was carried out with improved 3D GRIF calculative model. One of representative parameters that characterizes the transient as a whole and the rate of temperature redistribution in the upper plenum is the total duration of stage when stratification is still observed. The duration of that stratified stage (DSS) in the test is 7200-7400 seconds (Fig. 133).

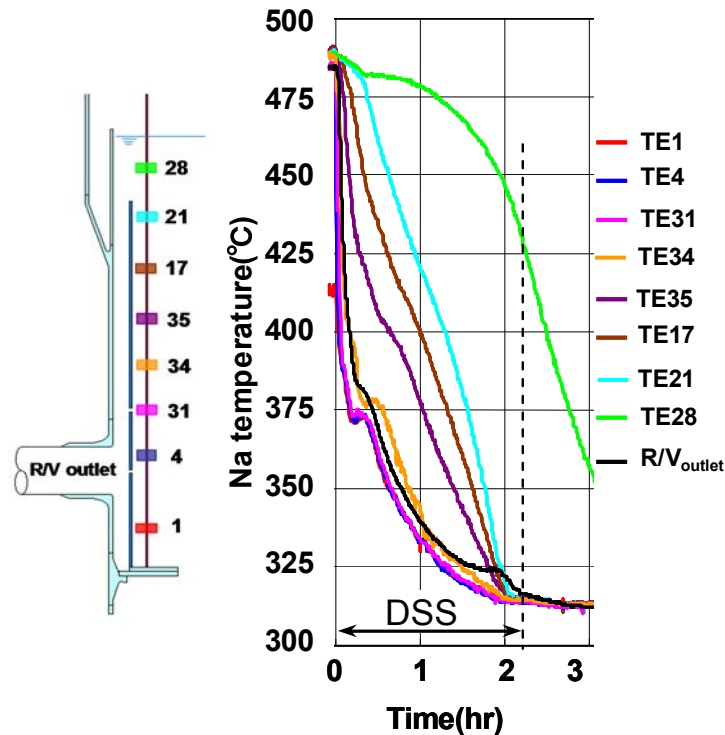


FIG. 133. Monju test, thermocouple readings versus time.

The heat conductivity of the inner barrel was varied in the range 20–50 W/(m·s) which covers variation of conductivity for typical stainless steels. The set of transient calculations with different heat conductivity of the inner barrel was carried out and the dependence of DSS versus heat conductivity λ was obtained (Fig. 134).

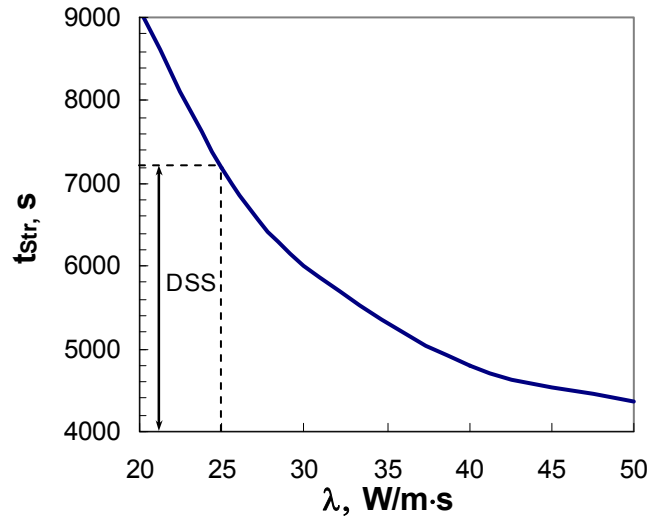


FIG. 134. Duration of stratified stage (DSS) versus heat conductivity of the inner barrel.

The conclusion from that sensitivity study is that the rate of flow and temperature redistribution in the upper plenum during the test is rather sensitive to heat exchange between sodium in the upper plenum and sodium flow in downcomer. This means that heat conductivity of the inner barrel and heat transfer coefficients on its inner and outer surfaces should be accurately calculated.

(5) Influence of pressure loss coefficient of the holes in the inner vessel on transient temperature distributions in the plenum

One more uncertainty could be related to calculation of pressure loss coefficient of the holes in the inner barrel. Empirical correlation for this coefficient is well known if the flow is perpendicularly directed to the wall but in our case the sodium flows angularly and the angle is changing versus time and position. The results of sensitivity study are presented on Fig. 135.

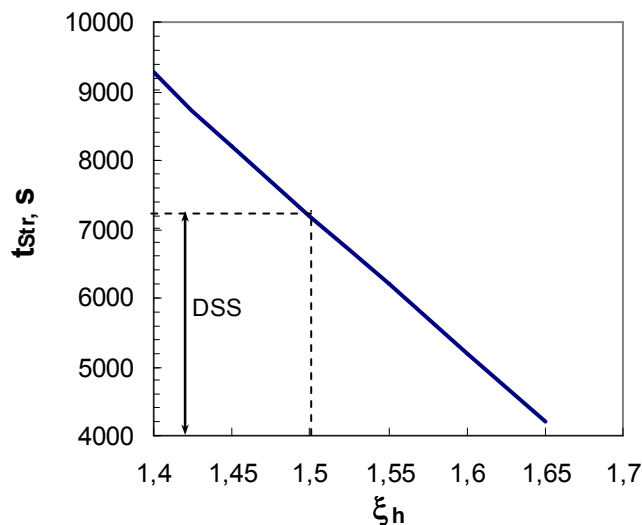


FIG. 135. Duration of stratified stage (DSS) versus pressure loss coefficient of the holes in the inner barrel.

It is clear from data on Fig. 135 that duration of stratified stage is extremely sensitive to pressure loss coefficient of the holes. The increase of the last only on 10% results in almost 2 times acceleration of temperature front movement along the plenum height. Therefore special attention should be paid to the simulation of pressure losses in the holes in the inner barrel.

7.2.8. ANL

The steady-state calculations at ANL predict about 5°C cooler sodium temperature in the upper portion of the reactor vessel (above the core outlet level) than the experimental data. Since most of sodium coolant in the upper plenum above the elevation of the holes on the inner barrel is at that temperature, this discrepancy corresponds to either an underestimation of flow through the bypass holes or about 4% uncertainty in energy balance for measured core flow or power during the initial steady-state conditions. In order to better understand this discrepancy, the importance of inner barrel holes to provide a bypass flow path for colder sodium (leaving the sodium hotter in higher elevations) was evaluated using an alternative model with blocked holes. As shown in Fig. 136, the model with blocked inner barrel holes shows a similar temperature distribution, confirming the conclusion that the influence of holes is negligible at steady-state with full-flow. However, it does not rule out the possibility of greater bypass flow than what is predicted with the CFD model.

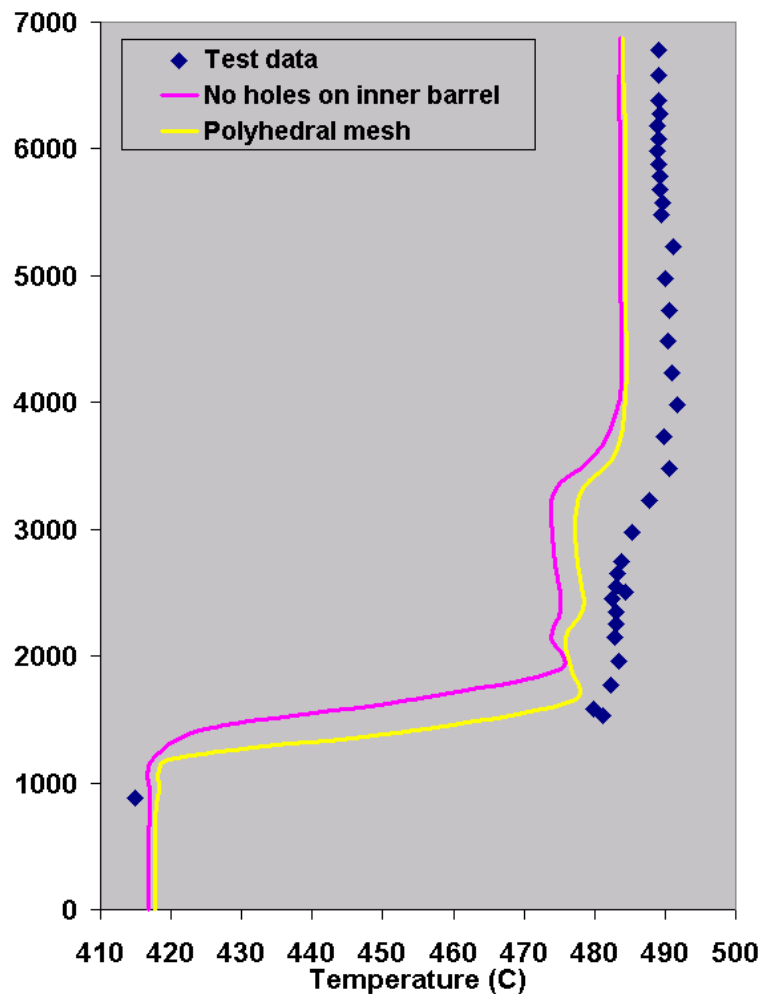


FIG. 136. Comparison to assess the effect of inner barrel holes at steady-state.

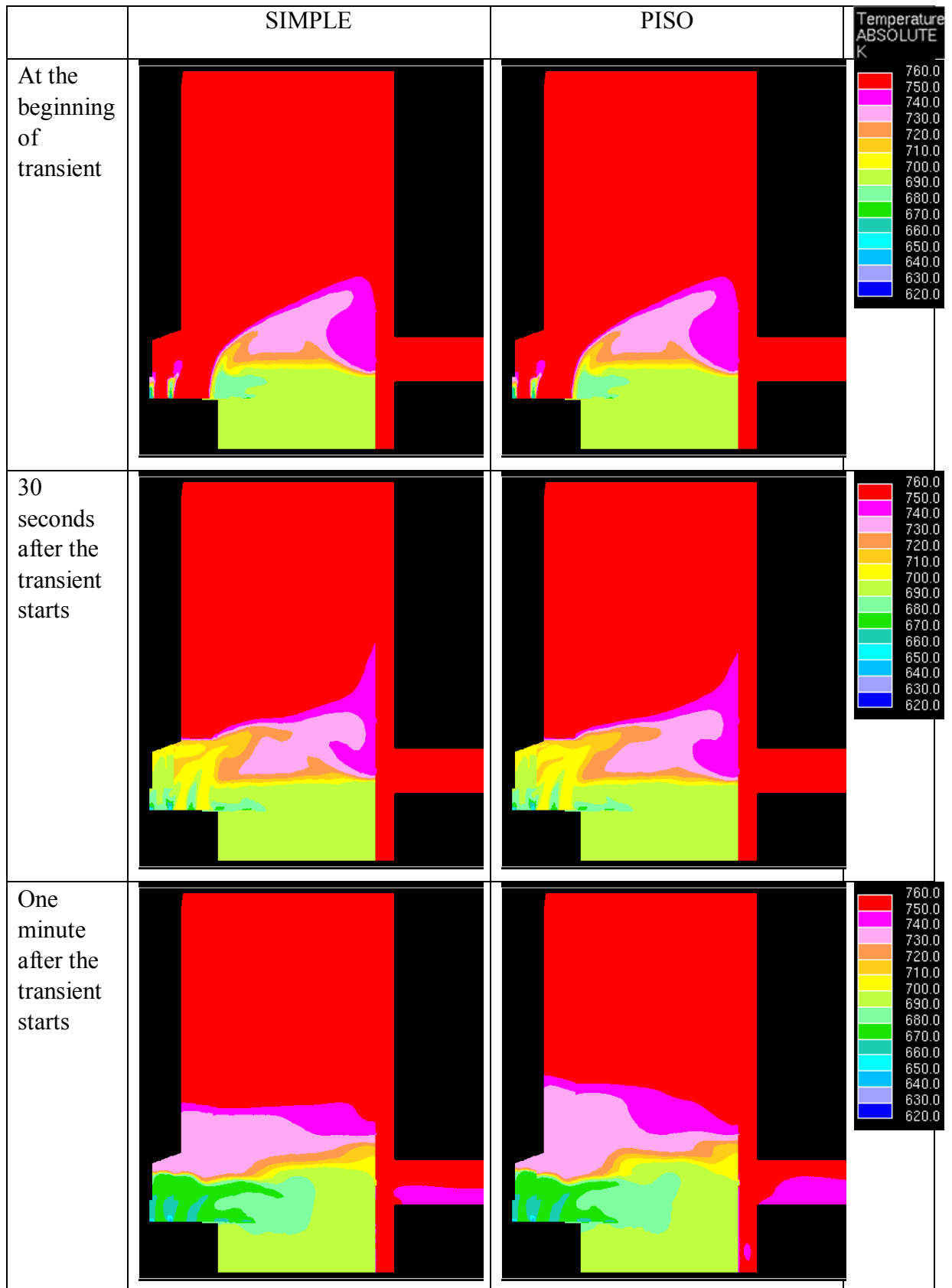
Although a similar degree of agreement between ANL predictions and test data prevails during the first few minutes of the transient, comparisons using the reference CFD model described in Section 7.1 indicates large discrepancies after the first few minutes of the transient, especially above the elevation of the holes on the inner barrel. While the test data shows that the thermal stratification persists in the upper plenum for well over an hour, the simulations suggest fairly uniform sodium temperature in the entire upper plenum after 15 minutes into transient.

In order to eliminate the transient solver option as the potential source of discrepancy, the first ten minutes of the transient calculations are repeated with the PISO predictor-corrector scheme. The temperature contour plots on the symmetry plane through the outlet nozzle calculated with both SIMPLE and PISO transient solver options are compared in Fig. 137 during various stages of the transient. The relative consistency of the solutions with SIMPLE and PISO schemes in Fig. 137 eliminates the transient solver option as the potential source of discrepancy between the calculations and the experiment.

To assess the impact of turbulence modelling on the mixing, two extreme case simulations are also performed at ANL: one using a small constant value for the turbulent viscosity, and another with laminar flow. As expected, the case with small constant value for turbulent viscosity does not differ much from the earlier predictions since the impact of turbulent mixing dies down once the primary pump stops and turbulence dissipates. Although the laminar flow solution exhibits convergence problems, it is more or less consistent with the solutions using turbulence models and does not address the observed discrepancies.

The impact of stored heat in the upper core structure and the stagnant sodium above the dip plate is also evaluated using a constant temperature (755 K) boundary condition at those surfaces to exaggerate these effects. However, these changes in the boundary conditions did not extend the thermal stratification in the upper plenum significantly to explain the discrepancy with experimental data. Finally the cross code comparison between STAR-CD and STAR-CCM+ codes using the same mesh structure and almost identical CFD models (material properties, boundary conditions, and solver options) resulted almost identical thermal stratification patterns, failing to explain the discrepancy between the calculations and test results.

As suggested by IPPE analyses, the most plausible explanation of the discrepancies between the calculations and test data is that the bypass flow through the holes on the inner barrel is underestimated in the CFD model. In Monju design, these holes provide alternative flow paths between the core outlet and outlet nozzle. These alternate flow paths are especially effective in bypassing the thermally stratified region of the upper plenum following a reactor shutdown (to facilitate natural convection to cool the core). If the bypass flow is greater than what is predicted in the simulations, it could account for a larger fraction of the primary system flow both before and after the turbine trip, leaving the bulk of the sodium coolant in the upper plenum (above the holes on the inner barrel) stagnant for a longer period of time.



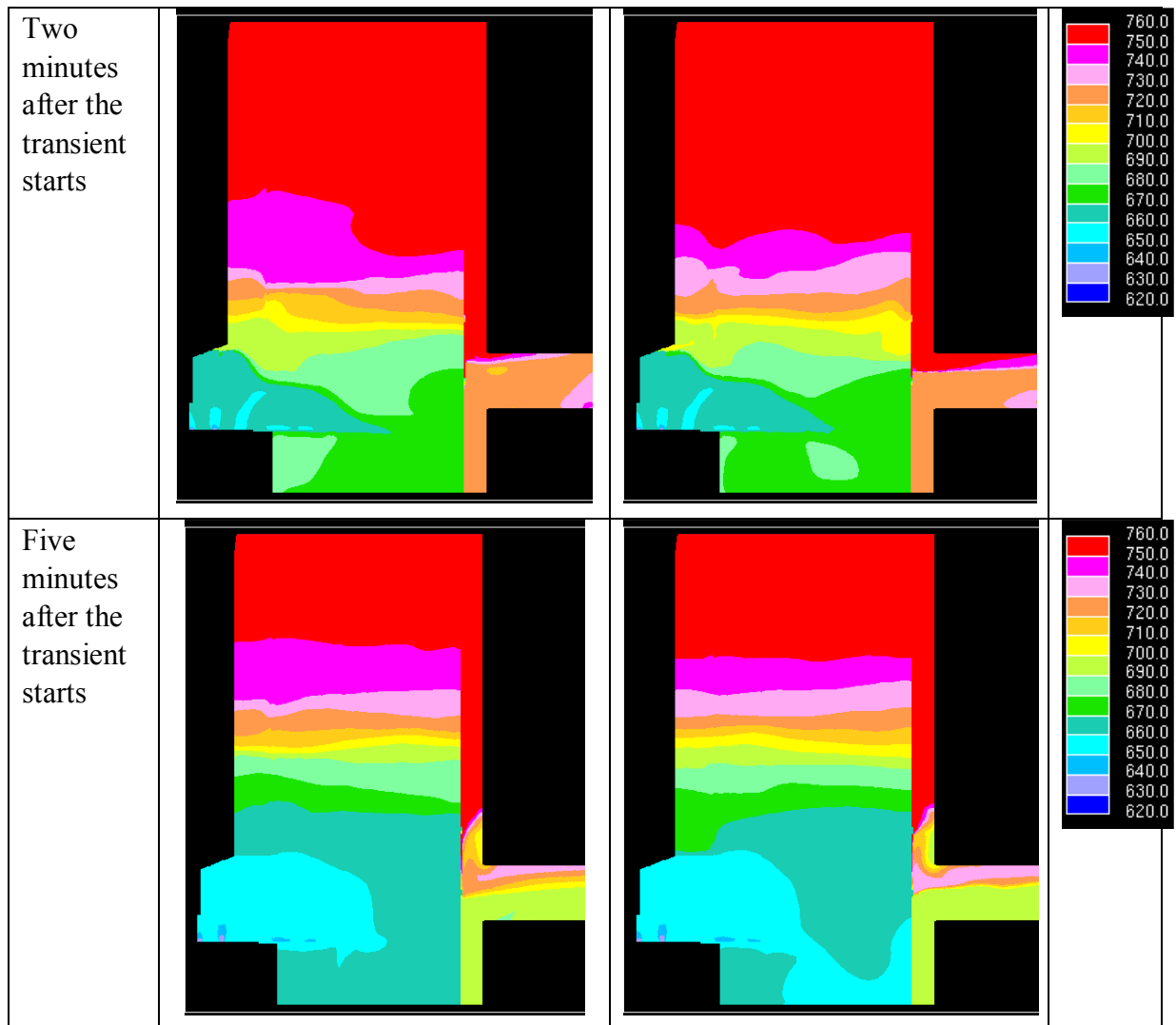


FIG. 137. The temperature contour plots on the symmetry plane through the outlet nozzle for various stages during the transient calculations.

Since the holes in the simplified model described in Section 6.1 are represented explicitly based on the benchmark specifications provided by JAEA (with a given diameter and inner barrel thickness), the only flexibility for a sensitivity analysis is to assume rounded edge for the holes. A quick review of the literature for flow through orifices suggests that round edge holes could reduce the pressure drop by as much as an order of magnitude in comparison to the current configuration with sharp edge holes. In order to assess the importance of bypass flow through the holes on the inner barrel, the calculations are repeated at ANL using rounded edge hole profiles (using fillet option to smooth the edges on both sides) as shown in Fig. 138.

Since the pressure drop for flow through the inner barrel holes with the sharp edge is significantly greater than the pressure drop for holes with round edge, the hole profile makes the most significant difference. In the configuration analyzed here, the maximum diameter fillets are considered on both edges of the holes resulting in the least possible pressure drop for the through-flow. A comparison of the calculated thermal stratification patterns with both sharp- and round-edge hole models is shown in Fig. 139 for 15 minute after the transient starts.

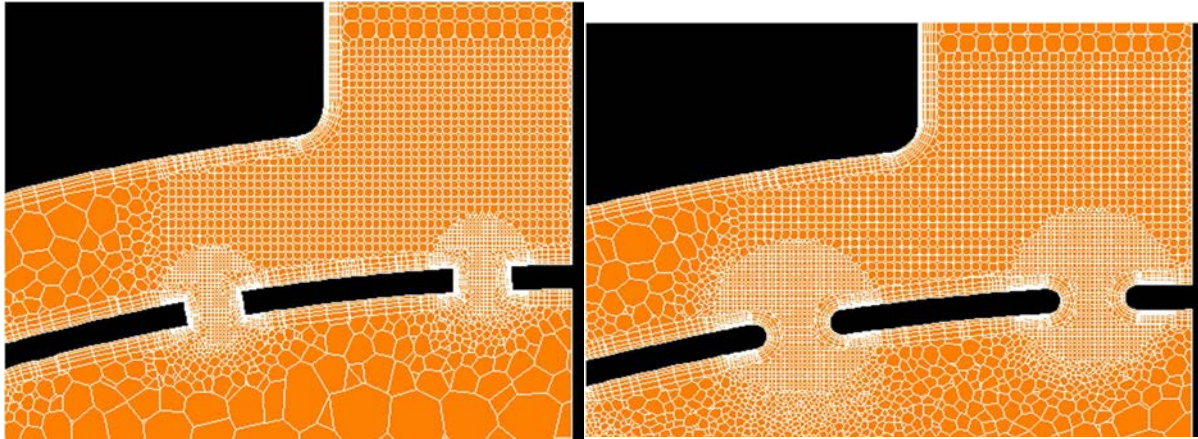


FIG. 138. Mesh structure in a horizontal plane through the holes on the inner barrel: (a) for the reference model with sharp edge holes (left), (b) for an alternative model with round edge holes (right).

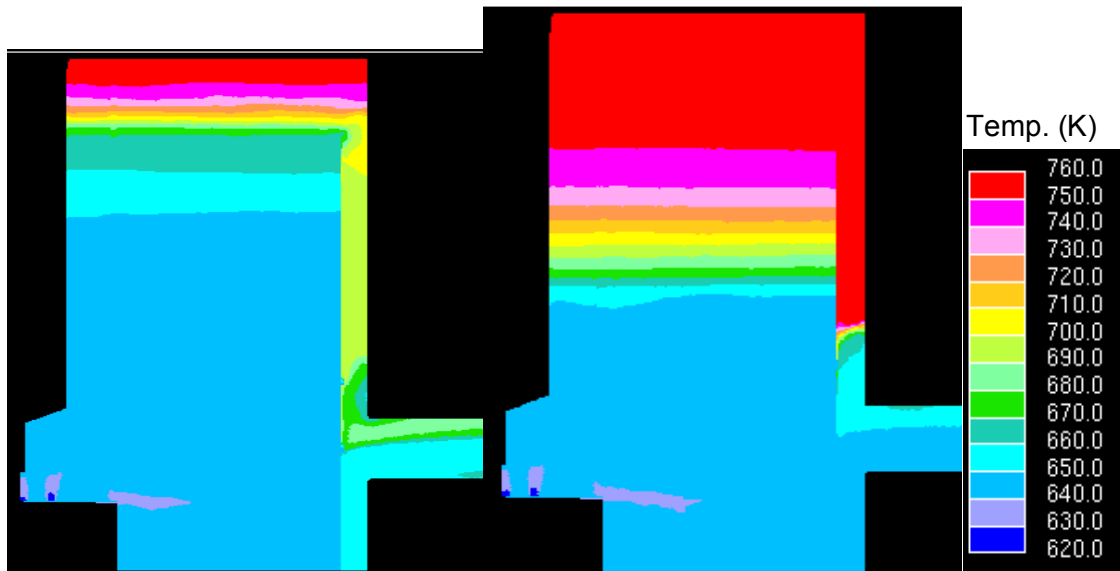


FIG. 139. Comparison of thermal stratification patterns at 15 min mark during the transient: (a) with sharp edge holes as reference case (left), (b) with round edge holes (right).

7.3. OUTCOME OF SENSITIVITY ANALYSIS AND RECOMMENDATIONS FOR FURTHER SIMULATIONS

7.3.1. CIAE

The preliminary analysis calculation result with the CFD code STAR-CCM+ shows great discrepancies with the experimental results. It was well known that the flow resistant coefficient through the upper and lower flow holes cannot be set by manual in the CFD code which may have a great effect on the flow distribution between the annulus flow rate and by-pass flow through the two roles of holes in the inner barrel. Of course, some other factors such as the thermal capacity of the structures included in the upper plenum, heat transfer and thermal conduction of the inner barrel, turbulence model used in this benchmark calculation and the modelling of the upper core structure, fuel handling machine also had some effects on the thermal stratification process more or less. But all of these were not the crucial factors expect of the flow rate distribution between the annulus and the by-pass flow according to other institutes of CRP researches. In addition, the sensitivity analysis to flow rate

distribution in the different flow paths in previous section also gave us the right direction that the kind of shape of the edge of the flow holes may be the pride of place in the final simulation. One reason was that the sharp holes provided the maximum pressure loss and result in the minimum flow rate through the holes. The second was that the sharp holes were rarely used in the design and fabrication of the inner barrel from an engineering perspective. So the round-edged model should be adopted in the final simulation.

7.3.2. CEA

The flow and temperature distributions in the upper plenum of the Monju reactor has been analysed with the CFD code Trio_U. In angular direction only 1/6 of the Monju upper plenum has been taken into account in the analysis. This reduced domain was discretized in up to 3.3 Million tetrahedral elements. A high Reynolds number turbulence model (k-ε) was used to account for turbulent mixing with additional terms for treating buoyancy effects.

For the steady state initial condition before the pump trip transient, a bifurcation of the solutions into a ‘momentum dominated solution’ and a ‘buoyancy dominated solution’ was observed. Such a bifurcation has also been found experimentally at CEA in similar mixed convection experiments. Initializing the coarsest mesh with a reposing fluid and using a 1st order convection scheme, the momentum dominated solution was attained. Initializing the fine mesh with a reposing fluid and using a 2nd order convection scheme, the buoyancy dominated solution was attained. After successively refining the mesh, each solution was found to be meshing independent. The experimentally detected temperature stratification seems not being a good indicator to distinguish the flow fields of the two solutions. For a more profound understanding, further numerical analysis is necessary. This concerns the solution procedure (iterative methods as SIMPLE instead of a transient calculation as presented) and maybe the use of more sophisticated turbulence modelling approaches.

The pump trip experiment has shown the formation of a thermal stratification within the plenum. The calculations with the intermediate mesh predict well the stratification formation in the first 10 minutes of the pump trip. In the experiment, the stratification persists for more than two hours whereas all calculations of Trio_U have shown a homogenization of the temperature in the plenum after about 15 to 20 minutes (significant overestimation of the internal mixing). Further analysis seems to be necessary to better understand the overestimation of the mixing in the upper plenum. One reason for the overestimation might be the assumed form of the inner barrel flow holes (possible overestimation of the pressure drop by using the sharp edges given in the JAEA CAD file), however, as long as the real form of the flow holes is not known, this explanation is not totally satisfying. Special attention should also be turned on the capacity of the numerical schemes to balance in reposing fluids linear temperature gradients by the pressure without creating spurious velocity modes.

7.3.3. IGCAR

Flow and temperature distributions in the hot pool of Monju, during the simulated event of reactor trip following a ‘condenser vacuum low’ signal have been simulated. The analyses indicate that stratification is present during initial steady state itself. The predicted vertical temperature distribution along the thermocouple stack in transient analysis deviated from the measured data. To find out the reason for this difference between the measured data and the CFD predicted data, sensitivity studies have been performed. The parameters of these studies are: (i) thermal capacity of upper core structures and (ii) turbulence models. It was found that the thermal capacity of the upper core structure does not affect the thermal stratification characteristics in the plenum. The standard high Reynolds number k-ε model and RSTM

model predict identical results and also, k-e model good enough for prediction of stratification. Finally it is noticed that the configuration of holes in the inner barrel influences the stratification interface movement significantly. Simulation using round edged holes in the inner barrel predicted stratification interface movement which closely matched with measured data. Thus, the major findings of the studies are: (i) standard high Reynolds number k-e model is adequate to simulate thermal stratification and (ii) detailed modeling of the hole-profile is very critical for stratification prediction.

7.3.4. JAEA

In the sensitivity study of this CRP, almost all possibilities to affect the moving-up rate of the thermal stratification front were discussed in the RCMs and participants performed various parameter simulations concerning the pressure loss of the flow holes on inner barrel. Consequently the only possibility to largely affect the moving-up rate was the shape of flow holes. Therefore JAEA provided information that the rounded edge was the actual shape but could not provide the curvature because of keeping manufacture's designing know-how. Nevertheless, the CRP participants could predict the experimental data with good accuracy when they apply a round edge to either simplified or full-sector model.

7.3.5. University of Fukui

As a sensitivity study relating the flow-hole configuration, the modelling of the flow-hole is most important thing to simulate the behaviour of the thermal stratification in the upper plenum. In order to discuss the thermal hydraulics, the precise configuration of the flow-hole should be known.

7.3.6. KAERI

The simple gradient diffusion hypothesis for a treatment of the turbulent heat flux in the CFX-13 code predicts very well when the flow is a mixed convection; however, the model invokes a relatively strong mixing for a natural convection flow. Thus, a faster thermal mixing is observed than that shown in the experiment after 10 minutes. This discrepancy may be due to the shortcomings of the thermal turbulence models available in the CFX-13 code for a natural convection flow with thermal stratification. The use of an advanced turbulence model like the algebraic heat flux model with the elliptic-blending second-moment closure is recommended. In the future study, the heat conduction heat transfer in the inner barrel should be included and the LES solution may cure the turbulence model problem.

7.3.7. IPPE

Sensitivity study enables to make the following conclusions and recommendations:

- After first round of calculations some inconsistencies between GRIF calculations and the results of other participants were revealed. For steady state GRIF predicted a flow pattern that can be called as 'ascending flow mode' but calculations of other participants predicted another flow picture in the upper plenum - flow pattern that can be called as 'jet flow mode'. Special parametric study showed that the calculated flow pattern in the upper plenum depends on total flow and on velocity and temperature distributions that used as initial approach for steady state calculations.

This means that the problem has two different steady state solutions and what solution of that two is realized depends on value of total flow and specified initial approach.

- Parametric analysis of the influence of heat exchange with cold plenum (through support plate) showed that this phenomenon can be neglected;

- Mesh refinement in the regions where large temperature gradients are observed is desirable;
- The rate of flow and temperature redistribution in the upper plenum during the test is rather sensitive to heat exchange between sodium in the upper plenum and sodium in downcomer. This means that heat conductivity of the inner barrel and heat transfer coefficients on its inner and outer surfaces should be accurately calculated;
- The transient behavior of flow and temperature in the Monju upper plenum and particularly the duration of ‘stratified stage’ are extremely sensitive to pressure loss coefficient of the holes in the inner barrel. Therefore special attention should be paid to the simulation of pressure losses in the holes in the inner barrel.

7.3.8. ANL

Sensitivity analyses performed by ANL using different transient solvers, different grid types and structures, and turbulence models ruled these factors out as a source of discrepancy between the calculated and measured thermal stratification patterns a few minutes into the transient. The main conclusion of ANL results is the importance of the bypass flow through the holes on the inner barrel. If the pressure drop for flow through the inner barrel holes is much less than what is predicted with sharp edge shapes of these holes in the benchmark specifications, much of the cold sodium coming out of the core after reactor shutdown goes through these holes, bypassing the upper plenum and extending the thermally stratified pattern prevail much longer. In fact, when one assumes a round edge profile (with maximum diameter fillets considered on both edges of the holes as shown in FIG. 7.86), ANL results agree well with the measurements along the thermocouple-tree throughout the transient. Therefore, the hole profile makes the most significant difference.

8. FINAL CRP RESULTS

8.1. STEADY STATE AND TRANSIENT RESULTS

8.1.1. CIAE

(1) Steady and transient simulation

To concern on the precision calculation, the round edge of the flow holes in the inner barrel is used just as shown in Fig. 140.

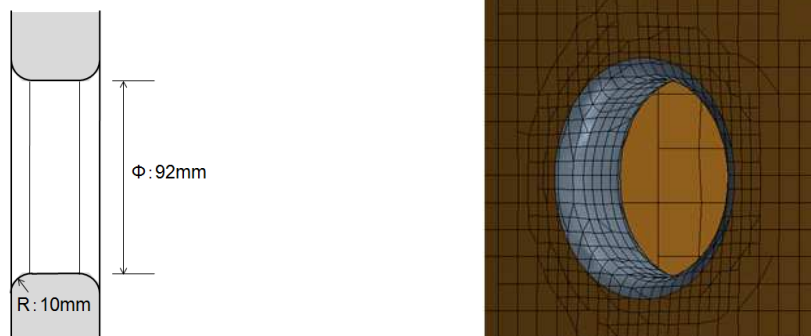


FIG. 140. Configuration of the flow holes and the mesh description (round edge).

Figs. 141–150 show the velocity and temperature distribution of the vertical section at the typical time. From these pictures, we can see the formation and development of the thermal stratification and the different results by using the sharp and round shape of the flow holes. It can be showed that the cold sodium from the core outlet has the strong motion energy at 30 second in Fig. 141. Compared to the previous figure at the same time, the interface of the hot and cold sodium is lower than that in Fig. 141. So the effect of shape of the flow holes is very distinct, which means that the flow resistance is getting smaller in the round holes and more cold sodium flows to the outlet nozzle through by-pass channel.

It can be seen that the upward flow kinetic energy of the cold sodium is getting weak at 60 sec in Figs. 141–144 and the outlet flow from the reactor core then turns to the horizontal flow and cold sodium remains at the bottom of the plenum. But in the following time, the flow in the plenum is very slow and the interface of the thermal stratification is formed.

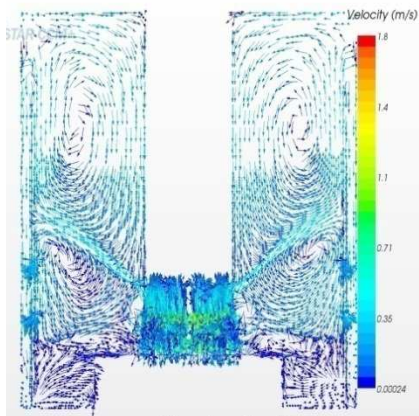


FIG. 141. Velocity distribution of the vertical section at 30s.

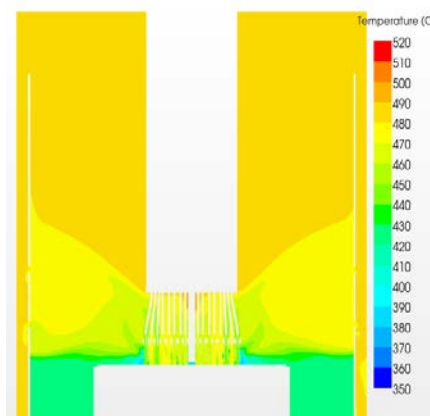


FIG. 142. Temperature distribution of the vertical section at 30s.

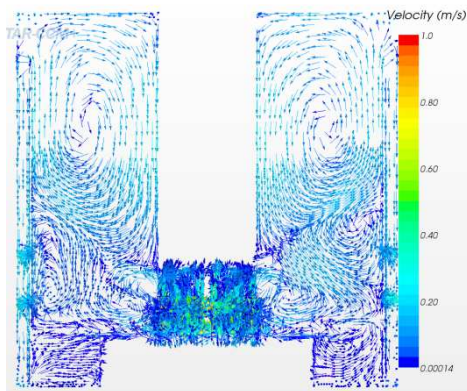


FIG. 143. Velocity distribution of the vertical section at 60s.

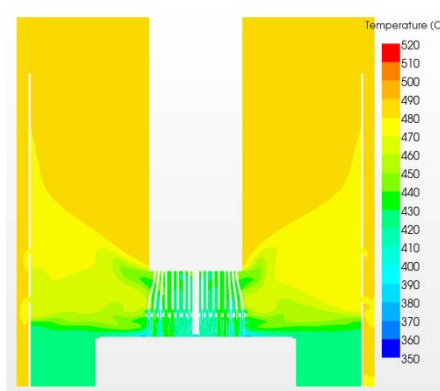


FIG. 144. Temperature distribution of the vertical section at 60s.

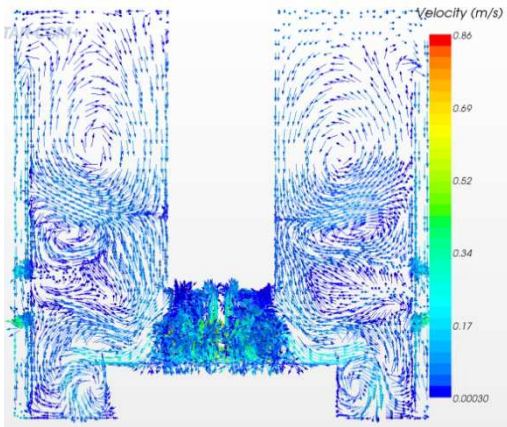


FIG. 145. Velocity distribution of the vertical section at 120s.

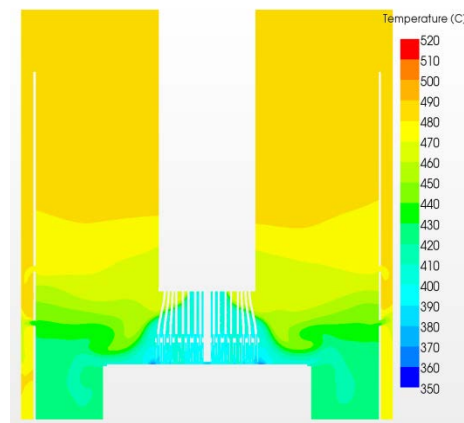


FIG. 146. Temperature distribution of the vertical section at 120s.

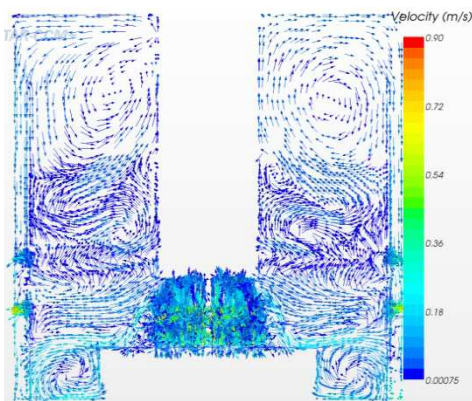


FIG. 147. Velocity distribution of the vertical section at 240s.

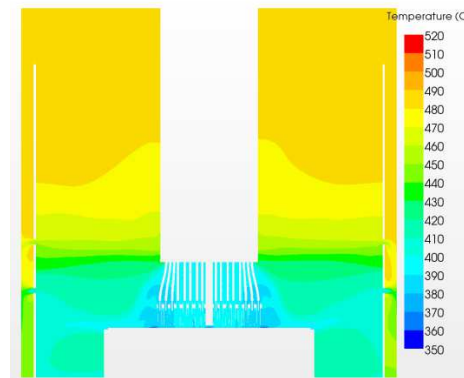


FIG. 148. Temperature distribution of the vertical section at 240s.

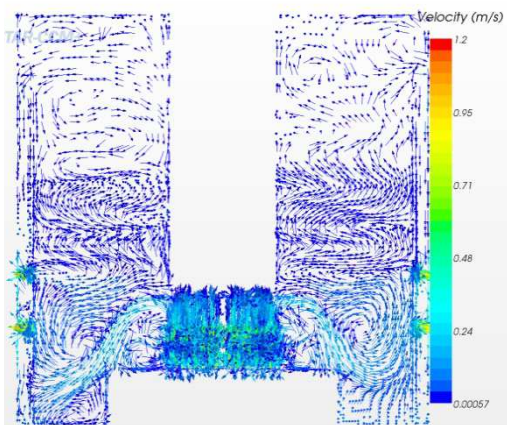


FIG. 149. Velocity distribution of the vertical section at 600s.

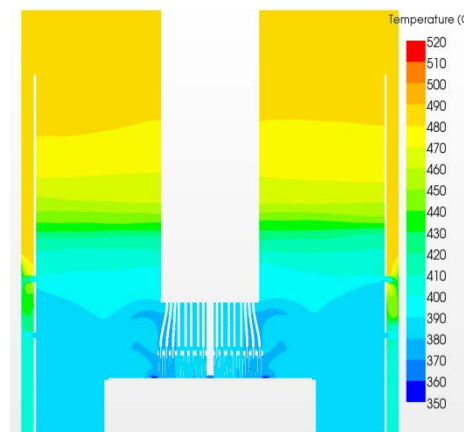


FIG. 150. Temperature distribution of the vertical section at 600s.

(2) Sensitivity analysis to investigate the discrepancies with experimental

Fig. 151 shows the final simulation results in 30 minutes with the test using the round edge of the flow holes, the same colour of the lines represent the same time. Fig. 152 shows the flow rate change and distribution in the three different paths after the reactor trip. Compared to the

previous calculation, the flow rate in the annulus in Fig. 152 show an obvious difference using the round edge of the flow holes. The flow rate of annulus flow decrease quickly at the initial 600 seconds and then it change to decrease smoothly in the following time. This trend keeps to the end of the calculation time. Meanwhile the flow rate of the upper holes, lower holes in the inner barrel increase quickly and changes very little after 600 seconds. These change can be reflected in the temperature distribution of Fig. 151 that the good agreement between the calculation data for the case of the holes with round edge and the test data.

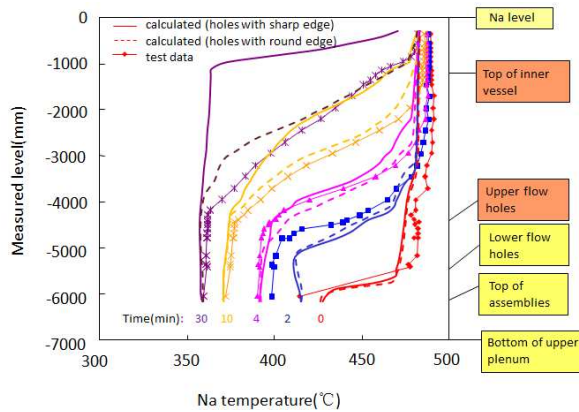


FIG. 151. Comparison between the test and calculation (flow holes with round edge).

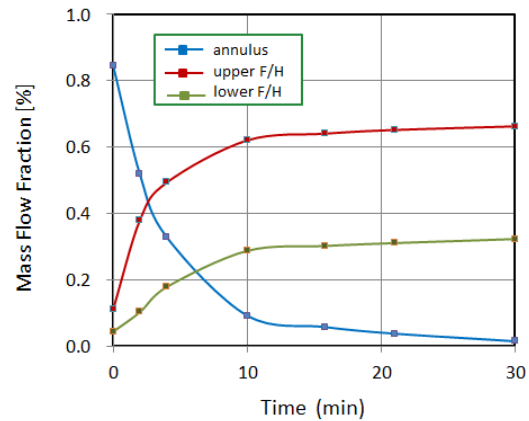


FIG. 152. The flow rate distribution in the different flow paths (flow holes with round edge).

8.1.2. CEA

As shown in Section 7.1.1, the analysis of the pump trip transient gave a fairly well prediction of the thermal stratification formation in the first 10 minutes after the pump trip. In the experiment, the thermal stratification persists for more than one hour. However, the stratification disappears in the calculation after about 15 minutes and a homogeneous temperature distribution is predicted for the upper plenum.

During the 3rd IAEA-RCM, an underestimation of the flow passing through the core barrel holes has been identified as a potential source of uncertainty regarding long term stratification formation. For the exact form of the holes is not known to date, the impact of the two extreme hole-forms on the stratification formation was analysed; sharp edged holes and rounded holes (fillet) which have the same minimum cross section as the sharp edged holes.

Separate effects calculations with successive refinement of the meshing of a rounded flow hole have shown convergence on the mesh-refinement with about 30 to 35 calculation points per diameter of the hole. Due to the required small time step imposed by the CFL stability criteria, it was not possible to conduct a transient calculation of a length of 20 minutes with such a fine mesh in the flow holes. As a consequence, it was not possible to improve the result already presented in Section 7.1.2.

8.1.3. IGCAR

(1) Model

It may be recalled that there was significant difference between the plant data and CFD results predicted by the simplified benchmark model. In order to identify the reason for this

difference, the effect of thermal capacity of UCS, core barrel, inner barrel and outer vessel has been accounted and CFD simulations repeated. But no visible improvement in the predictions has been observed. Following this, various turbulence models have also been tested and all the turbulence models were found to over-predict the movement of stratification interface. Finally, it was noticed that the flow bypassing the holes in the inner barrel was critical and required accurate treatment. This aspect led to study pressure drop across the holes. It is known that sharp edged holes (Fig. 153) offer a large resistance for sodium to flow from hot pool to exit nozzle leading to enhanced upward flow and hence a faster movement stratification interface. However, round edged holes (Fig. 154) offer a low flow resistance and hence an easy by-pass of sodium from hot pool to exit nozzle. There is lack of data on the exact profile/shape of the holes incorporated in the inner barrel of the reactor. Hence, holes with fillet equal to hole radius are chosen in the CFD simulations. This treatment for the holes demanded a larger mesh count (about 0.76 millions). Other details of the computational model, viz, schemes, solver, turbulence model are same as that given in Section 6.3.



FIG. 153. Straight edged holes considered for the preliminary studies.

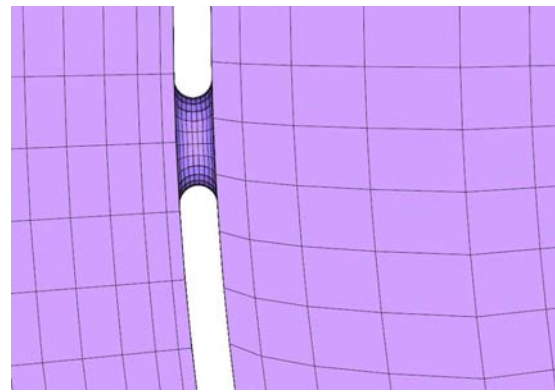


FIG. 154. Round edged holes considered for the final simulation.

(2) Final results

The evolution of predicted transient temperature in the pool is depicted in Fig. 155. It can be seen that there is strong stratification prevailing in the hot pool. Similar stratification is observed in the exit nozzle also. The depth of hot sodium in the pool is less than that in the annulus between the inner barrel and reactor vessel. This suggests that the entire core flow is not by-passing the hot pool. Investigation of the results corresponding to 5 minutes indicates that there is hot sodium in the cavity region during the initial phase of the transient.

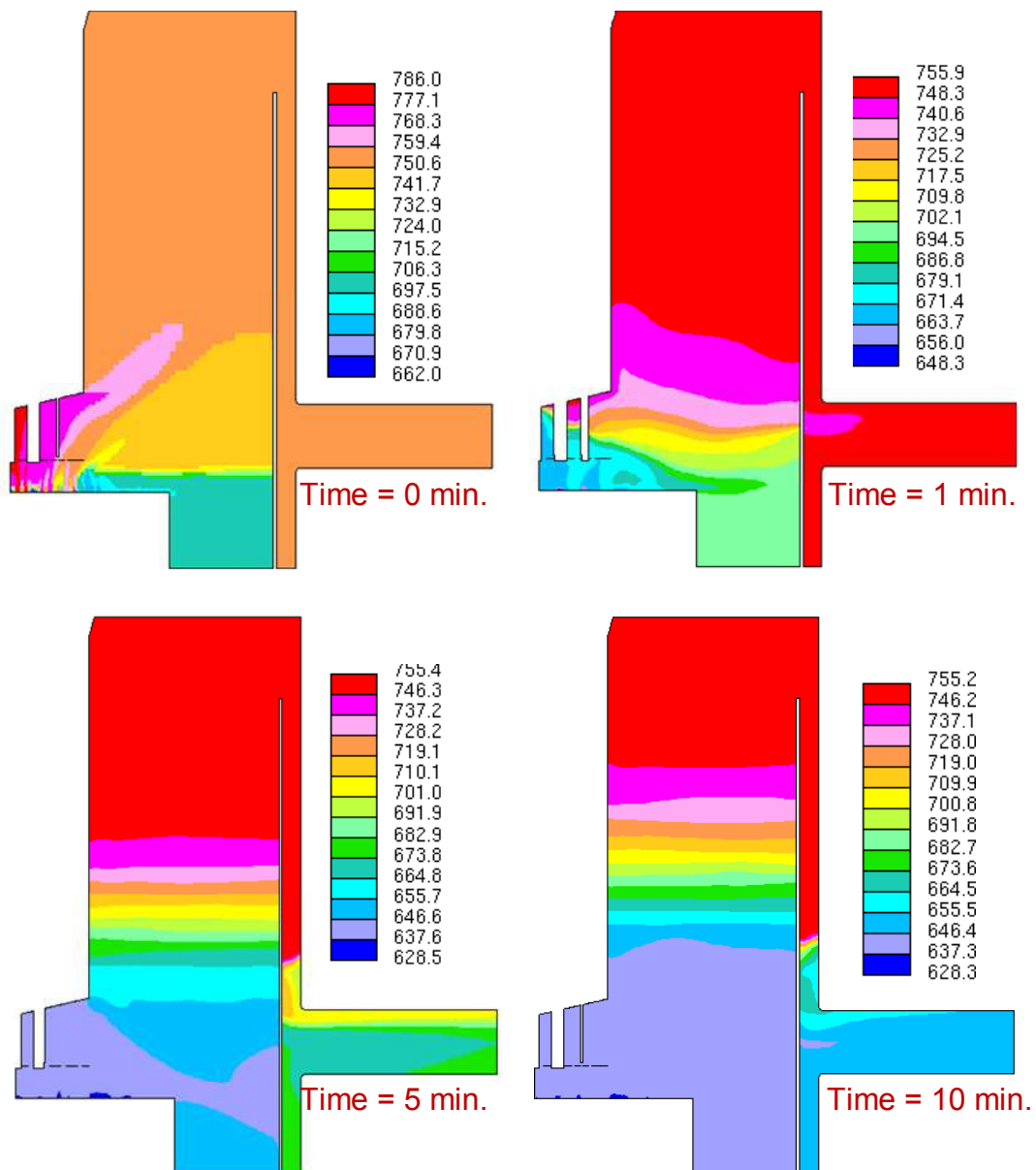


FIG. 155. Temperature contours (K) at different instants with round edged holes.

3) Comparison of predicted results with plant data

Predicted steady state and transient data at three different instants are depicted in Fig. 156. Also shown in the same figure are the thermocouple data measured in the reactor at the corresponding times. It can be seen that there is a good match between the measured and predicted data, especially at the stratification interface. However, some minor deviation is observed in the cavity region for initial phase of the transient. But as time progresses the comparison in the cavity region also improves. Comparing Fig. 156 with Fig. 79, it is clear that the hole profile has a significant influence on the stratification pattern.

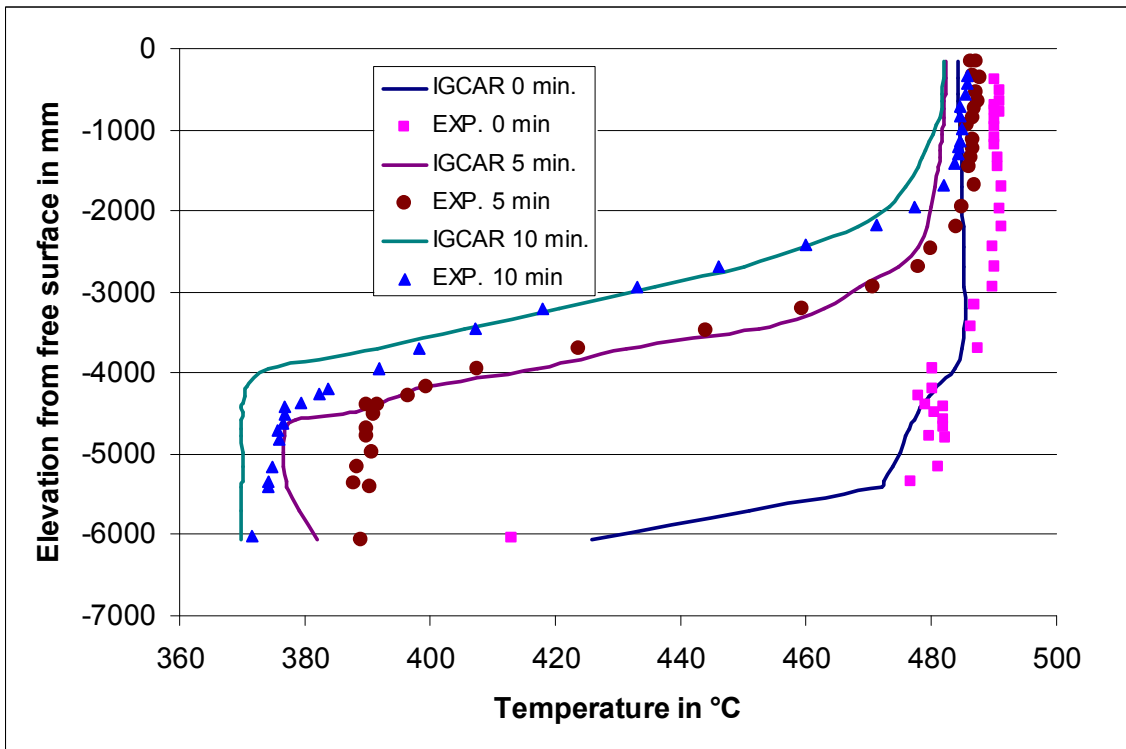


FIG. 156. Comparison of predicted data with round edged holes against plant measurements.

8.1.4. JAEA

JAEA provided the detail geometry data of the Monju RV upper plenum and the boundary conditions of the turbine trip test under the 40% rated electrical power condition. The designed flow rates were applied to these conditions, while the measured temperatures in the core region and designed temperatures in the outside of core region were also applied to the outlet of these subassemblies. These boundary conditions are considered to produce the energy imbalance. However, it is not considered to become a critical problem to attain the CRP objectives of the improvement of the member states' analytical capabilities and identifying the key parameters of the moving-up rate of thermal stratification front.

In the benchmark simulation, JAEA investigated the effect of temperature distribution due to the asymmetric structure location, the pressure loss effects of flow hole shape on the inner barrel and the pressure loss effects of the honeycomb structure in the UCS region. These simulation results showed these parameters did not affect largely to the thermal-hydraulic behaviour in the steady state conditions. These results are shown in Figs. 114–124 in Section 7.2.4.

8.1.5. University of Fukui

(1) Steady-state and transient simulations

Based on the preliminary computation, the rounded edge flow-hole configuration is adopted as the final computation. Regarding the boundary conditions of the computation at the inlet of the upper plenum, the discussed result is reflected to the computation in order to correct the discrepancy of insufficient energy input into the upper plenum. The heat capacity of the upper instrumental structure is taken into account. Other conditions are the same as mentioned in the previous section.

Fig. 157 illustrates the comparison between measured result and the computed results. The characters 'R' and 'HC' in the legend stand for the flow-hole with rounded edge and the heat capacity of the UIS, respectively. As one can see from the comparison, good agreement is obtained between the measured and computed results. The temperature distributions from the initial up to around 5 minutes are predicted almost perfectly. However, the thermal stratification interface is over predicted a bit after 5 minutes. It is estimated that the meshed configuration has still several irregularity inside the flow-hole surface. The irregularity would increase the local loss coefficient at the flow-hole. The other important factor is overestimation of the inlet temperature of the plenum which is used as one of the boundary conditions. The temperature in the lower region of the plenum is overestimated because of the high temperature sodium flow. This flow pushes the thermal stratification interface upward.

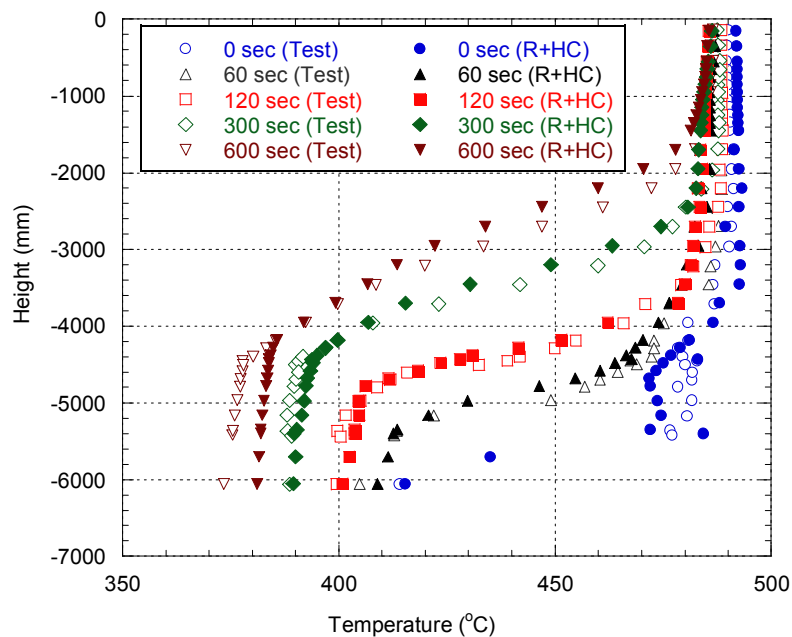
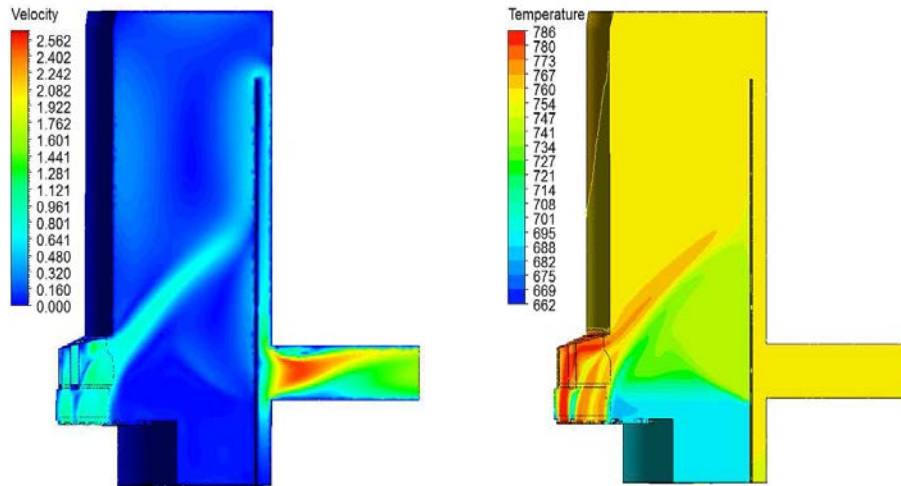


FIG. 157. Comparison between measured results and computed results from the steady state to 10 min.

8.1.6. KAERI

(1) Steady-state solution

Fig. 158 shows the steady-state velocity magnitude and temperature contour plots on the symmetry plane through the outlet and vertical temperature profile along the thermocouple plug. The hot sodium from the core spreads conically outward and then moves upward along the inner surface of the inner barrel. Owing to this strong flow, there exists a relatively weak counter current along the vertical surface of the upper structure main body, resulting in a large toroidal recirculation zone above the core outlet level. The sodium in the annular region between the inner barrel and reactor vessel flows downward and flows out of the reactor at the outlet. Below the core outlet level, the flow field is almost stagnant with significantly colder sodium. It is noted that the sodium in most of the upper plenum and outlet region is well mixed and the temperature of the sodium is nearly uniform. Small flow holes on the inner barrel do not play a significant role in mixing the fluid on the opposing sides of the inner barrel for the steady-state conditions.



(a) Velocity magnitude contour (b) Temperature contour

FIG. 158. Steady-state velocity magnitude and temperature contours.

Fig. 159 shows the predicted vertical temperature distribution along the thermocouple tree together with the experimental data. The predicted temperature distribution agrees fairly well with the experimental data, especially when the complex structures of the core upper plenum and the assumptions introduced for the 1/6 simplified model are considered. It was noted that the temperature varies rapidly at a height of $y=1.4$ m, and does not vary significantly above this height.

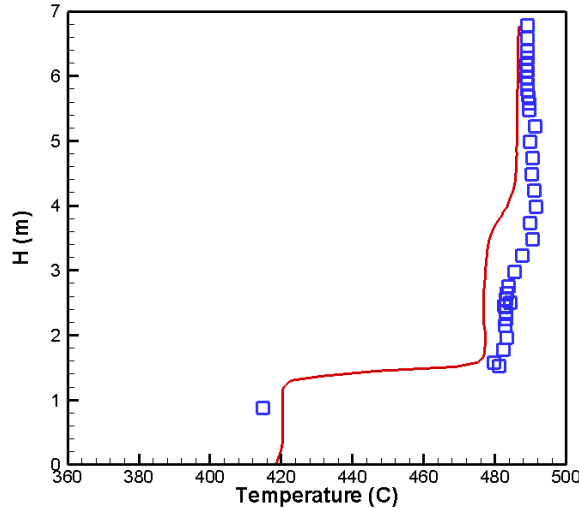


FIG. 159. Vertical temperature profile along the thermocouple tree.

(2) Transient solution

Fig. 160 shows the transient evolution of the temperature field at the upper plenum of the Monju reactor. When the transient starts and the core outlet temperature gradually drops owing to a reactor shutdown, the cooler sodium stays near the bottom of the vessel and the hotter primary sodium at the higher elevation in the upper plenum stays largely stagnant. As the transient continues, the cold sodium in the lower portion of the plenum moves upward and a thermal stratification begins to form. A rather stable thermal stratification is established at 300 seconds. A slow movement of cold sodium is observed between 240 and 300 seconds.

The rapid coast-down of the mass flow rate after a pump trip is finished at about 300 seconds, and the mass flow rate from the core becomes nearly constant after 300 seconds. Thus, the type of flow until 300 seconds is a mixed convection and the natural convection begins after 300 seconds. At 600 seconds, the thermal stratification interface moves upward rather quickly even though the flow is a natural convection. At 900 seconds, the thermal stratification interface reaches the top of the inner barrel and the temperature field in most of the upper plenum is mixed and homogenized. It shows that a relatively strong thermal mixing has occurred in a large portion of the upper plenum. Thus, the computed temperature field contradicts the real physics of the fluid flow and heat transfer in this region. A stable thermal stratification should form and persist after 300 seconds. The origin of this discrepancy is due to the turbulence model employed in the present calculation. As explained before, the simple gradient diffusion hypothesis for treatment of the turbulent heat flux invokes a relatively strong mixing. A more advanced thermal turbulence model like the algebraic flux model should be used for a prediction of the thermal stratification; however, such a turbulence model is not available in the CFX-13 code at present.

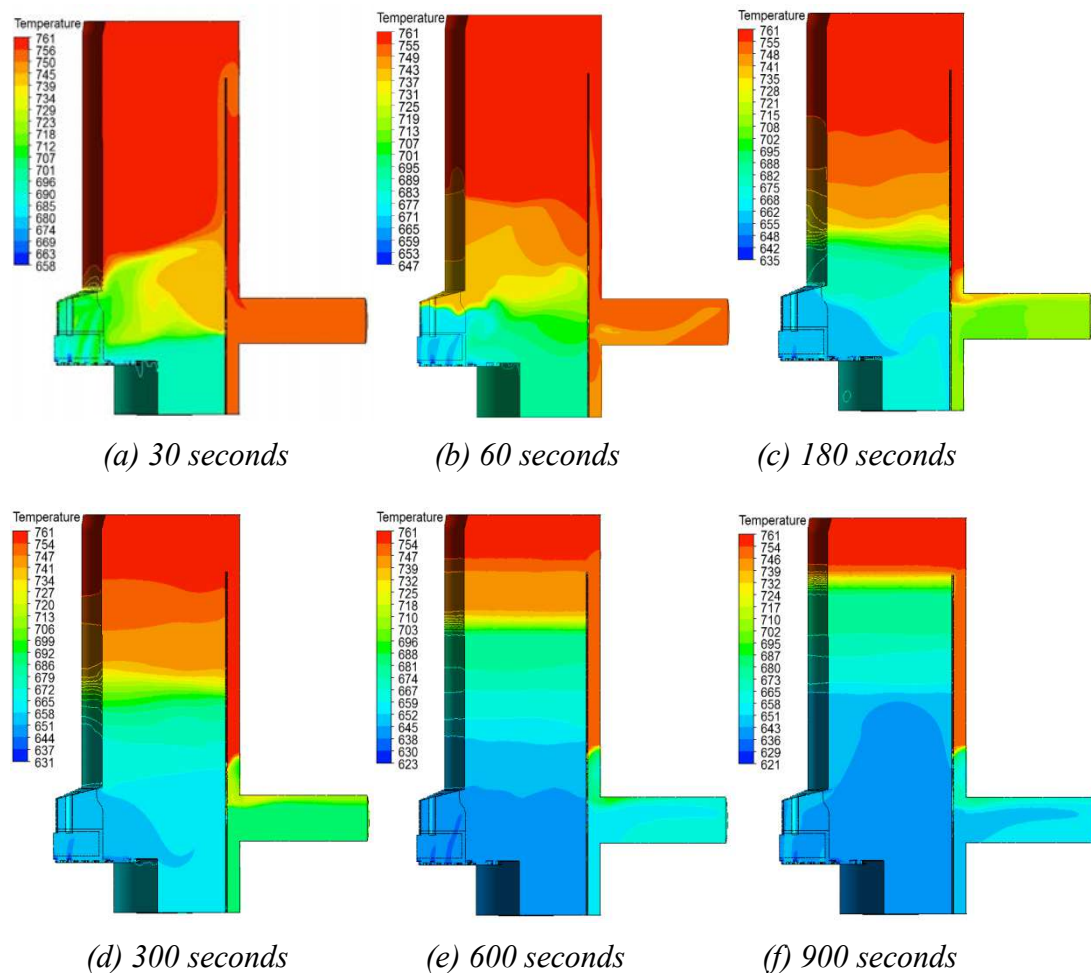


FIG. 160. Evolution of temperature contour during the transient calculations.

Fig. 161 shows the predicted transient temperature profiles along the thermocouple tree together with the experimental data. It is observed that the predicted temperature profiles agree very well the experimental data until 300 seconds. However, the predicted results deviate greatly from the experimental data at 600 and 900 seconds.

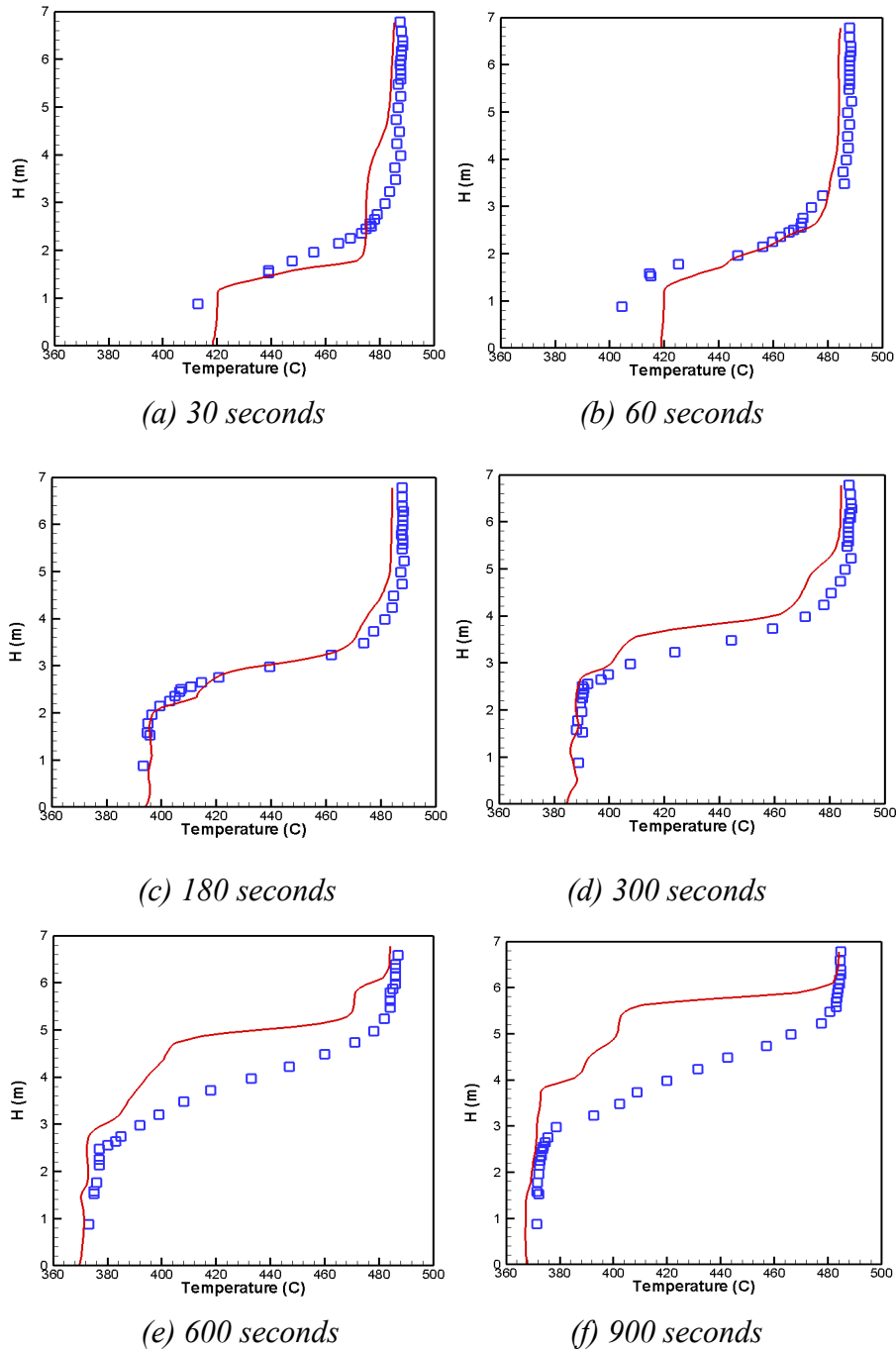


FIG. 161. Temperature profiles along the thermocouple tree during the transient calculations.

8.1.7. IPPE

(1) Final steady-state and transient results of NC-test calculation with improved model

The following modifications and amendments of GRIF calculative model simulating Monju upper plenum were made on the results of sensitivity study:

- Flow and temperature distributions corresponding to ‘jet flow mode’ were taken as initial approach for calculation of initial steady state;
- Heat conductivity of inner barrel was specified as equal to 25 W/(m·s);

- Calculation of heat transfer coefficient on the inner and outer surfaces was introduced in the code;
- Pressure loss coefficient for all holes (for upper and lower rows) was specified as equal to 1.5;
- The correlation used in the code for calculation of pressure losses in the holes was modified in order to simulate more correctly the dependence of the losses on the angle of oncoming flow.

As it can be seen from Fig. 162 the combined action of forced and natural convection leads to essential redistribution of flow and temperature in the plenum after total flow rundown. Stratification of sodium in the plenum and formation of ‘hot plug’ in the upper part occurs after 2 minutes. Then the ‘cold’ front moves upward and finally reaches the upper edge of inner barrel.

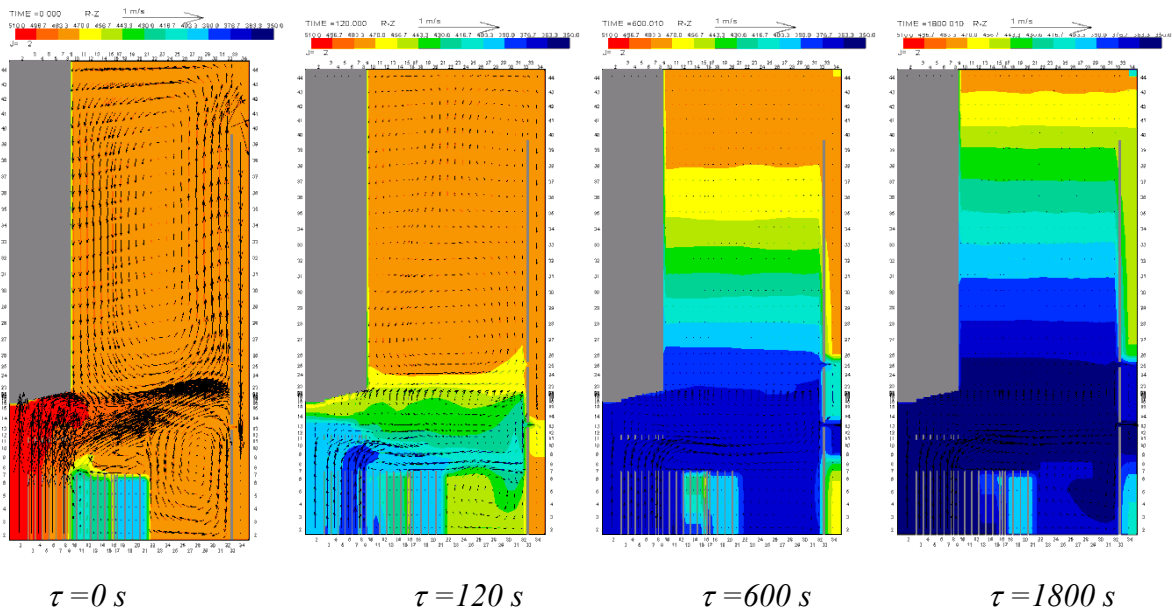


FIG. 162. Evolution of velocity and temperature distribution in the plenum (GRIF calculation).

The rate of the movement of stratification front is determined by relative distributions of sodium flows on the following three paths: path 1 - through lower flow holes, path 2 - through upper flow holes and path 3 - through the gap above the upper edge of inner barrel (Fig. 163). At initial state 95% of total sodium flow leaves the upper plenum through the gap above the upper edge of inner barrel. But total flow decreases soon and ‘hot plug’ almost totally blocks that path. As a result during whole part of transient for the time being the stratification exists in the plenum the sodium mostly releases from the plenum through the holes in the inner barrel (60% through path 1 and 30% through path 2).

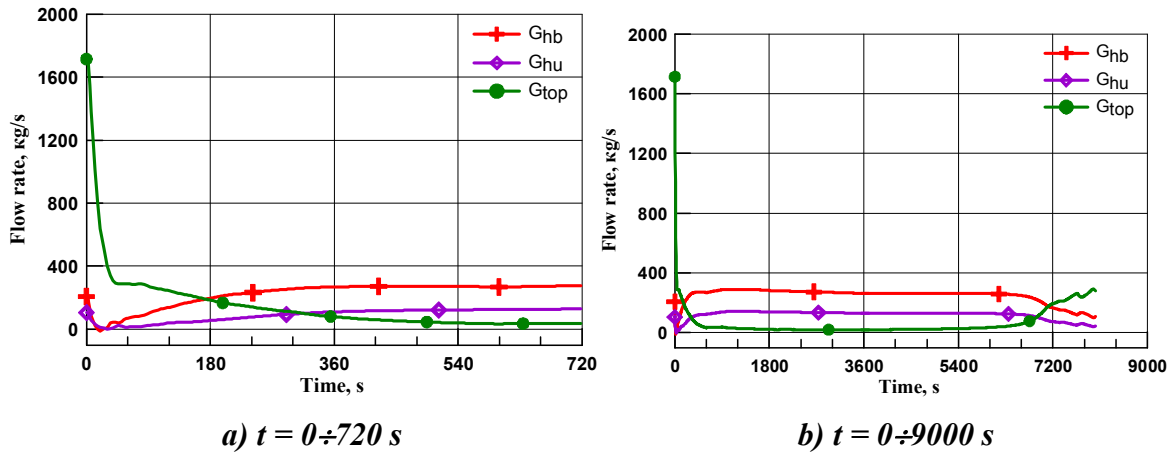


FIG. 163. Distributions of sodium flows on three paths: through lower flow holes (G_{hb}), through upper flow holes (G_{hu}) and through the gap above the upper edge of inner barrel (G_{top}).

Results of calculations of sodium temperature are compared with thermocouple readings on Fig. 164 and Fig. 165.

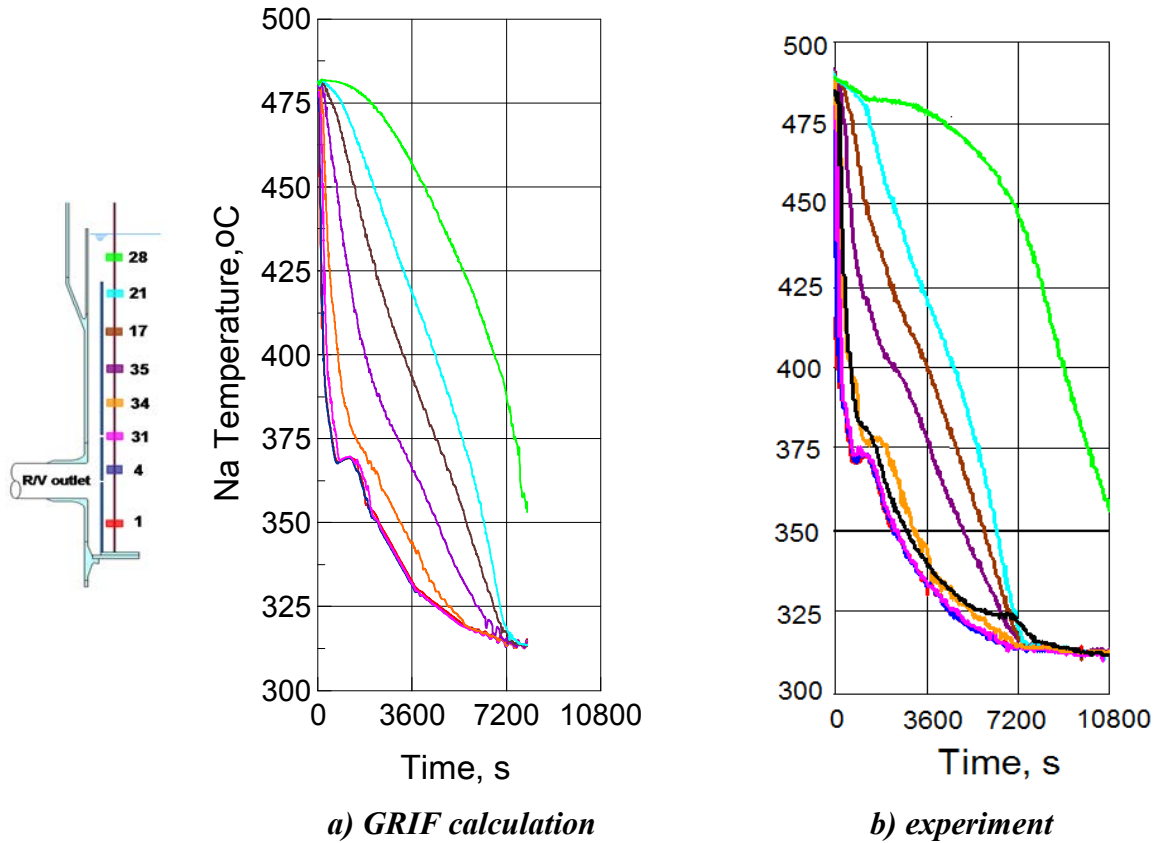


FIG. 164. Transient behavior of some selected thermocouple readings.

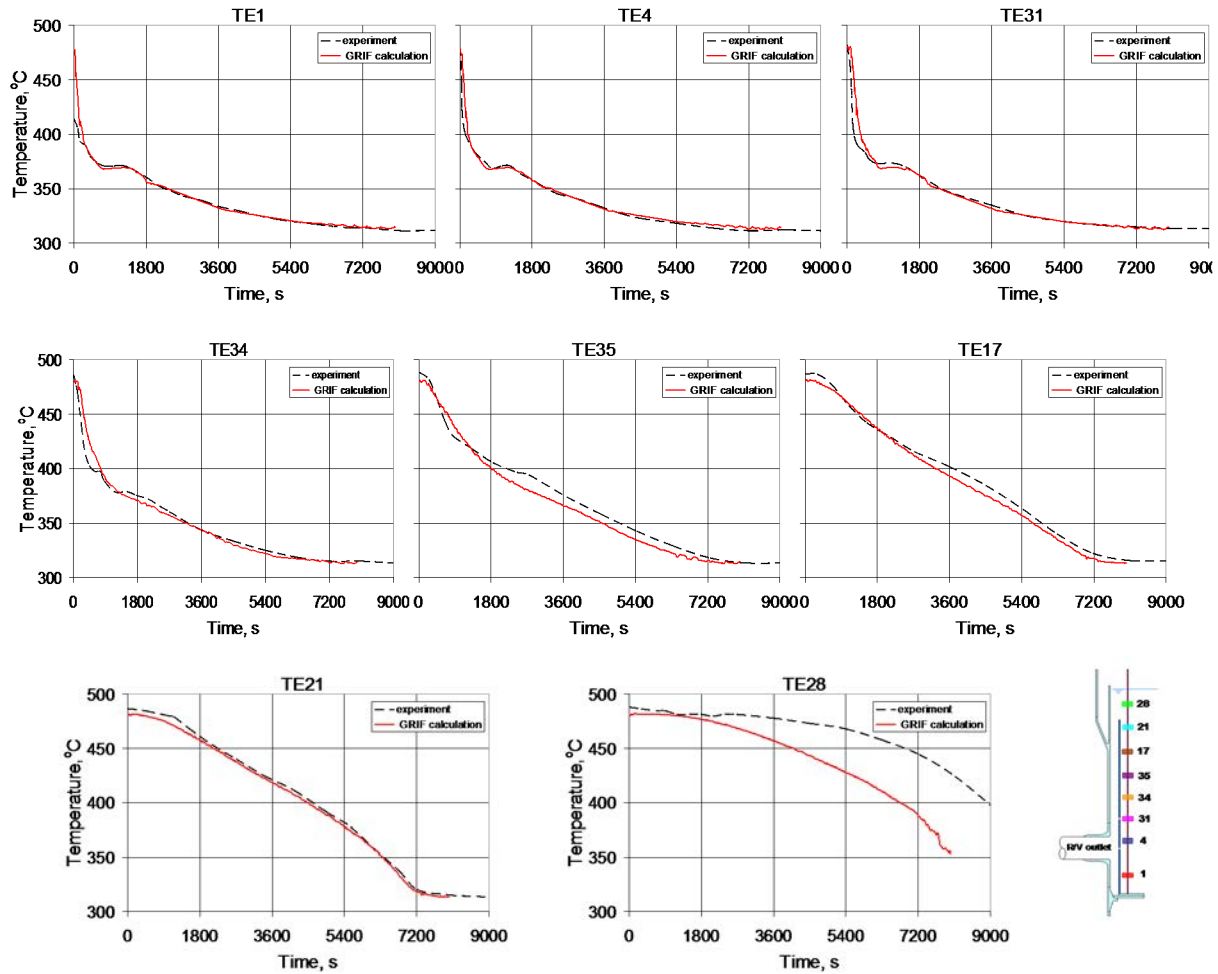


FIG. 165. Comparison of calculated by GRIF temperatures with thermocouple readings.

Significant deviation of calculation from experiment is observed only for one thermocouple - TE28. This thermocouple is located above upper edge of inner barrel, in the zone of flow stagnation where large temperature gradients occur. Probably this deviation can be attributed to relatively rough meshing in that area. The agreement for all other thermocouples can be recognized as satisfactory.

It is necessary to note that good agreement was obtained for fixed predetermined value of pressure loss coefficient of the holes in the inner barrel $\xi=1.5$. In practice this coefficient can depend on geometry of the holes and flow conditions in hole's vicinity and can be determined more precisely on the base of empirical information only. As it was demonstrated in section 2.3 the small error in calculation of pressure loss coefficient of the holes can result in essential error in calculation of transient flow and temperature in the plenum.

8.1.8. ANL

As explained in Section 7.2 for ANL sensitivity analyses, the most promising explanation of the discrepancy between the calculations and test data is the underestimation of the bypass flow through the holes on the inner barrel due to the shape of these holes.

Since the round edge holes could reduce the pressure drop by as much as an order of magnitude in comparison to the reference configuration with sharp edge holes, the hole profile makes a significant difference. When the bypass flow through these inner barrel holes

is greater than what is predicted with the reference model described in Section 7.1, it accounts for a larger fraction of the primary system flow, leaving the bulk of the sodium coolant in the upper plenum stagnant and thermally stratified for a longer period of time.

In the configuration presented here for the final ANL results, the maximum diameter fillets are considered on both edges of the holes resulting in the least possible pressure drop for the bypass flow. A comparison of the calculated bypass flow patterns with both sharp- and round-edge hole models is shown in Fig. 166 for comparison.

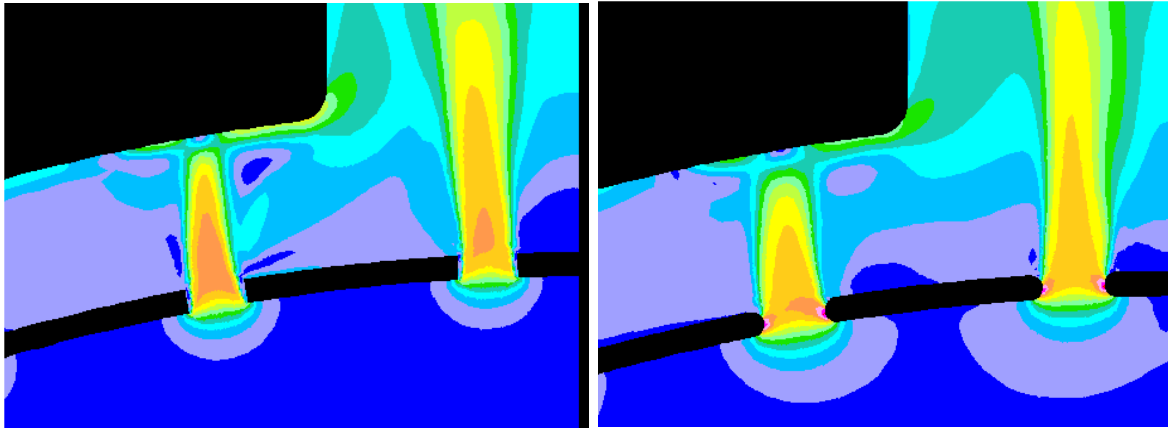


FIG. 166. Comparison of velocity magnitudes in a consistent scale on the horizontal plane through the lower inner barrel holes (a) with sharp edge holes (left), (b) with round edge holes (right).

A comparison of the calculated transient temperatures with the test data along the thermocouple tree during the first 15 minutes of test is also shown in Fig. 167. Other than the hole profiles, the two models have nearly identical mesh characteristics and consistent modelling assumptions (turbulence models, boundary conditions, material properties, boundary conditions etc.). As seen in Fig. 167, the predicted thermal stratification pattern with the model using round-edge holes is in much better agreement with the experimental data, confirming the importance of the bypass flow through the inner barrel holes. Since the actual shape of these holes is not specified, the analysis with round edge holes remains only a speculation at this point. Different hole profiles (with chamfer instead of fillet) and the effect of one-sided rounding need to be evaluated.

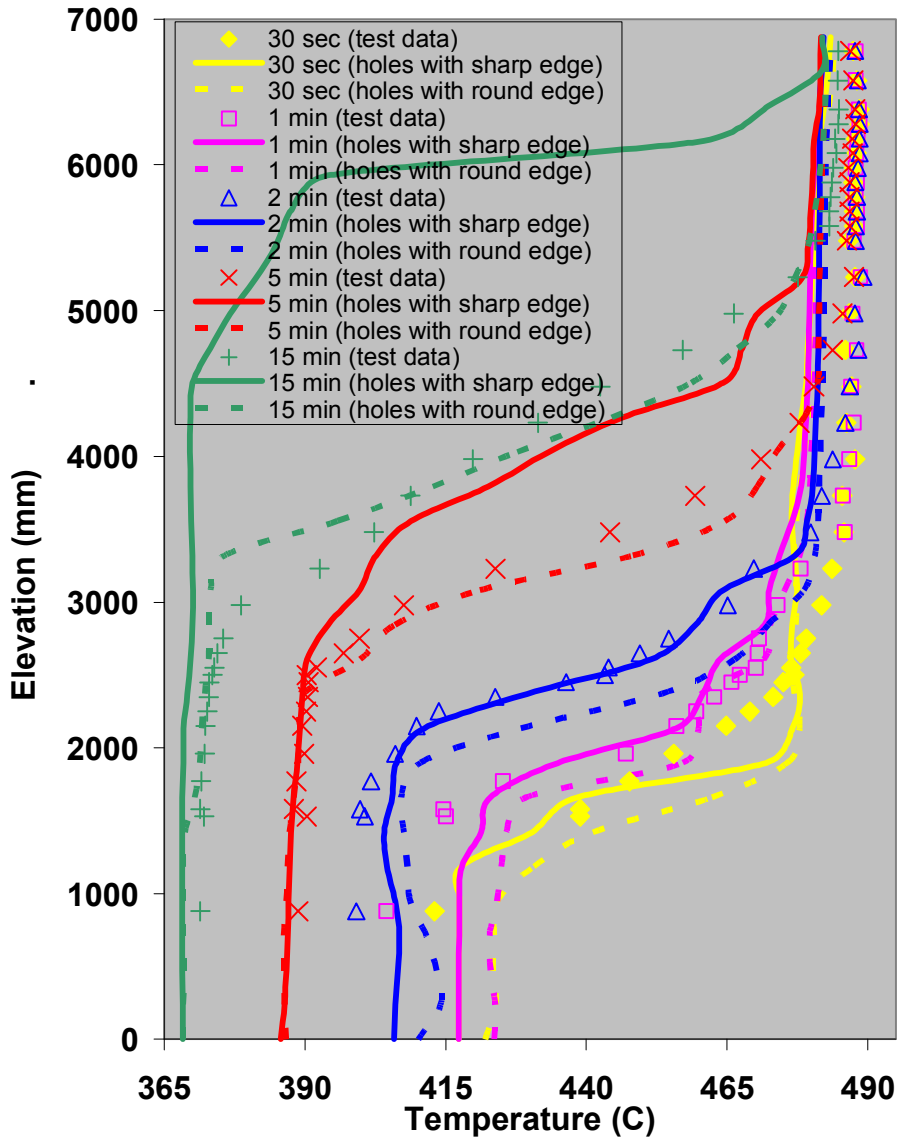


FIG. 167. Comparison of transient results for both sharp (reference model) and round edge inner barrel hole profiles with test data during the first 15 minutes of the Monju plant turbine test.

8.2. COMPARISON OF RESULTS

Steady state and transient temperature distributions on the TC-plug at different times calculated by the participating organizations are compiled in Fig. 168. As described in detail in the previous sections, in these simulations CEA and KAERI applied a sharp edge of the inner barrel holes, while CIAE, IGCAR, JAEA, University of Fukui and ANL applied round edge holes. IPPE applied the porous model approach.

As far as the steady state calculations, the following considerations can be drawn from the analysis of Fig. 168:

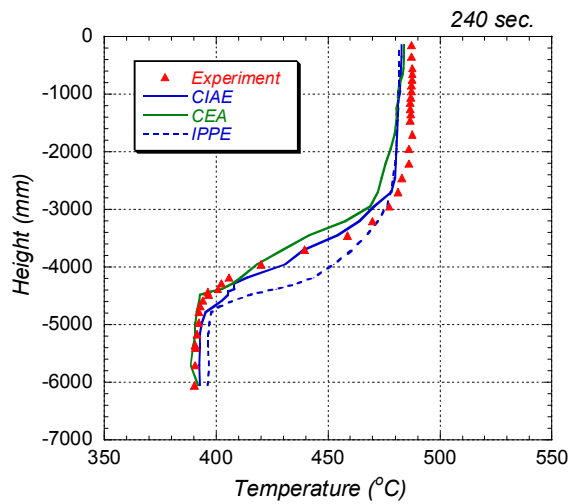
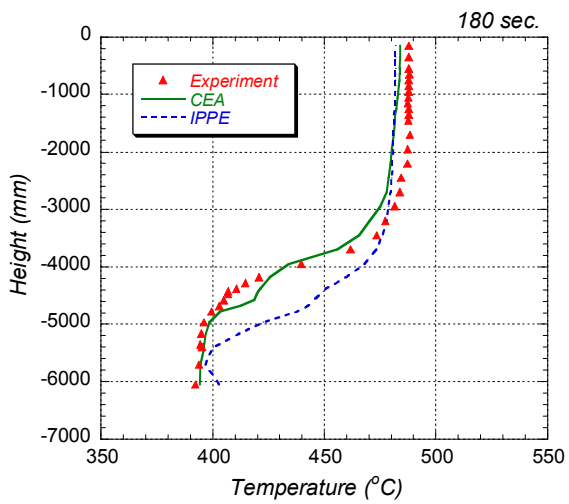
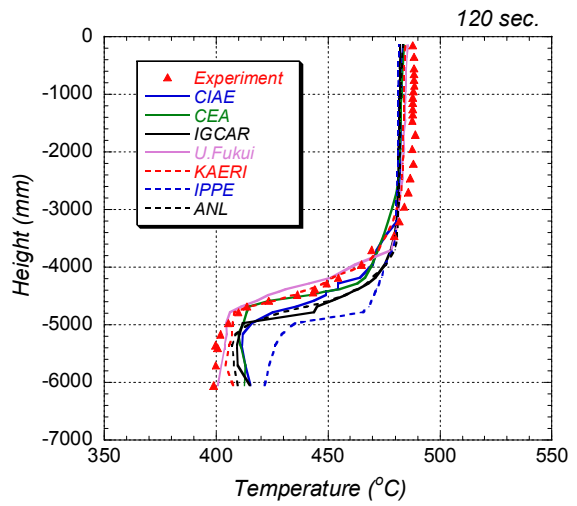
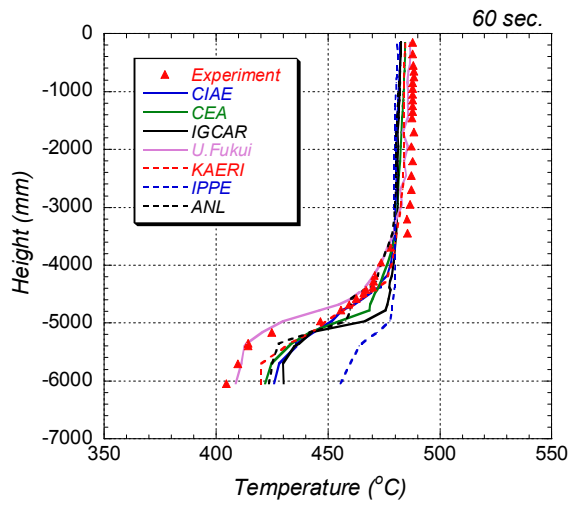
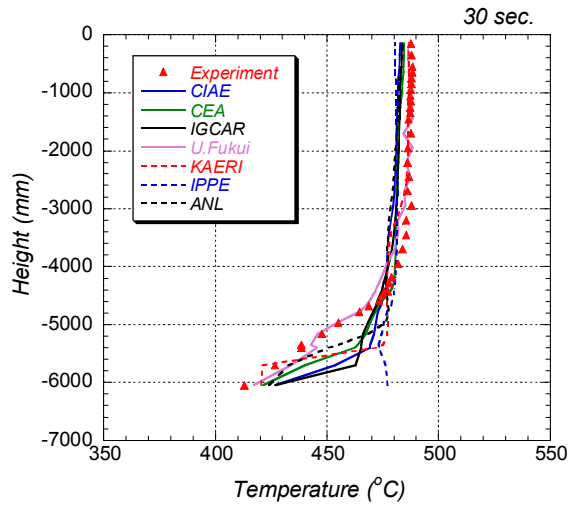
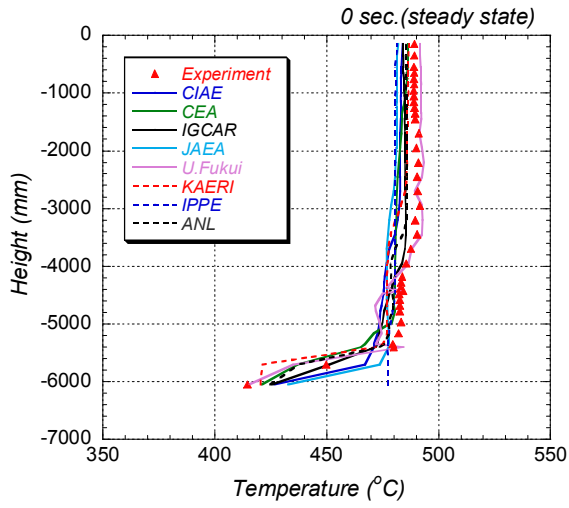
- Temperatures in the upper part of the plenum calculated by all organizations are lower than experimental data because of the energy imbalance at the subassembly outlet. The results of University of Fukui agreed well with test data by adjusting the imbalance;

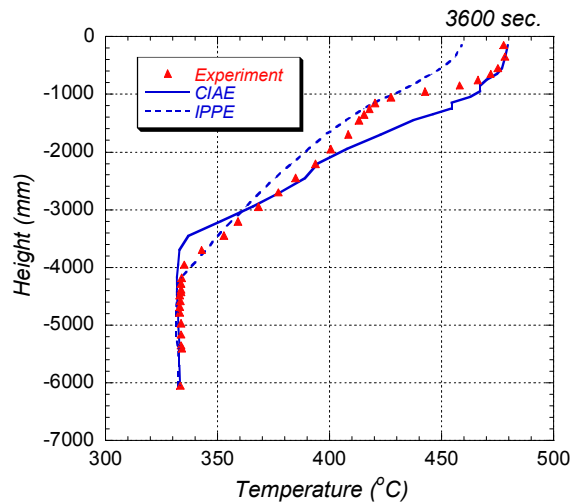
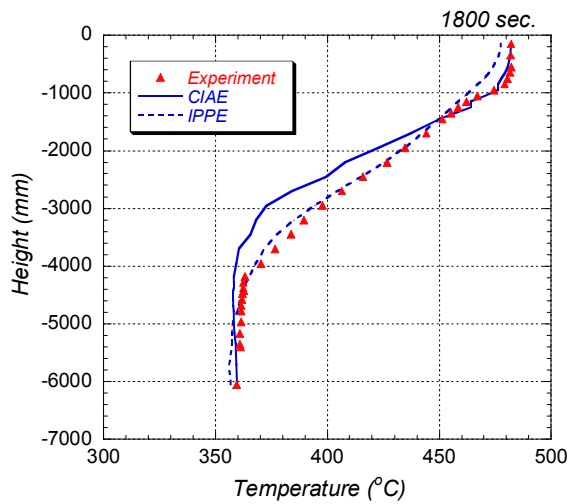
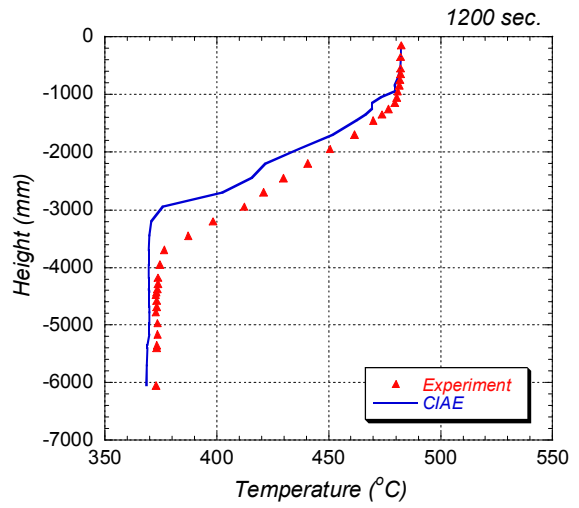
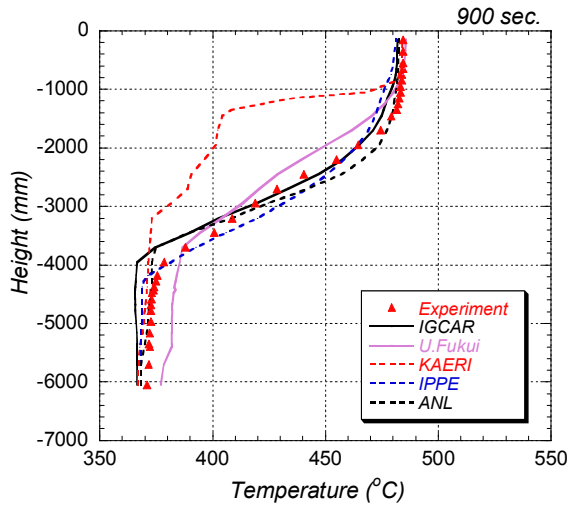
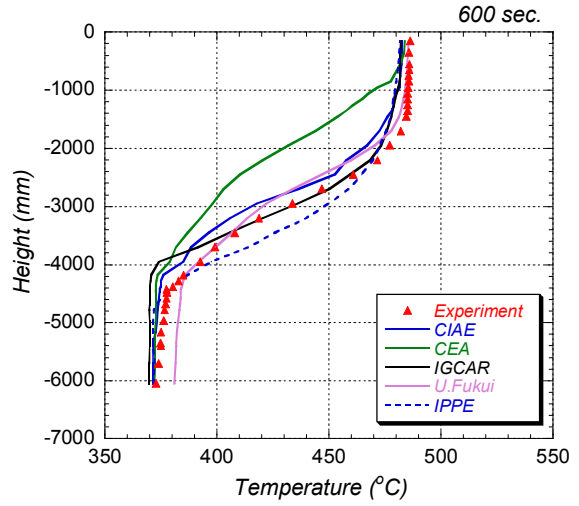
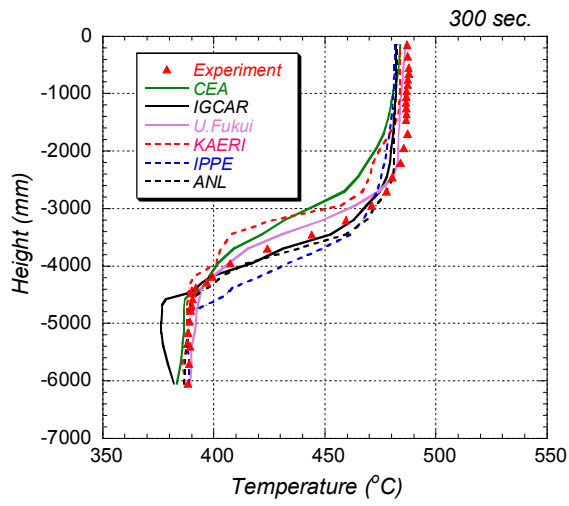
- The shape of the inner barrel holes do not largely affect these temperature profiles, both in simplified and full-sector models;
- Temperatures in the lower part of the plenum agree well with experiments when applying a constant heat capacity;
- In any cases, the temperature profile on the TC-plug can predict well the experiments by using the correct energy balance, as done by University of Fukui.

In the transient calculations, the formation of thermal stratification seems to be different; in fact:

- From 30 to 240 sec., both sharp edge and round edge hole models can capture the thermal stratification front with good accuracy. During this time interval, the front of the thermal stratification moving upwards is not affected by the pressure drop through the inner barrel holes;
- From 300 to 900 sec. the sharp edge hole model predicted larger moving-up rate of the front, while the round edge hole model and the porous model predicted it well, regardless of the different edge curvatures, both in simplified and full-sector models;
- From 1200 to 7200 sec., the porous model predicted the moving-up rate of the front of the thermal stratification with good accuracy except for the upper part of the plenum, while the full-sector and round edge hole model have some discrepancies with respect to the measured data. These results show that proper boundary conditions on the upper surface of the porous model allow to predict correctly the temperature in the upper region, and that a proper flow resistance of inner barrel holes allows to predict the moving-up rate pretty well.

In conclusion, the benchmark exercise performed during the CRP allowed to improve the analytical capabilities of the participating organizations in field of in-vessel sodium thermal-hydraulic, as well as to identify the key parameters which affect the moving-up rate of the thermal stratification.





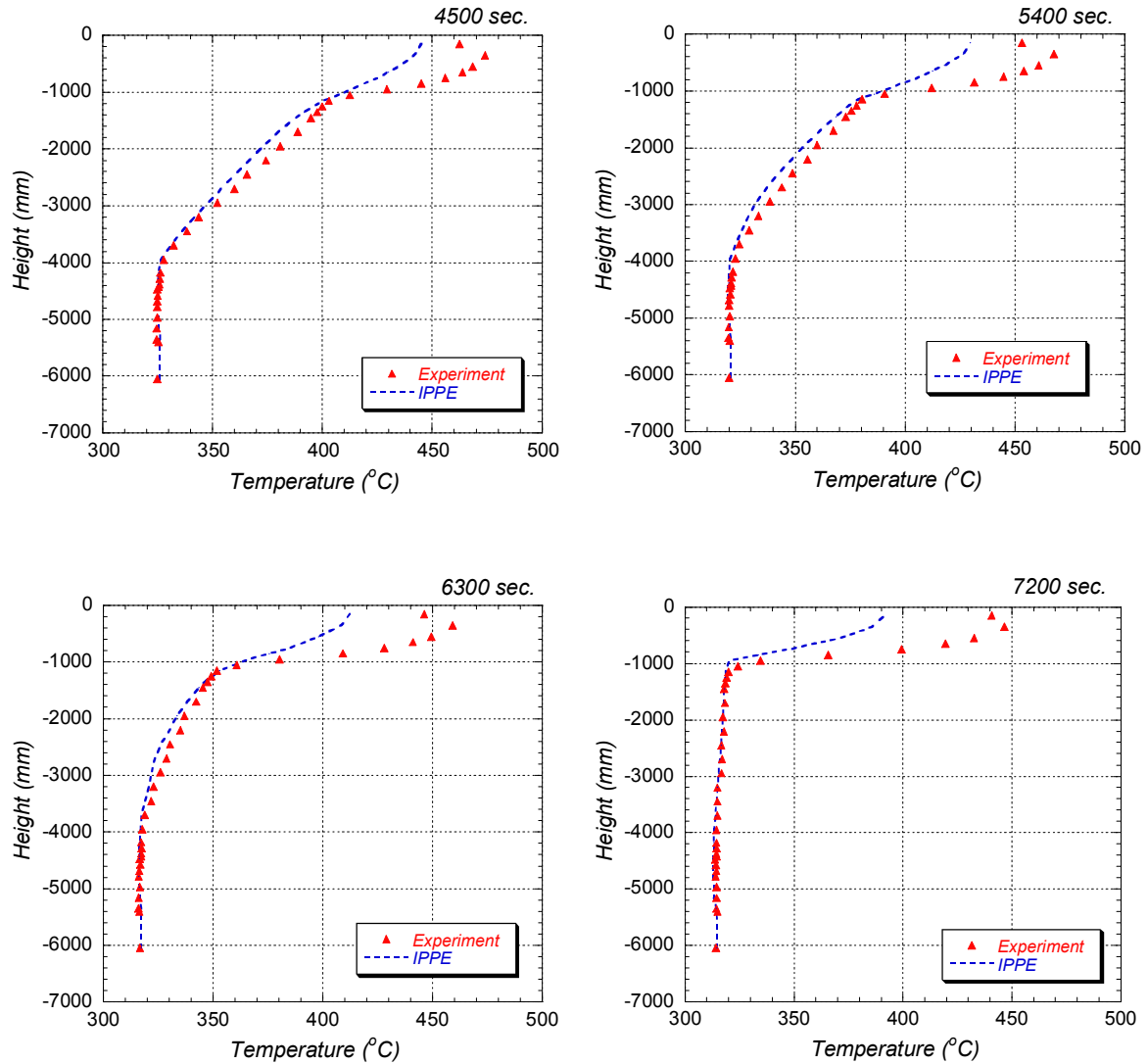


FIG. 168. Comparison of steady state and transient results on TC plug.

9. CONCLUSIONS

The CRP was carried out between 2008 and 2012, and eight research organizations from seven countries with an active programme on SFRs - namely China, France, India, Japan, Republic of Korea, Russian Federation and the USA - contributed to this CRP. The experimental data for the benchmark analysis were provided by JAEA and concerned the measurements of thermal stratification of sodium observed in the upper plenum of the Monju RV at a turbine trip test performed during the original SST of the reactor. In particular the CRP participants were provided with the vertical temperature distribution and outlet temperatures of fuel subassemblies measured during the test. The thermal-hydraulic simulations performed in view of the subsequent comparison with the experimental data were rather challenging due to the complex geometry of the upper plenum of the Monju RV which, in particular, includes an inner barrel with many flow holes, as well as an upper core structure (UCS) composed of fingers, control rod guide tubes (CRGTs), and flow guide tubes (FGTs).

Based on the geometry and the boundary conditions provided by JAEA, a simplified model (1/6 sector model) with detail meshing around each flow hole on the inner barrel and porous media approach for the UCS region was developed, and preliminary calculations were carried out. Different turbulence models and/or heat capacity of the UCS were applied.

The following results were obtained;

- In the steady state calculations, temperatures on the thermocouple tree (TC-plug) in the upper part are approximately 5–10°C lower than measured ones;
- Two kinds of solutions, i.e. buoyancy driven and momentum driven solution, were obtained in the steady state calculations by using different numerical schemes, namely time-marching approach and iterative method;
- In the transient calculations, the thermal stratification front moves upwards faster than shown by the measured data.

The CRP participants deem that the problem associated with the temperature discrepancies on the TC-plug was caused by a few percent of energy imbalance between the given temperature values imposed as boundary conditions and the actual values.

As far as discrepancies between simulation results and test data for the thermal stratification pattern over time, the following possible justifications were suggested:

- Influence of the thermal conductivity of the inner barrel, which was neglected in the simulation models;
- Pressure loss coefficients of the UCS assumed in the porous model were too small, and
- The calculated pressure loss through the holes on the inner barrel was too.

Therefore, in more refined simulations the thermal conductivity of the inner barrel and/or larger pressure loss coefficients of UCS were implemented in both simplified and full-sector models. However both factors could not explain the discrepancies with the experimental data. Too high pressure loss of the flow through the inner barrel holes was then anticipated to be the main source of the discrepancies. As a consequence the CRP participants focused on this issue and parametric simulations were performed using both simplified and full-sector models. By considering round edge instead of sharp edge holes, the simulation results with both models agreed pretty well with the experimental data, confirming the importance of the bypass flow through the inner barrel holes. However, since the actual shape of these holes is not specified, the analysis with round edge holes remains only a speculation at this point. Different hole profiles (with chamfer instead of fillet) and the effect of one-sided rounding still need to be evaluated.

In conclusion, the main achievements drawn from the benchmark analyses and the intense discussions between the CRP participants can be summarized as follows:

- Analytical capabilities of the participating organizations in the field in-vessel sodium thermal hydraulics, especially meshing and algorithm selection criteria, were improved by this CRP which presented challenging issues due to the complex geometry of Monju as well as the involved phenomena;
- In the steady state calculations, two kinds of solutions were obtained by different calculation approaches. The momentum driven solutions were considered as the actual flow pattern in the upper plenum of Monju RV at the 40% rated power operational condition;
- Turbulence models based on the standard k- ϵ model for high Reynolds number and the thermal capacity of the UIS did not significantly affect the moving up rate of the

thermal stratification front, even applying the higher order upwind method to the advection terms, and

- Since the pressure drop through the holes on the inner barrel strongly affect the moving-up rate of the thermal stratification front, the CRP participants concluded that the shape of the flow hole edge is an important factor for the correct prediction of this phenomenon.

REFERENCES

- [1] TSUBOKURA, M., KOBAYASHI, T., NAKASHIMA, T., NOUZAWA, T., NAKAMURA, T., ZHANG, H., ONISHI, K., OSHIMA, N., Computational visualization of unsteady flow around vehicles using high performance computing, *Computers & Fluids*, **38** (2009), pp. 981–990.
- [2] YOSHIKAWA, S., MINAMI, M., “Data description for coordinated research project on benchmark analyses of sodium natural convection in the upper plenum of the Monju reactor vessel under supervisory of the IAEA TWG-FR” Technical Report JAEA-Data/Code 2008-024, Japan Atomic Energy Agency, Japan (2009).
- [3] OHIRA, H., HONDA, K., SOTSU, M., “Numerical simulations of upper plenum thermal-hydraulics of Monju reactor vessel using high resolution mesh models”, Proceedings of the 14th International Topical Meeting on Nuclear Reactor Thermal Hydraulics (NURETH-14), Toronto, Canada, September 25–29, 2011.
- [4] MOCHIZUKI, H., TAKANO, M., “Analysis of thermal stratification in the upper plenum of the Monju reactor vessel – effect of chamfer of flow-hole on thermal stratification”, Proceedings of the 14th International Topical Meeting on Nuclear Reactor Thermal Hydraulics (NURETH-14), Toronto, Canada, September 25–29, 2011.
- [5] NISHI, Y., UEDA, N., YOSHIKAWA, S., MIYAKAWA, A., KATO, M., “Benchmark analyses of sodium convection in upper plenum of the Monju reactor vessel - comparison between plant system analysis code CERES and CFD code”, Proceedings of the 14th International Topical Meeting on Nuclear Reactor Thermal Hydraulics (NURETH-14), Toronto, Canada, September 25–29, 2011.
- [6] BIEDER, U., FAUCHET, G., YOSHIKAWA, S., “Trio_U analysis of natural convection in the upper plenum of the Monju reactor”, Proceedings of the 14th International Topical Meeting on Nuclear Reactor Thermal Hydraulics (NURETH-14), Toronto, Canada, September 25–29, 2011.
- [7] SHIBAHARA, M., TAKATA, T., YAMAGUCHI, A., “Numerical analysis of thermal stratification in the reactor upper plenum of Monju with 1/3 sector and full sector models”, Proceedings of the 14th International Topical Meeting on Nuclear Reactor Thermal Hydraulics (NURETH-14), Toronto, Canada, September 25–29, 2011.
- [8] SOFU, T., THOMAS, J., “Analysis of thermal stratification in the upper plenum of the Monju reactor vessel”, Proceedings of the 14th International Topical Meeting on Nuclear Reactor Thermal Hydraulics (NURETH-14), Toronto, Canada, September 25–29, 2011.
- [9] ABRAHAM, J., VELUSAMY, K., CHELLAPANDI, P., “Computational fluid dynamic investigation of thermal stratification in the hot pool of Monju reactor and comparison with measured data”, Proceedings of the 14th International Topical Meeting on Nuclear Reactor Thermal Hydraulics (NURETH-14), Toronto, Canada, September 25–29, 2011.
- [10] SOFU, T., “Parametric analysis of thermal stratification during the Monju turbine trip test”, Proceedings of the International Congress on Advances in Nuclear Power Plants (ICAPP 12), Chicago, USA, June 24–28, 2012.

- [11] IDEL'CIK I.E., Mémento des pertes de charges: Coefficient de pertes de charge singulières et de perte de charge par frottement, Direction des études et recherches d'Electricité de France (EDF), 1986.
- [12] BLIND, V., BIEDER, U., SOFU, T., "Benchmark Analysis of sodium natural convection in the upper plenum of the Monju reactor vessel: preparation of a simplified model for the upper core structures", Technical Report No. DEN/CAD/DER/SSTH/LMDL/NT/2009-105, CEA, France, 2009.
- [13] <http://www-trio-u.cea.fr/>
- [14] DUCROS, F., BIEDER, U., CIONI, O., FORTIN, T., FOURNIER, B., FAUCHET, G., QUÉMÉRÉ, P., Verification and validation considerations regarding the qualification of numerical schemes for LES for dilution problems, Nuclear Engineering and Design, **240** (2010), pp. 2123-2130.
- [15] LAUNDER, B. E., SPALDING, D. B., The numerical computation of turbulent flows, Computer Methods in Applied Mechanics and Eng., Vol. **3** (1974), pp. 269-289.
- [16] CD-ADAPCO GROUP, STAR-CD, ver. 3.2, Computational Dynamics Limited (2005).
- [17] BLIND, V., BIEDER, U., SOFU, T., "Preparation of simplified model of upper core structures", Technical Report No. DEN/CAD/DER/SSTH/LMDL/NT/2009-105/A, CEA, France (2009).
- [18] STAR-CD Versions 4.08-12, <http://www.cd-adapco.com/products/STAR-CD/>, CD-adapco Inc, Melville, NY (2009-2011).
- [19] BIEDER, U., FAUCHET, G., YOSHIKAWA, S., "TRIO_U analysis of natural convection in the upper plenum of the Monju reactor", Proceedings of the 14th International Topical Meeting on Nuclear Reactor Thermal Hydraulics (NURETH-14), Toronto, Ontario, Canada, September 25–29, 2011.
- [20] TSUBOKURA, M., KOBAYASHI, T., NAKASHIMA, T., NOUZAWA, T., NAKAMURA, T., ZHANG, H., ONISHI, K., OSHIMA, N., Computational visualization of unsteady flow around vehicles using high performance computing, Computers & Fluids, **38** (2009), pp. 981–990.
- [21] RHIE, C. M., CHOW, R. L., "Numerical study of the turbulent flow past an airfoil with trailing edge separation," AIAA J., **21**, (1983), pp.1525-1532.
- [22] VIOLLET, P-L., Mécanique des fluides à masse volumique variable. Aérodynamique, thermohydraulique, écoulements stratifiés, transferts de chaleur, Presses de l'école nationale des Ponts et chaussées, Paris (1997).
- [23] TENCHINE, D., Some thermalhydraulic challenges in sodium cooled fast reactors, Nuclear Engineering and Design, **240** (2010), pp. 1195–1217.
- [24] BIEDER, U., "Benchmark analyses of sodium natural convection in the upper plenum of the Monju reactor vessel: further analysis of the pulp trip experiment", Technical Report No. CEA/DEN/CAD/DER/SSTH/LMDL/NT/2009-112/A, CEA, France, 2009.
- [25] YAMAGUCHI, K., "IAEA CRP on natural convection tests in Monju", Proc. of the IAEA Annual Meeting of the TWGFR, Beijing, China, May 15–19, 2006.
- [26] SOFU, T., THOMAS, J., FANNING, T., "Analysis of thermal stratification in the upper plenum of the Monju reactor vessel using a simplified model", Second Research Coordination Meeting of the IAEA CRP on Benchmark Analysis of Monju Natural Convection, Marcoule, France, 12–14 October, 2009.

- [27] BLIND, V., BIEDER, U., "WP 2c: Porous body formulation for the region between core top and upper core structure," Second Research Coordination Meeting of the IAEA CRP on 'Benchmark Analyses of Sodium Natural Convection in the Upper Plenum of the Monju Reactor Vessel', Marcoule, France, 12–14, October 2009.
- [28] KUZMIN, D., TUREK, S., High-resolution FEM-TVD schemes based on a fully multi-dimensional flux limiter, *Journal of Computational Physics*, **198** (2004), pp. 131–158.
- [29] DUCROS, F., BIEDER, U., CIONI, O., FORTIN, T., FOURNIER, B., FAUCHET, G., QUÉMÉRÉ, P., Verification and validation considerations regarding the qualification of numerical schemes for LES for dilution problems, *Nuclear Engineering and Design*, **240** (2010), Issue 9, pp. 2123–2130.
- [30] KAYS W. M., Turbulent Prandtl Number: Where are we?, *Transactions of the ASME Journal of Heat Transfer*, **116** (1994), pp. 284–295.
- [31] IDEL'CIK I.E., "Mémento des pertes de charges: Coefficient de pertes de charge singulières et de perte de charge par frottement", Direction des études et recherches d'Electricité de France (EDF), 1986.
- [32] BLIND, V., BIEDER, U., SOFU, T., "Benchmark analysis of sodium natural convection in the upper plenum of the Monju reactor vessel: Preparation of a simplified model for the Upper Core Structures," CEA Technical Report No. DEN/CAD/DER/SSTH/LMDL/NT/2009-105/A, 2009, France.
- [33] MIYAKAWA, A., "System Start Up Test of the Prototype Fast Breeder Reactor Monju", *IAEA R&D Review* (2006), pp. 21.
- [34] MOCHIZUKI, H., Development of the plant dynamics analysis code NETFLOW++, *Nuclear Engineering and Design*, **240** (2010), pp. 577–587.

LIST OF ABBREVIATIONS

CRGT	Control rod guide tube
CRP	Coordinated research project
EV	Evaporator
FBR	Fast breeder reactor
FGT	Flow guide tube
GEN IV	Generation IV
GIF	Generation IV International Forum
IHX	Intermediate heat exchanger
ISI	In-service inspection
PHTS	Primary heat transport system
RCM	Research coordination meeting
RV	Reactor vessel
SFR	Sodium cooled fast reactor
SG	Steam generator
SH	Super heater
SHTS	Secondary heat transport system
SST	System startup test
UCS	Upper core structure
UIS	Upper instrumentation structure
TWG-FR	Technical Working Group on Fast Reactors

CONTRIBUTORS TO DRAFTING AND REVIEW

Bieder, U.	French Alternative Energies and Atomic Energy Commission (CEA), France
Choi, SK.	Korea Atomic Energy Research Institute (KAERI), Republic of Korea
Mochizuki, H.	University of Fukui, Japan
Monti, S.	International Atomic Energy Agency (IAEA)
Ohira, H.	Japan Atomic Energy Agency (JAEA), Japan
Shvetsov, I.	Institute of Physics and Power Engineering (IPPE), Russian Federation
Sofu, T.	Argonne National Laboratory (ANL), USA.
Stanculescu, A.	International Atomic Energy Agency (IAEA)
Thomas, J.W.	Argonne National Laboratory (ANL), USA.
Toti, A.	International Atomic Energy Agency (IAEA)
Velusamy, K.	Indira Gandhi Center for Atomic Energy (IGCAR), India
Xu, Y.	China Institute of Atomic Energy (CIAE), China
Yoshikawa, S.	Japan Atomic Energy Agency (JAEA), Japan



ORDERING LOCALLY

In the following countries, IAEA priced publications may be purchased from the sources listed below or from major local booksellers.

Orders for unpriced publications should be made directly to the IAEA. The contact details are given at the end of this list.

AUSTRALIA

DA Information Services

648 Whitehorse Road, Mitcham, VIC 3132, AUSTRALIA
Telephone: +61 3 9210 7777 • Fax: +61 3 9210 7788
Email: books@dadirect.com.au • Web site: <http://www.dadirect.com.au>

BELGIUM

Jean de Lannoy

Avenue du Roi 202, 1190 Brussels, BELGIUM
Telephone: +32 2 5384 308 • Fax: +32 2 5380 841
Email: jean.de.lannoy@euronet.be • Web site: <http://www.jean-de-lannoy.be>

CANADA

Renouf Publishing Co. Ltd.

5369 Canotek Road, Ottawa, ON K1J 9J3, CANADA
Telephone: +1 613 745 2665 • Fax: +1 643 745 7660
Email: order@renoufbooks.com • Web site: <http://www.renoufbooks.com>

Bernan Associates

4501 Forbes Blvd., Suite 200, Lanham, MD 20706-4391, USA
Telephone: +1 800 865 3457 • Fax: +1 800 865 3450
Email: orders@bernan.com • Web site: <http://www.bernan.com>

CZECH REPUBLIC

Suweco CZ, spol. S.r.o.

Klecakova 347, 180 21 Prague 9, CZECH REPUBLIC
Telephone: +420 242 459 202 • Fax: +420 242 459 203
Email: nakup@suweco.cz • Web site: <http://www.suweco.cz>

FINLAND

Akateeminen Kirjakauppa

PO Box 128 (Keskuskatu 1), 00101 Helsinki, FINLAND
Telephone: +358 9 121 41 • Fax: +358 9 121 4450
Email: akatilaus@akateeminen.com • Web site: <http://www.akateeminen.com>

FRANCE

Form-Edit

5 rue Janssen, PO Box 25, 75921 Paris CEDEX, FRANCE
Telephone: +33 1 42 01 49 49 • Fax: +33 1 42 01 90 90
Email: fabien.boucard@formedit.fr • Web site: <http://www.formedit.fr>

Lavoisier SAS

14 rue de Provigny, 94236 Cachan CEDEX, FRANCE
Telephone: +33 1 47 40 67 00 • Fax: +33 1 47 40 67 02
Email: livres@lavoisier.fr • Web site: <http://www.lavoisier.fr>

L'Appel du livre

99 rue de Charonne, 75011 Paris, FRANCE
Telephone: +33 1 43 07 50 80 • Fax: +33 1 43 07 50 80
Email: livres@appeldulivre.fr • Web site: <http://www.appeldulivre.fr>

GERMANY

Goethe Buchhandlung Teubig GmbH

Schweitzer Fachinformationen
Willstätterstrasse 15, 40549 Düsseldorf, GERMANY
Telephone: +49 (0) 211 49 8740 • Fax: +49 (0) 211 49 87428
Email: s.dehaan@schweitzer-online.de • Web site: <http://www.goethebuch.de>

HUNGARY

Librotade Ltd., Book Import

PF 126, 1656 Budapest, HUNGARY
Telephone: +36 1 257 7777 • Fax: +36 1 257 7472
Email: books@librotade.hu • Web site: <http://www.librotade.hu>

INDIA

Allied Publishers

1st Floor, Dubash House, 15, J.N. Heredi Marg, Ballard Estate, Mumbai 400001, INDIA
Telephone: +91 22 2261 7926/27 • Fax: +91 22 2261 7928
Email: alliedpl@vsnl.com • Web site: <http://www.alliedpublishers.com>

Bookwell

3/79 Nirankari, Delhi 110009, INDIA
Telephone: +91 11 2760 1283/4536
Email: bkwell@nde.vsnl.net.in • Web site: <http://www.bookwellindia.com>

ITALY

Libreria Scientifica "AEIOU"

Via Vincenzo Maria Coronelli 6, 20146 Milan, ITALY
Telephone: +39 02 48 95 45 52 • Fax: +39 02 48 95 45 48
Email: info@libreriaaeiou.eu • Web site: <http://www.libreriaaeiou.eu>

JAPAN

Maruzen Co., Ltd.

1-9-18 Kaigan, Minato-ku, Tokyo 105-0022, JAPAN
Telephone: +81 3 6367 6047 • Fax: +81 3 6367 6160
Email: journal@maruzen.co.jp • Web site: <http://maruzen.co.jp>

NETHERLANDS

Martinus Nijhoff International

Koraalrood 50, Postbus 1853, 2700 CZ Zoetermeer, NETHERLANDS
Telephone: +31 793 684 400 • Fax: +31 793 615 698
Email: info@nijhoff.nl • Web site: <http://www.nijhoff.nl>

Swets Information Services Ltd.

PO Box 26, 2300 AA Leiden
Dellaertweg 9b, 2316 WZ Leiden, NETHERLANDS
Telephone: +31 88 4679 387 • Fax: +31 88 4679 388
Email: tbeysens@nl.swets.com • Web site: <http://www.swets.com>

SLOVENIA

Cankarjeva Založba dd

Kopitarjeva 2, 1515 Ljubljana, SLOVENIA
Telephone: +386 1 432 31 44 • Fax: +386 1 230 14 35
Email: import.books@cankarjeva-z.si • Web site: http://www.mladinska.com/cankarjeva_zalozba

SPAIN

Diaz de Santos, S.A.

Librerias Bookshop • Departamento de pedidos
Calle Albasanz 2, esquina Hermanos Garcia Noblejas 21, 28037 Madrid, SPAIN
Telephone: +34 917 43 48 90 • Fax: +34 917 43 4023
Email: compras@diazdesantos.es • Web site: <http://www.diazdesantos.es>

UNITED KINGDOM

The Stationery Office Ltd. (TSO)

PO Box 29, Norwich, Norfolk, NR3 1PD, UNITED KINGDOM
Telephone: +44 870 600 5552
Email (orders): books.orders@tso.co.uk • (enquiries): book.enquiries@tso.co.uk • Web site: <http://www.tso.co.uk>

UNITED STATES OF AMERICA

Bernan Associates

4501 Forbes Blvd., Suite 200, Lanham, MD 20706-4391, USA
Telephone: +1 800 865 3457 • Fax: +1 800 865 3450
Email: orders@bernan.com • Web site: <http://www.bernan.com>

Renouf Publishing Co. Ltd.

812 Proctor Avenue, Ogdensburg, NY 13669, USA
Telephone: +1 888 551 7470 • Fax: +1 888 551 7471
Email: orders@renoufbooks.com • Web site: <http://www.renoufbooks.com>

United Nations

300 East 42nd Street, IN-919J, New York, NY 1001, USA
Telephone: +1 212 963 8302 • Fax: 1 212 963 3489
Email: publications@un.org • Web site: <http://www.unp.un.org>

Orders for both priced and unpriced publications may be addressed directly to:

IAEA Publishing Section, Marketing and Sales Unit, International Atomic Energy Agency
Vienna International Centre, PO Box 100, 1400 Vienna, Austria
Telephone: +43 1 2600 22529 or 22488 • Fax: +43 1 2600 29302
Email: sales.publications@iaea.org • Web site: <http://www.iaea.org/books>

International Atomic Energy Agency
Vienna
ISBN 978-92-0-109614-2
ISSN 1011-4289